Isotope measurements of carbonyl sulfide

Sophie L. Baartman

FSC
www.fsc.org

MIX
Paper from
responsible sources

Isotope measurements of carbonyl sulfide

Isotopen metingen van carbonylsulfide

(met een samenvatting in het Nederlands)

Proefschrift

ter verkrijging van de graad van doctor aan de Universiteit Utrecht op gezag van de rector magnificus, prof.dr. H.R.B.M. Kummeling, ingevolge het besluit van het college voor promoties in het openbaar te verdedigen op woensdag 11 oktober 2023 des middags te 2.15 uur

door

Sophia Louise Baartman

geboren op 3 augustus 1993 te Alkmaar

Promotor: Prof. dr. M. C. Krol
Copromotor: Dr. M. E. Popa

Beoordelingscommissie: Prof. dr. W. Peters
                        Prof. dr. T. Röckmann
                        Prof. dr. ir. C. P. Slomp
                        Prof. dr. P. Suntharalingam
                        Dr. L. Wingate

Contents

Summary

The Earth's climate is currently changing due to excessive human greenhouse gas emissions. It is necessary to drastically reduce these emissions in order to limit future climate change and prevent far reaching, and even irreversible, consequences for the environment. Further understanding of the climate system and its feedback mechanisms is needed for making accurate future climate projections and providing information for mitigation practices.

Carbon dioxide (CO_2) is the most important greenhouse gas, so it is essential to accurately understand the carbon cycle and its response to climate change. The largest sink of CO_2 is photosynthetic uptake by the terrestrial biosphere. However, directly measuring the isolated photosynthesis flux (gross primary productivity - GPP) is difficult because the terrestrial biosphere also emits CO_2 through respiration processes.

Another uncertainty in current climate models is the effect of aerosol particles in the stratosphere. Stratospheric sulfur aerosols (SSA), in particular, are known to reflect incoming solar radiation, thereby cooling the planet. The main contributor to the formation of the SSA layer under volcanic quiescent conditions is, however, still under debate.

Carbonyl sulfide (COS) is the most abundant sulfur-containing trace gas in the atmosphere, with a tropospheric mole fraction of around 500 parts per trillion (ppt). COS is taken up by plants through a similar pathway as CO_2, and has therefore been proposed as a proxy for estimating GPP. It has been observed that the rate of COS uptake by plants is proportional to that of CO_2. Thus, COS measurements can potentially be used for estimating GPP. Furthermore, COS has a relatively long lifetime of approximately 2 years, allowing it to be transported to the stratosphere. Therefore, it has been proposed as the most likely candidate for the main precursor of background SSA in volcanically quiescent times.

The budget of COS is currently under scrutiny. The largest natural source of COS is the ocean, through direct and indirect emissions via carbon disulfide (CS_2) and dimethyl sulfide (DMS). Other sources are mainly anthropogenic, including emissions during rayon and aluminum production, and coal combustion. Biomass burning and agricultural soils are also small sources of COS. The terrestrial sinks of COS are the large plant uptake flux mentioned earlier and a small soil uptake flux. Atmospheric sinks of COS include oxidation by OH, stratospheric photolysis, and the reaction with oxygen radicals. Despite significant measurement and modeling efforts to quantify the sources and sinks, the budget of COS is still not fully understood, with a large missing source of around 230 to 432 GgS a^{-1} in current budget estimations.

There are several techniques to measure the COS mole fraction that can help to better constrain the COS budget. Eddy Covariance methods can be used to estimate ecosystem fluxes. Long-term flask measurements of COS mole fractions have been performed at multiple NOAA stations around the globe since the year 2000, and satellite observations can be used to estimate both the latitudinal COS mole fraction gradient as well as the vertical profile. However, identifying specific sources and sinks of COS is difficult when only making use of these above-mentioned techniques.

Isotopes can be used to identify sources based on their distinct isotopic fingerprint and to quantify sink contributions by calculating isotope fractionation factors for these sink processes. Isotope measurements can thus provide valuable information regarding the sources and sinks of COS, as well as the potential role of COS as the main source of stratospheric sulfur aerosols (SSA).

During this PhD project, a measurement system was developed for determining the sulfur and carbon isotopic composition of COS in air, with the general goal of increasing the knowledge on the global COS budget. The system was optimized to obtain a precision that is sufficient for observing the small isotope signals expected in atmospheric COS, from relatively small air samples of around 2 - 6 L. **Chapter 2** of this thesis describes the newly developed system for measuring the sulfur isotopologues of COS, which was later expanded to measure the carbon isotope ratio δ^{13}C, as described in **Chapter 3**. With our system, we achieved precision levels (1σ) of 2.5 ‰, 0.9 ‰ and 2.5 ‰ for δ^{33}S, δ^{34}S, and δ^{13}C, respectively.

The first sample measurements presented in this thesis are a series of ambient air measurements in Utrecht, which are discussed in **Chapter 2**. Based on this dataset, we found ambient background COS sulfur isotopic compositions of +1.0 ± 3.4 ‰ and +15.5 ± 0.8 ‰ versus VCDT for δ^{33}S and δ^{34}S, respectively. We hypothesized that Utrecht likely receives relatively low amounts of COS-containing pollution, due to the absence of clear enhancements of COS, combined with relatively high background δ^{34}S. We observed a seasonal variation in COS mole fraction, but no significant change in isotope values. During this study period, we also collected air samples inside a highway tunnel in Utrecht to quantify and isotopically characterize the vehicle emissions. We found small emissions with relatively depleted sulfur isotope signatures of δ^{33}S = −71.5 ± 21.2 ‰ and δ^{34}S = +6.9 ± 4.7 ‰.

To investigate whether COS could be the main precursor of SSA, we measured the isotopic composition of air samples taken in the upper troposphere lower stratosphere (UTLS) region, as presented in **Chapter 3**. These samples were collected during two campaigns: StratoClim AMA-17, a high-altitude aircraft campaign in Kathmandu in 2017, and HEMERA - KLIMAT 2021, a zero-pressure balloon campaign, launched from Esrange, Sweden. Based on the COS mole fraction and isotopic composition measurements, and model simulations with the TM5 model, we estimated apparent fractionation factors of the stratospheric COS sink. We then compared our measured and modeled fractionation results with fractionation factors from previous studies.

As expected, we found decreasing mole fractions with altitude, for both sampling campaigns, with the strongest decrease observed above the tropopause, where photolysis rapidly destroys COS. We observed relatively small fractionation factors for ^{34}S ($^{34}\varepsilon$). These first ever measurements of δ^{34}S in COS in the stratosphere indicate that COS is likely the main

precursor of SSA. We did, however, find a much smaller than expected value for ^{13}C fractionation ($^{13}\varepsilon$), but this value was based on the KLIMAT 2021 data only, which showed signs of possible contamination or drift in COS mole fractions. Therefore, we are cautious in drawing firm conclusions from this estimated $^{13}\varepsilon$ value at this moment.

The TM5 model simulations yielded similar vertical mole fraction profiles to the measured data, especially for StratoClim AMA-17. Based on the modeled isotope results, we deduced that atmospheric mixing and transport processes likely dilute the isotope fractionation signal significantly: when using a +10 ‰ fractionation due to stratospheric destruction by photolysis as model input, the apparent fractionation in the model output is only +3.2 ‰; the difference is due to atmospheric mixing.

Another goal of this PhD project was to characterize isotopic fractionation during the uptake of COS by plants. We conducted flow-through chamber experiments, using both a C3 and a C4 species: sunflower and papyrus, respectively. While the plants were exposed to varying amounts of light, we measured CO_2 and COS mole fractions online and took samples for analysis of both CO_2 and COS isotopic composition. The data from these experiments are presented in **Chapter 4**.

The CO_2 isotope discrimination values for $^{13}C_{CO_2}$ and $^{18}O_{CO_2}$ ($^{13}\Delta_{CO_2}$ and $^{18}\Delta_{CO_2}$) increased with decreasing CO_2 uptake flux, as expected. The CO_2 isotope discrimination values also correlated with the ratio of ambient versus leaf internal CO_2 mole fraction (C_i/C_a). For $^{34}S_{COS}$ discrimination, $^{34}\Delta_{COS}$, we estimated values between +2.8 and +3.7 ‰ for sunflower and between +2.5 and +2.7 ‰ for papyrus, which are in the same range as results from previous studies. However, the COS sulfur isotope discrimination during plant uptake displayed less variability than expected and did not correlate with COS uptake flux. Furthermore, we did not find a significant difference in $^{34}S_{COS}$ fractionation between C3 and C4 species, whereas a previous study estimated higher fractionation for C4 species compared to C3 species. For $^{13}C_{COS}$ discrimination, $^{13}\Delta_{COS}$, we found larger values of between +6.1 and +30.9 ‰ for sunflower, and between +3.0 and +32.7 ‰ for papyrus.

This work demonstrated the benefits of using a flow-through gas exchange system for conducting COS uptake and photosynthesis experiments, as this method allows for online monitoring of photosynthesis and COS uptake rates. Furthermore, this method makes it easier to maintain stable environmental conditions inside the chamber compared to a closed-chamber approach. Future plant chamber experiments could focus on expanding the knowledge of the difference in COS isotope fractionation between C3 and C4 species, and could expand the isotope fractionation measurements to more plant species, which would be useful for further up-scaling of COS isotope fractionation values for global modeling. Furthermore, the addition of $^{13}\Delta_{COS}$ and CO_2 isotope discrimination measurements, next to the COS sulfur isotope discrimination, provides useful information on plant functioning and allows for comparison with a wider range of previous studies.

The overarching goal of this PhD project was to expand the current knowledge on COS isotopes by presenting a new method for measuring small air samples with sufficient precision, based on relatively simple principles, and by providing more measurement data. For future studies, we recommend focusing measurements on current knowledge gaps at the fundamental-process scale. For instance, more measurements are needed to characterize plant fractionation, and lab experiments could provide more insights into fractionation dur-

ing stratospheric reactions. Targeting individual (anthropogenic) sources could help in understanding the COS budget. Lastly, combining measurements with modeling is the most promising way to fully understand the COS budget, and future efforts should pursue this pathway.

Nederlandse samenvatting

Het klimaat op aarde verandert momenteel onder invloed van de grote hoeveelheid menselijke uitstoot van broeikasgassen. Het is noodzakelijk om deze uitstoot drastisch te verminderen om toekomstige klimaatverandering te beperken en verstrekkende, zelfs onomkeerbare, gevolgen voor het milieu te voorkomen. Daarnaast is het nodig om meer inzicht te vergaren in het klimaatsysteem en de terugkoppelingsmechanismen om nauwkeurige klimaatvoorspellingen te kunnen maken en informatie te verstrekken voor mitigatiepraktijken.

Koolstofdioxide (CO_2) is het belangrijkste broeikasgas. Daarom is het essentieel om de koolstofcyclus nauwkeurig te begrijpen en hoe deze zal veranderen als reactie op klimaatverandering. De grootste opslag van CO_2 is de fotosynthetische opname door de terrestrische biosfeer. Het kwantificeren van de fotosynthese flux (bruto primaire productiviteit - BPP) is echter moeilijk omdat de terrestrische biosfeer ook CO_2 uitstoot via respiratie.

Een andere onzekerheid in huidige klimaatmodellen is het effect van aerosoldeeltjes in de stratosfeer. Met name stratosferische zwavelaerosolen staan bekend om het weerkaatsen van inkomende zonnestraling en hebben daardoor een verkoelend effect op de planeet. De belangrijkste bijdrager aan de vorming van deze laag van zwavelaerosolen onder vulkanisch rustige omstandigheden is echter nog steeds onderwerp van discussie.

Carbonylsulfide (COS) is het meest voorkomende zwavelhoudende spoorgas in de atmosfeer, met een troposferische molfractie van ongeveer 500 delen per biljoen (ppt). COS wordt opgenomen door planten via een vergelijkbare weg als CO_2 en daarom wordt voorgesteld om COS te gebruiken als een proxy voor het schatten van BPP. Het is waargenomen dat de snelheid van COS opname door planten evenredig is met die van CO_2. Daarom kunnen COS metingen potentieel worden gebruikt voor het schatten van BPP. Daarnaast heeft COS een relatief lange levensduur van ongeveer 2 jaar, waardoor het naar de stratosfeer kan worden getransporteerd. Daarom zou COS de meest waarschijnlijke kandidaat kunnen zijn voor de belangrijkste bron van stratosferische zwavel aerosolen tijdens vulkanisch rustige periodes.

Het budget van COS staat momenteel ter discussie. De grootste natuurlijke bron van COS is de oceaan, door directe en indirecte emissies via koolstofdisulfide (CS_2) en dimethylsulfide (DMS). Andere bronnen zijn voornamelijk antropogeen, waaronder emissies tijdens rayon- en aluminiumproductie en kolenverbranding. Biomassa-verbranding en landbouwbodems zijn ook kleine bronnen van COS. De terrestrische opslag van COS bestaat uit de

eerder genoemde grote opname door planten en een kleine opname door de bodem. In de atmosfeer wordt COS vernietigd door de volgende reacties: oxidatie door OH, stratosferische fotolyse en de reactie met zuurstofradicalen. Ondanks aanzienlijke inspanningen op het gebied van meting en modellering om de bronnen en opslagplaatsen van COS te kwantificeren, is het budget van COS nog steeds niet volledig begrepen. In de huidige schattingen van het budget is er nog steeds een grote ontbrekende bron van ongeveer 230 tot 432 GgS a^{-1}.

Er zijn verschillende technieken om de molfractie van COS te meten die kunnen helpen om het COS budget beter te bepalen. Eddy Covariance-methoden kunnen worden gebruikt om ecosysteemfluxen te schatten. Langetermijnmetingen van de molfracties van COS worden uitgevoerd op meerdere NOAA-stations over de hele wereld sinds het jaar 2000, en satellietwaarnemingen kunnen worden gebruikt om zowel de longitudinale gradiënt als verticale profielen van COS te schatten. Het is echter moeilijk om specifieke bronnen en opslagplaatsen van COS te identificeren wanneer alleen gebruik wordt gemaakt van deze eerder genoemde technieken.

Isotopen kunnen worden gebruikt om bronnen te identificeren op basis van hun unieke isotopische vingerafdruk en de omvang van opslagplaatsen kan worden gekwantificeerd door isotopenfractionatiefactoren van deze opslagprocessen te bepalen. Isotoopmetingen kunnen dus waardevolle informatie verschaffen over de bronnen en opslagplaatsen van COS, evenals de mogelijke rol van COS als de belangrijkste bron van achtergrond-stratosferische zwavelaerosolen.

Tijdens dit promotieonderzoek is een meetsysteem ontwikkeld voor het bepalen van de zwavel- en koolstofisotopische samenstelling van COS in lucht, met als doel om de algemene kennis van het COS-budget te vergroten. Het systeem is geoptimaliseerd om een precisie te verkrijgen die voldoende is om de verwachte kleine atmosferische isotopensignalen te observeren in COS, van relatief kleine luchtsamples van ongeveer 2 - 6 L. **Hoofdstuk 2** van dit proefschrift beschrijft het nieuw ontwikkelde meetsysteem voor het meten van de zwavelisotopologen van COS. Het systeem werd later uitgebreid om ook de koolstofisotoop-verhouding $\delta^{13}C$ te meten, zoals beschreven in **Hoofdstuk 3**. Met ons systeem hebben we (1σ) precisies behaald van 2,5 ‰, 0,9 ‰ en 2,5 ‰ voor respectievelijk $\delta^{33}S$, $\delta^{34}S$ en $\delta^{13}C$.

De eerste luchtmonstermetingen die in dit proefschrift worden gepresenteerd zijn metingen van buitenlucht in Utrecht, die beschreven worden in **Hoofdstuk 2**. Op basis van deze dataset, hebben we achtergrondwaarden gevonden voor de zwavelisotopische samenstelling van COS van respectievelijk +1,0 ± 3,4 ‰ en +15,5 ± 0,8 ‰ versus VCDT, voor $\delta^{33}S$ en $\delta^{34}S$. We vermoeden dat Utrecht waarschijnlijk relatief lage hoeveelheden COS-bevattende vervuiling ontvangt, vanwege de vrij lage waargenomen maximale COS molfractie, in combinatie met een relatief hoge achtergrondwaarde voor $\delta^{34}S$. We hebben een seizoensgebonden trend waargenomen in de molfractie van COS, maar er was geen significante trend aanwezig in de isotopenwaarden. Tijdens deze studieperiode hebben we ook luchtmonsters verzameld in een snelwegtunnel in Utrecht, om voertuigemissies te kwantificeren en de isotopensamenstelling van deze emissies te karakteriseren. We vonden kleine emissies met lage zwavelisotoopsignaturen ten opzichte van achtergrondwaarden: $\delta^{33}S$ = −71,5 ± 21,2 ‰ en $\delta^{34}S$ = +6,9 ± 4,7 ‰.

Om te onderzoeken of COS de belangrijkste bron van stratosfersiche zwavelaerosolen zou kunnen zijn, hebben we de isotopensamenstelling van luchtsamples gemeten die zijn genomen in het bovenste deel van de troposfeer en de onderste laag van de stratosfeer, zoals gepresenteerd in **Hoofdstuk 3**. Deze samples werden verzameld tijdens twee campagnes: StratoClim AMA-17, een vliegtuigcampagne in Kathmandu in 2017, en HEMERA-KLIMAT 2021, een balloncampagne, gelanceerd vanuit Esrange, Zweden. Op basis van de metingen van de COS-molfractie en isotopensamenstelling, en modelsimulaties met het TM5-model, hebben we schijnbare fractionatiefactoren van de stratosferische COS afbraak geschat. Vervolgens hebben we onze gemeten en gemodelleerde resultaten vergeleken met fractionatiefactoren uit eerdere studies.

Zoals verwacht vonden we een afnemende molfractie met toenemende hoogte, voor beide meetcampagnes, met de sterkste afname boven de tropopauze, waar fotolyse COS snel afbreekt. We vonden relatief kleine fractionatiefactoren voor ^{34}S ($^{34}\varepsilon$). Daarom geven deze eerste metingen van δ^{34}S in COS in de stratosfeer aan dat COS waarschijnlijk de belangrijkste voorloper van stratosferische zwavelaerosolen is. We vonden echter een veel kleinere dan verwachte waarde voor ^{13}C-fractionering ($^{13}\varepsilon$), maar deze waarde was alleen gebaseerd op de KLIMAT 2021-gegevens, en de monsters van deze campagne waren mogelijk gecontamineerd. Op dit moment moeten we dus voorzichtig zijn bij het trekken van conclusies uit deze geschatte $^{13}\varepsilon$-waarde.

De modelsimulaties met het TM5-model leverden vergelijkbare verticale molfractieprofielen op als de metingen, vooral voor StratoClim AMA-17. Op basis van de gemodelleerde isotoperesultaten hebben we afgeleid dat atmosferische meng- en transportprocessen waarschijnlijk het isotoopfractionatie-signaal aanzienlijk verdunnen: bij een invoer in het model van +10 ‰ fractionering als gevolg van stratosferische afbraak door fotolyse, is de schijnbare fractionering in de modeluitvoer slechts +3,2 ‰; het verschil is te wijten aan atmosferische menging.

Een ander doel van dit promotieonderzoek was om de isotopische fractionering tijdens de opname van COS door planten te karakteriseren. We hebben plantenkamerexperimenten uitgevoerd met zowel een C3- als een C4-soort: zonnebloem en papyrus, respectievelijk. Terwijl de planten werden blootgesteld aan variërende hoeveelheden licht, hebben we online CO_2- en COS-molfracties gemeten en monsters genomen voor analyse van zowel de CO_2- als de COS-isotopensamenstelling. De data van deze experimenten worden gepresenteerd in **Hoofdstuk 4**.

Zoals verwacht namen de isotopendiscriminatiewaarden van CO_2, $^{13}\Delta C_{CO_2}$ en $^{18}\Delta C_{CO_2}$, toe naarmate de opname van CO_2 afnam. Deze isotopendiscriminatiewaarden correleerden ook met de ratio van interne- versus externe CO_2 molfracties (C_i/C_a). Voor de ^{34}S$_{COS}$-discriminatie, $^{34}\Delta_{COS}$, schatten we waarden tussen +2,8 en +3,7 ‰ voor zonnebloem en tussen +2,5 en +2,7 ‰ voor papyrus. Deze waarden liggen in hetzelfde bereik als de resultaten van eerdere studies. De COS-isotopendiscriminatie tijdens de opname door planten vertoonde echter minder variabiliteit dan verwacht en correleerde niet met de COS-opnameflux. Tijdens onze experimenten hebben we ook geen significant verschil gevonden in ^{34}S$_{COS}$-fractionering tussen C3- en C4-soorten, terwijl een eerdere studie een hogere fractionering vond voor C4-soorten ten opzichte van C3-soorten. Voor ^{13}C$_{COS}$-discriminatie, $^{13}\Delta_{COS}$, vonden we grotere waarden tussen +6,1 en +30,9 ‰ voor zonnebloem en tussen +3,0 en +32,7 ‰ voor papyrus.

Met dit werk hebben we aangetoond dat het gebruik van een plantenkamersysteem met continue luchtdoorstroom geschikt is voor het uitvoeren van COS opname- en fotosynthese-experimenten, omdat het op deze manier mogelijk is om fotosynthese en COS opname on-line te monitoren. Bovendien is het bij deze methode makkelijker om de condities in de plantenkamer stabiel te houden, in vergelijking met een gesloten-kamermethode. Toekomstige experimenten met plantenkamers kunnen zich richten op het vergroten van de kennis over het verschil in COS-isotopenfractionatie tussen C3- en C4-soorten en kunnen de isotopenmetingen uitbreiden naar meer plantensoorten. Dit laatste zou nuttig zijn voor verdere opschaling van COS-isotopenfractionatiewaarden voor modelsimulaites op mondiale schaal. Bovendien biedt de toevoeging van $^{13}\Delta_{COS}$ en CO_2-isotopenmetingen, naast de COS-zwavelisotopen, nuttige informatie over de werking van planten en maakt het vergelijking mogelijk met een breder scala aan eerdere studies.

Het overkoepelende doel van dit promotieproject was om de huidige kennis over COS isotopen uit te breiden door een nieuwe, relatief eenvoudige methode te presenteren voor het meten van kleine luchtmonsters met voldoende precisie, en daarmee meer meetdata te verschaffen. Voor toekomstig onderzoek raden we aan om de metingen voornamelijk te focussen op fundamentele processen. Er zijn bijvoorbeeld meer metingen nodig om de fractionering door planten te karakteriseren, en laboratoriumexperimenten kunnen meer inzicht verschaffen in de COS fractionering in de stratosfeer. Het karakteriseren van de COS isotopensamenstelling van individuele (antropogene) bronnen kan helpen om meer inzicht te krijgen in het COS-budget. Ten slotte is het combineren van metingen met modellering de meest veelbelovende manier om het COS-budget volledig te begrijpen, en voor toekomstige studies zou het goed zijn om dit pad volgen.

1

Introduction

1.1   Climate change

Our climate is always changing under the influence of natural forces. However, since the start of the industrial revolution, it has been humans that have been injecting large amounts of carbon dioxide (CO_2) into the atmosphere. As a result, the atmospheric CO_2 mole fraction has increased from approximately 277 parts per million (ppm) in the year 1750 to 412 ppm in 2020 (Friedlingstein et al., 2022). By absorbing long-wave radiation, CO_2 and other greenhouse gases like methane (CH_4) and nitrous oxide (N_2O) increase the Earth's temperature. Figure 1.1, taken from the sixth Intergovernmental Panel on Climate Change (IPCC) report (Masson-Delmotte et al., 2021), shows the historical reconstructed (for years 1 - 2000) and observed (1850 - 2020) temperature anomaly, relative to the average over 1850 - 1900. Panel b of this figure includes a simulation of the relative temperature as it would be if there were only natural processes influencing temperature change, and a simulation including human and natural forcing. It can be clearly observed that human emissions are the main cause for increasing the Earth's temperature during at least the last century. The IPCC also reports that this change in our climate brings forth many consequences like rising sea-levels and increasing occurrences of weather extremes like drought, floods and long-lasting heat spells (Portner et al., 2022). The impacts of climate change are already being observed world-wide in the form of changing ecosystems, extinction of species, water and food scarcity, storm damage, among many others.

The Earth has already warmed 0.8 to 1.2 °C since pre-industrial times and, if the temperature continues to increase at the current rate, warming will likely reach 1.5 °C between 2030 and 2052 (Allen et al., 2018). In a special report, the IPCC emphasized the importance of limiting warming to +1.5 °C, as the consequences of exceeding such warming will be widespread and likely irreversible (Allen et al., 2018). In order to stay below this +1.5 °C warming scenario, decreasing the rate of emissions of greenhouse gases, especially CO_2, is vital. Limiting the emissions of other greenhouse gases like methane and nitrous oxide is also important as their radiative forcing (W m^{-2}) per molecule is actually higher than that of CO_2. However, the atmospheric mole fractions of these other greenhouse gases are much lower and thus the total radiative forcing of CO_2 is still the most important. Therefore, fully understanding the carbon cycle and how it will respond to increasing mole fractions of atmospheric CO_2 as well as to rising temperatures is essential for making accurate climate projections (Friedlingstein et al., 2022).

Furthermore, fully understanding the Earth's radiative balance and its feedback mechanisms is important for making such climate projections. Figure 1.2 shows a schematic of the radiative balance from the fourth Assessment Report of the IPCC (Solomon et al., 2007). It can be observed that a large amount of long-wave radiation from the Earth's surface is absorbed by greenhouse gases and radiated back to the surface, causing the warming effect. Aerosols in the atmosphere can have both a cooling and a heating effect on the Earth's temperature. Absorption of radiation by aerosol particles could have a similar heating effect as the absorption by GHG's. However, scattering and reflection of shortwave radiation back into space by aerosols has a net cooling effect. Figure 1.3 shows a summary of the estimated net radiative forcing taken from the Fifth Assesment Report of the IPCC (Stocker, 2014), which indicates the large uncertainty regarding the net radiative forcing of aerosols and clouds. Therefore, it is also of high importance to understand the origin and fate of aerosol particles and the formation of clouds, as well as their net radiative forcing.

Changes in global surface temperature relative to 1850–1900

(a) Change in global surface temperature (decadal average) as **reconstructed** (1–2000) and **observed** (1850–2020)

(b) Change in global surface temperature (annual average) as **observed** and simulated using **human & natural** and **only natural** factors (both 1850–2020)
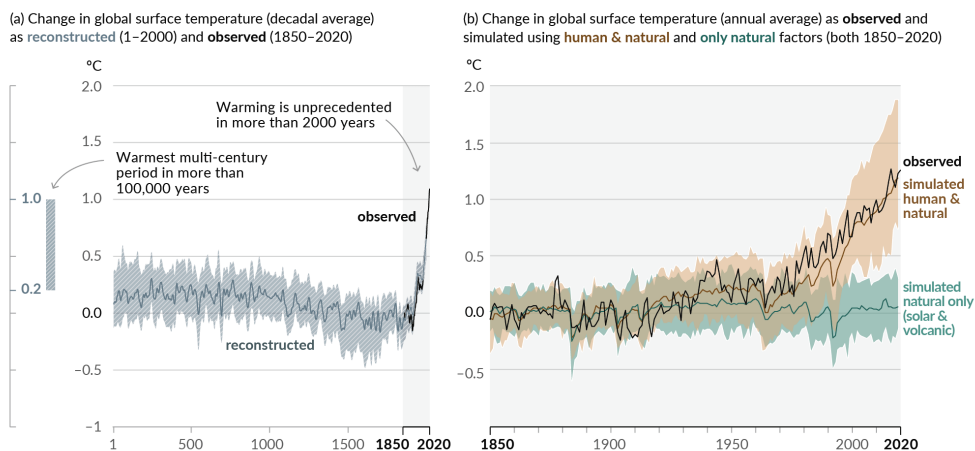

Figure 1.1: Figure adapted from Figure SPM.1 in IPCC, 2021: Summary for Policymakers, History of global temperature change and causes of recent warming (Masson-Delmotte et al., 2021).

Panel (a) Changes in global surface temperature reconstructed from paleoclimate archives (solid grey line, years 1–2000) and from direct observations (solid black line, 1850–2020), both relative to 1850–1900 and decadally averaged. The vertical bar on the left shows the estimated temperature (very likely range) during the warmest multi-century period in at least the last 100,000 years, which occurred around 6500 years ago during the current interglacial period (Holocene). The Last Interglacial, around 125,000 years ago, is the next most recent candidate for a period of higher temperature. These past warm periods were caused by slow (multi-millennial) orbital variations. The grey shading with white diagonal lines shows the very likely ranges for the temperature reconstructions.

Panel (b) Changes in global surface temperature over the past 170 years (black line) relative to 1850–1900 and annually averaged, compared to Coupled Model Intercomparison Project Phase 6 (CMIP6) climate model simulations of the temperature response to both human and natural drivers (brown) and to only natural drivers (solar and volcanic activity, green). Solid coloured lines show the multi-model average, and coloured shades show the very likely range of simulations.
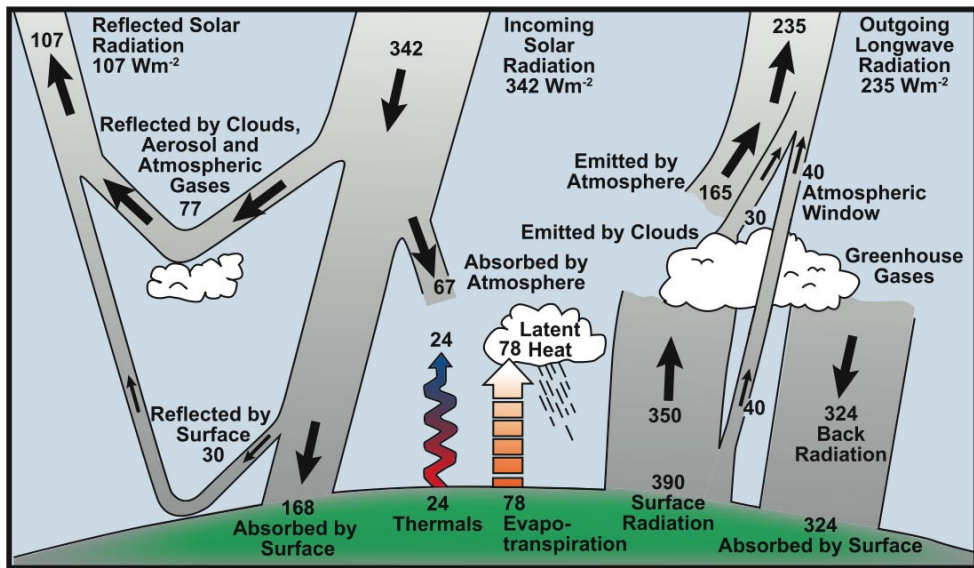
Figure 1.2: Figure from the IPCC fourth assessment report (Solomon et al., 2007). Schematic of the Earth's annual and global mean energy balance. Over the long term, the amount of incoming solar radiation absorbed by the Earth and atmosphere is balanced by the Earth and atmosphere releasing the same amount of outgoing longwave radiation. About half of the incoming solar radiation is absorbed by the Earth's surface. This energy is transferred to the atmosphere by warming the air in contact with the surface (thermals), by evapotranspiration and by longwave radiation that is absorbed by clouds and greenhouse gases. The atmosphere in turn radiates longwave energy back to Earth as well as out to space. The numbers in the figure are in W m^{-2}.
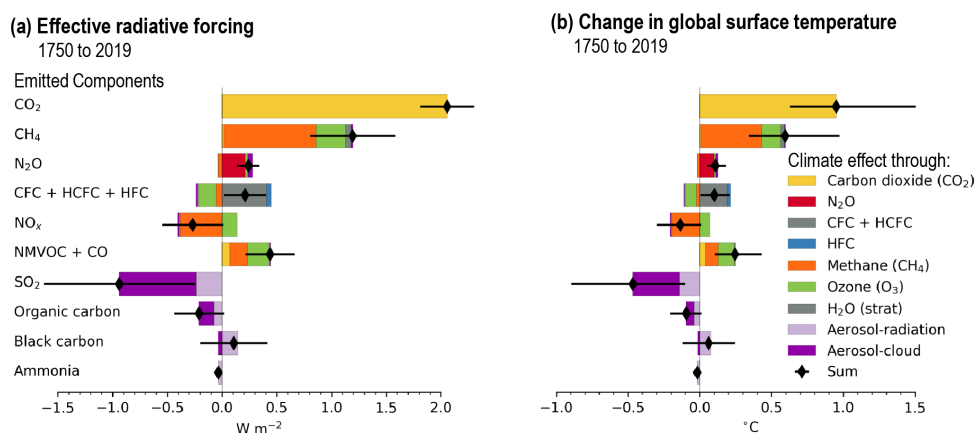
Figure 1.3: Figure adapted from TS.15 in IPCC, 2021: Technical Summary. In: Climate Change 2021: The Physical Science Basis. Contribution of Working Group I to the Sixth Assessment Report of the IPCC (Masson-Delmotte et al., 2021) Panel a shows the contribution to effective radiative forcing from component emissions for 1750-2019, panel b shows the effect of these components on global surface temperature change.

1.1.1 Carbon cycle

The carbon cycle consists of movement of carbon between the following reservoirs: oceans, atmosphere, lithosphere and the biosphere (Figure 1.4) (Masson-Delmotte et al., 2021). The carbon cycle can be split up into a slow and a fast cycle, where the slow cycle represents carbon that is being moved between the lithosphere, oceans and the atmosphere over geological time-scales of 100 to 200 million years.

The fast carbon cycle consist of carbon that is being moved between the biosphere, atmosphere and ocean. This fast carbon cycle determines the amount of CO_2 present in our atmosphere at relevant time-scales of the current global warming. While the carbon cycle is well understood on a fundamental level, uncertainties still exist on the interactions and feedback systems between the changing climate and the carbon fluxes. Furthermore, uncertainties persist on the magnitude of the gross carbon fluxes between the reservoirs.

The most relevant gross carbon fluxes are those between the biosphere and atmosphere, and are called photosynthesis and respiration, as can be seen on the left side of Figure 1.4. Photosynthesis or gross primary production (GPP) is the uptake flux of CO_2 by the biosphere, with a global annual flux of 113 PgC yr^{-1}, and total ecosystem respiration (Re) is the process where sugars and oxygen are used by the plant to produce energy. During this reaction, CO_2 is released, with a total annual flux of 111.1 PgC yr^{-1}. How the terrestrial carbon sink will change in response to increasing atmospheric CO_2 mole fraction and increasing temperatures is still a source of uncertainty in current climate models (Friedlingstein et al., 2022).

On ecosystem scale, the exchange between the biosphere and the atmosphere is called Net Ecosystem Exchange (NEE), and is defined as the difference between GPP and Re:
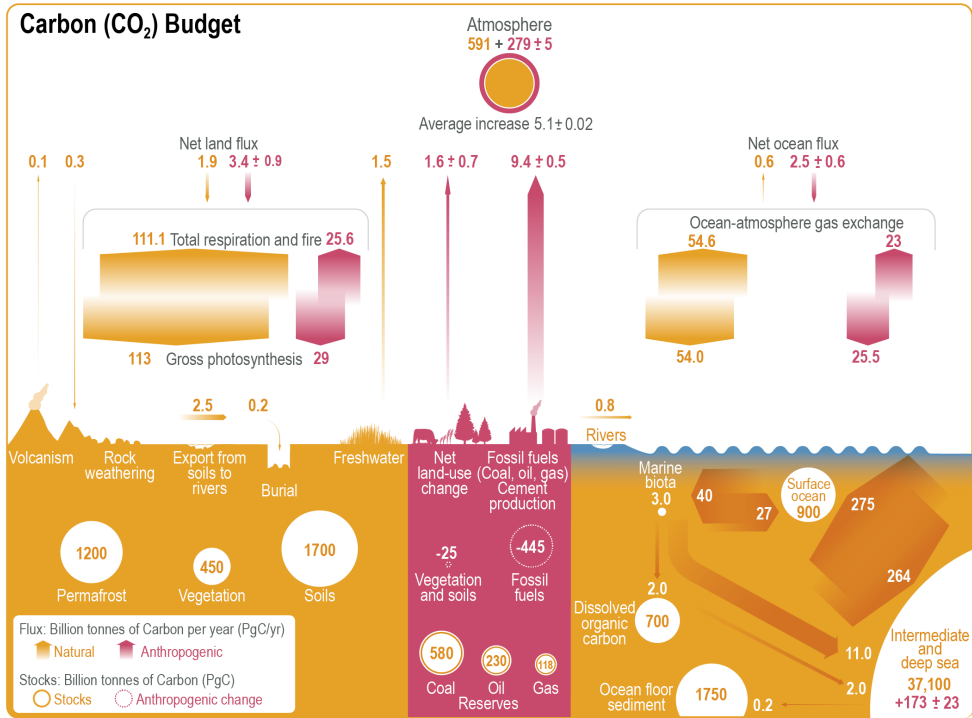
$$NEE = GPP - Re \qquad (1.1.1)$$

Figure 1.4: Figure 5.12 in IPCC, 2021: Chapter 5. In: Climate Change 2021: The Physical Science Basis. Contribution of Working Group I to the Sixth Assessment Report of the Intergovernmental Panel on Climate Change (Masson-Delmotte et al., 2021). Global carbon (CO$_2$ budget (2010-2019) where the yellow arrows represent annual carbon fluxes (in PgC yr^{-1}) associated with the natural carbon cycle, estimated for the time prior to the industrial era, around 1750. Pink arrows represent anthropogenic fluxes averaged over the period 2010–2019. The rate of carbon accumulation in the atmosphere is equal to net land-use change emissions, including land management plus fossil fuel emissions, minus land and ocean net sinks. Circles with yellow numbers represent pre-industrial carbon stocks in PgC. Circles with pink numbers represent anthropogenic changes to these stocks (cumulative anthropogenic fluxes) since 1750.

The two plant fluxes GPP and Re are important to quantify separately as they are affected differently by environmental changes such as increases in global atmospheric CO$_2$ and temperature. Partitioning NEE into GPP and Re is, however, challenging, as measurements of an ecosystem will yield the sum of the two fluxes.

Eddy covariance (EC) measurement techniques include partitioning algorithms that succeed to distinguish between the fluxes (Asaf et al., 2013; Billesbach et al., 2014; Commane et al., 2015; Wehr et al., 2017; Vesala et al., 2022). Stable carbon and oxygen isotope measurements of CO$_2$ can also be used as a tool for partitioning the fluxes (Farquhar et al., 1993; Farquhar and Lloyd, 1993; Wingate et al., 2007; Gentsch et al., 2014). However, these measurements each have their limitations, because they measure net CO$_2$ fluxes, in the case of EC and require intricate algorithms to partition the fluxes (Reichstein et al., 2005; Wohlfahrt

et al., 2012; Kooijmans et al., 2017), or they require additional measurements such as the oxygen isotope composition of water pools, in the case of oxygen isotope measurements of CO_2 (Wingate et al., 2010). Furthermore, EC methods require a homogeneous ecosystem surface and night-time EC measurements are less reliable (Papale et al., 2006; Aubinet et al., 2012).

Another suggested tool for estimating GPP is using the trace gas called carbonyl sulfide (COS or OCS, henceforth referred to as COS). COS is taken up by the plants in an essentially one-way reaction that is similar to the uptake of CO_2 during photosynthesis, and can therefore possibly be used as a proxy for GPP. The following section introduces the gas carbonyl sulfide and its applications in quantifying GPP as well as its role in stratospheric chemistry.

1.2 Carbonyl sulfide

Carbonyl sulfide (COS) is a linear molecule and consists of a carbonyl group connected to a sulfur atom with a double bond. It is a colorless gas with an unpleasant sulfur-like odor, and it has a molar mass of 60.075 g/mol (NIST, 2021). COS is the most abundant sulfur compound in the atmosphere, with a tropospheric mole fraction of around 500 parts per trillion (ppt).

$$O = C = S$$
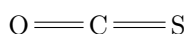
1.2.1 The tropospheric COS budget

Figure 1.5 provides a schematic overview of the currently identified sources and sinks of atmospheric COS, including their estimated magnitudes in GgS yr^{-1} (Ma et al., 2021;Kettle et al., 2002; Montzka et al., 2007; Berry et al., 2013; Kuai et al., 2015). The largest natural source of COS is the ocean (277 GgS yr^{-1}), where COS is emitted directly and indirectly via carbon disulfide (CS_2) and dimethyl sulfide (DMS) (Kettle et al., 2002; Lennartz et al., 2017; Lennartz et al., 2020). The other main sources of COS are mostly anthropogenic (349 GgS yr^{-1}), which include rayon and aluminum production, and coal combustion. Biomass burning, both anthropogenic and natural, is also a small source of COS (Stinecipher et al., 2019; Zumkehr et al., 2018), with an estimated emission of 136 GgS yr^{-1}. COS sinks include the before-mentioned large plant uptake, and a smaller and less well characterized soil uptake flux (Whelan et al., 2018), although some (agricultural) soils have been reported to actually emit COS (Whelan et al., 2022). Together, plant and soil COS uptake have an estimated flux of –1053 GgS yr^{-1}. Other sinks of COS are located in the troposphere and stratosphere, where COS is broken down by three different atmospheric sink reactions above the ozone layer, including oxidation (–101 GgS yr^{-1}), photolysis (–40 GgS yr^{-1}) and the reaction with oxygen radicals, which will be elaborated on later in this chapter.

While large efforts are being made to characterize the budget of COS, it is still not completely understood and uncertainties persist in the location and magnitude of the sinks and sources of COS (Whelan et al., 2018). From Figure 1.5 it becomes evident that the magnitude of the sources and sinks as they are constrained now do not add up to a closed budget. However, the absence of long-term trends in the tropospheric mole fraction of COS does point to a balancing of the sinks and sources (Montzka et al., 2007). Satellite observations and (inverse) modeling studies can help to further constrain the COS budget (Barkley et al., 2008; Glatthor et al., 2017; Kettle et al., 2002; Kuai et al., 2014; Suntharalingam et al., 2008;

Remaud et al., 2022), but the latest studies still point to an unknown missing source of 230 − 432 Gg S a^{-1} (Ma et al., 2021).
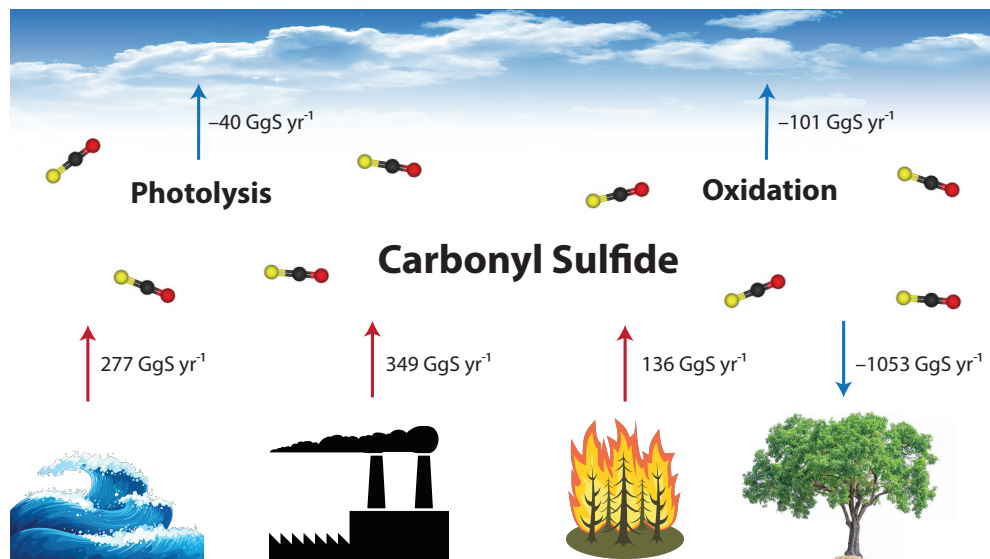

Figure 1.5: Schematic overview of the COS budget, where red arrows represent sources of COS and blue arrows are the sinks. The estimated magnitudes for the sources and sinks are given in GgS^{-1} which were obtained from the prior estimates from Ma et al. (2021), which in turn were compiled from the COS budget estimates and measurements by Kettle et al. (2002), Montzka et al. (2007), Berry et al. (2013), Kuai et al. (2015) and Zumkehr et al. (2018).

Closing the COS budget is important if one wishes to use COS as a proxy for GPP. Furthermore, understanding and quantifying the stratospheric sink of COS can help to resolve unanswered questions on stratospheric sulfur chemistry. The following sections will elaborate further on these two roles that COS plays in resolving uncertainties in the climate system.

1.2.2   COS in the biosphere

As mentioned in the previous section, COS is taken up by plants through a partly similar pathway as CO_2. The uptake pathways of CO_2 and COS into a leaf are shown schematically in Figure 1.6. COS and CO_2 first diffuse through the leaf boundary layer (1 in Figure 1.6) and the stomata, which are small pores on the leaf epidermis that are adjustable in size and can open and close depending on water availability, temperature and light (2 in Figure 1.6), and thereby control leaf gas exchange. The gases enter the mesophyll cells (3 in Figure 1.6), which contain chloroplasts (4 in Figure 1.6). There, CO_2 is fixated by a reaction catalyzed by the enzymes Rubisco and PEPC, and COS undergoes hydrolysis, catalyzed by an enzyme called carbonic anhydrase (CA) (Equation 1.2.1) (Protoschill-Krebs and Kesselmeier, 1992; Protoschill-Krebs et al., 1996; Stimler et al., 2010a). An important difference between the fixation of CO_2 and COS by plants is that the reaction of CO_2 with Rubisco is light-dependent

and thus only occurs during the day, whereas the reaction of COS with CA does not require light and can therefore continue during the night.

$$\text{COS} + \text{H}_2\text{O} \xrightarrow{\text{CA}} \text{HCOOS}^- + \text{H}^+ \rightarrow \text{H}_2\text{S} + \text{CO}_2 \tag{1.2.1}$$
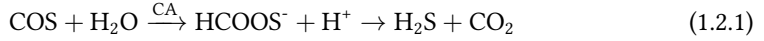
Unlike the uptake of CO_2, which also shows a reverse autotrophic respiration flux, the reaction of COS with CA is considered to be a one-way reaction as the reverse reaction is strongly unfavorable (Elliott et al., 1989). As the sources and other sinks of COS are spatially well separated from the biosphere sink, the uptake of COS of an ecosystem will be largely determined by the biosphere sink (Montzka et al., 2007). Given the fact that the uptake pathway of COS is so similar to that of CO_2, the relationship between the COS and CO_2 draw-down has been proposed to quantify GPP and thereby partition the fluxes of NEE (Sandoval-Soto et al., 2005; Montzka et al., 2007; Campbell et al. (2008), and others):

$$GPP = -F_{\text{COS}} \frac{c_{a_{\text{CO}_2}}}{c_{a_{\text{COS}}}} \frac{1}{LRU}, \tag{1.2.2}$$

where F_{COS} is the COS flux in pmol m^{-2} s^{-1}, $c_{a_{CO_2}}$ and $c_{a_{COS}}$ are the ambient mole fractions of CO_2 and COS, respectively. The negative sign is present in the equation as GPP is usually reported in positive values, while COS plant uptake fluxes are conventionally reported as negative values. LRU is the leaf-scale relative uptake ratio of COS and CO_2 given by:

$$LRU = \frac{F_{\text{COS}}}{F_{\text{CO}_2}} \frac{c_{a_{\text{CO}_2}}}{c_{a_{\text{COS}}}} \tag{1.2.3}$$

One difficulty is, however, that LRU can vary with ecosystem, environmental conditions and time. Kooijmans et al. (2017) found nighttime uptake fluxes of COS in a boreal forest, while CO_2 uptake completely ceases during the night. As a results, LRU increases drastically during day-night transitions and during the night. Furthermore, LRU was found to be light-dependent even during the day (Kooijmans et al., 2019; Stimler et al., 2011; Sun et al., 2018). Thus, this story is not simple and therefore, it is important to understand the mechanistic plant physiological principles of COS and CO_2 uptake at the leaf-scale.

Berry et al. (2013) implemented a mechanistic and empirical representation of leaf and soil COS uptake into a global carbon cycle model (SiB 3) in order to better constrain COS land fluxes. For the leaf-scale COS uptake, they presented a resistance analog model of CO_2 and COS uptake, as can be seen in Figure 1.6. This model includes several conductance (=1/resistance) steps that determine the rate at which these two gases are entering the leaf and moving through its different layers, which are the boundary layer conductance g_b, stomatal conductance g_s, mesophyll conductance g_i and the biochemical rate constant of COS and CO_2 fixation. The reaction rate of COS with CA is determined by its partial pressure in the chloroplast (Berry et al., 2013) and the overall consumption rate of COS is then dependent on the diffusion rate into the leaf and this reaction rate. CA activity and mesophyll conductance are related to the photosynthetic capacity of Rubisco in the leaf, V_{max} (Badger and Price, 1994; Evans et al., 1994), and are often scaled together as one conductance g_{COS} that is proportional to V_{max}.
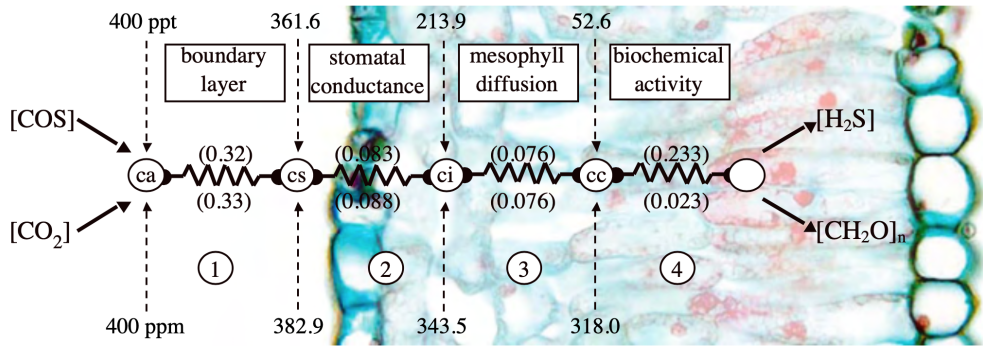
Figure 1.6: Figure from Berry et al. (2013). Resistance analog model of CO_2 and COS uptake. Numbers in parentheses are conductance values (mol m^{-2}s^{-1}) corresponding to the numbered key: (1) Boundary layer conductance, g_b. (2) Stomatal conductance, g_s. (3) Mesophyll conductance, g_i. (4) Biochemical rate constant used approximate photosynthetic CO_2 uptake by Rubisco or the reaction of COS with carbonic anhydrase as a linear function of the partial pressure of these gases in the chloroplast. In this case, COS uptake is 12.6 pmol m^{-2}s^{-1} and that of CO_2 is 5.6 μmol m^{-2}s^{-1}.

C3, C4 and CAM species

In nature, three different photosynthetic pathways have been identified: C3, C4 and CAM. C3 species make up approximately 90% of all shrubs, trees and plants and use the C3 photosynthetic pathway (Thomas, 2016), where all photosynthetic reactions take place in the mesophyll cells. C4 species are less abundant and, as the name suggests, use the C4 photosynthetic pathway, which separates the photosynthetic reactions between the mesophyll cells and the bundle-sheath cells that surround the leaf vein. In C4, CO_2 that enters the leaf is first stored as an intermediate acid, which is transported to the bundle-sheath cells. There, the final fixation of CO_2 by Rubisco takes places. This adaptation is beneficial to the plant as it leads to less loss of CO_2 and moisture through respiration and evaporation. CAM plants use the crassulacean acid metabolism, where the different steps of photosynthesis are separated in time. The stomata are open during the night, which allows the plant to assimilate CO_2 during that time, without much water loss. During the day, the stomata will be closed and the stored CO_2 is released for the Calvin cycle. CAM plants are therefore highly adapted to arid environments. In this thesis we will, however, only focus on C3 and C4 species.

Berry et al. (2013) and Stimler et al. (2011) found that COS uptake fluxes of C3 and C4 species are similar, but that C4 species likely have lower CA activity compared to C3 species. This lower CA activity leads to a higher leaf internal COS mole fraction at the assimilation cite. CO_2 assimilation rate is generally higher for C4 species, because of higher PEPC activity. Understanding the plant physiological mechanisms for COS and CO_2 assimilation and the differences between C3 and C4 species is important for accurate modeling of fluxes of these gases on larger scales.

1.2.3   COS in the stratosphere

COS is not only relevant for understanding the carbon cycle, but also plays a role in the formation of aerosols in the stratosphere. Stratospheric sulfur aerosols (SSA) are particles of sulfate, which form a layer at around 20 km height, that reflect and scatter incoming shortwave solar radiation and thereby have a cooling effect on the Earth (Junge and Manson, 1961; Junge, 1966). Figure 1.3 (Stocker, 2014) also indicates this net negative radiative forcing of sulfate aerosols in the yellow bar, under the category aerosols and precursors. Volcanic eruptions inject large amounts of sulfur species into the stratosphere that end up forming SSA. During volcanically non-active times, however, a layer of aerosols persists in the stratosphere. Thus, a source of SSA must exist to replenish this layer during these volcanically quiescent times.

COS has a long lifetime of 2 years (Brühl et al., 2012) and is therefore also transported into the stratosphere by global circulation. In the stratosphere, COS is broken down through oxidation by OH (Equation 1.2.5), a reaction with oxygen radicals (O^3P) (Equation 1.2.6) and by photolysis (Equation 1.2.4). The products of these reactions can eventually form sulfate (Schmidt et al., 2012a; Hattori et al., 2012; Danielache et al., 2008; Danielache et al., 2009; McKee and Wine, 2001). Therefore, it is hypothesized that COS is the main source of background SSA. However, a long debate has been taking place on whether COS could indeed be the main precursor of SSA, involving lab studies on COS stratospheric sink reactions and satellite observations of tropospheric and stratospheric COS. Still, the results of these experiments and observations are not consistent with each other and thus the role of COS in SSA formation remains under debate.

$$COS + hv \rightarrow CO + S \ \ (\lambda \leq 300nm) \tag{1.2.4}$$

$$COS + OH \rightarrow CO_2 + HS \tag{1.2.5}$$

$$COS + O^3P \rightarrow CO + SO \tag{1.2.6}$$

Atmospheric circulation

In order to understand the fate of COS in the stratosphere and its contribution to SSA, we have to have an understanding of the atmospheric, and specifically stratospheric, circulation. Global atmospheric circulation is caused by spatial differences in temperature, and thereby air pressure. Air generally moves from higher to lower pressure areas, and, on a global scale, this movement consists of air that is transported pole-wards from the equator, which descends again from the stratosphere to the troposphere at higher latitudes. Global atmospheric circulation consists of three cells: the Hadley Cell, which transports air from the equator to around 30°N and S, the Ferrel Cell that transports air from around 60°N and S to 30°N and S and the Polar Cell that transports air from 60°N and S to the poles.

Stratospheric circulation is characterized by the Brewer-Dobson circulation, which is driven by dissipating tropospheric waves (Butchart, 2014). The Brewer-Dobson circulation generally consists of large-scale ascending air in the tropics and descending air at the poles, which is strongest in boreal winter. This stratospheric circulation includes two residual
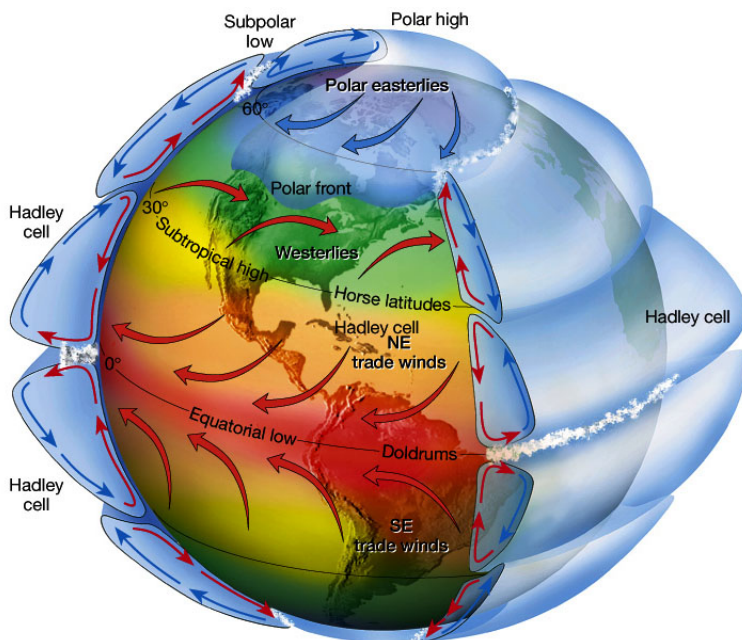
Figure 1.7: Idealized "three cell" atmospheric circulation model, obtained from Lutgens and Tarbuck (2001)

branches: a deeper branch which transports air slowly from the middle and upper stratosphere to the higher latitude stratosphere, where it descends to the troposphere, and a shallow branch, which transports air relatively fast from the tropical tropopause to the extratropical regions (Plumb, 2002; Birner and Bönisch, 2011). Besides these large-scale circulation patterns, relatively fast stratosphere-troposphere exchange can also take place in the form of bidirectional vertical mixing (Bönisch et al., 2009).

Trace gases, including COS, are transported through these global circulation pathways from the troposphere to the stratosphere, and from the equator pole-wards. The stratosphere is stratified, thus vertical mixing is slow. Trace gases are generally removed by sink reactions in the stratosphere and their mole fractions decrease with altitude, depending on their lifetime.

For COS, all sources are located in the troposphere (see Figure 1.5) and tropospheric mole fraction is around 500 ppt. In the stratosphere, COS is broken down by the three sink reactions described above (Equations 1.2.4, 1.2.5 and 1.2.6), and its mole fraction decreases with altitude. The global atmospheric distribution of COS and how it is influenced by atmospheric circulation patterns will be briefly discussed at the end of the next section.

1.2.4   Observations of COS

COS measurement techniques

Measuring the atmospheric mole fraction of COS is challenging because of its low abundance and its instability in certain storage materials. Furthermore, some materials are

even known to emit (large) quantities of COS. Thus, much care needs to be taken when sampling air for COS measurements or when performing on-line COS measurements (see COSANOVA, (n.d.) for a list of materials to avoid when working with COS). Nevertheless, there are several techniques for measuring COS mole fractions. One technique is gas chromatography and mass spectrometry (GC-MS) measurement of discrete air samples, usually taken in stainless steel or glass flasks. While these measurements yield high precision values, disadvantages are that they are quite time-consuming and require a lot of logistics (e.g. shipping samples, cleaning flasks).

The NOAA Global Monitoring Laboratory created a global network of observation stations at remote sites in the northern and southern hemisphere. Within the HATS (Halocarbons and other Atmospheric Trace Species) program, ground-based COS mole fraction measurements are being made since the year 2000, using glass and stainless steel flasks that are analyzed in the NOAA/ESRL/GMD's Boulder laboratories with GC-MS detection. Figure 1.8 shows the locations of these NOAA measurement stations at which sampling for COS has been taking place and the data up to April 2022 are shown in Figure 1.9.

Surface and boundary layer observations of COS can be made using spectroscopy methods. Quantum Cascade Laser Spectrometers (QCLS) can perform high-precision, continuous measurements of trace gases, including COS (Stimler et al., 2010b), and these instruments can be deployed in the field. In the last 12 years, these laser instruments have provided useful COS measurement data, mostly over ecosystems (Kooijmans et al., 2016; Vesala et al., 2022; Kooijmans et al., 2017; Kooijmans et al., 2019; Commane et al., 2015; Berkelhammer et al., 2014; Billesbach et al., 2014; and others). However, the use of QCLS instruments is not trivial and detailed testing and calibration is required to obtain reliable measurements.

The vertical and latitudinal distribution of COS can be studied with the use of satellite observations, as already briefly mentioned before. Yousefi et al. (2019) presented near global atmospheric measurements of COS with the Atmospheric Chemistry Experiment Fourier transform spectrometer (ACE-FTS) on the SCISAT-1 satellite in low Earth orbit, and they presented COS observations with the MkIV balloon-borne FTS instrument (Figure 1.10).

Atmospheric observations of COS

Looking at the COS mole fraction observations at the NOAA stations displayed in Figure 1.9, we can observe a seasonal cycle that is has a slight phase lag between the Northern (NH) and Southern Hemisphere (SH). Montzka et al. (2007) analyzed a large dataset of these ground-based ambient air measurements at 12 of the NOAA measurement sites described above (Figure 1.8), in both hemispheres over the years 2002 to 2005, as well as aircraft-based ambient air measurements of COS across the Midwestern United States. Their first observation was indeed that COS mole fractions undergo substantial variations in both hemispheres, with peak mole fractions in the SH being observed in February and for the NH between April and June. The fact that the seasonal variations do not display a lag of around 6 months between the hemispheres, points to different processes driving the seasonal cycle of COS in the two hemispheres.

Montzka et al. (2007) found that terrestrial biosphere uptake most likely dominates the seasonality of COS in the NH, as the strongest amplitudes are found in regions with the largest influence of the continental boundary layer. Furthermore, the strongest seasonal

amplitudes were also found at the sites with the lowest annual mean COS mole fractions, indicating the important influence of a COS sink process. In the SH, the seasonal cycle is probably driven by oceanic emissions, which peak during summer because COS and CS_2 are photo-chemically produced from oceanic dissolved organic matter (Kettle et al., 2002). This phase lag in COS seasonal variation between the two hemispheres leads to a mole fraction gradient across the equator that seasonally changes sign.

Another interesting feature of this long time-series of COS data displayed in Figure 1.9, is the absence of a long-term trend in global mean COS mole fraction (Montzka et al., 2007), which provides evidence for a balance in the global sources and sinks, and thus a closed budget of COS. However, on a regional scale, there is evidence for changes in atmospheric COS mole fraction over time. Belviso et al. (2022) found a decline in the seasonal amplitude of COS at the GIF site in France between 2014 and 2021, which pointed to a possible decrease in peak plant uptake due to lower ambient tropospheric COS in this region (Hannigan et al., 2022), which was attributed to a decreasing amount of anthropogenic sources present in Western Europe.

As described in the previous section, global COS mole fractions can also be analyzed
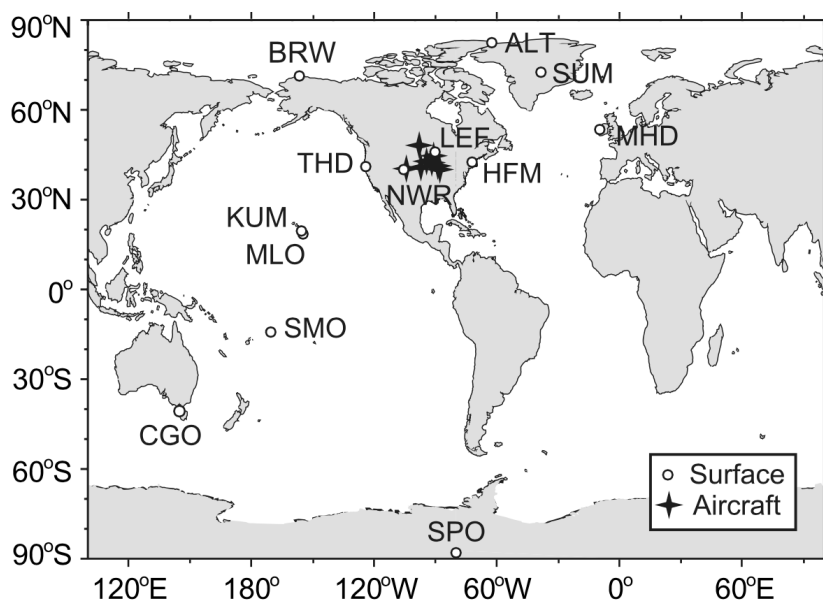

Figure 1.8: Map of NOAA stations at which samples are collected for COS mole fraction measurements. The white circles indicate ground-based stations and the black crosses are locations at which aircraft samples were regularly collected (Montzka et al., 2007).

using satellite observations. The average global latitudinal and vertical distribution of COS mole fractions from the ACE-FTS measurements is shown in Figure 1.10. The global circulation patterns, as well as the COS breakdown in the stratosphere, are well reflected in the mole fraction distribution. Around the equator, the COS mole fraction is higher than at higher latitudes, as tropospheric transportation is generally towards the equator. Furthermore, COS mole fraction decreases quickly with elevation above the tropopause, as sink
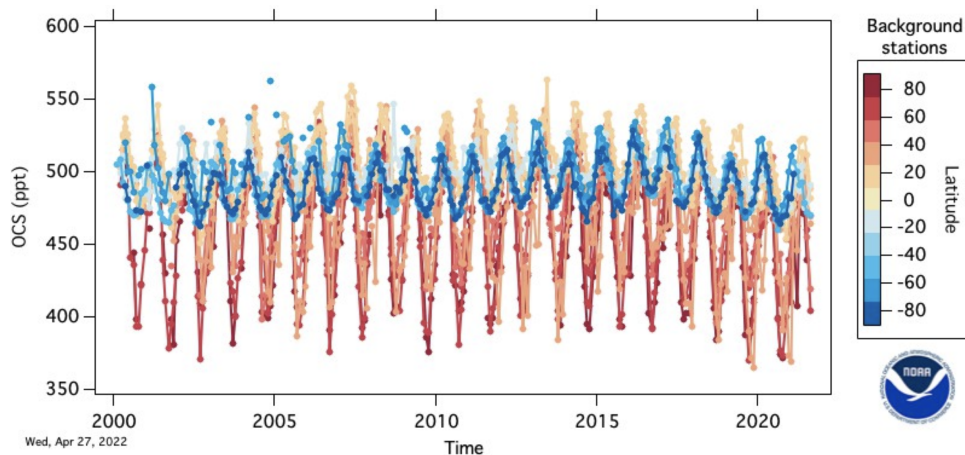
Figure 1.9: Atmospheric dry mole fractions of COS measured by GC-MSD in the NOAA HATS flask program (NOAA, 2022). Each point represents a monthly mean at one of 8-12 stations: Alert, Canada (ALT), Summit Greenland (SUM), Barrow, Alaska (BRW), Mace Head, Ireland (MHD), Trinidad Head, California (THD), Niwot Ridge, Colorado (NWR), Cape Kumukahi, Hawaii (KUM), Manua Loa, Hawaii (MLO), American Samoa (SMO), Cape Grim, Australia (CGO), Palmer Station, Antarctica (PSA), South Pole, Antarctica (SPO)

reactions consume COS (Equations 1.2.4, 1.2.5, 1.2.6). Around the equator, this sharp decrease starts at a higher altitude, as the tropopause is located higher around these latitudes. The altitude profile of decreasing COS above the tropopause is more pronounced at higher latitudes as the stratosphere around these latitudes contains older air that has been transported through the branches of the Brewer-Dobson circulation, and thus COS has had more time be consumed by the above-mentioned sink reactions. Yousefi et al. (2019) also presented isotope ratio measurements of COS from the ACE-FTS data, which will be discussed in more detail in Chapter 3 of this thesis.
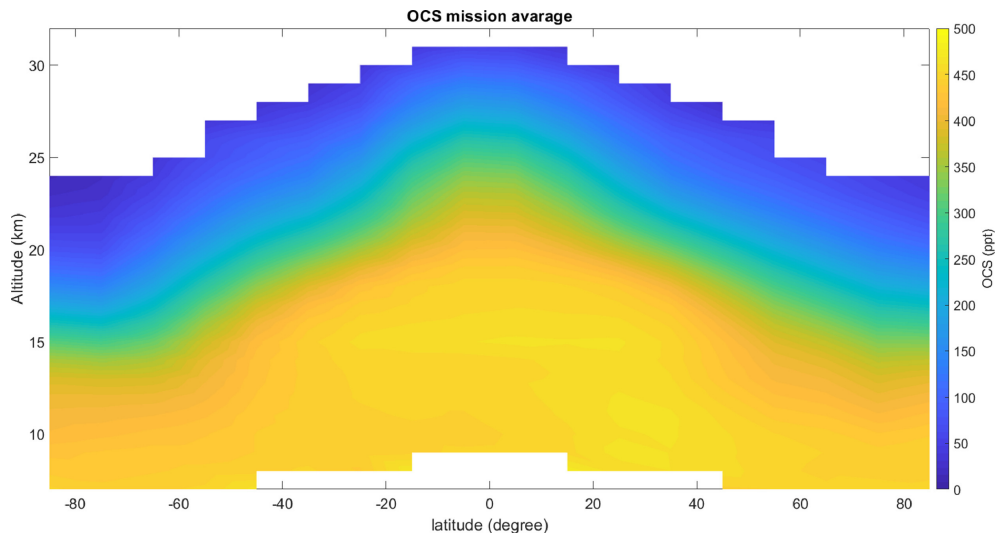
Figure 1.10: Global atmospheric distribution of COS from the ACE mission average. The COS volume mole fraction values have been grouped together in $10°$ latitude bins (Yousefi et al., 2019)

1.3   The use of stable isotopes

In the paragraphs above, it has become evident that there are still many questions and uncertainties regarding atmospheric COS; mainly, understanding the budget of COS and the role of COS in the formation of SSA. Measurements of stable isotopes can be a tool to help answer these questions as they can be used to trace sources and constrain the magnitude of sink reactions (De Groot, 2004).

Isotopes are atoms with the same amount of protons and electrons, but different amounts of neutrons. Therefore, isotopes have the same charge but a different mass. Isotopologues are molecules with the same chemical formula, which differ in their isotopic composition. In the scope of this thesis, only the stable isotopologues of COS are being measured.

1.3.1   Stable isotopologues of COS

As COS has three atoms, each with more than one stable isotope, it has many isotopologues. This thesis focuses on single substituted isotopologues of COS, which are molecules with only one rare isotope. Table 1.1 contains the stable isotopes of sulfur and carbon and their relative abundances. The stable isotopes of oxygen are not included because the COS oxygen isotopologues were not measured during the research described in this thesis, and have never been measured to this date. $CO^{36}S$ was also not measured during the scope of this research, because of its low abundance.

Table 1.1: Stable isotopes of sulfur and carbon and their relative abundances in nature (De Laeter et al., 2003).

Element	Isotope	Relative abundance
Sulfur	^{32}S	94.99%
Sulfur	^{33}S	0.75%
Sulfur	^{34}S	4.25%
Sulfur	^{36}S	0.01%
Carbon	^{12}C	98.84% - 99.04%
Carbon	^{13}C	0.96% - 1.16%

1.3.2 Reporting isotope values

Isotope ratios of the minor to the most abundant isotope (shown in Equations 1.3.1 and 1.3.2) are commonly used to quantify the isotopic composition of a compound. These are usually reported relative to the same ratio in a reference material, expressed as δ values, as shown in Equations 1.3.3 and 1.3.4. For sulfur isotopes, the standard international reference material is the Vienna Canyon Diablo Troilite (VCDT). For carbon isotopes, the reference material is the Vienna Pee Dee Belemnite (VPDB).

$$^{33,34}R = \frac{^{33,34}S}{^{32}S} \tag{1.3.1}$$

$$^{13}R = \frac{^{13}C}{^{12}C} \tag{1.3.2}$$

$$\delta^{33,34}S = \frac{^{33,34}R_{sample}}{^{33,34}R_{standard}} - 1 \tag{1.3.3}$$

$$\delta^{13}C = \frac{^{13}R_{sample}}{^{13}R_{standard}} - 1 \tag{1.3.4}$$

1.3.3 Constraining sources

Sources and processes often have characteristic isotopic signatures, and this information can help in recognizing them or disentangling their contributions to a mixture. When measuring air samples that consist of different mole fractions of a compound from a single source, diluted into stable background air, a Keeling approach can be used to find the isotopic signature of that particular source (Keeling, 1958; Keeling, 1961; Pataki et al., 2003). The sampled air consists of a mixture of two reservoirs with different isotopic composition and the isotopic composition δ_s of the source can then be calculated from the following mass balance equation:

$$C_m\delta_m = C_{bg}\delta_{bg} + C_s\delta_s, \tag{1.3.5}$$

where C_m, C_{bg} and C_s are the mole fractions of the measured air, the background air and the source, respectively. The δ values are the corresponding isotopic compositions of these reservoirs. Rearranging Equation 1.3.5 yields the following expression:

$$\delta_m = C_{bg} * (\delta_{bg} - \delta_s)(1/C_m) + \delta_s \qquad (1.3.6)$$

From this equation, inserting a measurement series of δ_m and C_m with varying mixtures of source and background air, the isotopic signature of the source δ_s can be found using a so-called Keeling plot, which plots δ_m versus $1/C_m$ (Keeling, 1958; Keeling, 1961; Pataki et al., 2003). If the assumption of a single source mixed into stable background air is met, the intercept with the y-axis of a linear function fit of the data will yield δ_s.

1.3.4   Isotope fractionation

During chemical or physical processes such as diffusion or chemical reactions, isotope fractionation can occur. The lighter isotopologues diffuse faster and the chemical bond with a lighter isotope is easier to break than the bond with a heavier isotope. In a reaction that consumes a species like COS, the lighter isotopologue typically reacts faster and therefore, the reaction product will be depleted in the heavy isotopes. As more of the lighter isotope is being reacted away, the remaining pool of the reactant will become enriched in the heavier isotope. This type of fractionation is often called "normal fractionation" and it occurs most frequently in nature. Sometimes, however, the heavier isotope is being favored by the reaction instead of the lighter - in this case we talk about "inverse fractionation".

Another concept that will be used in this thesis is Rayleigh fractionation. Rayleigh fractionation assumes that a substance is removed from a reservoir without having any further contact with the initial pool of substance, e.g. in a first order reaction. Using the reaction coefficients (k) of both the light and heavy isotopologue reaction, the Rayleigh fractionation Equations (1.3.7 and 1.3.8) can be constructed. In the case of COS, the relevant fractionation constants are:

$$^{33,34}\varepsilon = \frac{^{33,34}k}{^{32}k} - 1 \qquad (1.3.7)$$

and

$$^{13}\varepsilon = \frac{^{13}k}{^{12}k} - 1, \qquad (1.3.8)$$

where $^{33,34}\varepsilon$ and $^{13}\varepsilon$ are fractionation constants for CO^{33}S, CO^{34}S and ^{13}COS, respectively. A negative ε indicates "normal fractionation"; the remaining COS is getting enriched in the heavier isotope and a positive ε indicates "inverse fractionation", in which the remaining pool of COS is getting depleted. These ε values can be calculated from a measurement dataset series over the reaction progress by constructing a so-called Rayleigh plot, where one plots $ln(1+\delta)$ versus ln of the remaining fraction of the reactant. The slope of a linear

regression of this dataset then yields the fractionation constant ε. More information on the use of stable isotopes and different measurement and analytical techniques can be found in De Groot (2004).

For COS, isotope fractionation occurs for instance during uptake by plants, where, as previously explained, COS enters the leaf through several diffusion steps (Figure 1.6) and is in the end hydrolyzed by carbonic anhydrase (CA). Both diffusion and the fixation reactions can cause isotope fractionation. Figure 1.11 shows an example of a Rayleigh plot from Davidson et al. (2022), who conducted closed-chamber plant experiments with both C3 and C4 species. The data are plotted in the green and orange circles and the trend-lines are given in dashed lines, of which the slopes provide the estimated fractionation factors $^{34}\varepsilon$.

The sink reactions in the stratosphere are also expected to cause COS isotope fractionation. This fractionation signal should be apparent in the isotopic composition of COS in the stratosphere and in that of its reaction products. Thus, by measuring the isotopic compositions of both SSA and COS, and comparing those with the known or expected fractionation of COS in the stratosphere, one can investigate whether COS could be the main source of SSA.
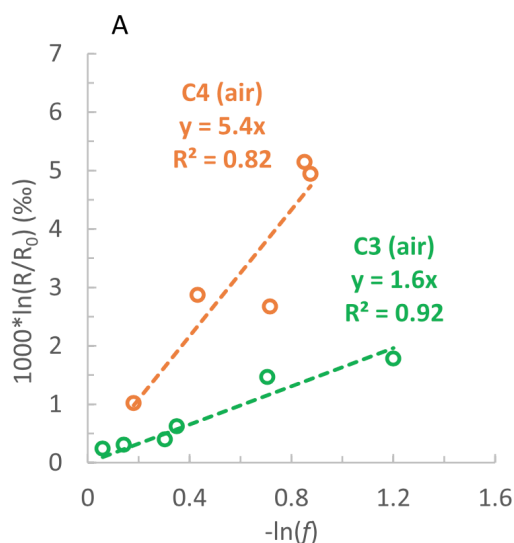

Figure 1.11: Rayleigh plot of fractionation during COS uptake by C3 and C4 species during a closed-chamber experiment, taken from a figure by Davidson et al. (2022), where $-ln(f)$ on the x-axis is the natural logarithm of the remaining fraction of COS during the experiment. On the y-axis is the natural logarithm of $\delta^{34}S$, here presented as (R/R_0). The slope of the fit represents the fractionation factor. In this figure, the estimated fractionation for both a C3 (green) and C4 (orange) plant species are presented.

1.3.5   Measuring COS isotopologues

Measurements of COS isotopologues, and using the Keeling plot and Rayleigh fractionation approach described above can provide information on the location and magnitude of

sources, and could also help to better understand and quantify the sink processes such as the biosphere sink and the stratospheric reactions. However, measuring isotopologues of COS is rather complex because of its low atmospheric mole fraction and the fact that the techniques to perform such measurements were only recently developed.

Measurement principles

Isotope ratio measurements are conducted using mass spectrometry, which is an analytical technique where the mass-to-charge ratio (m/z) of ions is measured using a mass spectrometer (De Groot, 2004). Sample gas is injected into the mass spectrometer, where it is first ionized in the ion source. Then, the beam of ions passes through an electric or magnetic field, which causes the paths of the different ions to deflect in a slightly different way. The ions with a lower m/z are deflected more than the heavier ions. Eventually, the separated ion beams end up at the detector that records the relative abundance of each m/z present in the sample. There are many different types of mass spectrometers. For our measurements, we used an isotope ratio mass spectrometer (IRMS), which is a multicollector instrument and includes several Faraday cups in the detector that collect the ions.

Before the sample is injected into the mass spectrometer, COS first needs to be separated from the other compounds in air. This separation is done using a pre-concentration system, which uses several freezing and heating steps to collect COS, while letting the other air elements pass through. At the end of the pre-concentration system, a gas chromatograph (GC) column is used to separate the remaining compounds and inject them into the mass spectrometer at different times.

COS isotope measurement systems

The first system for measuring COS isotopologues from air samples was developed by Hattori et al. (2015) and consisted of a pre-concentration system coupled to a GC-IRMS. They presented the first δ^{33}S and δ^{34}S measurements of COS from ambient air in Japan with precisions of 0.42 ‰ and 0.62 ‰, respectively. Hattori et al. (2015), however, needed large quantities of air (about 100 L) to obtain such a precision, as they wished to avoid the effects of nonlinearity, which is the dependence of the measured isotope ratios on the amount of COS injected into the IRMS. This effect was present in their measurements at lower quantities of air. Thus, in order to increase the amount of COS that was pre-concentrated, they needed to drastically increase the amount of air injected for a single measurement.

Angert et al. (2019) recently developed another system to measure δ^{34}S from COS, and also other sulfur species like carbon disulfude (CS$_2$) and dimethyl sulfide (DMS). For their measurements, they used a similar pre-concentration system but coupled to a different type of mass spectrometer: an inductively coupled plasma mass spectrometer (ICP-MS), which yields more precise results for smaller samples. However, this method is also more expensive than regular IRMS measurements. Angert et al. (2019) obtained a precision of around 0.5 ‰ for 2 L air sample measurements, and in their further works they presented various measurements ranging from outside air in Israel and the Canary Islands, air containing oceanic emissions, and air from experiments targeting plant fractionation (Angert et al., 2019; Davidson et al., 2021; Davidson et al., 2022).

The system developed during this thesis research at IMAU, Utrecht University, was built using the information on the pre-concentration system provided by Hattori et al. (2015) and,

as mentioned previously, also uses an IRMS to measure the isotope ratios. Our system was however optimized to measure COS isotopologues from small air samples of around 3 to 6 L. The nonlinearity effect described above was overcome by characterizing it meticulously and correcting for the nonlinearity afterwards. In this thesis, the methods and data are presented for the sulfur isotope ratios δ^{33}S and δ^{34}S from COS, as well as the and the first ever measurements of δ^{13}C from COS. Our measurement system and the data corrections are described in much detail in Chapter 2 of this thesis.

During the research of this thesis, we used two different mass spectrometer to perform COS isotope ratio measurements. The measurements presented in Chapter 2 were carried out using a Delta V Advantage IRMS (Thermo Fisher Scientific, USA), which contained the Faraday collector cups originally designed for measuring oxygen isotopes with m/z 32, 33 and 34. On these m/z, we measured S$^+$ fragment ions that are formed from COS in the ion source of the IRMS. Chapter 3 contains some measurements that were performed using the same Delta V Advantage, but the newer measurements were carried out using a Delta V Plus (Thermo Fisher Scientific, USA) that included 11 Faraday collector cups, which could additionally measure m/z 28 and 29. On these m/z, we were able to measure CO$^+$ fragment ions formed in the ion source from COS. From these measurements, the carbon isotope ratio in COS, δ^{13}C, could be obtained. The data presented in Chapter 4 are all conducted with the newer Delta V Plus and thus also include the δ^{13}C values.

Current knowledge on COS isotopes

The three measurement systems described above were all recently developed and these are currently the only labs that are measuring COS isotopologues. Therefore, only a limited amount of COS isotope data exists at this moment. Table 1.2 summarizes the COS isotopic composition of ambient air, and source signatures as well as fractionation values that have been reported thus far, not including the measurements presented in this thesis. Figure 1.12 presents an overview of the estimated δ^{34}S values for the sources of COS and the estimated fractionation factors, $^{34}\varepsilon$, for the COS sinks.

Ambient tropospheric COS sulfur isotopic composition values reported thus far range between 9.7 and 13.9 ‰ for δ^{34}S. The first study presenting COS sulfur isotope ratio measurements of ambient air was by Hattori et al. (2015), and they found 4.9 ± 0.3 ‰ and 1.6 ± 0.5 ‰ for δ^{34}S and δ^{33}S, respectively. However, these measurements were later deemed likely unreliable. For δ^{33}S in ambient air, no other measurements exist to date. Most of the ambient air sampling has been performed in Japan, Israël, the Canary Islands and the United States, and Davidson et al. (2021) also included data from a couple of samples collected in Portugal (4 samples), India (3 samples) and one sample in the Southern Ocean. Thus, almost all data was collected in the Northern Hemisphere, and the total amount of ambient air samples measured is still quite small.

The overall isotopic source signature of anthropogenic emissions has been estimated by both Davidson et al. (2021), who found an anthropogenic signature δ^{34}S = 8 ± 1 ‰, and Hattori et al. (2015), who found a δ^{34}S value of 4.7 ± 0.8 ‰. These estimates were based on Keeling plot intercept values, with the assumption that the measured air consisted of a mixture of clean ambient background air and COS emitted by anthropogenic activities. These assumptions were based on above-background COS mole fractions in their samples, together with backward trajectory modeling of air parcels. However, no specific targeting
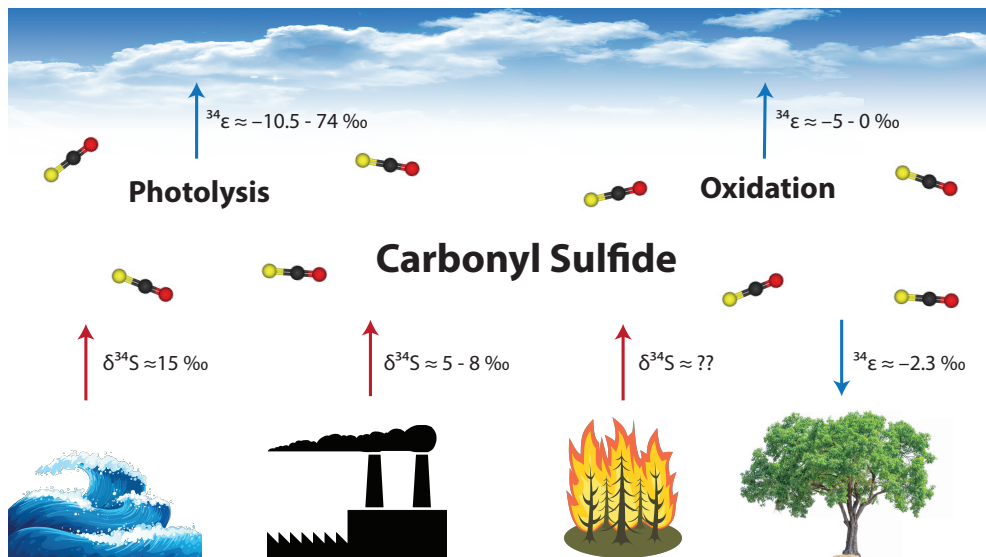
Figure 1.12: Schematic overview of the COS budget, where red arrows represent sources of COS and blue arrows are the sinks, including the estimated δ^{34}S source signatures of anthropogenic sources (Hattori et al., 2020; Davidson et al., 2021) and the oceans (Davidson et al., 2021), and the estimated fractionation factors $^{34}\varepsilon$ of the photolysis, oxidation and biosphere sinks (Kamezaki et al., 2016; Davidson et al., 2022; Leung et al., 2002; Colussi et al., 2004; Lin et al., 2011; Hattori et al., 2011; Schmidt et al., 2012a), see also Table 1.2.

of anthropogenic COS emissions from for instance certain factories or traffic has been performed yet.

The isotopic composition, δ^{34}S, of COS from oceans was first estimated by Angert et al. (2019) to be around 19 ‰, being similar to the sulfur isotopic composition of DMS presented by Amrani et al. (2013) and assuming that COS and DMS are both degradation products of the same oceanic organic sulfur material. Davidson et al. (2021) characterized the δ^{34}S value of oceanic COS by measuring the mole fractions and δ^{34}S values of dissolved COS, CS_2 and DMS in seawater. They estimated an average oceanic δ^{34}S value, which contained both direct and indirect COS emissions, of 14.7 ± 1 ‰.

The isotope fractionation factor of COS during uptake by plants was studied by Davidson et al. (2022). As briefly mentioned before in Section 1.3.4, they conducted closed-chamber plant experiments and obtained estimations for the fractionation factors during uptake by C3 and C4 plant species. From this dataset, Davidson et al. (2022) made an estimation of overall global fractionation, $^{34}\varepsilon$, during plant uptake of −2.3 ± 0.5 ‰. This first global estimate of plant fractionation is, however, only based on experiments conducted on two species. Thus, more plant fractionation data is required to better constrain this estimate.

For COS isotope fractionation during uptake by soil, only one estimate is currently available, presented by Kamezaki et al. (2016), who conducted lab experiments with two species of bacteria, isolated from the soil. They found fractionation values, $^{34}\varepsilon$, during COS consumption by these bacteria between −2.1 and −3.7 ‰.

Sulfur and carbon isotope fractionation during the stratospheric removal reactions of COS, have been investigated using theoretical calculations, lab studies, remote sensing and

modeling. Knowledge on isotope fractionation of COS in the stratosphere, in combination with the isotopic composition of SSA, can be used to investigate whether COS is the main precursor of SSA. Castleman et al. (1974) performed the first and to date only measurements of the sulfur isotopic composition of SSA during a volcanically quiet period, and found a global average δ^{34}S in SSA of 2.6 ± 0.3 ‰. Leung et al. (2002) presented some of the first measurement-based estimates of stratospheric CO^{34}S profiles, using infrared limb-transmittance spectra acquired during several balloon flights. Surprisingly, they derived a large and positive fractionation factor of $^{34}\varepsilon$ = +73.8 ± 8.6 ‰. In their study on infra-red (IR) absorption band spectra of COS at different elevations, Colussi et al. (2004) also found a large positive fractionation of +67 ± 7 ‰. Lin et al. (2011) performed lab experiments to determine the sulfur isotope effects during UV photolysis of COS, and found a $^{34}\varepsilon$ of −10.5 to +5.3 ‰. Hattori et al. (2011) experimentally determined UV cross sections for different COS isotopologues and from these, they estimated the wavelength-integrated photolysis rates and fractionation constants similar to 20 km altitude. They obtained fractionation constants of $^{33}\varepsilon$ = −3.7 ± 4.5 ‰ and $^{34}\varepsilon$ = +1.1 ± 4.2 ‰. For $^{13}\varepsilon$, Hattori et al. (2011) found a larger fractionation constant of −26.8 ± 4.3 ‰. Schmidt et al. (2013) theoretically calculated the COS photolytic isotope effect as a function of wavelength and found a small negative fractionation for $^{34}\varepsilon$. They also found that the carbon isotopic fractionation, $^{13}\varepsilon$, due to photolysis of COS in the upper stratosphere is likely significantly negative and will leave a clear positive δ^{13}C signal in the remaining COS.

For the oxidation reaction with OH, Schmidt et al. (2012a) calculated a kinetic isotope effect, $^{34}\varepsilon$, between −5 and 0 ‰ in the troposphere and lower stratosphere. For $^{13}\varepsilon$, they found a stronger fractionation factor between −70 and −40 ‰. The isotope effect of the reaction with $O(^3P)$ was investigated by Hattori et al. (2012) by lab experiments using a photochemical reactor, and found a $^{34}\varepsilon$ value of −14.8 ‰.

The study by Yousefi et al. (2019) that was already discussed previously also presented δ^{34}S and δ^{13}C estimates from the ACE-FTS balloon-borne FTS data. They estimated fractionation factors $^{34}\varepsilon$ for stratospheric destruction of COS of +3.64 ± 0.57 ‰, +5.91 ± 0.63 ‰ and +8.91 ± 0.47 ‰, for latitude bins of 60-30°S, 30S-30°N and 30N-60°N, respectively. For $^{13}\varepsilon$ they found large negative fractionation constants −90 ± 1.4 ‰, −88 ± 1.92 ‰ and −65 ± 1.16 ‰ for the same latitude bins.

Finally, Nagori et al. (2022) conducted a modeling study in which they investigated how the isotopic composition and fractionation of COS in the stratosphere would propagate to the isotopic composition of SSA. They concluded that a small and negative fractionation of COS in the stratosphere is needed to propagate to a δ^{34}S value of 2.6 ‰, as found by Castleman et al. (1974). Thus, the above-mentioned studies do not all agree on COS isotope fractionation in the stratosphere and whether COS could indeed be the main precursor of SSA. More data, and preferably measurements of the isotopic composition of COS from air samples taken in the stratosphere, are needed in order to fully understand the role of COS in the formation of SSA.

Table 1.2: COS isotope ratio measurements, and calculated source signatures and fractionation constants, not including the work presented in this thesis. Note that the fractionation values provided for photolysis, the reactions with OH and O^{3}P and the overall stratospheric fractionation by Yousefi et al. (2019) are estimates from remote-sensing studies, and calculations from spectroscopic measurements, rather than measurements obtained from the stratosphere directly.

	$\delta^{34}S_{VCDT}$ (‰)	$\delta^{33}S_{VCDT}$ (‰)	$^{34}\varepsilon$ (‰)	$^{13}\varepsilon$ (‰)	Source
Ambient air	4.9 ± 0.3	1.6 ± 0.5	-	-	Hattori et al. (2015)
	10.5 ± 0.4	-	-	-	Kamezaki et al. (2019)
	13.2 ± 0.6	-	-	-	Angert et al. (2019)
	9.7 to 14.5	-	-	-	Hattori et al. (2020)
	13.9 ± 0.1	-	-	-	Davidson et al. (2021)
Anthropogenic emissions	4.7 ± 0.8	-	-	-	Hattori et al. (2020)
	8 ± 1	-	-	-	Davidson et al. (2021)
Oceanic emissions	19	-	-	-	Angert et al. (2019)
	14.7 ± 1	-	-	-	Davidson et al. (2021)
Biosphere sink	-	-	−2.3 ± 0.5	-	Davidson et al. (2022)
Soil sink	-	-	−2.1 to −3.7	-	Kamezaki et al. (2016)
Photolysis sink	-	-	+73.8	-	Leung et al. (2002)
	-	-	+67 ± 7	-	Colussi et al. (2004)
	-	-	−10.5 to +5.3	-	Lin et al. (2011)
	-	-	+1.1 ± 4.2	−26.8 ± 4.3	Hattori et al. (2011)
OH oxidation sink	-	-	−5 to 0	−70 to −40	Schmidt et al. (2012a)
O^{3}P reaction sink	-	-	−14.8	-	Hattori et al. (2012)
Overall stratospheric sink	-	-	+3.6 to +8.9	−65 to −90	Yousefi et al. (2019)

1.4 Thesis motivation and research questions

The general motivation for the work presented in this thesis was to perform measurements of COS isotopologues in order to contribute to answering lingering questions on the COS budget and the contribution of COS to SSA. We therefore aimed to broaden the knowledge on COS isotopic composition and fractionation processes. For these measurements, we developed a new system for measuring COS isotopologues from smaller air samples to make these measurements easier, faster and wider applicable.

1.4.1 Research questions and thesis outline

During this PhD work, my aim was to answer following research questions:

1. Is it possible to measure COS isotopologues in a way that is usable for advancing the understanding of the global COS cycle i.e.

   (a) with a precision that is good enough to distinguish between sources, and to observe atmospheric variations in time and space?

   (b) from air samples small enough (several L) to allow collecting samples globally, including in situations where the sampled air is limited, like firn, ice, stratosphere, or small-scale lab experiments?

2. How can isotope measurements contribute to understanding the COS budget?

3. How uniform is the tropospheric ambient isotopic composition of COS?

   (a) How much is the tropospheric isotopic composition influenced by local sources?

   (b) Can we distinguish the influences of different sinks and sources by measuring the ambient tropospheric isotopic composition of COS?

4. Is COS the main source of background stratospheric sulfur aerosols (SSA), during volcanically quiet times and can we determine this by using isotope measurements of COS in the stratosphere?

   (a) What are the total isotope fractionation factors of the different COS isotopologues, $CO^{33}S$, $CO^{34}S$ and ^{13}COS, in the stratosphere?

   (b) How do these COS fractionation factors compare with previous estimates from lab experiments and remote sensing studies?

   (c) Is the ^{34}S fractionation factor, $^{34}\varepsilon$, observed in the stratosphere compatible with COS being the main source of SSA?

5. What is the COS isotopic fractionation during plant uptake?

   (a) How does the isotope fractionation differ between C3 and C4 species?

   (b) How does the isotope fractionation vary with changing ambient conditions (e.g. light availability)?

These research questions are addressed throughout the chapters of this thesis. **Chapter 2** contains a detailed description of the new system that we developed at IMAU for measuring sulfur isotope ratios of COS from small air samples, which addresses the first research question. This chapter also presents the first measurements of COS isotopologues in ambient air in the Netherlands, as well as from samples taken inside a highway tunnel, to characterize COS traffic emissions. The contribution of different sources and sinks to the ambient COS isotopic composition in Utrecht is evaluated and the third research question is thereby addressed.

Chapter 3 presents measurements of COS isotopic composition in the upper troposphere and lower stratosphere, and thereby provides data to help answer the fourth research question. Samples were measured from two campaigns: one campaign with a high-altitude airplane that was operated from Kathmandu, Nepal in 2017 and a second campaign conducted in Kiruna, Sweden in 2021, where samples were taken using a stratospheric balloon. This chapter compares our measurement data to previous stratospheric COS fractionation estimates and the isotopic composition in SSA, and discusses the possibility of COS being the main precursor of SSA. This chapter also presents the first measurements of carbon isotope ratios from COS, and the method for these measurements are explained.

Chapter 4 addresses the fifth research question, presenting plant gas exchange experiments conducted at Wageningen University and Research. The aim of these experiments was to quantify sulfur and carbon isotope fractionation of COS during plant uptake, using a flow-through whole plant chamber. These experiments were conducted using plants with different photosynthetic pathways (C3 and C4) and in different light conditions. Both CO_2 and COS mole fractions were measured in real-time to monitor the behavior of the plants, as well as to partition the GPP and respiration fluxes and to calculate LRU. The fractionation constants obtained from the experiments are compared to values from literature and discussed in detail.

Chapter 5 provides a synthesis of all the work presented in this thesis. This chapter reflects back on all research questions and provides an outlook and recommendations for future research on COS isotopologues, and COS research in general. In this chapter, the contribution of our work to understanding the COS budget is discussed and recommendations are given for future research for further constraining the COS budget, thereby addressing the second research question.

2

A GC-IRMS method for measuring sulfur isotope ratios of carbonyl sulfide from small air samples

A new system was developed for measuring sulfur isotopes $\delta^{33}S$ and $\delta^{34}S$ from atmospheric carbonyl sulfide (COS) on small air samples of several liters, using pre-concentration and gas chromatography – isotope ratio mass spectrometry (GC-IRMS). Measurements of COS isotopes provide a tool for quantifying the COS budget, which will help towards better understanding climate feedback mechanisms. For a 4 liter sample at ambient COS mole fraction, 500 parts per trillion (ppt), we obtain a reproducibility error of 2.1 ‰ for $\delta^{33}S$ and 0.4 ‰ for $\delta^{34}S$. After applying corrections, the uncertainty for an individual ambient air sample measurement is 2.5 ‰ for $\delta^{33}S$ and 0.9 ‰ for $\delta^{34}S$. The ability to measure small samples allows application to a global-scale sampling program with limited logistical effort. To illustrate the application of this newly developed system, we present a timeseries of ambient air measurements, during the fall and winter of 2020 and 2021 in Utrecht, the Netherlands. The observed background values were $\delta^{33}S$ = 1.0 ± 3.4 ‰ and $\delta^{34}S$ = 15.5 ± 0.8 ‰ (VCDT). The maximum observed COS mole fractions was only 620 ppt. This, in combination with the relatively high $\delta^{34}S$ suggests that the Netherlands receives little COS-containing anthropogenic emissions. We observed a change in COS mole fraction and $\delta^{34}S$ with different air mass origin, as modelled with HYSPLIT backward trajectory analyses. An increase of 40 ppt in mean COS mole fraction was observed between fall and winter, which is consistent with the expected seasonal cycle in the Netherlands. Additionally, we present the results of samples from a highway tunnel to characterize vehicle COS emissions and isotopic composition. The vehicle emissions were small, with COS/CO_2 being 0.4 ppt/ppm; the isotopic signatures are depleted relatively to background atmospheric COS.

2.1 Introduction

Carbonyl sulfide (COS) is the most abundant sulfur-containing trace gas in the atmosphere, with an average mole fraction of 500 parts per trillion (ppt) (Chin and Davis, 1995). It has a lifetime of around two years, which permits it to be transported into the stratosphere. There, it is likely the main source of stratospheric sulfur aerosols (SSA) during volcanically quiescent periods. These aerosols regulate the Earth's albedo and play a crucial role in stratospheric chemistry (Brühl et al., 2012; Crutzen, 1976; Kremser et al., 2016). Understanding the role of COS in stratospheric chemistry is therefore highly important for understanding cooling mechanisms of the Earth.

Another way in which COS can be used to better understand the climate system is through its potential use for the quantification of gross primary production (GPP) of the biosphere. It is difficult to derive GPP from measurements of CO_2, because flux measurements only yield the sum the two almost cancelling fluxes: GPP and respiration. COS, however, is taken up by plants in an essentially one-way reaction, during which it follows almost the same pathway as CO_2 (Protoschill-Krebs and Kesselmeier, 1992;Protoschill-Krebs et al., 1996; Whelan et al., 2018). Therefore, measurements of the unidirectional COS uptake could be used as a tracer for photosynthetic CO_2 uptake and help to quantify GPP (Asaf et al., 2013; Berry et al., 2013; Blonquist Jr et al., 2011; Campbell et al., 2008; Kooijmans et al., 2016).

The largest natural source of COS is the ocean, in the form of direct emission and indirect emission via carbon disulfide (CS_2) and possibly dimethyl sulfide (DMS) (Kettle et al., 2002; Lennartz et al., 2017; Lennartz et al., 2020). The other main sources of COS are anthropogenic, and include rayon production, aluminum production, coal combustion and other smaller sources such as biomass burning (Stinecipher et al., 2019; Zumkehr et al., 2018). Sinks of COS include the above-mentioned large biosphere uptake, and a smaller and less well characterized soil uptake sink (Whelan et al., 2018). Unfortunately, the budget of COS is still not well understood and large uncertainties exist in the strengths of the sinks and particularly the sources of COS (Whelan et al., 2018). Modelling studies and satellite observations can help further constrain the COS budget (Barkley et al., 2008; Glatthor et al., 2017; Kettle et al., 2002; Kuai et al., 2014; Suntharalingam et al., 2008; Yousefi et al., 2019), but the latest studies still point to an unknown missing source of $230 - 432$ Gg S a^{-1} (Ma et al., 2021). Isotopic measurements could provide a tool for overcoming these budget uncertainties, as they can be used to characterize source and sink contributions. Different types of COS sources have distinct sulfur isotopic compositions, which can be used to identify these sources. In COS removal reactions, the lighter isotope is usually preferred over the heavier one because of differences in chemical bond strength. These principles can be used to characterize the influences of sources and sinks. The sulfur isotope ratios are reported as δ values, which are defined by Equation 2.1.1 and Equation 2.1.2, where R is the ratio between the heavier and the lighter isotope, which is then used to calculate the δ^{33}S and δ^{34}S values. The δ values are reported relative to the international sulfur standard; the Vienna Canyon Diablo Troilite (VCDT).

$$^{33,34}R = \frac{^{33,34}\text{S}}{^{32}\text{S}} \qquad (2.1.1)$$

$$\delta^{33,34}\text{S} = \frac{^{33,34}R_{sample}}{^{33,34}R_{standard}} - 1 \qquad\qquad (2.1.2)$$

To date, two methods have been developed for measuring the sulfur isotopic composition of COS. The first method, described by Hattori et al. (2015) and Kamezaki et al. (2019), uses gas chromatography - continuous flow isotope ratio mass spectrometry (GC-CF-IRMS) to measure S^+ fragment ions, and requires very large air samples of several hundreds of liters. This is because of the dependence of the isotope values on the sample amount, usually referred to as non-linearity, that arises when using smaller sample sizes. The second method was first presented by Angert et al. (2019) and uses a multi collector inductively coupled plasma mass spectrometer (MC-ICP-MS), which can measure sulfur isotopic composition of COS from smaller sample sizes of around 3 L. The method we present here is in principle similar to the CF-IRMS method of Hattori et al. (2015), but optimized for small sample volumes of 3 – 4 L of air. This is possible because we characterized the nonlinearity of our system and we apply a correction factor to our isotope measurements that accounts for this nonlinearity.

Newman et al. (1991) presented the first global estimate of δ^{34}S in tropospheric COS of 11 ‰, based on mass-balance calculations. Angert et al. (2019) measured COS sulfur isotopologues from clean ambient air at the Canary Islands and Israel. They found a mean δ^{34}S of 13.4 ± 0.5 ‰, which is roughly in agreement with the estimate by Newman et al. (1991). Kamezaki et al. (2019) showed results from four measurements in Yokohama, with a mean δ^{34}S of 10.5 ± 0.4 ‰. They explained their slightly lower δ^{34}S than Angert et al. (2019) by the presence of anthropogenic COS emissions from China, which have an estimated lower δ^{34}S value of 3 to 8 ‰ (Davidson et al., 2021; Hattori et al., 2020). In a later paper, Hattori et al. (2020) presented new results from air collected at three different locations at different latitudes in Japan during both winter and summer. They found significantly higher mole fractions and lower δ^{34}S values for the most northerly location in winter, which predominantly received air from highly industrialized regions in China. In addition, they found higher δ^{34}S values when the air was predominantly coming from the East, where the ocean source dominates. Based on these results and the Keeling plot intercepts (Keeling, 1961; Pataki et al., 2003), Hattori et al. (2020) deduced an anthropogenic emission value for δ^{34}S of 4 to 5 ‰ and a value of 19 ‰ for the ocean source. These results are roughly in agreement with the newest results presented by Davidson et al. (2021), who measured COS mole fractions and δ^{34}S from 89 air samples from multiple locations around the world. By dividing their dataset in high (>600 ppt) and low (<600 ppt) mole fraction data and calculating the Keeling plot intercepts they found an anthropogenic source value of 8.1 ± 1 ‰. Davidson et al. (2021) also measured direct and indirect COS emissions from the Mediterranean Sea and found a combined δ^{34}S signature of 13.2 ± 2 ‰ for the ocean source. Thus, the ocean source δ^{34}S signature is estimated to be between 13 and 19 ‰ (Davidson et al., 2021; Hattori et al., 2020). The anthropogenic emission signature is estimated to be slightly lower than the ambient δ^{34}S and ranges between 4 and 8 ‰. The biosphere fractionation sink was estimated by Davidson et al. (2021) in a plant chamber experiment, and yielded a fractionation factor $^{34}\varepsilon$, of −1.9 ± 0.3 ‰ for one plant species, thus making the remaining COS pool enriched in δ^{34}S. The fractionation during uptake by three different types of soil bacteria has been measured by Kamezaki et al. (2016) and Ogawa et al. (2017) and they found a similar small

negative $^{34}\varepsilon$ between −3.7 and −2.1 ‰. The destruction reaction of COS with hydroxyl radicals (OH) will likely make the COS more enriched in the heavier sulfur and carbon isotopes (Schmidt et al., 2012a). An experimental study by Hattori et al. (2011) found sulfur isotopic fractionation factors for photolysis destruction of COS of −3.7 ± 4.5 ‰ and 1.1 ± 4.2 ‰ for $^{33}\varepsilon$ and $^{34}\varepsilon$, respectively. The sulfur isotope effects during the reaction with atomic oxygen (O(^{3}P)) were investigated by Hattori et al. (2012) and a fractionation factor $^{34}\varepsilon$, = −21.7 ± 6.2 ‰ was found. However, large uncertainties in these values remain and more research is needed on the isotopic compositions or fractionation factors of sources and sink processes of COS, such as traffic and biomass burning emissions, destruction by atmospheric oxidation and photolysis in the stratosphere.

In summary, substantial progress has been made in the last years on measuring COS sulfur isotopologues. However, in order to fully characterize the global COS budget and its sulfur isotopic composition, more measurements are needed, including atmospheric measurements from several different climatic zones, latitudes and altitudes (Ma et al., 2021). This chapter presents the methodology and first results of our new system that can measure sulfur isotopes of COS using GC-IRMS at Utrecht University, the Netherlands. We present results from online ambient air measurements at the Utrecht University campus, over a time-span of five months in the fall and winter of 2020/2021. We also provide an estimate on the isotopic signature of COS vehicle emissions from air samples taken in a highway tunnel.

2.2 Methods

2.2.1 Measurement system

Figure 2.1 shows a schematic overview of the pre-concentration coupled with a CF-IRMS system, that was developed at the Institute for Marine and Atmospheric research Utrecht (IMAU). The system is partially similar to the ones described in Hattori et al. (2015), Kamezaki et al. (2019), and Angert et al. (2019) and consists of several traps to collect the COS, while discarding the other air compounds. In short, the sample gas is first directed through a cooled Tenax trap, where the COS is preferentially collected. The collected gas is then transferred to the cryo-focus and afterwards further purified in a GC column, before being sent via an open split system to the IRMS for isotope ratio measurements.

Samples, reference gases and COS-free "zero" air for blank measurements are connected to the system with a 12 port multi-position selection valve (EMT2CSD12MWE, dead-end path, 200C/400 psi, Vico Valco Instruments Co. Inc., USA). The selected sample is passed through a dryer, which consists of a glass tube containing magnesium perchlorate $(Mg(ClO_2)_4)$ (63095, Fluka Analytical, Switzerland), held in place by silane treated glass wool at both ends of the tube. As we mostly measure already pre-dried samples, the dryer is replaced approximately every three to four months, when the material starts to look moist. The Tenax trap consists of a 1/16" sulfinert-treated tube (29229, Restek, USA) filled with approximately 200 mg of Tenax TA (60 − 80 mesh, 11982, Supelco Analytical, USA) and silane treated glass wool (20411, Supelco, USA), and is cooled with a mixture of ethanol and dry ice to −72 °C to trap COS. The Tenax trap also contains some 1 mm diameter glass beads to allow for slightly larger pore spaces, to reduce the flow resistance of the trap. Before use, the Tenax is conditioned for 24 hours at a temperature of 200°C under helium flow. After every measurement,

the Tenax trap is flushed forward with a helium flow of 30 mL min^{-1} and heated to 200°C for 30 minutes, in order to limit memory from the previous sample. Sample flow into the trap is kept at or below 80 mL min^{-1} using a mass flow controller, depending on the pressure of the sample being measured. A membrane vacuum pump (type N920 G, KNF, France) is used at the outlet of the trap in order to maintain a high enough flow rate, even when measuring samples with lower than atmospheric pressure. After the desired volume of sample gas is injected in the Tenax trap, the collected gas is released from the Tenax by heating the trap to 130°C with a heating wire. The gas is transported with helium carrier gas, through a six-port valve (A4C6UWM, Vici Valco Instruments Co. Inc., USA) to the cryo-focus trap, where the gas is collected for 30 min at a temperature of –196°C, using liquid nitrogen. This second cold trap consists of a 320 μm inner diameter capillary tube (P/N 064052, Trajan, Australia) and is used to focus the COS in a smaller volume and release it all at the same time, creating a narrower peak on the chromatograph than if only the first cold trap would be used, which is larger and heats up slower. After this focusing step, the remaining compounds in the gas mixture are separated on a gas chromatographic column (CP7549, PoraPLOT Q, 25m, 0.25 mm, Agilent Technologies, USA) heated to 80°C. A ConFlo IV universal continuous flow interface (IQLAAEGAATFAETMAXB, Thermo Fisher Scientific, USA) is used to inject the gas into the IRMS (IQLAAEGAATFABHMZZZ, Delta V Advantage, Thermo Fisher Scientific, USA), where the COS is ionized and fragmented, with a S$^+$ fragment yield of approximately 30% (National Institute of Standards & Technology and Linstrom, P.J. and Mallard, W.G. (Ed.), nd). The fragment ions ^{32}S$^+$, ^{33}S$^+$ and ^{34}S$^+$ are collected on triple Faraday collector cups for m/z 32, 33 and 34, with resistors 3*10^9 Ω, 1*10^{12} Ω and 3*10^{11} Ω. Altogether, one sample measurement takes 2 to 3 hours, depending on initial pressure and the volume of sample that was injected. The injected sample volume was chosen based on the expected COS mole fraction in the sample, and adjusted so that the sample COS peak area would be similar to the reference gas COS peak area.

At the start of each measurement, a working gas is injected into the IRMS via the ConFlo three times. As working gas, pure O$_2$ is used, which has the three isotope masses needed. Additionally, since pure COS is highly toxic, it is much safer and more convenient to use O$_2$ as a working gas. The isotope ratios of all sample and reference measurements are first calculated relative to our working gas. From these, the sample values are calculated relative to the reference gas, which is calibrated against the international standard VCDT National Institute of Standards & Technology and Gonzales, C.A. and Watters, R.L. (Ed.) (2013). This calibration process and other data corrections and processing are further elaborated in the next section.

Figure 2.2 shows an example of a chromatogram of a COS measurement with the three square peaks of the working gas at the beginning, followed by additional peaks including the COS sample peak. The peak that arrives after the O$_2$ square peaks, with a retention time of around 320 seconds, is likely from the O$_2^+$ fragment of remaining CO$_2$ that is also being trapped in the Tenax trap, as this peak increases for gases with elevated CO$_2$ mole fraction. Most of the CO$_2$ that is trapped on the Tenax is removed through timed valve switching, thus we expect that the peak on the chromatogram is only the "tail" of the peak. At 410 seconds, the COS peak elutes, with the m/z of 33 and 34 traces having larger amplitudes than m/z 32 trace because of the much higher resistors. The several peaks that follow the COS peak, but are well separated, mostly show on m/z 33 and are possibly organic compounds as mentioned by Kamezaki et al. (2019).
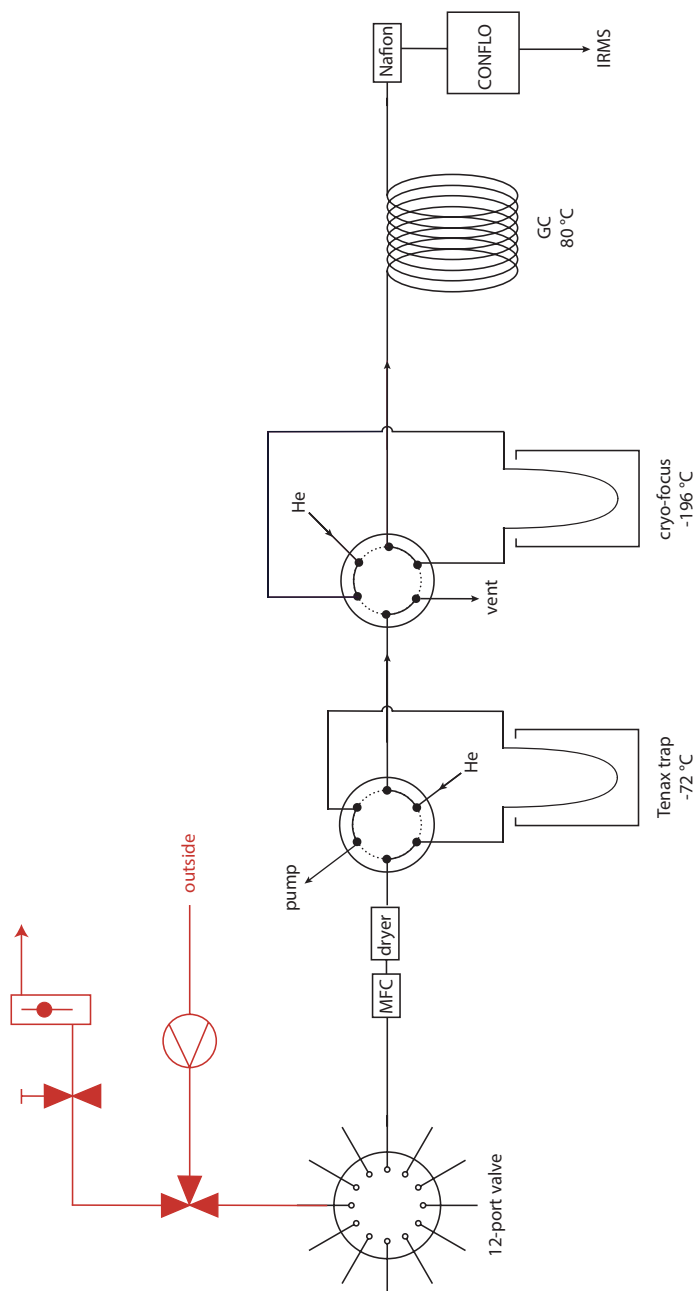
Figure 2.1: Schematic overview of the COS pre-concentration system, with in red the ambient air sampling system including a three-way valve, a pump, a needle valve and a flow controller and in black the pre-concentration system, with a 12-port dead-end multi-position valve, a mass flow controller (MFC), a magnesium perchlorate dryer, two 6 port valves, a Tenax TA trap and a cryo-focus trap, a gas chromatographic column (GC), a Nafion dryer, a ConFlo interface and an isotope ratio mass spectrometer.
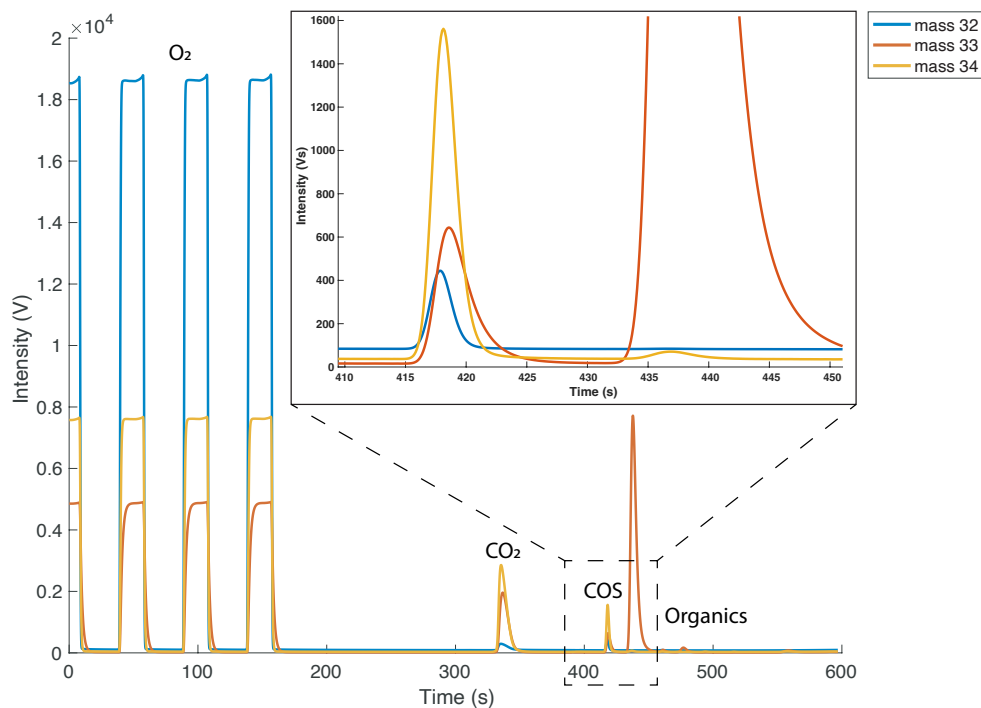
Figure 2.2: Full chromatograph of one reference gas measurement. First three peaks are the O_2 working gas peaks. The chromatogram starts with O_2 in the source flushing because the IRMS source is constantly flushed with O2 in between measurements. After the working gas peaks we see a peak which is suspected to be CO_2, which is followed by the small COS peak, and several other peaks that appear on m/z 33 only. The inset in the top right corner zooms in on the COS peak.

2.2.2 Testing the pre-concentration system

Reproducibility

The reproducibility of the system was characterized by measuring 1 L, 2 L and 3 L volumes of the same gas with 6 to 8 repetitions, using the same method for all measurements. The gases used were target gas 2 (ambient air reference gas for CO isotope measurements) and a 5 L stainless steel cylinder filled with ambient air during EastGRIP 2018 in Greenland. From these measurements, we estimated the typical reproducibility as the two-tailed 70% confidence interval using the student t-distribution with n−1 degrees of freedom. The total error of individual sample measurements is slightly higher because of the addition of the nonlinearity correction error of $\delta^{34}S$ of both $\delta^{33}S$ and $\delta^{34}S$, as shown below. The statistical analysis and all other analyses and creation of figures further described in this chapter and the rest of this thesis were performed using MATLAB R2020b.

Nonlinearity

Nonlinearity is the dependence of δ values on the integrated ion signal (peak area) of all isotope masses contributing to a certain peak in the IRMS chromatogram. Hattori et al. (2015) found a strong nonlinearity for their system between a COS total peak area of 0 and 8 Vs (mass 32, 33 and 34 combined), and they therefore decided to only measure total peak areas above 8 Vs. This meant, however, that a very large sample size of several hundreds of liters was required for a single measurement. For our measurements, in order to be able to measure smaller samples, the nonlinearity of the system was characterized and a correction factor to account for this nonlinearity was determined and applied to our data. This was done in two ways. For the first set of experiments, a 2 L glass flask (Norrmag, Ilmenau, Gerrmany with PCTFE sealing; Rothe et al., 2005) was filled with a gas mixture containing 2 ppb COS and zero air. The flask was connected on one side to the COS isotope measurement system and the other side of the flask was connected to a zero air cylinder. While keeping overpressure on the flask from the zero air cylinder, a series of 3 L measurements was conducted during which the gas mixture in the flask was more and more diluted with zero air with each subsequent measurement.

The second method for characterizing the nonlinearity was done by injecting different volumes of the target gas, starting at 1 L and increasing in steps of 250 to 500 mL up to a volume of 4 L. In both methods, the dependence of the isotope values on the peak area was characterized by fitting a function through the data. From this trendline, a correction factor for the isotope values was calculated. The non-simultaneous 68% function bounds give the uncertainty of this function and thus the uncertainty added to the data when applying the nonlinearity correction.

The error from the nonlinearity correction (σ_{nonlin}) and the reproducibility (σ_{reprod}) were combined following error propagation using Equation 2.2.1. This error represents the internal error, or how well individual measurements can be related to the internal lab scale.

$$\sigma_{total} = \sqrt{\sigma_{reprod}^2 + \sigma_{nonlin}^2} \tag{2.2.1}$$

Calibration

All measurements were first measured against the O_2 working gas. Each sample was measured against our lab reference gas, which was a high-pressure cylinder, filled with ambient air at the surface of Greenland during the 2017 EastGRIP campaign (EastGrip, 2022). For the calibration against the international sulfur standard Vienna Canyon Diablo Troilite (VCDT), we used four COS calibration gases produced and calibrated at Tokyo Institute for Technology, which contained high mole fraction COS (50 to 200 ppm) in nitrogen. The first calibration gas called "10.5% COS" was a commercially obtained COS gas in high-purity He (99.99995% purity; Japan Fine Products Co. Ltd., Kawasaki, Japan). The other three calibration gases were synthesized as described in Hattori et al. (2015) from three kinds of sulfur powders: Wako, Sigma-Aldrich and a mixture of the two. The synthesized COS gases were prepared at Tokyo Institute of Technology through a reaction of the sulfur powders and CO gas (99.99% purity; Japan Fine Products Co. Lt., Kawasaki, Japan) in glass tubes at 573 K for 24 hours. The gases were purified using a GC, equipped with a thermal conductivity detector (GC-14B; Shimadzu, Kyoto, Japan) and a packed column (Porapak Q, 2 mm i.d. 2.4 m; GL Science, Tokyo, Japan) maintained at 333 K.

The above-mentioned calibration gases were assigned $\delta^{34}S$ values on the VCDT scale by both an off-line and on-line method performed in the Geo Science Laboratory in Nagoya, Japan. For the off-line method, 20 μmol of each COS gas was reacted with an alkaline zinc solution (zinc acetate NaOH), and the sulfur was precipitated as ZnS overnight. The ZnS was washed by adding 18 MΩcm water (ZRXQ005T0, MerckMillipore, Corp., Burlington, MA, USA) and centrifuging, three times. The ZnS was combusted to SO_2, of which the $\delta^{34}S$ values were measured on the VCDT scale by elemental analyzer (EA)-IRMS. The total error (1 σ) derived from repeatability and accuracy was 0.4 ‰ for the off-line method. The remaining COS gases were pressurized with high-purity nitrogen (99.99995% purity; Japan Fine Products Co. Ltd., Kawasaki, Japan) to 1067 mbar and were stored in 3 L SilcoCan canisters (27303, Restek Corp., Pennsylvania, USA) for the on-line measurement. The on-line measurements were performed by Tokyo Institute of Technology according to the method developed previously (Hattori et al., 2015; Kamezaki et al., 2019). The total error (1 σ) derived from repeatability, size dependence and accuracy was 0.3 ‰ for the on-line method. The $\delta^{34}S$ VCDT values of the on-line and off-line measurements were very similar. The off-line values were used for fitting the calibration line, which yielded a calibration range for $\delta^{34}S$ of −8.9 ‰ to 13.3 ‰.

The calibration of $\delta^{33}S$ of these same calibration gases on the VCDT scale was done by calculating their values relatively to the $\delta^{33}S$ of a calibration gas (11 ppm COS) that has been used for $\delta^{33}S$ calibration in the past by Kamezaki et al. (2019). This method assumes that the $\delta^{33}S$ of this calibration gas has not changed since it was last measured in 2017. This assumption is supported by the fact that the $\delta^{34}S$ value of this same gas has been confirmed several times between 2017 and the present and no drift has been found. A mass-dependent relationship between $\delta^{33}S$ and $\delta^{34}S$ was found for all other calibration gases in the past, thus we assume that no mass-independent drift has occurred in the "11 ppm OCS" calibration gas. The calibration range for $\delta^{33}S$ is −7.8 ‰ to 6.6 ‰.

During our calibration procedure, the high COS mole fraction calibration gases were diluted into 6 L canisters using zero air to a mole fraction of 30 to 50 ppb. Two of the gases were chosen for further dilutions, which were the ones that had isotopic compositions that

were most different from ambient air. These gases were diluted further in 5 L cylinders to a pressure of 100 bar, and a mole fraction of approximately 700 ppt. During the calibration procedure we performed measurements of different volumes of all the dilutions made from the initial gases. We measured at different total peak areas between 1 and 6 Vs, to check for any nonlinearity effects.

All measurements were combined to derive a calibration curve, where the assigned $\delta^{33}S_{VCDT}$ and $\delta^{34}S_{VCDT}$ values from Japan are plotted against the $\delta^{33}S$ and $\delta^{34}S$ values measured in Utrecht, relatively to our reference gas. Trendlines were fitted using a linear regression method (York et al., 2004) which considers the errors in both the X and Y direction. A slope of the calibration line >1 was considered as an evidence of scale contraction and, if needed, a correction method was developed. The results of the calibration procedure are presented below. The 68% uncertainty bounds were calculated using a bootstrapping resampling procedure to calculate the calibration error, which indicates how well the measurements in Utrecht can be linked to measurements in other labs on the VCDT scale.

Data corrections, quality check and long-term stability

At the beginning and end of each measurement sequence, blank measurements were performed, which were either 3 L injections of COS-free "zero air", or "no-load" blanks in which no gas was injected into the pre-concentration system. The blank was found to be less than 5% of the reference gas peak area and these blank measurement values were used to correct the peak area and isotope values of the measurements.

To monitor the long-term measurement stability, COS in air from a target cylinder (5 L, dried ambient air filled in Greenland in 2017 at 39 m depth) was measured approximately weekly. A second target cylinder was introduced after the first gas cylinder was exhausted (ambient air high-pressure cylinder no. 1341). If an error occurred during the pre-concentration phase (e.g. incorrectly timed valve switching, sample not opened properly), or if a measurement looked clearly not good (e.g. bad GC separation or strange peak shape), those measurements were flagged and not included into the final dataset. In the end approximately 7% of the measurements, including blank and reference gas measurements, had to be flagged due to the above-mentioned reasons.

Additional tests

This section describes some additional tests that were performed with the COS measurement system. These tests were performed to fully characterize the behavior of separate elements of the measurement set-up and to optimize the steps undertaken during the measurement procedure. The detailed results of these tests can be found in Underlying data Baartman et al. (2021).

Some materials are known or suspected to influence COS mole fractions by either emitting COS or trapping it on their surfaces (COSANOVA, n.d.). Therefore, several parts of the pre-concentration system were tested to make sure they did not affect our COS measurements. Firstly, the interference of the magnesium perchlorate dryer was tested, by comparing measurements of the same known gas with and without dryer. The influence of the vacuum pump at the end of the Tenax trap was also tested, by comparing measurements of the same gas with the pump turned on or off. No significant influences of the dryer or the vacuum pump were found.

Several tests were performed to optimize the release of COS from the Tenax trap. We investigated the effect of the heating temperature of the trap on the amount of COS that was released from the trap, in various ways. First, multiple COS isotope measurements were conducted using the same EastGRIP 2017 gas cylinder but using different Tenax trap heating temperatures of 100℃ and 130℃, where the measured COS peak areas were compared. Another test was to heat the Tenax in steps, increasing from room temperature to 200 ℃ with a 10 ℃ increase every 10 minutes, to see at which temperature the COS would be released. The effect of the duration of the Tenax trap heating was tested by comparing different heating durations to the COS peak area. The optimal heating procedure for COS release from the Tenax was 130℃ for 30 minutes.

The optimal time for flushing and heating the Tenax trap during the cleaning procedure in between measurements was also tested. This was done by performing 10 measurements with 15 minutes of heating and flushing and 10 measurements of the same EastGRIP 2017 gas cylinder with 30 minutes of heating and flushing. The results were compared by checking the trend in COS peak areas within each measurement sequence of 10 measurements. An upward trend in peak areas of the measurements would point to an insufficient cleaning of the Tenax, leading to contamination of the next measurement. The optimal cleaning time for the trap was found to be 30 minutes.

The trapping efficiency of the Tenax trap was tested by placing a second Tenax trap after the first one and measuring a gas with ambient COS mole fraction (target gas from EGRIP 2017). The COS that escaped the first trap would be trapped on this second trap. The traps were heated separately and the COS released from the trap could be measured independently. Tests were performed injecting volumes of air of 3 L, 4 L, 5 L and 6 L, to see if any breakthrough would occur at higher injected volumes. The trapping efficiency was found to be 100% for all injected volumes that were tested.

Because of the presence of other compounds in the chromatogram (Figure 2.2), we tested the possible interference of several available compounds on the trapping of COS, by measuring gas mixtures with known mole fractions of 1.6% CO_2, 1% CH_4 and 4.5% H_2 and comparing these to measurements of gases without those gases present. CO_2 interference was specifically tested since it was suspected to be one of the larger peaks on the chromatogram and since its possible interference was also mentioned by Angert et al. (2019). No interference of these compounds on COS trapping was found.

The memory effect and thereby also the blank peak area of the system was tested by first measuring a 3 L injection of a gas with a COS mole fraction of approximately 900 ppt, followed by a sequence of zero air measurements. By inspecting the peak area of the zero air measurements in the chromatogram, the memory effect was characterized. No significant memory was found with the current heating and flushing time of the Tenax, thus the influence of the previous sample measurement on the next is negligible.

2.2.3   Ambient air measurements in Utrecht

Ambient air was drawn from outside the Buys Ballot building on the Utrecht University Campus (coordinates: 52.087471, 5.165394) with a sampling system that was directly connected to the pre-concentration system, as indicated in Figure 2.1 in red. The sampling system consisted of a 1/4" Dekabon tube, which ran through a small hole in the wall of the lab to the outside. The opening of the tube was about one meter from the building wall,

and at an altitude of approximately 15 m from the ground (on the 6th floor). A magnesium perchlorate dryer was installed at the end of the sampling tube and was replaced regularly while sampling. The air was drawn in using a small membrane pump (type PM22874-86, KNF, France), which created a continuous flow rate of around 2 L min^{-1}. When sampling air, 80 mL min^{-1} was split into the pre-concentration system, while the rest of the air was vented. The pressure of ambient air going into the pre-concentration system was regulated by a needle valve and a flow controller at the outlet of the sampling system. Setting up the system in this way allowed for a continuous high flow through the Dekabon tube, so that there would be no stagnant air in the tube, and therefore less chance of contamination. One measurement with this set-up, including flushing and cleaning time of the Tenax trap, takes three hours.

Because the ambient air was running through the KNF pump before entering the pre-concentration system, we tested the possible interference of this pump on COS mole fractions and isotopic composition. This was done by connecting one of the target gas cylinders to a 2 L glass flask, and connecting the sampling pump to the other end of the flask. The glass flask was added to create a volume of air between the pressurized cylinder and the pump, to prevent harm to the cylinder regulator. The outlet of the pump was then connected to the multi-position valve of the pre-concentration system. Using this set-up, we measured the same injected volume of the same gas 10 times. The results of this test were then compared to 10 measurements of the same gas with the same set-up, but with the pump removed. No significant effect of the pump on the measurement results was found.

A series of 15 sequences of COS isotope measurements from ambient air were performed between mid-October 2020 and January 2021, which yielded a total of 80 individual outside air measurement points. Each sequence consisted of four up to 12 ambient air measurements, interspersed with reference gas measurements.

Backward trajectory analysis using the Hybrid Single-Particle Lagrangian Integrated Trajectory model (HYSPLIT) was performed in order to determine the prevailing wind directions during sampling and the main air origins (Stein et al., 2015). The backward trajectories were calculated going back 96 hours from the time of the last sampling, with a new trajectory being calculated every 2 hours during the measurement period for an altitude of 20 m.

2.2.4 Highway tunnel measurements

The Utrecht University campus is situated close to a busy highway and some highway junctions. As it is reported that cars do emit small amounts of COS both by combustion and tire wear (Lee and Brimblecombe, 2016; Zumkehr et al., 2018), this highway could be a potential local source influencing our ambient air measurements. In order to assess the possible influence of traffic emissions, we collected some samples from a highway tunnel in the Utrecht region. Samples were taken in the Leidsche Rijntunnel (52°05'09.6" N 5°04'32.2" E), which has a length of 1650 m, a speed limit of 100 km/h and consists of four separated unidirectional tubes. The inner tubes have three driving lanes, while the outer have two lanes. The average traffic intensity for this tunnel was 200.000 vehicles per 24 hours (Rijkswaterstaat, 2020). We drove with a 2012 Volkswagen transporter, equipped with a cavity ring-down analyzer, Picarro Inc. G2301. The G2301 was able to measure mole fractions of CO_2, CH_4 and H_2O. For a full description of the van and the analyzers, see Maazallahi et al. (2020),

who used the same set-up for mobile CH_4 measurements.

The samples for COS analysis were collected in pre-evacuated 6 L ENTECH Silonite canisters as follows: a 1.5 m Dekabon tube was connected to the outside of the van and sticking 1 m upwards from the top of the van door. A magnesium perchlorate dryer was installed between the tubing and the canister, which was replaced every two canisters. When sampling, the canister was opened a couple of seconds after entering the tunnel and closed again some seconds after exiting. An air inflow was maintained all throughout the sampling in the tunnel, however, with the canisters being evacuated at the start, the samples could have been slightly biased to the air at the entrance of the tunnel. The resulting pressure in the canisters was slightly below atmospheric as no pump was used during the sampling procedure. A total of six canisters was collected during the six tunnel drive throughs, of which one in the inner tube of the tunnel and the other 5 in the outer tubes. One day after sampling, the samples were diluted with COS-free synthetic air to increase the pressure of about 1.7 bar and measured with the COS isotope measurement system. Besides the online measurements, the samples were also measured for CO_2 and CH_4 mole fractions, using the above mentioned Picarro G2301 instrument.

For interpretation of the COS isotope and mole fraction data, Keeling plots (Keeling, 1961; Pataki et al., 2003) were created using MATLAB R2020b.

2.3   Results and discussion

2.3.1   Reproducibility

Figure 2.3 shows the measurement reproducibility as a function of the measured COS peak area (n = 6 to 8), where each dot in the scatter plot represents the precision of a set of measurements. A trendline was fitted through the data-points to use as a continuous function for the precision when calculating the error for individual samples. The dependence of the precision on peak area, within the range of our measurements (peak area between 1 and 0.2 Vs), can best be described by the exponential functions given in Equation 2.3.1 (R^2 = 0.76) and Equation 2.3.2 (R^2 = 0.40).

$$\sigma_{\delta^{33}S}(A) = 3.70e^{-0.67A} \tag{2.3.1}$$

$$\sigma_{\delta^{34}S}(A) = 0.97e^{-1.01A}, \tag{2.3.2}$$

where σ is the reproducibility error in ‰, and A is the peak area of a measurement in Vs. For reference, a measurement of 4 L of ambient air with an ambient mole fraction of 550 ppt will give a peak area of approximately 0.68 Vs, which would correspond to a system error of 2.1 ‰ for $\delta^{33}S$ and 0.4 ‰ for $\delta^{34}S$.
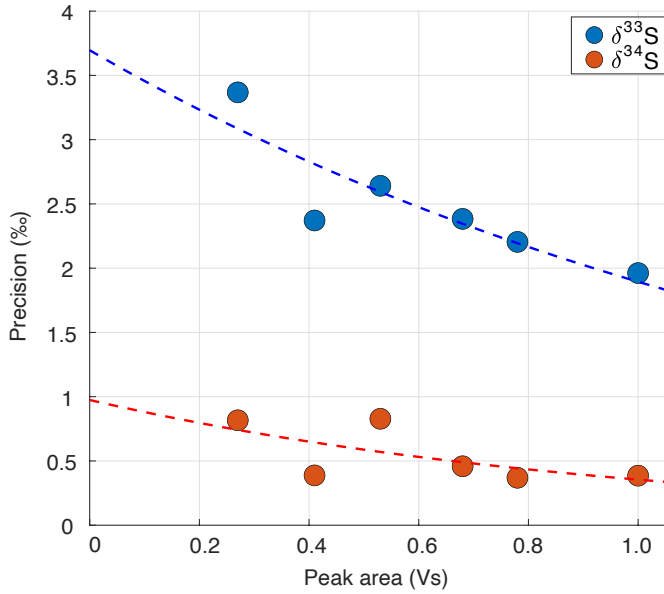
Figure 2.3: The precision in ‰ as a function of total peak area in Volt seconds (Vs). Every data point represents the 70% confidence interval from a student t-distribution of 6 – 8 measurements combined.

2.3.2 Nonlinearity

Figure 2.4 shows the nonlinearity data including a regression line and the 68% functional bounds for the δ^{34}S data. It can be observed that the nonlinearity effect for δ^{34}S is minor and only a small correction was needed for the ambient air measurements, which had peak areas between 0.65 and 0.8 Vs (indicated with the shaded area in Figure 2.4). Equations 2.3.3 and 2.3.4 describe the correction made for δ^{34}S with a peak area smaller than 1 Vs, where A_{ref} is the peak area of the reference measurements and A_{sample} is the sample peak area. For δ^{33}S, the nonlinearity effect only starts to be evident from peak areas smaller than 0.4 Vs. Since our dataset does not include any measurements with such low peak areas, no correction for δ^{33}S was applied.

$$\delta^{34}S_{correction} = (5.17e^{-0.49A_{ref}} + 9.66e^{0.1A_{ref}})- \\ (5.17e^{-0.49A_{sample}} + 9.66e^{0.1A_{sample}}) \tag{2.3.3}$$

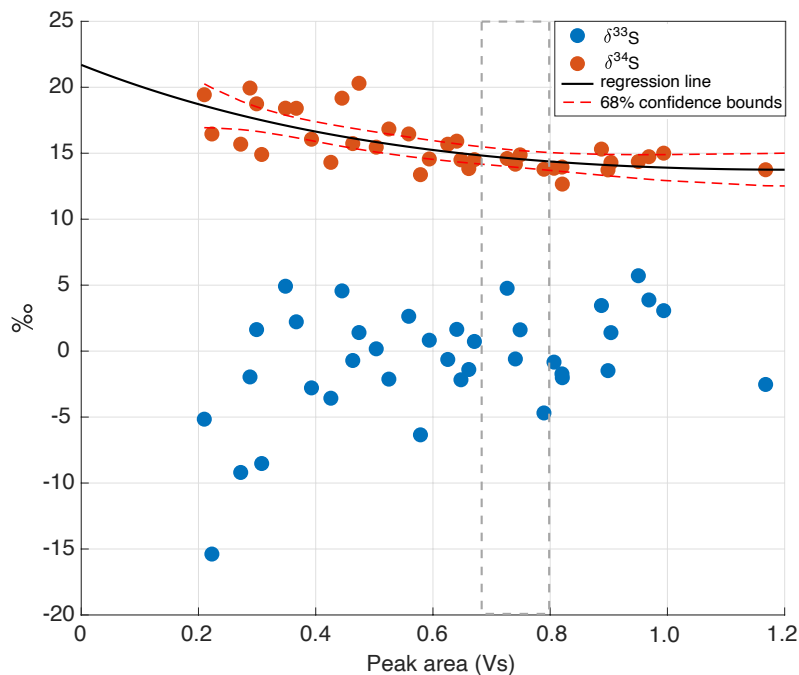$$\delta^{34}S_{corrected}(A_{sample} \geq 1) = \delta^{34}S(A_{sample} \geq 1)+ \\ \delta^{34}S_{correction}(A_{sample} \geq 1) \tag{2.3.4}$$

Figure 2.4: Nonlinearity plot for both δ^{33}S and δ^{34}S, with the total peak area in Volt seconds (Vs) on the x axis and the isotope values in ‰ on the y axis. The black line is the linear regression line for δ^{34}S, including the 68% confidence bounds in red dashed lines. The grey dashed lines indicate the usual peak area for a 4 L ambient air measurement.

2.3.3   Calibration

The results of the calibration are available in Underlying data Baartman et al. (2021). Table 2.1 shows the results of the calibration with the four calibration gases: Wako, Sigma-Aldrich, Mix (a mixture of Wako and Sigma-Aldrich) and 10.5% COS. Figure 2.5 shows the assigned δ^{33}S$_{VCDT}$ and δ^{34}S$_{VCDT}$ values of the calibration gases against the results of our measurements relative to the reference gas. These were used to calculate the calibration functions for our measurements, also shown in the figure.

For δ^{34}S, the slope of the calibration line is 1.01 ± 0.01, which means there was no significant scale contraction and no correction was necessary. The calibration gases gave us a broad calibration range, from δ^{34}S = −15.7 ‰ to +13.3 ‰ VCDT, bracketing the atmospheric δ^{34}S values. For δ^{33}S, a slope of 1.15 ± 0.12 was found, which means that there may be some small-scale contraction effect for δ^{33}S and a correction was applied. Furthermore, a larger spread in the measurement data for δ^{33}S lead to a larger error of the calibration line (red dotted lines in Figure 2.5), and to a substantially larger total error. One of the calibration gases (gas 2, Sigma-Aldrich) showed a larger spread in the results for both isotopes, which increased the uncertainty in both calibration lines, but especially the calibration line of δ^{33}S. When combining the errors from the reproducibility, the nonlinearity correction

and the calibration, the total error for a 4 L ambient air sample is 3.3 ‰ for δ^{33}S and 0.9 ‰ for δ^{34}S.

Table 2.1: Results of the COS calibration with four calibration gases "Wako", "Sigma-Aldrich", "Mix" and "10.5% OCS", where δ^{34}S Utrecht and δ^{33}S Utrecht are the isotope values measured by our measurement system in Utrecht, δ^{34}S$_{VCDT}$ off-line are the δ^{34}S values measured by the off-line method in Japan, δ^{34}S$_{VCDT}$ on-line are the δ^{34}S values measured by the on-line method in Japan and δ^{33}S vs "11 ppm OCS" gas are the δ^{33}S values on the VCDT scale calculated relatively to the δ^{33}S of a calibration gas called "11 ppm OCS" that was used previously for the δ^{33}S calibration by Kamezaki et al. (2019).

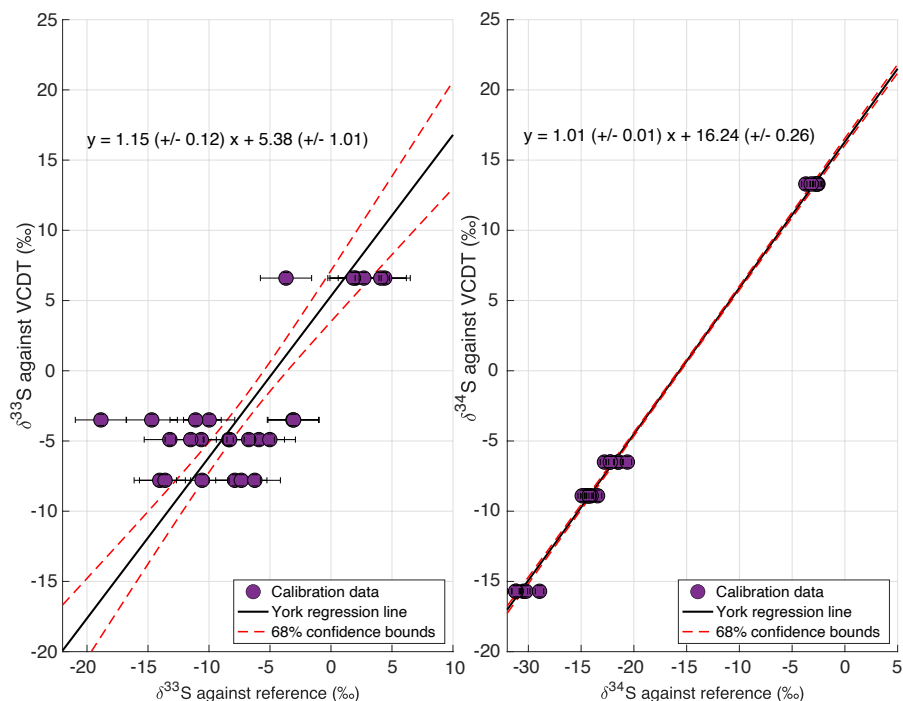| Gas	δ^{34}S$_{ref-Utrecht}$	δ^{34}S$_{VCDT}$ off-line	δ^{34}S$_{VCDT}$ on-line	$\delta^{33}$$_{ref-Utrecht}$	δ^{33}S vs "11 ppm OCS" gas
Wako	−24.3 ± 0.4	−8.9 ± 0.4	−9.3 ± 0.3	−8.7 ± 2.9	−4.9 ± 0.4
Sigma-Aldrich	−21.8 ± 0.8	−6.5 ± 0.4	−6.1 ± 0.3	−10.1 ± 3.3	−3.5 ± 0.4
Mix	−30.7 ± 0.4	−15.7 ± 0.4	−15.0 ± 0.3	−10.0 ± 3.3	−7.8 ± 0.4
10.5% OCS	−2.9 ± 0.4	13.3 ± 0.4	13.5 ± 0.3	1.9 ± 2.9	6.6 ± 0.4

Figure 2.5: Results of the isotope calibration of δ^{33}S and δ^{34}S based on calibration gases provided by Tokyo Institute of Technology. The data points represent the individual calibration measurements. The black line is the York regression line (York et al., 2004), and the red dashed lines represent the 68% confidence bounds of the regression line.

2.3.4   Additional tests

The magnesium perchlorate dryer did not have a significant effect on the amount of COS trapped in the Tenax trap nor on the isotopic composition of the measurements. There was no significant difference in mean peak area or δ^{33}S and δ^{34}S with and without the dryer. Because the presence of water in the system could be detrimental to the pre-concentration system, we decided to keep a dryer the line before the Tenax trap for all measurements.

The membrane pump at the end of the system also did not significantly change the peak area nor the isotopic composition of the COS measurements. This pump allowed us to measure at higher flows and measure from samples until lower pressures, thus the pump was included for all measurements.

The optimal heating temperature of the Tenax for COS release to the focus trap is 130°C. This temperature yielded the highest peak area for the same amount of injected gas, and when heating to higher temperatures, no more COS was released from the trap. It was found that most of the COS was already released at room temperature, which was also noticed by Tangerman (1986). The optimal cleaning time of the trap in between measurements was found to be 30 minutes. During the Tenax trapping efficiency test with the second Tenax trap we found that the peak area of COS released from the second trap was equal to blank measurements. This test was performed up to volumes of 6 L of injected air. In all tests, the

Tenax trap had a >99% trapping efficiency.

The presence of CO_2, CH_4 or nitrogen did not have an influence on the trapping efficiency or isotopic composition of the measured COS, which is in agreement with similar tests performed by Angert et al. (2019).

When testing the memory effect in the system, we found that the peak area of the first zero air measurement after the sample measurement was 5.1% of the sample measurement peak size. The peak area did not decrease much in the subsequent zero air measurements. By the 9th measurement, the peak area had decreased only to 4.9% of the sample peak size. The other type of blank measurements, where no sample was loaded at all, also yielded a peak area between 2 and 5% of the sample measurement peak area. We therefore assumed that the interference of the previous gas on the next measurement was minimal, and that our system has a constant 5% blank level. However, we made sure to always measure a 3 L zero air injection after a measurement of a gas with higher COS mole fraction, in order to minimize a potential memory effect on the subsequent measurement.

2.3.5 Long-term stability of the measurement system

Figure 2.6 shows the time series of online ambient air measurements with the target gas measurements plotted as grey and purple asterisks in the background. Target measurements were performed throughout the measurement period in order to monitor long-term variability and characterize potential drift in the system. The two different target gases are indicated as different color asterisks in the figure. It can be observed that for the COS mole fraction there is little variability in these target measurements on the daily scale and also no evidence of drift on the longer time-scale. The variations in COS mole fractions of the ambient air measurements are clearly larger than in the target measurements. For δ^{34}S, the day-to-day variability of the target is up to a maximum of 2 ‰ and there is no evidence for drift visible on longer time-scales. The error of the target measurements over the course of the measurement period was 0.5 ‰ (1 σ). The day-to-day variability of the target measurements is larger for δ^{33}S; from 5 ‰ up to around 12 ‰, indicating that measurements of δ^{33}S with our system are less stable and we should be careful with drawing conclusions on small variations of δ^{33}S in sample measurements. However, also for δ^{33}S there is no apparent long-term drift in the target measurements, and the error of the target over the measurement period was 3.4 ‰ (1 σ), which is similar to the total error for an ambient mole fraction 4 L air sample.
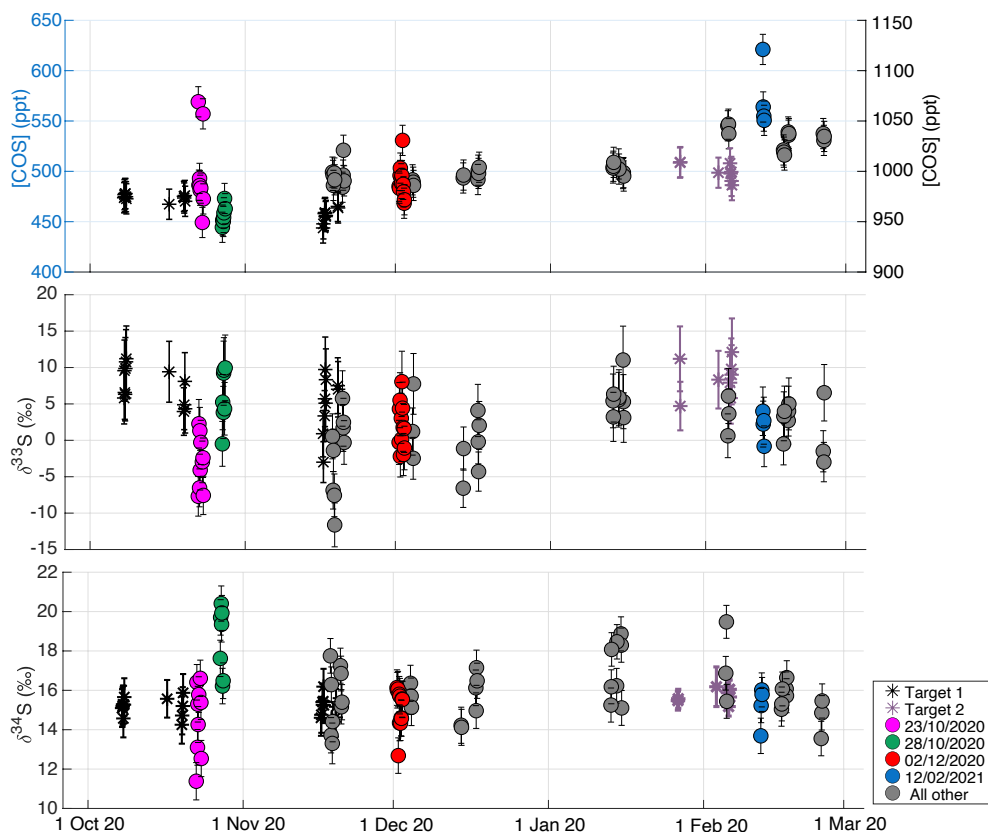
Figure 2.6: Ambient air time-series plotted together with measurements of two target gases in black and purple asterisks, to show the long-term variability of the measurement system. The second target gas (purple asterisks) was introduced after the first one was exhausted, and has slightly higher mole fraction than the first target gas (black asterisks). Upper figure shows COS mole fraction with the ambient air measurements plotted on the left y-axis and the target measurements on the right y-axis. Middle figure shows $\delta^{33}S$, and the lower panel shows $\delta^{34}S$. All data are plotted against date and time on the x-axis. some sequences of special interest are highlighted in the colors pink (Oct 22 – Oct 23), green (Oct 27 – Oct 28), red (Dec 1 – Dec 2) and blue (Feb 12). The grey colors represent all other measurements.

2.3.6   Ambient air measurements Utrecht

The Utrecht ambient air dataset is available in Underlying data Baartman et al. (2021). Figure 2.6 shows all air measurements, and, indicated with different colors, measurement sequences of special interest that correspond to the HYSPLIT backward trajectory results shown in Figure 2.7. The trajectories for all the measurement days in the time-series can be found in Underlying data, and the supplementary material of this chapter. The mean COS mole fraction during the measurement period was 503 ± 15 ppt, with a variation between 450 and 650 ppt. An increasing trend was observed in the transition from the fall to the winter season, from a mean of 488 ± 15 ppt in fall to 530 ±15 ppt in winter. This trend is to be expected as the biosphere is the largest sink of COS and becomes mostly inactive during

winter in the Northern Hemisphere (Montzka et al., 2007). The maximum observed mole fraction observed was 621 ppt on Feb 12 th 2021.

The mean δ^{33}S and δ^{34}S over the measurement period were 1.1 ± 3.3 ‰ VCDT and 15.7 ± 0.9 ‰ VCDT respectively. We estimate the background δ^{33}S and δ^{34}S values in Utrecht by assuming a background COS mole fraction between 480 and 510 ppt and selecting the mean δ values ± 1 σ from this background mole fraction selection. Using this method, we obtain background values of 1.0 ± 3.4 ‰ (μ ± SE) and 15.5 ± 0.8 ‰ (μ ± SE) for δ^{33}S and δ^{34}S respectively. Our background value for δ^{34}S value is slightly higher than the numbers that have been reported in previous studies. Davidson et al. (2021) found a mean tropospheric δ^{34}S of 13.9 ± 0.1 ‰ and Hattori et al. (2020) estimated a background δ^{34}S of 12 to 13.5 ‰ for Japan. This higher background δ^{34}S and also the lack of very high COS mole fractions in our measurements from Utrecht could possibly be explained by a lower amount of anthropogenic emissions in this region, but could also be due to a larger influence of the biosphere sink that enriched Northern Hemisphere air masses during summer and fall Davidson et al. (2021), or a larger contribution of the ocean source.

A cross-calibration of measurements between different measurement laboratories would be useful to investigate whether differences in measured background δ^{34}S are significant atmospheric signals or are still due to measurement uncertainty. The value for δ^{33}S of 1.0 ± 3.4 ‰ is lower than expected from mass-dependent processes. Equation 2.3.5 presents the calculation of δ^{33}S, which describes the deviation of δ^{33}S from the mass-dependent fractionation line (Farquhar and Wing, 2003; Ono et al., 2006). δ^{33}S would in this case be slightly negative, however, as there is still a substantial uncertainty in our calibration of the δ^{33}S measurements, we should be careful with the interpretation of these values.

$$\Delta^{33}\text{S} = \delta^{33}\text{S} - ((\delta^{34}\text{S} + 1) * 0.515 - 1) \tag{2.3.5}$$

While there are some short-time variations in δ values, there is no significant seasonal trend visible in δ^{34}S, with a mean δ^{34}S value in the fall (22 October – 22 December) of 15.8 ± 0.9 ‰ and 16.2 ± 0.9 ‰ in winter (22 December onwards). Davidson et al. (2021) found a seasonal variation in δ^{34}S between spring and fall of 1.2 ‰, which was ascribed to the effect of a small fractionation during plant uptake of −1.9 ‰. As our time-series does not include the spring and summer seasons yet, and as the seasonal trend is expected to be small, it is not surprising that we do not observe such a seasonal trend in our dataset.

More information can be gained from this dataset when looking more closely at the variability on the day-to-day to weekly scale, and a comparison to the backward trajectory analyses shown in Figure 2.7. Potentially interesting are the days that were influenced by anthropogenic industrial emissions. Hattori et al. (2020) reported large enhancements in COS mole fractions, accompanied by depleted δ^{34}S values, when measuring air from the Chinese mainland. It is likely that in Europe there is less anthropogenic COS emission, but no measurements have been presented so far on these emissions, nor has their sulfur isotopic composition been reported. On the 1st and 2nd of December, the Netherlands experienced mostly easterly winds, bringing in polluted air from the Ruhr area, a large industrial region in Western Germany. COS data from these days are shown separately in Figure 2.8, together with CH_4 and CO_2 mole fractions. During these days, CO_2 and CH_4 mole fractions increased, with a maximum CO_2 mole fraction of 480 ppm and CH_4 mole fraction peaking at 2.5 ppb. During the first hours of this pollution accumulation, COS mole fractions also
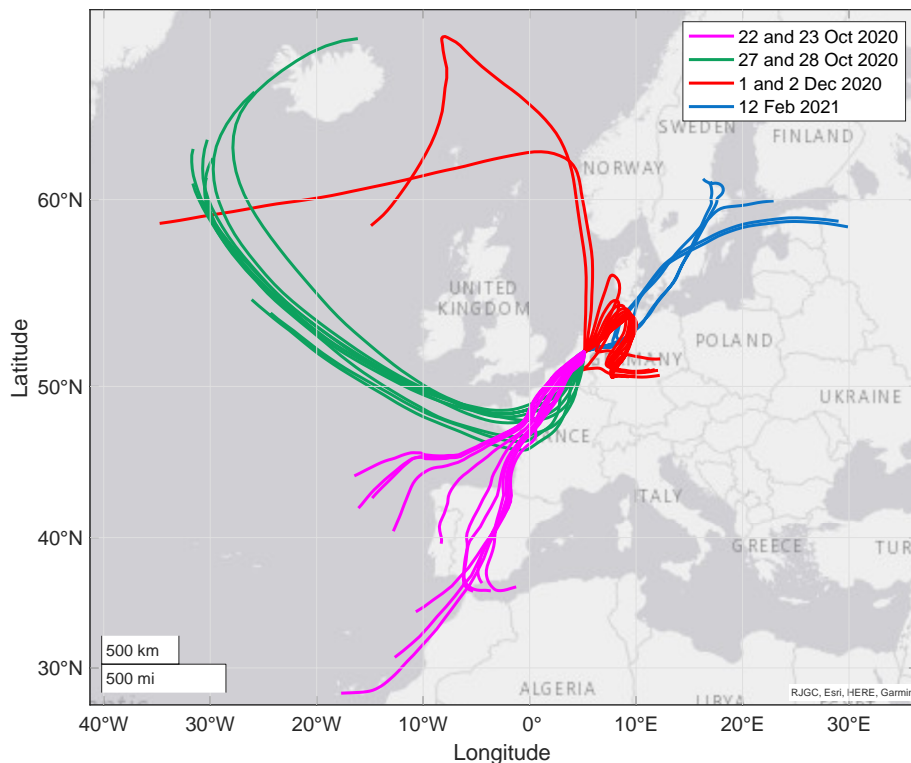
Figure 2.7: Results from backward trajectory modelling using HYSPLIT (Stein et al., 2015). The colors correspond to the measurement days, highlighted with the same colors as the data points in Figure 2.6.

increased from around 480 to 520 ppt at the maximum. The ratio COS/CO_2 for these first four measurements was approximately 0.7 ppt/ppm. However, while during the evening of the 2nd of December both CO_2 and CH_4 mole fractions continued to increase, COS mole fractions decreased again to below 480 ppt. During this period, we see small variations in both $\delta^{33}S$ and $\delta^{34}S$, with some depleted values for the highest mole fractions, but the differences are generally small.

Thus, while there was a large increase in both CO_2 and CH_4 mole fractions, we did not observe a substantial increase in COS mole fraction, nor was there a large trend in $\delta^{33}S$ or $\delta^{34}S$ values. We can therefore conclude that this pollution plume did not contain large amounts of COS, and this major industrial area in Germany may not contribute much to the global anthropogenic COS emissions. More generally, the impact of European anthropogenic emissions on the COS budget in the Netherlands is likely small, because we generally do not see events with high COS mole fractions and/or very depleted values of $\delta^{34}S$ during our measurement period. Looking at the gridded global anthropogenic inventory data of Zumkehr et al. (2018), there is some emission visible in western Europe, and indeed also in the Ruhr area. However, when comparing the European anthropogenic COS emission to that of East Asia, there are fewer sources, and also lower COS emissions from these source locations. Zumkehr et al. (2018) also state in their paper that 45% of the global

anthropogenic COS emissions come from China, and the rest of the emissions are relatively evenly spread over India, North America and Europe. This would explain the absence of large COS enhancements during our measurement period compared to previous studies by Hattori et al. (2020), who measured enhancements in air originating from China.

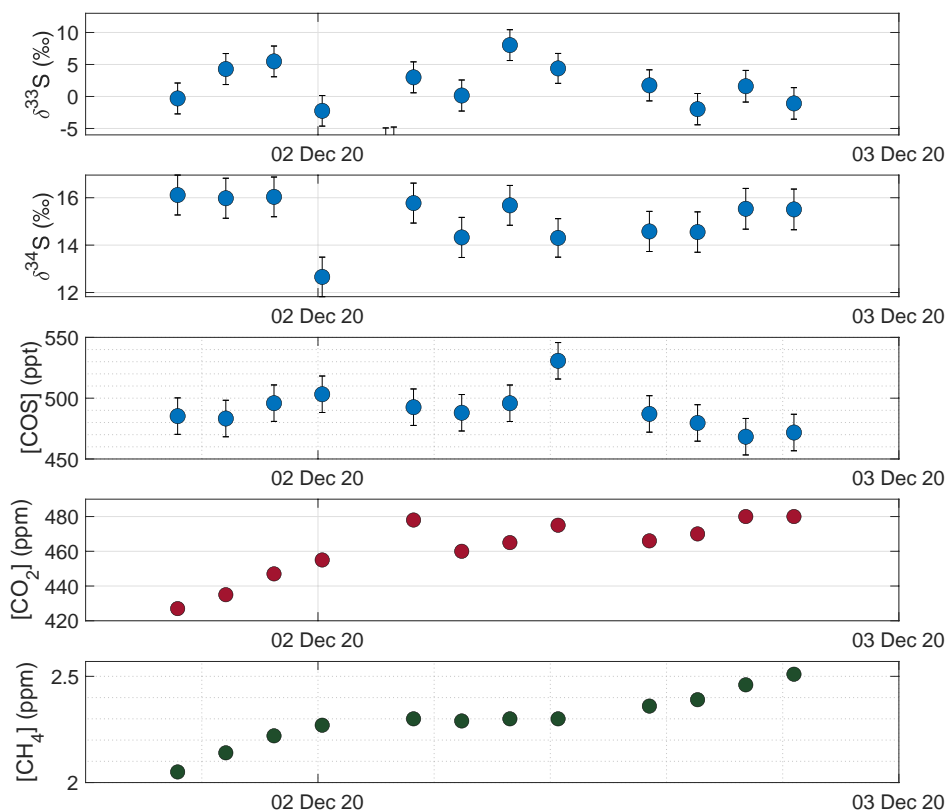Analysis of air origins through backward trajectory modelling provides insight into

Figure 2.8: Results from a measurement sequence on the 1st and 2nd of December, during which a pollution plume advected from Germany was observed. Figures from high to low: δ^{33}S, δ^{34}S, COS mole fraction, CO_2 mole fraction and CH_4 mole fraction.

the regional sources and sinks of COS. The Netherlands is situated in the mid-latitudes and receives air from very different origins, which can change the influence of different sources and sinks on the COS that we measure in Utrecht. When we for instance look at the data subset of the 23rd of October and compare it to the 28th of October, we see large differences in both COS mole fraction and δ values. The backward trajectories of these two days, indicated with pink (22 and 23 Oct) and green (28 Oct) in Figure 2.7, show that on Oct 23rd, the air came mostly from the south and travelled far over the continent across Spain and France at an altitude of just below 500 m, before reaching Utrecht. On Oct 28th, the air originated from the north and travelled mostly over the ocean at low altitude of mostly below 200 m, according to the HYSPLIT trajectories. On Oct 28th we see a lower and more stable COS

mole fraction of 455 ± 9.5 ppt than on the 23rd, which had a mean mole fraction of 509 ± 39 ppt. On the 28th, we also observe high mean δ values of 5.3 ± 3.3 ‰ and 18.9 ± 1.2 ‰ for δ^{33}S and δ^{34}S respectively. In contrast, on the 23rd we find mean δ values of −2.7 ± 3.1 ‰ and 14.0 ± 1.2 ‰ for δ^{33}S and δ^{34}S respectively. One explanation for these differences could be that on land there are more sources and sinks influencing COS (being biosphere uptake and anthropogenic emissions), which would create more variability in the mole fraction; a phenomenon we see on the 23rd. On the 28th we probably see a representation of rather clean background air, probably affected by ocean emissions, which is proposed to have a value of 19 ‰ (Angert et al., 2019; Davidson et al., 2021; Hattori et al., 2020), which is higher than the background. Biosphere uptake in the higher latitudes could be a stable sink decreasing the mole fraction and due to fractionation effects also making the COS more enriched in ^{34}S (Davidson et al., 2021). However, quantification of these sources and sinks requires more observations and the use of models.

To gain more insight into the processes influencing the COS from different air origins, the following data subsets were created: only northern air, only southern air and all "other directions" air. Relatively high mole fractions were found in the northern air data subset, thus Keeling plots were created of the data subsets to assess whether there were any trends present and whether source signatures could be identified. As can be seen in Figure 2.9, a dependence of the δ values on the mole fraction can only be found for the northern air data. This Keeling plot shows a picture that is consistent with an isotopically depleted COS source, with a Keeling plot intercept of −3.5 ± 2.9 ‰. A potential ^{34}S depleted source could be anthropogenic COS, however, previous estimates of δ^{34}S from anthropogenic COS were slightly higher than this Keeling intercept (Davidson et al., 2021; Hattori et al., 2020). While there are some large industrial areas in in the North of the Netherlands, more local measurements are needed to confirm this rather depleted anthropogenic source. On the low mole fraction end of the Keeling plot, COS is enriched in ^{34}S, which could be due to fractionation taking place during biosphere uptake in higher latitudes.
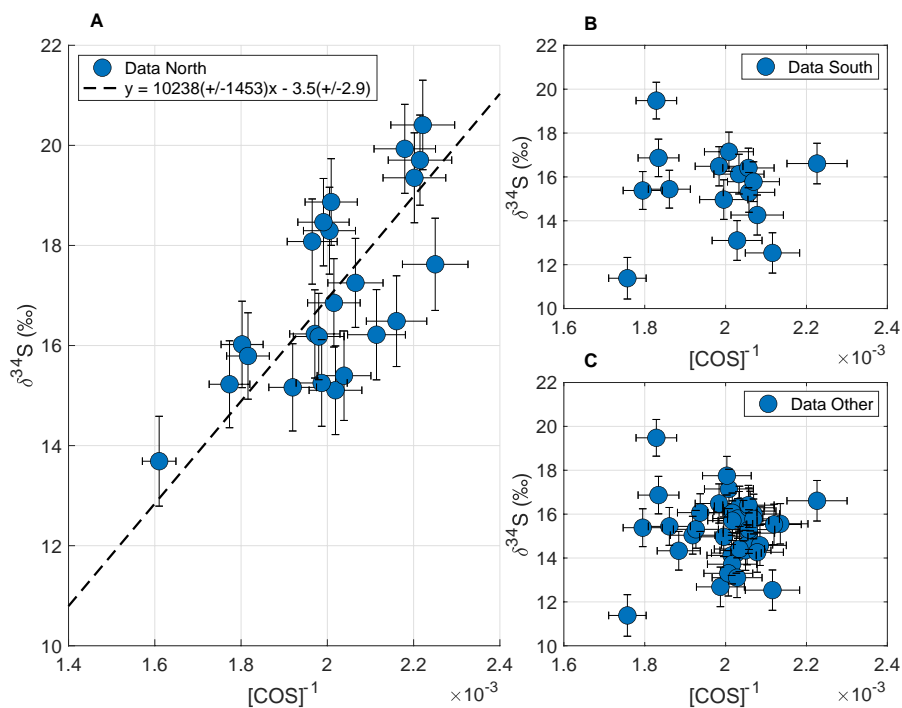
Figure 2.9: Keeling plots for δ^{34}S for data subsets from different wind directions. A: wind direction from the North, B: wind direction from the South, C: all data excluding wind direction from the North.

2.3.7 Highway tunnel measurements

The highway tunnel dataset is available in Underlying data Baartman et al. (2021). While driving through the several tunnel tubes, the Picarro analyzers clearly measured an increase of CO_2 from the entrance to the exit of the tunnel, indicating a build-up of exhaust gases inside all the tunnel tubes. The on-line CO_2 mole fraction data can be found in Extended data Baartman et al. (2021), and the supplementary material of this chapter. Besides CO_2, no clear elevation of the other compounds (CH_4 and H_2O) was measured. From the total of six samples taken in the tunnel for COS measurements, two samples were not suitable for isotope measurements as they had too low pressure and therefore, we only report the results of four tunnel samples.

The results of our sample measurements show elevated COS mole fractions in the tunnel, with a maximum increase of around 50 to 160 ppt compared to the background mole fraction of 490 ppt. The maximum mole fraction in a sample taken inside the tunnel was around 650 ± 15 ppt. The CO_2 mole fraction in the samples was between 541 and 606 ppm. From these values we calculated the COS/CO_2 enhancement ratio, which was 0.4 ± 0.08 ppt/ppm for the first three samples and 1.15 ± 0.1 ppt/ppm for the last sample. As the first three samples had such a consistent COS/CO_2 ratio, we assumed that the fourth sample was possibly contaminated by a single high COS-emitting vehicle, and we excluded it from the ratio estimation. If we assume that this ratio of 0.4 ppt/ppm is typical for a European fleet, we

can make a very rough estimate of the annual European COS emissions from road traffic. Using the annual CO_2 emission from road transport (sector name 1.A.3b) for the year 2018 (European Environment Agency, 2020) of around 888 Tg CO_2, we find a COS emission of 0.19 GgS a^{-1}. Earlier estimates of global COS emissions from road traffic are in the range of 0.8 – 8 GgS a^{-1} (Chin and Davis, 1995; Fried et al., 1992; Watts, 2000; Lee and Brimblecombe, 2016) with the most recent estimate being on the higher side of this range with 6 ± 4 GgS a^{-1} (Watts, 2000). Because the European Committee for Standardization (CEN) fuel content standard states a maximum sulfur content of only 10 ppm European Environment Agency (2003) since the year 2009, we consider 0.19 GgS a^{-1} for Europe a reasonable estimate. However, as our calculated COS/CO_2 ratio is only based on a small dataset, this can only be seen as a rough first estimate of European COS traffic emissions.

Figure 2.10 shows the Keeling plots for $\delta^{33}S$ (left) and $\delta^{34}S$ (right), with the four tunnel samples and the average background value ± 1 σ uncertainty. A two-isotope plot of all the ambient air data and the tunnel sample data can be found in Extended data Baartman et al. (2021), and in the supplementary material of this chapter. The COS in the tunnel samples is depleted in both ^{33}S and ^{34}S with a Keeling intercept of −71.5 ± 21.2 ‰ for $\delta^{33}S$ and 6.9 ± 4.7 ‰ for $\delta^{34}S$. In previous studies (Angert et al., 2019; Davidson et al., 2021; Hattori et al., 2020), only the COS sulfur isotope ratios for total anthropogenic emissions have been reported, and a distinction between different anthropogenic sources has not been made thus far. The general trend of depleted values for $\delta^{34}S$ for traffic emissions roughly agrees with the current estimate for the anthropogenic emission signature of 3 to 8 ‰. The very low Keeling plot intercept for $\delta^{33}S$ of −71.5 ± 21.2 ‰ would indicate a strongly mass-independent process, which is unexpected, and it would be helpful to confirm this with additional studies. With the present evidence being based on only four samples, which were also processed slightly differently from ambient air (e.g. including a dilution step), we consider it premature to draw reliable conclusions. We note, however, that the sulfur in gasoline and diesel in Europe is highly modified by the complex sulfur removal process (Srivastava, 2012) to reduce the sulfur content from % to ppm level (European Environment Agency, 2003), which could in principle lead to anomalous $\delta^{33}S$ in fuel. If this low $\delta^{33}S$ is confirmed, strong processing might explain the unexpected sulfur isotopic composition of the COS emissions, although the mass-independent fractionation processes involved are still unexplained.
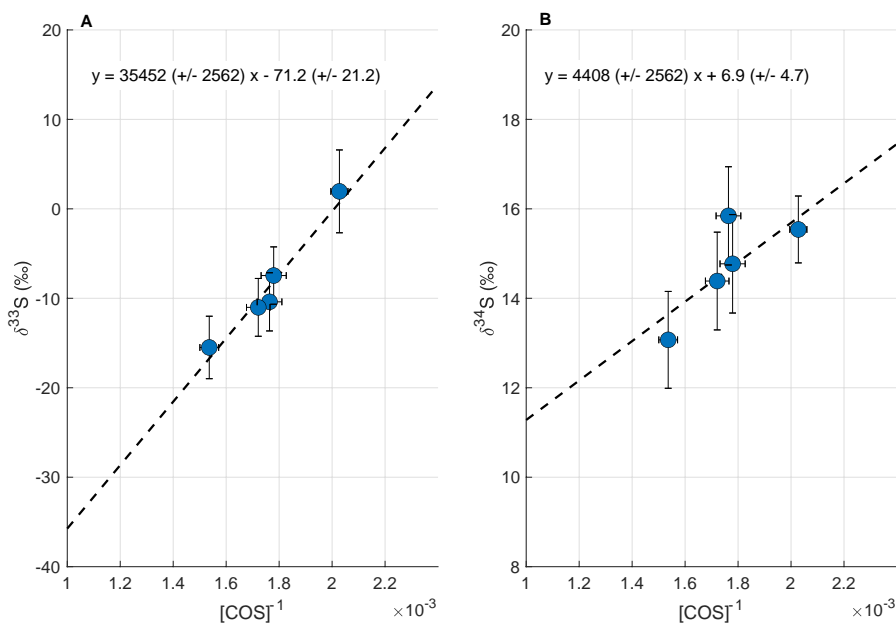
Figure 2.10: Keeling plot of the samples taken inside a highway tunnel, for δ^{33}S (A) and δ^{34}S (B).

2.4 Conclusion

In this chapter, we described a new measurement system for δ^{33}S and δ^{34}S in COS, developed at Utrecht University, which enables measurements of small samples, with a relatively simple GC-IRMS system. A single measurement only takes 2 to 3 hours. We obtained a total precision for 4 L ambient air samples of 2.4 ‰ for δ^{33}S and 0.9 ‰ for δ^{34}S, when including the error in the nonlinearity correction. The ability to measure small samples allows us to measure air from a wide variety of locations, which will allow us to characterize latitudinal and altitudinal variations in COS isotopologues.

The sampling system coupled to the pre-concentration system can measure ambient air in Utrecht with little maintenance effort. This will enable us to create a long-term record of COS mole fraction and isotopic composition in the Netherlands, which will help to gain more insight in the seasonal and year to year variability of COS. The first results from ambient air measurement in Utrecht show a small increase in COS mole fraction of 40 ppt from fall to winter. During the measurement period, no mole fractions higher than 620 ppt were observed and the mean δ^{34}S of 15.9 ± 0.9 ‰ was relatively high compared to previously reported results by Angert et al. (2019), Kamezaki et al. (2019), Hattori et al. (2020), and Davidson et al. (2021). This leads us to conclude that the air in Utrecht likely receives relatively little COS from anthropogenic sources.

Three out of four measurements of samples taken inside a highway tunnel yielded a COS/CO_2 ratio of 0.4 ppt/ppm, which can be extrapolated into a European estimate of COS from traffic emissions of 0.19 GgS a^{-1}, which is in rough agreement with the current global estimates of COS emissions from traffic (Chin and Davis, 1995; Fried et al., 1992; Lee and

Brimblecombe, 2016; Watts, 2000). The derived value of δ^{34}S = 6.9 ± 4.7 ‰ of traffic emissions is close to the reported values for anthropogenic emissions (Angert et al., 2019; Davidson et al., 2021; Hattori et al., 2020). The very low value of −71.5 ± 21.2 ‰ for δ^{33}S in COS from traffic is unexpected and further measurements would be helpful to confirm this value. However, COS emissions from traffic make only a small contribution to the overall budget. Thus, more effort is needed to reduce uncertainties in the dominating sources and sinks in the COS budget using isotopic analysis.

2.5   Supplementary material

Figure 2.11: Results from all the backward trajectory modeling using HYSPLIT (Stein et al., 2015). The colors correspond to the measurement days, highlighted with the same colors as the data points in Figure 2.6.

Figure 2.12: CO_2 mole fraction (ppm) as measured by the Picarro instrument on board of the van while driving through the high way tunnel and collecting samples. The numbers correspond to the samples taken for COS isotope analysis.

Figure 2.13: $\delta^{33}S$ plotted against $\delta^{34}S$ for all the ambient air measurement data from Utrecht (blue), as well as the highway tunnel samples (red). The dashed line is a linear integration of the relationship between the two isotope ratios for the ambient air samples only, of which the equation is given in the legend of the figure. It can be seen that the relationship between $\delta^{33}S$ and $\delta^{34}S$ is different for the tunnel samples, compared to the ambient air samples.

3

Measurements of carbonyl sulfide isotopologues in the upper troposphere and lower stratosphere in a low and a high latitude region

Stratospheric sulfur aerosols (SSA) reflect incoming solar radiation and thereby have a cooling effect on the Earth. During volcanically quiet times, this layer of SSA is maintained by a constant input of sulfur species. Carbonyl sulfide (COS) is hypothesized to be the main contributor to this background SSA, which could possibly be proven by measuring the isotopic composition of COS in the stratosphere. However, direct measurements of stratospheric COS isotopologues are not yet available to date. In this chapter, data is presented from two different stratospheric sampling campaigns, of which samples were analyzed for COS mole fractions and isotopic composition. The first campaign was the StratoClim AMA 2017 campaign in Kathmandu, Nepal, during which samples were taken on board of the Geophysica high-altitude research aircraft. The second campaign was a zero-pressure stratospheric balloon campaign, which was launched from Esrange Space Center in Sweden in August 2021. The goal of these measurements was to provide estimates of COS isotope fractionation during destruction in the stratosphere and thereby provide information on the contribution of COS to SSA. The measurement data were combined with model simulations using the TM5 model, which was expanded to include COS sulfur isotopologues. As expected, we found a decrease in COS mole fraction with altitude for both campaigns, which was especially sharp above the tropopause. For $^{34}\varepsilon$, we found relatively small, negative values, which was in line with most estimates from recent literature and complies with COS being the main precursor of SSA. However, as these estimates are based on

only a few measurement data points, the errors on the fractionation estimates are still quite large. Therefore, more measurements would be useful for further constraining this fractionation estimate. The TM5 model simulations were able to capture the measured mole fractions for StratoClim 2017 quite accurately. However, they showed much less variability in the isotope ratios than the measurements. These model simulations also indicated the importance of mixing and transport processes, which affect the observed COS isotope ratios in the stratosphere.

3.1 Introduction

Carbonyl sulfide (COS or OCS, here further referred to as COS) is the most abundant sulfur-containing compound in the atmosphere, with a tropospheric mole fraction of around 500 parts per trillion (ppt) (Chin and Davis, 1995). The largest natural source of COS is the ocean, with direct and indirect emissions, through carbon disulfide (CS_2) and dimethyl sulfide (DMS) (Kettle et al., 2002; Lennartz et al., 2017; Lennartz et al., 2020). Other sources include anthropogenic emissions, biomass burning and soils (Stinecipher et al., 2019; Zumkehr et al., 2018). The main tropospheric sink of COS is the terrestrial biosphere, where it diffuses into plants in a similar way as CO_2 during photosynthesis, but COS is broken down through a different reaction, catalyzed by carbonic anhydrase (CA) (Protoschill-Krebs and Kesselmeier, 1992; Protoschill-Krebs et al., 1996; Kettle et al., 2002; Berry et al., 2013). Because of its relatively long lifetime of approximately 2 years, COS is transported to the stratosphere (Brühl et al., 2012), where it is broken down by three different sink reactions. These reactions are photolysis at wavelengths smaller than 300 nm (3.1.1), oxidation by OH (3.1.2) and the reaction with oxygen radicals $O(^3P)$ (3.1.3), with photolysis being the largest sink of COS in the stratosphere (Schmidt et al., 2012a; Hattori et al., 2012; Danielache et al., 2008; Danielache et al., 2009; McKee and Wine, 2001).

$$COS + hv \rightarrow CO + S \qquad (3.1.1)$$

$$COS + OH \rightarrow CO_2 + HS \qquad (3.1.2)$$

$$COS + O^3P \rightarrow CO + SO \qquad (3.1.3)$$

The sulfur compounds S, HS and SO, that are the products of these reactions are rapidly oxidized to form SO_2, which is then further converted to H_2SO_4. This H_2SO_4 is the principal precursor of stratospheric sulfur aerosols (Chin and Davis, 1995). The layer of stratospheric sulfur aerosols (SSA) or Junge layer (Junge, 1966) is important for regulating the Earth's temperature by reflecting incoming shortwave solar radiation (Junge and Manson, 1961; Crutzen, 1976). During volcanically active periods, direct injection of SO_2 in the stratosphere is the main contributor to SSA. However, during volcanically quiescent periods, this layer of SSA is still maintained by a constant input of sulfur-containing compounds. The main source of this background SSA has long been debated but at this moment, COS is considered to likely be the largest contributor (Crutzen, 1976; Notholt et al., 2003; Brühl et al., 2012; Engel and Schmidt, 1994). Yet, direct measurements of COS and sulfate in the stratosphere are scarce, and thus, additional measurements are needed to better quantify the role of COS in SSA formation.

Isotope measurements could provide useful information for answering the question whether COS that is transported to the stratosphere could indeed be the main precursor of background SSA. Sources of COS (or other chemical compounds) can be detected and constrained by using their distinct isotopic signatures. During sink processes such as diffusion or chemical reactions, isotope fractionation can occur, where one isotopologue is reacting faster than the other. Isotope fractionation constants can be used to gain information on (chemical) sink processes and can thus also be used to characterize stratospheric COS sink

reactions, as will be further elaborated on in the next section.

The isotope ratios that are addressed in this work are δ^{33}S, δ^{34}S, and δ^{13}C. Equations 3.1.4 and 3.1.5 describe the isotope δ notation, where the sulfur isotope ratios are given as an example. Likewise, in the remainder of this chapter, the isotope ratio ^{13}R is defined as the ratio of ^{13}C to ^{12}C and δ^{13}C is the double relative carbon isotope ratio, of $^{13}R_{sample}$, relative to $^{13}R_{ref}$. Equation 3.1.6 defines the fractionation constant, where k and k' are the reaction coefficients of the main and rare isotopologue, respectively. A positive ε implies that the remaining COS is getting depleted and a negative ε indicates that the remaining pool of COS is getting enriched in the heavier isotope. In nature, the most occurring fractionation, where the lighter isotopologue reacts faster than the heavier, would give a negative ε.

$$^{33,34}R = \frac{^{33,34}\text{S}}{^{32}\text{S}} \tag{3.1.4}$$

$$\delta^{33,34}\text{S} = \frac{^{33,34}R_{sample}}{^{33,34}R_{standard}} - 1 \tag{3.1.5}$$

$$\varepsilon = \frac{k'}{k} - 1 \tag{3.1.6}$$

3.1.1   Knowledge on stratospheric COS fractionation

Castleman et al. (1974) performed the first and to date only measurements of the sulfur isotopic composition of SSA during a volcanically quiet period. In this study Castleman et al. (1974) analyzed aerosol samples that were taken by air crafts at different latitudes, both in the Southern and Northern Hemisphere, over a time-span of 10 years. They selected the samples that were collected during volcanically quiescent times and calculated a global average δ^{34}S of 2.6 ± 0.3 ‰ between 17 and 18 km. If we consider this value representative for SSA, the isotopic composition and fractionation of COS in the stratosphere can help provide insight into whether the conversion of COS to SSA could yield such a δ^{34}S at that elevation. Theoretical calculation studies, modeling, remote-sensing studies and lab experiments have already provided insight into stratospheric COS fractionation and how the isotopic signature propagates to δ^{34}S in SSA, and a long debate has been taking place as to whether COS could indeed be the main SSA precursor (Leung et al., 2002; Colussi et al., 2004; Lin et al. (2011); Hattori et al., 2011; Hattori et al., 2012; Schmidt et al., 2012b; Schmidt et al., 2013).

Nagori et al. (2022) modeled the vertical distribution of sulfur species and their isotopic composition, in order to evaluate COS as a potential source for background SSA. In their study, they presented a good overview of the current knowledge of COS isotope fractionation during stratospheric break-down reactions and how the isotopic composition of several compounds propagates to that of SSA. They found that the isotopic composition of SSA is likely determined by both tropospheric SO_2 that is directly emitted from anthropogenic and natural sources, and by COS. Tropospheric SO_2 has a low δ^{34}S of 3 ‰ (Nagori et al., 2022; Mukai et al., 2001), and its primary sink reaction with OH has an inverse kinetic isotope effect (Harris et al., 2012), making the remaining SO_2 increasingly depleted in ^{34}S. This depleted signal propagates to SSA that is formed from SO_2 in the lower stratosphere. Higher up in the stratosphere, Nagori et al. (2022) modeled that COS becomes the main source of SO_2 and thereby also of SSA. At those elevations, the isotopic composition of COS, as well

as the fractionation during the conversion of COS to SO_2, through photolysis mostly, will determine the isotopic signature of SSA. Nagori et al. (2022) concluded that the fractionation constant of COS photolysis, $^{34}\varepsilon$, has to be small and slightly negative in order for COS to be a realistic candidate as the main precursor of SSA. Note, however, that this reasoning is based on this single δ^{34}S SSA value reported by (Castleman et al., 1974).

Keeping in mind the stratospheric fractionation factor that is likely needed for COS to be the main precursor of SSA, we will now list the first studies that estimated this fractionation factor. Some of the first measurement-based estimates of stratospheric CO^{34}S profiles were presented by Leung et al. (2002), using infrared limb-transmittance spectra acquired during several balloon flights. Surprisingly, they derived a large and positive fractionation factor of $^{34}\varepsilon$ = +73.8 ± 8.6 ‰, which would make the S products of the stratospheric sink reactions highly enriched in the heavier isotope. This would result in an enriched signal in SSA and would leave the remaining COS depleted in the heavier isotope ^{34}S. Thus, these values for δ^{34}S in COS are inconsistent with it being the main source of SSA, as the resulting SSA would become much more enriched than the value found by Castleman et al. (1974) (Nagori et al., 2022). In their study on infra-red (IR) absorption band spectra of COS at different elevations, Colussi et al. (2004) also found a large positive fractionation for ^{34}S of +67 ± 7 ‰. They found that the electronic absorption spectral band of CO^{34}S at 298 K potential temperature was much more intense than that of CO^{32}S. Due to these large stratospheric fractionation values, these first studies thus concluded that COS could not be the main source of background SSA.

However, several later studies suggested much lower, mostly negative stratospheric COS fractionation. Lin et al. (2011) performed lab experiments to determine the sulfur isotope effects during UV photolysis of COS. They also estimated the isotope effect for the S abstraction reaction which occurs after COS photolysis, where S_2 is formed, and concluded that the overall isotope effect due to photolysis under experimental conditions is constrained between −10.5 and + 5.3 ‰, again making COS a good candidate for the main contributor to background SSA. Hattori et al. (2011) experimentally determined UV cross sections for different COS isotopologues and from these, they estimated the wavelength-integrated photolysis rates and fractionation constants similar to 20 km altitude. They obtained fractionation constants of $^{33}\varepsilon$ = −3.7 ± 4.5 ‰ and $^{34}\varepsilon$ = +1.1 ± 4.2 ‰, which is again inconsistent with the large fractionations reported by Leung et al. (2002) and Colussi et al. (2004). For $^{13}\varepsilon$, Hattori et al. (2011) found a larger fractionation constant of −26.8 ± 4.3 ‰. Schmidt et al. (2013) theoretically calculated the COS photolytic isotope effect as a function of wavelength and found a small negative fractionation for $^{34}\varepsilon$, which is in good agreement with the measurements by Hattori et al. (2011). They predicted that the the combination of all stratospheric removal reactions (Equations 3.1.1, 3.1.2 and 3.1.3) overall slightly favors the lighter sulfur isotope. Schmidt et al. (2013) also found that the ^{13}C isotopic fractionation due to photolysis of COS in the upper stratosphere ($^{13}\varepsilon$) is likely significantly negative and will leave a clear positive δ^{13}C signal in the remaining COS.

For the oxidation reaction with OH (Equation 3.1.2), Schmidt et al. (2012a) calculated a kinetic isotope effect, $^{34}\varepsilon$, between −5 and 0 ‰ in the troposphere and lower stratosphere. For ^{13}C, they found a stronger fractionation factor $^{13}\varepsilon$ of between −70 and −40 ‰. The isotope effect of the reaction with O(^{3}P) was investigated by Hattori et al. (2012) by lab experiments using a photochemical reactor. They found a $^{34}\varepsilon$ value of −14.8 ‰ and concluded that the combined fractionation of COS photolysis, the reaction with OH and the reaction

with $O(^3P)$ would not be much stronger than -10 ‰, which would result in slightly enriched (positive $\delta^{34}S$) SSA (Nagori et al., 2022), indicating that COS could be an acceptable source for background SSA.

Finally, Yousefi et al. (2019) presented Atmospheric Chemistry Experiment Fourier Transform Spectrometer (ACE-FTS) data and balloon-borne FTS measurements, including $\delta^{34}S$ and $\delta^{13}C$ data, over all latitudes. The ACE satellite is used for IR remote sensing of the Earth's atmospheric composition and the ACE-FTS instrument records the atmospheric transmission spectra during sunrise and sunset using the Sun as IR source (Yousefi et al., 2019). Using the spectra of the different sulfur isotopologues of COS with a vertical resolution of 3 km, Yousefi et al. (2019) estimated fractionation factors $^{34}\varepsilon$ for stratospheric destruction of COS of +3.64 ± 0.57 ‰, +5.91 ± 0.63 ‰ and +8.91 ± 0.47 ‰, for latitude bins of 60-30°S, 30S-30°N and 30N-60°N, respectively. For $^{13}\varepsilon$ they found large negative fractionation constants $-90 ± 1.4$ ‰, $-88 ± 1.92$ ‰ and $-65 ± 1.16$ ‰ for the same latitude bins.

3.1.2 Study aim

While the lab experiments and remote-sensing studies discussed in the previous section already provide much information on the potential isotopic fractionation of COS in the stratosphere, the reported stratospheric fractionation constants do not agree. Furthermore, none of these data include direct measurements of COS isotopologues extracted from air sampled in the stratosphere, which would be important for confirming the lab-based and remote-sensing isotope studies. The study presented in this chapter includes the first $\delta^{33}S$, $\delta^{34}S$ and $\delta^{13}C$ measurements from whole air samples taken in the upper troposphere and lower stratosphere during two campaigns: the StratoClim AMA-17 campaign in Kathmandu, Nepal in 2017 and the KLIMAT 2021 balloon flight campaign launched from Esrange, Sweden in August 2021. From these measurements we calculated apparent fractionation constants $^{33}\varepsilon$, $^{34}\varepsilon$ and $^{13}\varepsilon$ of the total stratospheric sink of COS. These values are compared to model simulations using the TM5 model, including a COS isotope module (Ma et al, in prep).

3.1.3 Stratospheric circulation and isotope implications

Not only the fractionation during sink reactions in the stratosphere determines the COS isotopic profile, but transport and mixing also play an important role. The combined effect of transport, mixing and chemical removal leads to differences in apparent fractionation between latitudes, seasons and individual years that observations were made (Kaiser et al., 2006). The photolysis rate of COS is dependent on the quantity of light available at the photolysis wavelength, the actinic flux (Schmidt et al., 2013). As ozone absorbs most radiation, photolysis starts to become the predominant sink of COS above the ozone layer. Though, the isotope fractionation signal from photolysis is transported to other altitudes in the atmosphere through various transportation pathways.

The predominant transport mechanism in the stratosphere is the Brewer-Dobson circulation, which transports air from the tropical tropopause to the polar stratosphere (Butchart, 2014). This circulation includes two residual circulation branches (Birner and Bönisch, 2011; Plumb, 2002). The deeper branch slowly transports air from the middle and upper stratosphere (approximately 15 to 50 km) to the higher latitude stratosphere, where it de-

scends to the troposphere. The shallow branch transports air relatively fast from the tropical tropopause layer (TTL) to the extratropics. In addition to these latitudinal transport processes, relatively fast extra-tropical stratosphere-troposphere exchange (STE) can also occur in the form of bidirectional mixing. Thus, an air mass at higher latitudes will be influenced by descending higher stratospheric air, transported air from the TTL and local bidirectional vertical mixing (Bönisch et al., 2009).

Kaiser et al. (2006) used a large dataset of N_2O isotope measurements to investigate how mixing and transport processes influence the isotopic composition of N_2O. They used two conceptual models to explain the vertical isotopic profiles and the stratospheric fractionation that could be inferred from those data: a "two-end-member mixing" model and a "continuous weak mixing" model. The two-end-member mixing model is similar to a Keeling plot approach where simple mixing of two air masses occurs, giving rise to a linear relationship between δ values and mole fraction. This relationship would be observed if transport processes are fast in comparison to photo-chemistry. Kaiser et al. (2006), however, found that the relationship between N_2O isotopic composition and the lower N_2O mole fraction (<200 ppb) could not be described by two-end-member mixing only. The upper samples with low N_2O mole fraction were influenced by continuous weak mixing of upper stratospheric air. Furthermore, one profile showed that in the upper stratosphere, the N_2O isotopic composition stayed the same while the mole fraction still decreased with altitude. This could be explained by a process in which descending N_2O-free upper stratospheric air was mixing with the local air, still containing N_2O. This process lowers the mole fraction at that elevation but does not influence the isotopic composition. However, this phenomenon was only observed in one profile in which a special event was sampled, where mesospheric air intruded into the stratosphere.

For COS we also expect the fractionation that we observe in the upper troposphere and lower stratosphere to be a combination of fractionation taking place during sink reactions (mostly photolysis) and the effect of mixing. As COS has a shorter life-time compared to N_2O, transport processes will likely mostly not be faster than photo-chemistry. Thus, a two-end-member mixing model will probably not be a good representation for COS stratospheric fractionation. More likely to be representative is the more complex continuous weak mixing model of Kaiser et al. (2006). Furthermore, with COS break-down by photolysis being faster than photolysis of N_2O, COS-free air already occurs at lower altitudes of around 30 - 35 km. Thus, the process of COS-free air descending and mixing with COS-containing air is probably more likely to occur compared to the case of N_2O.

3.2 Methods

3.2.1 Sampling campaigns

StratoClim

The StratoClim AMA-17 campaign took place from Kathmandu Airport, Nepal (27°42' N,85°19' E) in July and August 2017 (StratoClim, 2022). During this campaign, eight scientific flights were performed with the high-altitude M55-Geophysica research aircraft (Cairo et al., 2010), which covered the Nepalese and Northern Indian region. The aim of the campaign was to perform measurements of greenhouse gasses (GHGs), aerosols and their precursors in the

Asian Monsoon Anticyclone (AMA), in order to assess the role of the Upper Troposphere and Lower Stratosphere (UTLS) in climate change.

In the AMA, air masses from the Boundary Layer (BL) can be effectively uplifted to the UTLS and subsequently transported into the higher stratosphere, which makes it an important transport mechanism for GHGs and aerosol (precursors). Flights 1, 3, 6 and 7 covered North India and Southern Bangladesh, while flights 2, 4 and 5 took samples over Nepal at different altitudes (Bucci et al., 2020). During flight 8, the aircraft flew over a convective system, developed on the boundary between Nepal and Northern India. During flight 6, the aircraft cruised at the same altitude of approximately 16.9 km for the majority of the flight and performed one dive to 15 km in the middle of the flight trajectory. This particular flight captured both North Indian air and clean Tibetan convective air, but also saw some plumes of polluted air coming from South-China, which could be recognized by increased CO mole fractions (Bucci et al., 2020).

Figure 3.1 shows the locations of the samples that were analyzed for COS mole fraction and isotopic composition measurements during the different flights performed during the campaign. The samples were collected with a whole air sampler developed at the Max Planck Institute for Nuclear Physics, Heidelberg, Germany that compressed the air using a metal bellows pump that was previously shown not to affect trace gas mole fractions (Kaiser et al., 2006). The samples were collected in 2 L cylindrical stainless-steel canisters, of which some were Silco-coated, which is a treatment on the inner walls of the canisters in order to minimize the breakdown of reactive gasses, including COS.

The COS mole fraction in the canisters was measured by the University of East Anglia (UEA) on a high sensitivity gas chromatograph—tri-sector mass spectrometer system (Waters AutoSpec GC-MS). The samples were dried using magnesium perchlorate ($Mg(ClO_4)_2$) and COS, among other gases, was cryogenically extracted and pre-concentrated. The different compounds were separated on a GS-GasPro column (length: 50 m; ID: 0.32 mm). All samples were bracketed by measurements of a working standard. A full description of this system can be found in Laube et al. (2010). Afterwards, the samples were measured for COS isotopologues at Utrecht University. Only the samples which contained stable COS mole fractions, which were almost exclusively the Silco-coated canisters, were measured for COS isotopologues.
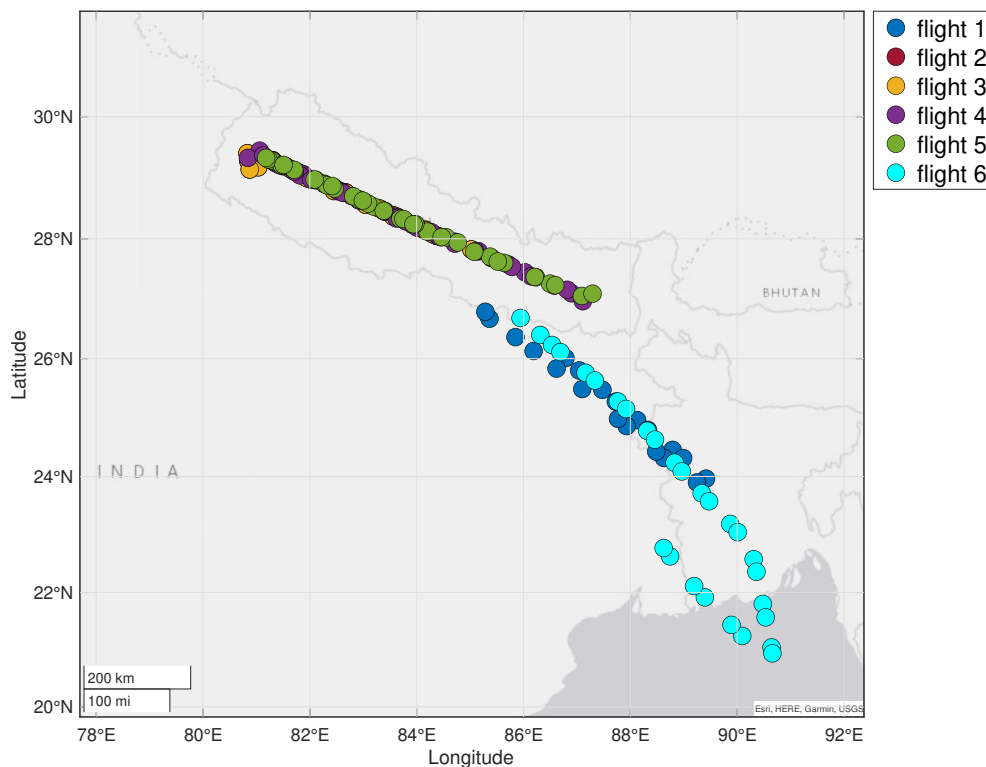
Figure 3.1: Locations of the samples taken during StratoClim AMA-17. The colors indicate the different flights that were performed during the campaign and are the same as in Figure 3.7. Note that these are not the entire flight tracks but only the locations of the individuals samples that were taken and analyzed for COS isotopologues. The flight tracks of flight 2, 4 and 5 were virtually identical and are therefore not all visible in the figure.

KLIMAT 2021

The KLIMAT 2021 campaign took place at Esrange Space Center, Sweden (67° 53'N, 21° 04' E), close to the city of Kiruna. The campaign was supported by the HEMERA H2020 research infrastructure and was organized by Centre National d'Études Spatiales (CNES) and the Swedish Space Corporation (SSC). During this campaign, a zero-pressure balloon flight was performed on August 12th, 2021. The flight trajectory is displayed in Figure 3.4 and the altitude of the balloon flight against time is give in Figure 3.5. The flight included a quick ascend and a slow descend with the gondola still attached to the balloon. At just before 3:00 on August 13th, the balloon and the gondola were detached and the payload came down with a parachute. After landing, the payload was retrieved with a helicopter and brought back to Esrange.

The payload of the TWIN gondola consisted of a cryogenic whole air sampler (BONBON) (Engel and Schmidt, 1994), four AirCores (two from Center for Isotope Research (CIO) at the Rijksuniversiteit Groningen (RUG) and two from Frankfurt University), a Mega-AirCore deployed (Jülich), the LIghtweight Stratospheric Air (LISA) sampler (CIO-RUG) which col-

Figure 3.2: Picture of the auxiliary balloon attached to the TWIN gondola during the HEMERA KLI-MAT 2021 campaign at Esrange, Sweden.

lected air into sampling bags for measurements of CO_2, CH_4, CO and COS mole fractions and two Pico-SDLA (Spectromètre à Diode Laser Accordable) instruments (Groupe de Spectrométrie Moléculaire et Atmosphérique, GSMA) which measured in-situ CO_2, CH_4 mole fractions during ascent and descent of the balloon. The cryosampler was used to take whole-air samples for COS isotope analysis, among other species, and carried 15 sample flasks that were filled during the slow descend of the balloon and the gondola, up to a maximum pressure of 30 bar, using a cryogenic pump principle with liquid neon. In order to check whether the isotopic composition of COS would be affected by the cryogenic sampling procedure, tests were performed with the sampler in Utrecht, prior to the campaign. The details of these tests can be found in the supplementary material.

The sampler contained 10 flasks with a volume of 330 mL and 5 larger flasks with a volume of 580 mL. The larger samples were specifically meant for COS isotope measurements and were flown with an ozone scrubber. Engel and Schmidt (1994) found that COS will be decomposed during or shortly after sampling, in the presence of high ozone (O_3) mole fraction, thus ozone had to be removed during the sampling procedure. As the samples were collected at liquid neon temperature (24 – 27 K), the air was liquid for some time after sampling. In this liquid phase, chemical reactions are more likely to happen and therefore the destruction of COS by O_3 is likely also happening faster than in a gas-phase sample.

The ozone scrubber that we used consisted of a stainless-steel cartridge with a stack of pure cotton make-up remover pads (Etos). Cotton wadding was found to be an excellent

Figure 3.3: The two balloons just before launch during the HEMERA KLIMAT 2021 campaign 2021 at Esrange, Sweden. The left balloon is the auxiliary balloon carrying and stabilizing the TWIN gondola for the very first part of the ascend, before the main, large balloon (right) takes over.

scrubber by Hofmann et al. (1992), removing oxidants like ozone, while having little effect on the trapping of COS and other sulfur compounds. Persson and Leck (1994) performed similar measurements for trapping and measuring DMS, CS_2 and DMDS. They found 100% removal of ozone by cotton wadding and little effect on the sulfur compounds, under low relative humidity. The ozone scrubbers used during the KLIMAT campaign in 2021 were tested for ozone scrubbing capacity, as well as for their influence on COS mole fractions and isotopic composition the CIO lab in Groningen (Zanchetta et al., in prep). The specific effect of the scrubbers on the isotopic composition of COS was tested in the isotope lab in Utrecht. A description of the scrubber tests performed in Utrecht can be found in the supplementary material of this paper.

After the campaign, the sampled air in the cryosampler was first measured at Frankfurt University, Forschungszentrum Jülich and CIO Groningen. They measured CO_2, CH_4, CO, N_2O and COS mole fractions. Afterwards, the sampler was transported to Utrecht University, where COS isotopologue measurements were performed.

Figure 3.4: Trajectory of the zero-pressure balloon flight launched from Esrange Space Center, Sweden on the 12th of August, 2021. The right top panel shows a map with the red rectangle indicating the area of the zoomed-in main panel which includes the balloon trajectory in the blue line.
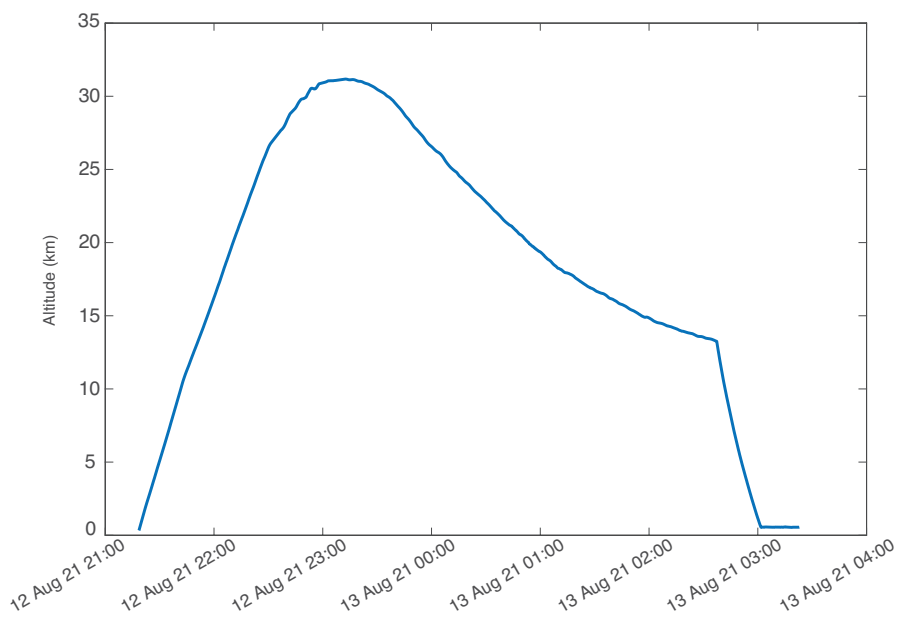

Figure 3.5: Altitude trajectory of the zero-pressure balloon flight launched from Esrange Space Center, Sweden on the 12th of August, 2021. With altitude in km on the y-axis and date and time CET on the x-axis

3.2.2 COS isotopologue measurements

The StratoClim samples were measured in 2019 and 2020 using the pre-concentration and GC-IRMS method described in Baartman et al. (2022) (Chapter 2 of this thesis). For these measurements, 2 to 4 L of air was injected into the system, depending on the sample volume and pressure that was available. A few samples, which contained enough gas, were measured twice. The sample flow into the pre-concentration system started at 80 mL min^{-1} and decreased as the sample pressure dropped, where the lowest sample end-pressure was approximately 300 mbar. The final injected volume was calculated from the integrated flow rate over injection time. For the StratoClim samples, only the sulfur isotope ratios, δ^{33}S and δ^{34}S, were measured as these measurements were still performed with the older measurement system that could not yet measure the carbon isotopologues of COS.

The COS isotopic composition of the samples collected with the cryosampler during KLIMAT 2021 were measured using the same pre-concentration system but coupled to a new, custom-built Delta V Plus mass spectrometer, which contained 11 Faraday collector cups (Thermo Fisher Scientific, USA). With this new set-up, we were able to measure δ^{33}S, δ^{34}S as well as δ^{13}C simultaneously from one sample. For δ^{13}C, we measured the CO$^+$ fragment ion that is created in the ion source of the IRMS as COS is split up. We used pure CO$_2$ as a working gas, and we used the CO$^+$ fragment ions to calculate the carbon isotope ratio. The CO$^+$ fragment ions were measured on m/z 28 and 29 and a correction was made for the occurrence of C^{17}O, when calculating ^{13}CO. The δ^{13}C values are presented against our own reference gas (D853421), which is a cylinder filled with outside air and spiked with 700 ppb COS in synthetic "zero" air, to create a mixture that contains approximately 800 ppt of COS. Thus, one must bear in mind that the δ^{13}C values presented for the KLIMAT 2021 samples are not calibrated relative to the international VPDB standard, but only relative to our own reference gas.

As the cryosampler samples from KLIMAT 2021 contained high pressure (>8 bar for all samples), a mass flow controller was connected right after the sample valve, in order to regulate the pressure downstream and to not damage the pre-concentration system. After this valve, a stainless-steel tube was connecting the sample to the multi-position valve of the COS isotope measurement system. Before measuring, the mass flow controller and lines were evacuated and afterwards flushed with sample air, in order to avoid contamination from outside and from previously measured samples. For the KLIMAT samples, between 4 and 6 L of air was injected for a single measurement, depending on the known COS mole fraction (from the previous measurements) and pressure remaining in the sample.

3.2.3 TM5 COS isotope model simulations

In order to compare our measurement results from these two different campaigns to theoretical COS (isotope) profiles in these areas, we performed simulations with the TM5 model, which was extended with a COS isotopologues module. In short, instead of simulating only COS as a tracer (Ma et al., 2021), we simulated CO^{32}S and CO^{34}S separately. Whenever COS is emitted, chemically formed, taken up by the biosphere, or chemically removed, we accounted for (potential) fractionation effects. The applied source signature and fractionation values are listed in Table 3.1. These values are based on previously reported measurements and estimates.

We applied sources and sinks of COS and the COS precursors CS$_2$ and DMS according

to the optimization results presented in Ma et al. (2021), scenario S_u. The optimized unknown emissions in that paper are given the emission signature of ocean emissions (+14.7 ‰). As listed in Table 3.1, we assumed COS yields from CS_2 and DMS of 0.83 and 0.007%, respectively, and assumed no fractionation during those reactions. Compared to Ma et al. (2021), we increased the resolution to 3° longitude and 2° latitude, and to 68 vertical layers, with the aim to better capture the sampling locations in the model.

We started the simulations at 01-01-2015 and simulated up to 01-01-2022. We started the simulations with a prescribed $CO^{32}S$ mole fraction of 500 ppt, and a $CO^{34}S$ mole fraction of 22.81 ppt, implying a background $\delta^{34}S$ value of +14 ‰. We then allowed more than 2.5 years of spin-up (before the StratoClim campaign) to allow the isotopic imprints of the various processes to reach their equilibrium. This time-span is rather short for the upper stratosphere, but COS mole fractions drop quickly above 20-25 km due to efficient photolysis above the ozone layer, thus the upper stratosphere region is less relevant for our current study objective. We verified that the lower stratospheric profiles reached a steady state with respect to the sources and sinks.

Table 3.1: TM5 isotope model input and their values. The yield of COS production from CS_2 was obtained from Stickel et al. (1993) and the yield COS production from DMS was obtained from Barnes et al. (1996). $^{34}\varepsilon$ of the reaction with OH was obtained from Schmidt et al. (2012a), $\delta^{34}S$ for anthropogenic signal was given by Davidson et al. (2021) and Hattori et al. (2020). $\delta^{34}S$ of the oceanic emission was obtained from Davidson et al. (2021) and the $^{34}\varepsilon$ of biosphere uptake was acquired from Davidson et al. (2022). The biomass burning $\delta^{34}S$ signal was actually not included separately but implemented as part of the general anthropogenic emission signal, thus also has a value of +8 ‰

Parameter	Value (yield or ‰)
yield of COS production from CS_2	0.83
yield of COS production from DMS	0.007
$^{34}\varepsilon$ of COS + OH reaction	−2.56
$^{34}\varepsilon$ of COS + hv	−3.0
$^{34}\varepsilon$ of CS_2 + OH reaction	0.0
$^{34}\varepsilon$ of DMS + OH reaction	0.0
$\delta^{34}S$ of anthropogenic COS emission	+8.0
$\delta^{34}S$ of oceanic emission	+14.7
$^{34}\varepsilon$ of biosphere COS uptake	−1.9
$\delta^{34}S$ of COS emission from biomass burning	+8.0

3.3   Results & discussion

The results of the two campaigns are first presented and discussed separately. Next, we discuss the comparison of the two campaigns, and the TM5 modeling results. Flight 4 and 6 of the StratoClim campaign are discussed in more detail as the COS data of these individual flights include some interesting features.

3.3.1 StratoClim AMA-17

The leftmost pane of Figure 3.6 shows the COS mole fraction profile of StratoClim 2017 plotted against altitude in km in filled orange circles. A clear profile is observed, with a relatively constant mole fraction between 8 and 18 km. Above the tropopause, located around 18.5 km during this campaign, a sharp decrease in COS is visible, indicative of stratospheric removal of COS. Between 14 and 16.5 km, measured mole fractions vary between 520 ppt to around 620 ppt. Note that the displayed mole fractions are from samples taken during different flights, with different flight trajectories and altitudes. Thus, the air present in the samples could represent different air masses, with different ages and composition. For instance, the presence of young pollution plumes can lead to the sampling of different COS mole fractions compared to samples that were collected in clean, or older recirculated air.

The isotopic profiles of δ^{33}S and δ^{34}S of the individual flights during the StratoClim
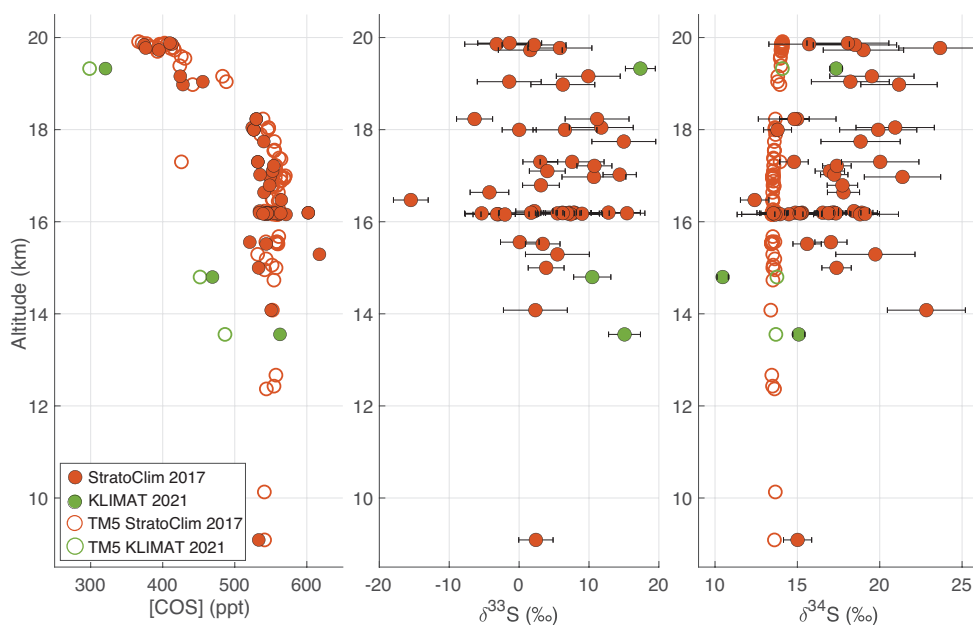

Figure 3.6: Overview of the measurements and TM5 modeling results for both campaigns, where the left panel shows COS mole fraction, the middle panel shows δ^{33}S (‰) and the right panel shows δ^{34}S (‰), all plotted against altitude in km. The green and orange closed circles show the measurement results for StratoClim 2017 and KLIMAT 2021 respectively and the open circles in the same colors show the TM5 modeling results sampled for these campaigns. Note that the TM5 model did not simulate δ^{33}S.

2017 campaign are displayed in Figure 3.7, with the colors indicating the different flights described in the methods section and the trajectories displayed in Figure 3.1. The spread in the isotope data is quite large. The general trend, however, is a slight enrichment in the heavier isotope ^{34}S with higher altitude and a slight depletion of ^{33}S.

In the next section we will highlight flights 4 and 6 of the campaign, and analyze the air masses sampled during these flights to gain more insight into the processes that might have influenced the isotopic composition of COS. Bucci et al. (2020) presented back trajectories along all StratoClim 2017 flight tracks, which we use in this study to link trends or variations in the COS data to potential pollution sources. We also used their CO and O_3 data in order to assess whether samples contain mostly tropospheric air or a mixture of tropospheric and stratospheric air.
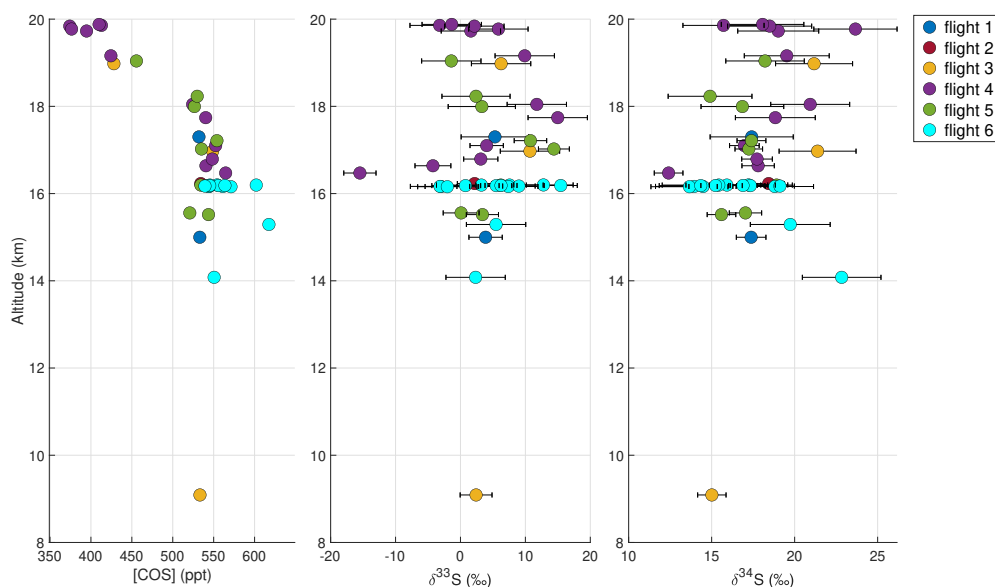

Figure 3.7: StratoClim AMA-17 data plotted against altitude in km on the y-axis. Left panel shows COS mole fractions in ppt, middle panel shows $\delta^{33}S$ and right panel shows $\delta^{34}S$. Different colors indicate the different flights during the campaign, carried out on different days, with different flight trajectories.

Flight 4

Flight 4 had a trajectory over Nepal, with increasing altitude, and captured relatively clean, older air from the Tibetan Plateau and Northern India, which had been partly re-circulated in the AMA. As the sampled air was old and potentially stratospheric, we aimed to use the data from this flight to possibly characterize stratospheric isotope fractionation of COS. In order to assess whether the samples captured stratospheric air, we plotted the COS isotope data together with altitude and against potential temperature and we also looked at the N_2O mole fraction of the samples (the latter being Figure 3.19 in the supplementary material). N_2O is an indicator of both the presence of anthropogenic pollution and whether the air mass mostly consists of tropospheric or stratospheric air, or a mixture of both, and is thus also an indicator for altitude in the atmosphere (Andrews et al., 2001).

Figure 3.8 shows the flight 4 COS mole fraction and sulfur isotope data against time and altitude. Based on the trajectory analysis by Bucci et al. (2020), the first and lowest four samples were taken in the higher troposphere and likely captured air from the Indian sub-continent and the Tibetan Plateau. The next two samples were taken around 18 km in the tropopause region, with increasing influence of older, re-circulated air. The last samples, taken after 10:30 UTC at an altitude above 19 km likely contained a mixture of stratospheric and tropospheric air, which can also be deduced from the elevated O_3 mole fractions reported by Bucci et al. (2020) and lower N_2O mole fractions at these altitudes. The four samples taken in this lower stratospheric air mass have COS mole fractions between 350 and 400 ppt, which is clearly lower than background tropospheric COS. However, the sulfur isotope ratios do not change drastically from the tropospheric samples taken around or below the tropopause to these more stratospheric samples taken later in the flight, which is indicative of a relatively small overall fractionation.

Figure 3.9 shows the COS mole fraction, and $\delta^{33}S$ and $\delta^{34}S$ data against potential temperature, in order to compare our data with previous studies. The samples with higher COS, at lower potential temperature – hence taken at lower altitude – show lower $\delta^{33}S$ and $\delta^{34}S$, which are reflecting the tropospheric background values. These samples are possibly influenced by anthropogenic emissions, which have a lower $\delta^{34}S$ (Angert et al., 2019; Hattori et al., 2020). The tropopause was located at a potential temperature between 355 and 375 K, above which the air consisted of a mixture of tropospheric and stratospheric air (von Hobe et al., 2021), with more stratospheric contribution with increasing potential temperature. In the COS data above 400 K, we observe relatively constant sulfur isotope ratios with averages of 5.2 ‰ and 19.3 ‰ for $\delta^{33}S$ and $\delta^{34}S$ respectively. Above 450 K, we see a slight decrease in $\delta^{33}S$ while $\delta^{34}S$ stays constant, with the exception of the highest sample that has a slightly lower $\delta^{34}S$. When we look at the isotope ratios against N_2O mole fractions (Figure 3.19 in supplementary material), we see that for N_2O mole fractions below 280 ppb, there is a decrease in COS mole fraction, but both isotope ratios are quite constant, with $\delta^{33}S$ around 0 ‰ and $\delta^{34}S$ around 18 ‰, implying a rather stable isotopic composition of COS around this altitude.

Figure 3.8: Data from flight 4 plotted against time of the day UTC. The middle figure shows δ^{33}S in green circles, the bottom figure shows δ^{34}S in blue circles and the top figure shows the COS mole fraction in parts per trillion in black circles. The red line in each plot indicates the altitude at which the aircraft was flying and thus the samples were taken.

Figure 3.9: Data from flight 4 from StratoClim AMA-17 plotted against potential temperature in Kelvin on the y-axis. The left panel shows the COS mole fraction in parts per trillion, the middle panel shows δ^{33}S and the right panel shows δ^{34}S.

Flight 6

During flight 6, the Geophysica aircraft flew over India and Bangladesh at a constant altitude of around 16.5 km, and performed a dive to 15 km at 9:24 UTC. Figure 3.10 shows the COS mole fraction and sulfur isotope ratios against time and altitude of the flight. During this flight, several pollution plumes were observed that were characterized by elevated CO mole fractions, with the highest CO being observed during the dive. According to Bucci et al. (2020) these pollution plumes consisted of very young air that originated from South China and the Southeast Asia peninsula. The other air measured during this flight consisted mostly of older, relatively clean air from the Indian sub-continent and the Tibetan Plateau.
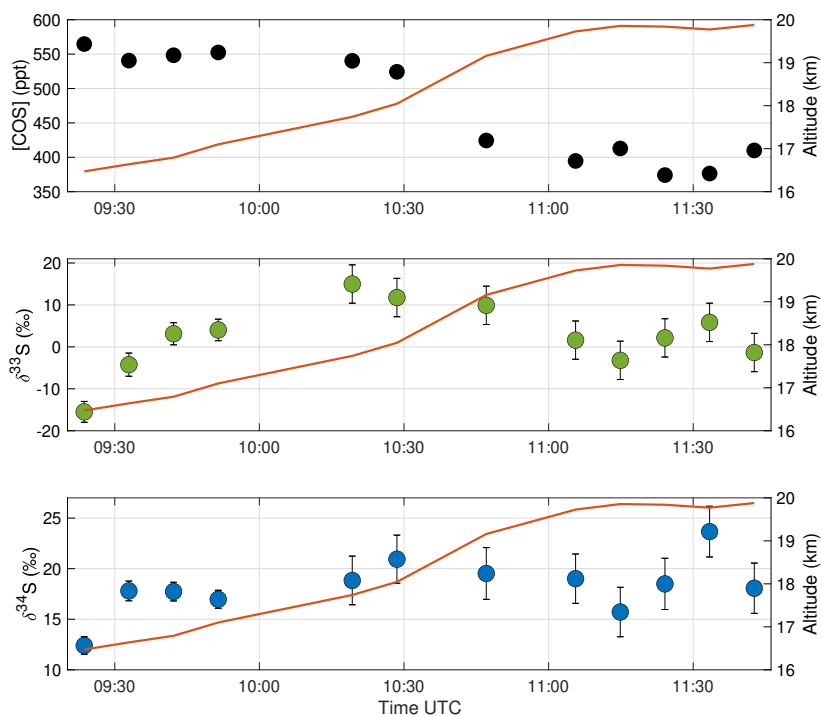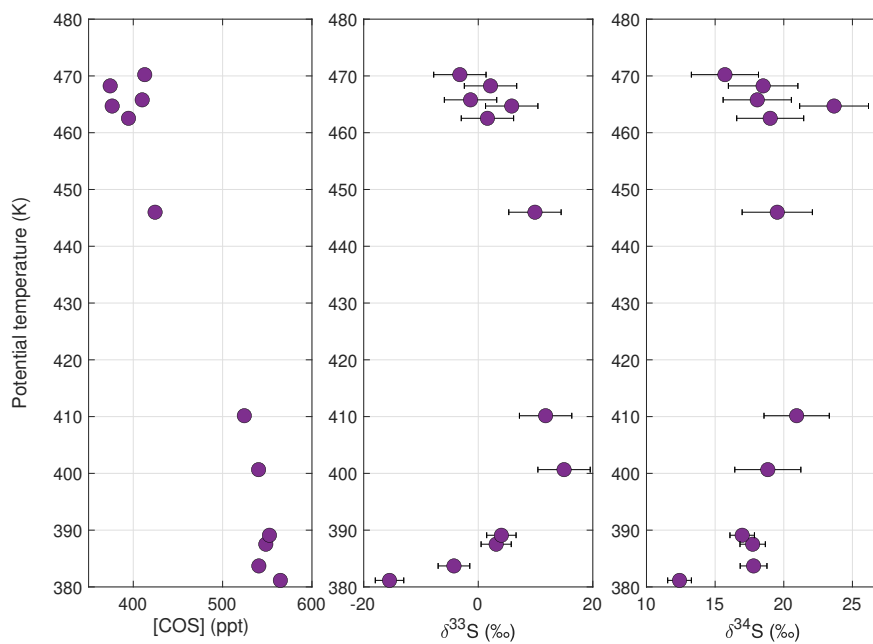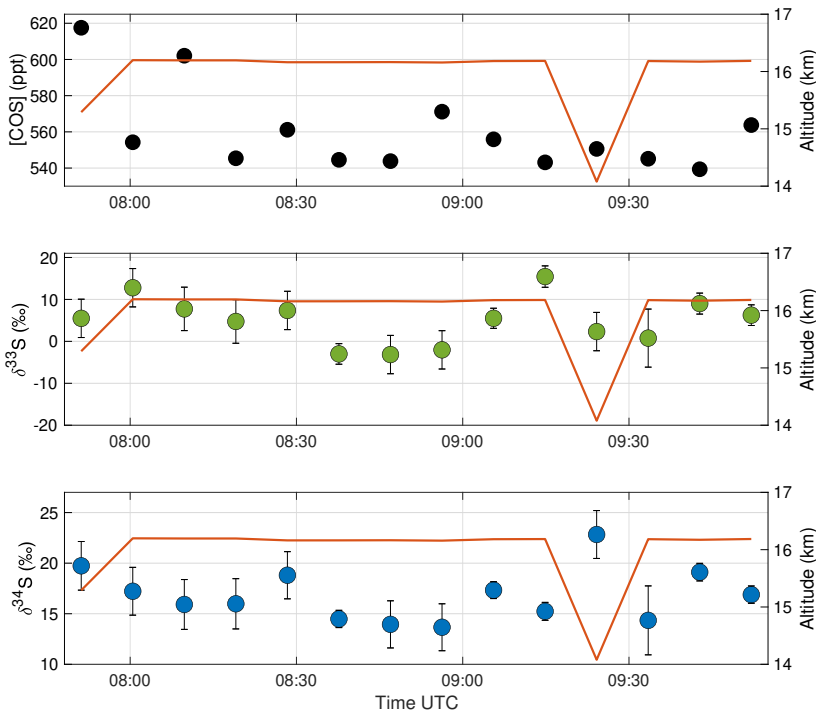

Figure 3.10: Data from flight 6 plotted against time of the day UTC in seconds. The middle figure shows δ^{33}S in green circles, the bottom figure shows δ^{34}S in blue circles and the top figure shows the COS mole fraction in parts per trillion in black circles. The red line in each plot indicates the altitude at which the aircraft was flying and thus the samples were taken.

In the COS data from this flight, we do not clearly observe all these pollution plumes. The highest COS mole fraction is found right after take-off at 7:50 UTC. For the rest of the flight, COS is mostly stable around 550 ppt. However, we observe higher mole fractions in the samples taken at 8:09, 8:28 and 8:56, of which the latter coincides with an observed CO

pollution plume. Yet, the first two samples that contained higher COS do not match with elevated CO. Interestingly, we do not observe higher COS during the dive at 9:24, which suggests that this young pollution plume did not contain much COS pollution.

Looking at the isotopic composition of COS, we find some variation during the flight in both δ^{33}S and δ^{34}S. For δ^{34}S, we find slightly higher values than the average tropospheric background throughout almost the entire flight, with the global ambient tropospheric δ^{34}S being between 10.5 and 15.5 ‰ (Angert et al., 2019; Hattori et al., 2020; Davidson et al., 2021; Baartman et al., 2022). Especially in the first sample, as well as the samples taken around 8:30, just after 9:00 and during the dive at 9:24 we find COS that is slightly enriched in ^{34}S, with the highest enrichment occurring during the dive. These enriched δ^{34}S values in pollution plumes are unexpected, since we generally expect to find relatively depleted CO^{34}S from anthropogenic emissions (Hattori et al., 2015; Angert et al., 2019; Hattori et al., 2020; Davidson et al., 2021; Baartman et al., 2022). However, the relatively low COS measured in the sample taken during the dive also suggests that this sample may not contain much fresh anthropogenic COS emissions. Hence, the isotopic signature of this sample does not necessarily represent direct anthropogenic emissions of COS.

3.3.2 KLIMAT 2021

Data quality

The KLIMAT 2021 campaign data are included in Figure 3.6 with the filled green circles. These data points only include the samples that were flown with an ozone scrubber. When we compared the KLIMAT 2021 samples with scrubber to the ones without scrubber, we could clearly see that the non-scrubber samples have a lower COS mole fraction than the samples with scrubber, possibly indicative of destruction of COS by ozone in the samples. Of the five samples collected with an O_3 scrubber active only three could be measured for COS isotopologues, as the other two sample canisters had indications of contamination. One sample showed high mole fractions for all species measured, including a COS mole fraction of 786 ± 4 ppt at an altitude of 17.5 km. The other sample collected at 16 km also had an unrealistically high COS mole fraction of 733 ± 32 ppt. Therefore, we will only consider the three samples that were flown with an O_3 scrubber and that did not show indications of contamination.

There are, however, some additional concerns about the stability of COS in the three samples that are analyzed further in this chapter. The samples of the cryosampler were first measured at the Goethe Universität in Frankfurt am Main for a various trace gas species, including COS. The same samples were later also measured at the Forzungszentrum Jülich and after that they were measured at the Rijksuniversiteit Groningen. With each measurement at a different institute, the COS mole fraction inside the samples was higher than the previous measurements, probably indicating that the COS inside the samples was not stable in time. There were also indications for a calibration offset between Groningen and Frankfurt, where the Groningen measurements were consistently higher than the measurements performed in Frankfurt. Additionally, as will be discussed below, the COS isotope results from our measurements in Utrecht for these three cryosampler samples also seem credible (i.e. they compare well with clean ambient air COS isotopic composition). Furthermore, the differences in COS mole fraction measurements between the labs were quite consistent

among the samples, and proportional to the mole fraction, which hints more towards a calibration issue rather than a drift in the samples.

Because of these concerns, some of the samples, including the three samples described above, were again measured at Jülich in February 2023. These measurements showed that the COS inside the samples that flew with an ozone scrubber increased substantially since they were last measured in Jülich, with differences between 300 and 900 ppt. At this moment, we do not know exactly what caused the increase in mole fraction for these samples, specifically. The results of the isotope measurements will still be shown, as well as the mole fractions as they were first measured in Jülich, which is the same group that measured the COS mole fractions in the StratoClim AMA-2017 samples. Nevertheless, we need to bear in mind the uncertainty regarding the quality of these measurements and we will be careful when interpreting the data and drawing conclusions from the KLIMAT 2021 campaign throughout the rest of this chapter.

Results

Figure 3.11 shows COS mole fractions, δ^{33}S, δ^{34}S and δ^{13}C for the KLIMAT 2021 campaign, against altitude together in one figure. The lowest sample, taken at an altitude of 13.5 km, had a COS mole fraction of 563 ppt (Figure 3.6 left panel and Figure 3.11 in grey on the upper axis). This sample likely reflects background tropospheric air. In the two samples above, we see a sharp decrease in COS, where the upper sample, taken at 19.3 km has a COS mole fraction of just above 300 ppt. This upper sample therefore likely contains lower (younger) stratospheric air or a mixture of stratospheric and tropospheric air. This is also reflected in mole fractions of other tracers in this sample, with CH_4 and N_2O mole fractions of 1518 ppb and 248 ppb, respectively.

For the lowest sample, the values for the sulfur isotope ratios, δ^{33}S and δ^{34}S, are −5 and +15 ‰, respectively. This δ^{34}S value agrees well with the range of tropospheric ambient background values (Angert et al., 2019; Hattori et al., 2020; Davidson et al., 2021; Baartman et al., 2022). The middle sample, taken at 14.8 km has slightly lower values for δ^{33}S and δ^{34}S compared to the lower sample, and the highest sample is slightly enriched in ^{33}S and ^{34}S. Both sulfur isotope ratios show the same trend, which for δ^{33}S is just within the error bars, thus they are not significantly different. For δ^{34}S, the errors are smaller, thus the differences between samples are small, yet significant. The enrichment in δ^{34}S of the upper sample compared to the lower samples is expected from the fractionation due to chemical sink reactions in the stratosphere. The values for δ^{33}S are within the range of tropospheric values found in Utrecht (Baartman et al., 2022). δ^{13}C shows a different trend where the values get slightly more depleted in the heavier isotope ^{13}C with increasing altitude, but the difference between the lowermost and uppermost sample of +2.4 ‰ is rather small. This small positive δ^{13}C value is not at all as expected from previous studies, which predicted large negative fractionation factors $^{13}\varepsilon$ (Hattori et al., 2011; Schmidt et al., 2012b; Schmidt et al., 2013).

As there have been some campaigns before at Esrange that measured COS, we can compare our mole fraction measurements to these earlier observations. Engel and Schmidt (1994), performed a similar balloon campaign at Esrange in November and December 1991 using the same cryosampler including O_3 scrubbers and found lower COS mole fractions
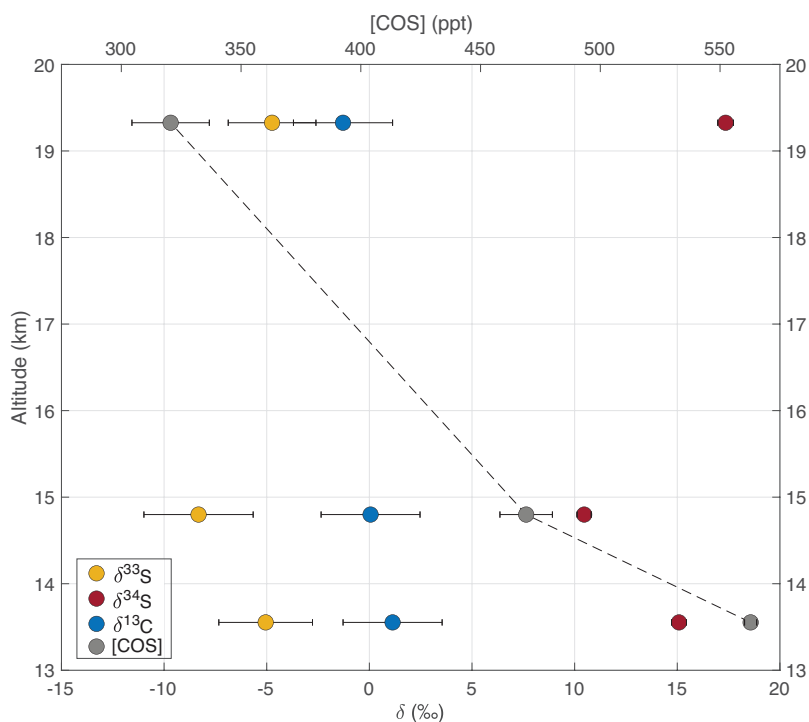
Figure 3.11: Data profile from KLIMAT 2021, where the isotope ratios are plotted against altitude in km, with δ^{33}S in yellow, δ^{34}S in maroon and δ^{13}C in blue. The grey circles, connected with the dashed lines are the COS mole fractions with the corresponding x-axis on top of the figure. Error bars are the 1σ errors, although the are not shown for δ^{34}S as the errors are too small to display.

compared to our measurements from KLIMAT 2021. They did, however, use a different type of O_3 scrubber: manganese dioxide (MnO_2). For the KLIMAT 2021 campaign, we also tested MnO_2 as an O_3 scrubber, but we found less efficient scrubbing capacity and break-through of O_3, whereas the cotton pads performed much better (Zanchetta et al., in prep). Engel and Schmidt (1994) found COS mole fractions of 168 to 210 ppt between 17.7 and 17.9 km and as low as 122 ppt at 20.8 km, whereas our measurements still show a COS mole fraction of 321 ± 16 ppt at 19.3 km. However, these measurements were performed in November and December, whereas the KLIMAT 2021 campaign took place in the beginning of August, when the tropopause is located higher: 12.5 km in summer compared to 11 km during the measurements presented by Engel and Schmidt (1994) in winter. Additionally, stratospheric down-welling, bringing down air with low COS mole fractions, is stronger during winter compared to summer (Butchart, 2014).

The KLIMAT 2021 COS profile agrees better with the measurements from Toon et al. (2018), who presented MkIV FTIR balloon-borne measurements from Esrange, and with ACE-FTS remote-sensing data presented by Barkley et al. (2008). However, these profiles also show overall slightly lower COS mole fractions in the troposphere, which may again be due to the different seasons in which these measurements were performed, as the ACE-FTS

data presented in Barkley et al. (2008) are selected for December, March, and April. Toon et al. (2018) also show COS profiles from some locations at 35°N. Again, their mole fraction profile for Esrange shows lower COS in the troposphere. Their profiles from 35°N are more similar to the values found during KLIMAT 2021. They explain the difference between the profiles at different latitudes by the stratospheric descent occurring at high latitudes. The overall higher COS mole fractions in our measurements compared to the others could also be the result of the contamination or drift in our samples, as mentioned previously. Thus, we still need to be careful with drawing conclusions from these data.

3.3.3   Comparing the two campaigns

Looking at the COS mole fraction data in the leftmost panel of Figure 3.6, it can be observed that the sharp decrease in COS for StratoClim 2017 starts at a higher altitude than for the KLIMAT 2021 campaign. This can be explained by the difference in tropopause elevation during the two campaigns. As mentioned earlier, the tropopause during StratoClim was located around 18.5 km, as a result of the strong updraft of the AMA. During the KLIMAT 2021 campaign at Esrange, the tropopause was located at a lower altitude of around 12 km, and therefore the sharp COS decrease starts at a lower altitude as well. Not only the altitude of the tropopause is different between the two campaigns, but also the vertical transport and mixing of air. Northern Sweden is located at the down-welling branch of the Brewer-Dobson circulation, where stratospheric air is descending. StratoClim took place relatively close to the equator, during the AMA, the strongly up-welling branch of the Brewer-Dobson circulation.

The middle and right panel of Figure 3.6 show all δ^{33}S and δ^{34}S measurement data for both campaigns against altitude. When comparing δ^{34}S of the two campaigns, the samples from KLIMAT 2021 lie within the same range as the StratoClim 2017 data, with a slight enrichment in ^{34}S above the tropopause. The errors for δ^{34}S from KLIMAT 2021 are smaller than for the measurements of StratoClim 2017, because the KLIMAT 2021 samples were measured two years later, with the more precise measurement system. Furthermore, for the KLIMAT samples, more air was available (up to 6 L per sample compared to around 2 L for StratoClim), which led to larger peak areas and therefore higher precision.

The similarities in δ^{34}S between the lowest (tropospheric) samples of the two campaigns are consistent with the hypothesis that tropospheric δ^{34}S in COS is rather homogeneous, as has already been shown before by previous isotope measurements of ambient air in Israel, the Canary Islands, Harvard Forest, Japan, and the Netherlands (Angert et al., 2019; Hattori et al., 2020; Davidson et al., 2021; Baartman et al., 2022). The δ^{34}S for the lower stratospheric samples of the two campaign both show little signal, thus pointing at a relatively small fractionation $^{34}\varepsilon$. The similarities for these upper samples also show that this small fractionation signal is consistent between different latitudes, and also when using different sample collection techniques and measurement set-ups. The δ^{34}S results being quite similar for the lower stratospheric samples of the two campaigns is also somewhat surprising, considering that at Esrange (KLIMAT 2021) we would expect to see more contribution of stratospheric air in the higher samples compared to StratoClim. The δ^{33}S values of KLIMAT are slightly higher than StratoClim, but both campaigns similarly do not show a clear trend. As we only have δ^{13}C measurements from KLIMAT 2021, we cannot compare the δ^{13}C data

between the two campaigns.

3.3.4 TM5 COS isotope simulations

We sampled the TM5 model output at the same time, location and altitude as the samples. Figure 3.6 shows the modelling results as open orange and green circles for StratoClim and KLIMAT, respectively. TM5 only included $CO^{32}S$ and $CO^{34}S$ and therefore the $\delta^{33}S$ panel does not include model results. For the StratoClim COS mole fractions, the TM5 simulation matches the observations quite nicely. For KLIMAT, however, the modeled COS mole fractions are slightly lower than the observations, especially for the lowermost sample taken just below 14 km. For $\delta^{34}S$, the simulations show much less variability compared to the observed profile, for both campaigns. The modeled relative enrichment in $\delta^{34}S$ with height is only 0.5 ‰, while the observations show much more variability and generally also higher $\delta^{34}S$ values. The higher variability in the observations could be due to larger spatial variation and contribution of different (anthropogenic) sources compared to the modeled sources. In the model, no spatial and temporal heterogeneity is applied in the sources (Table 3.1). Also, COS produced from precursors (CS_2, DMS) may have different isotopic signatures. Moreover, we applied constant and slightly negative values for COS chemical removal and uptake by the biosphere (see Table 3.1).

As a next exercise we implemented a larger photolysis fractionation factor into the model, of 10 ‰. With this fractionation factor, for StratoClim 2017, we still only found an overall apparent fractionation of 3.2 ‰ in the lower stratosphere and 5.5 ‰ in the upper stratosphere. Thus, in the model, much of the fractionation is diluted by mixing and transport processes. Discrepancies and similarities between the TM5 results and observations will be further discussed in section 3.3.5, where we elaborate on the stratospheric fractionation that can be estimated from our dataset.

TM5 cross-sections StratoClim 2017

To visualize whether the TM5 model captures the patterns of the AMA and what the consequences are for COS, we extracted some model cross-sections over longitude and altitude, during the days of flight 4 and 6. Figure 3.12 shows a cross-section from around 65 to 85° E and from 2 to 20 km altitude. The color bar shows the simulated COS mole fraction in ppt. In this figure, we can clearly observe a column of higher COS around 80° E, with lower mole fractions East and West of this column. This column was formed by the strong updraft of the AMA that was centered around that longitude on the day of flight 4 Bucci et al. (2020), through which tropospheric air, with higher COS mole fraction, is transported upwards towards the stratosphere. At the tropopause of around 18.5 km, we observe a clear boundary, over which the air is fanned east- and westwards, as it can no longer travel upwards. Above the tropopause, we see lower COS because of the destruction in the stratosphere. From this flight, we measured samples taken up to an elevation of just below 20 km, and, according to these model cross-sections, these samples were clearly capturing stratospheric air.

Figure 3.13 shows the same cross-section for flight 4 with $\delta^{34}S$ of COS. The updraft column is again clearly visible, with lower $\delta^{34}S$ values than the surrounding air. This can be explained because this is tropospheric air, which may contain some depleted anthropogenic

emissions, which is quickly transported upwards. The column maintains its tropospheric isotopic composition as transport is proceeding faster than stratospheric destruction, which is also reflected by the higher mole fractions. Above the tropopause, COS is showing slightly enriched values of δ^{34}S because of stratospheric removal. We also observe higher δ^{34}S values just west of the updraft column, which might be an indication of biosphere uptake or direct or indirect (through CS_2 or DMS) ocean emissions. This is, however, not clearly reflected in the mole fractions (Figure 3.12).

Figure 3.14 shows a cross-section over the same longitude and altitude range, but for StratoClim flight 6, on the 6th of August, 2017. As also stated by Bucci et al. (2020), the AMA was less pronounced during this day and we do not see a strong updraft in TM5. We do, however, see a band of higher COS mole fraction situated around 17.5 km altitude, which is likely the remainder of a previous updraft event, or updraft at another longitude that is carried to the longitudes in the cross-section. Flight 6 of StratoClim mostly flew at an altitude of 16.5 km. We see quite uniform mole fractions at this location, which is also reflected in the measurements presented in Figure 3.10.

Figure 3.12: COS mole fraction (ppt) cross-section at 29°N latitude from the TM5 model simulations on the day and time of flight 4 (2nd of August 2017). The longitude ranges from 65 to 95°E. The strong updraft due to the AMA is clearly visible between 70 and 85°E where high COS mole fractions (>550 ppt) persist to an altitude of around 17.5 km. The tropopause region around 18.5 km is also visible, above which the COS mole fraction drops quickly and below the tropopause we see a fanning effect; the COS that has been carried by the updraft is transported east- and westwards just below the tropopause.

Figure 3.13: Cross-section at 29°N latitude of δ^{34}S from COS from the TM5 model simulations on the day and time of flight 4 (2nd of August 2017). The longitude ranges from 65 to 95°E. Also here, the strong updraft around the upper air anticyclone center is clearly visible between 70 and 85°E where tropospheric COS with slightly lower δ^{34}S values is being transported upwards to the lower stratosphere.
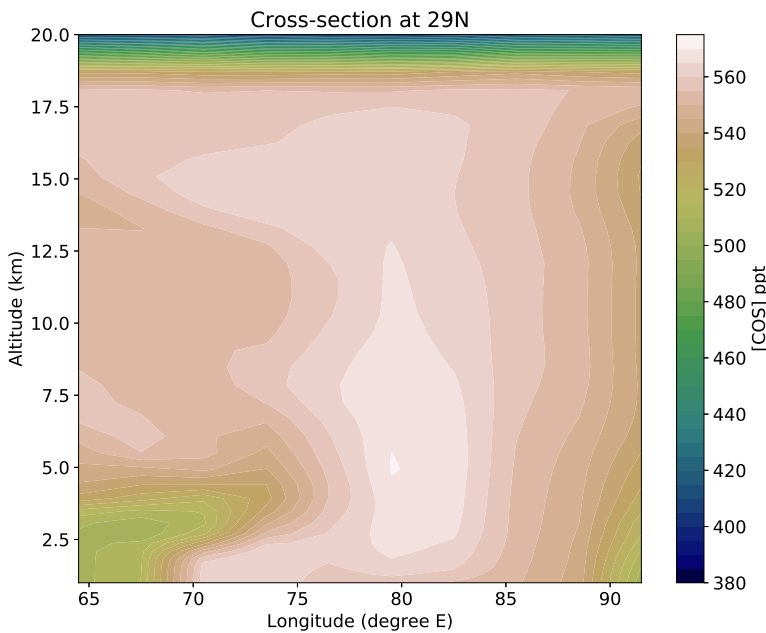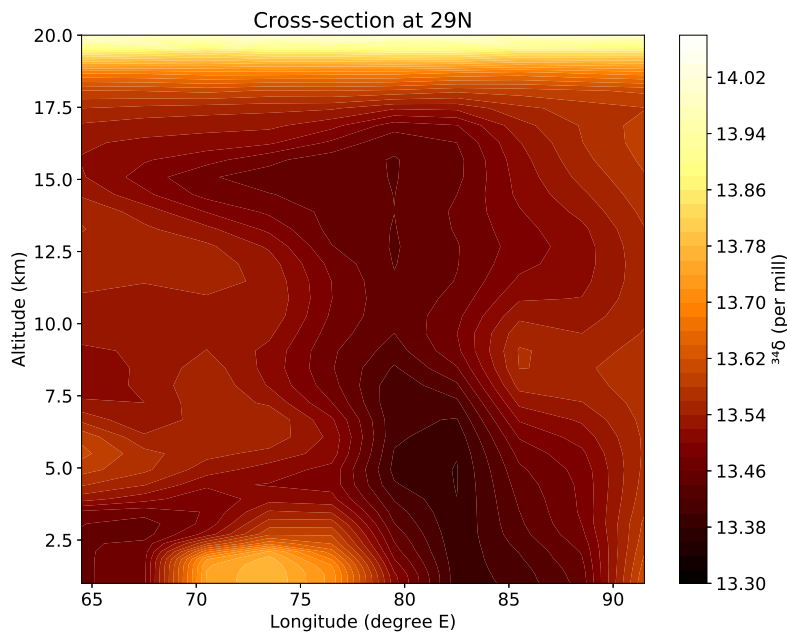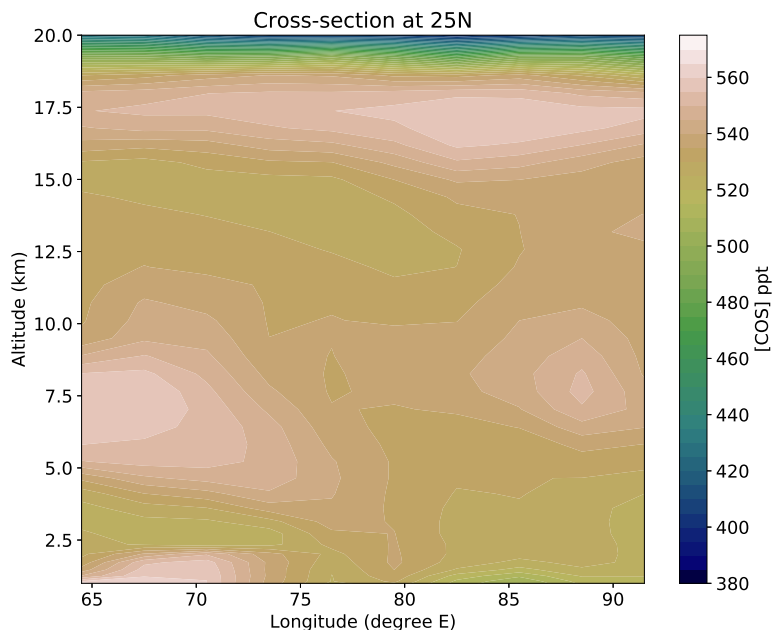
Figure 3.14: COS mole fraction (ppt) cross-section at $25°N$ latitude from the TM5 model simulations on the day and time of flight 6 (6th of August 2017). In this region, on this day, the AMA updraft is less visible than in Figure 3.13, though we do see a band of higher mole fraction COS between approximately 17 and 18 km altitude.

3.3.5   Stratospheric fractionation

Figure 3.15 shows a Rayleigh plot for ^{34}S, which can be used to visualize and calculate fractionation constants from the slope of the fitted line through the data, assuming a stable background mole fraction and one first-order sink process, where the green points are again the KLIMAT 2021 data and the orange points are the StratoClim data. For the three data points obtained from KLIMAT 2021, we estimated an overall apparent $^{34}\varepsilon$ of -6.1 ± 7.8 ‰ (note the large uncertainty). For StratoClim 2017, we only included the samples that were considered not influenced by pollution. The selection of samples with clean air was based on the correlation between CH_4 and COS, and N_2O and COS. A linear trend line was fitted between COS and CH_4, and between COS and N_2O. Samples that fell above these trend lines, and thus had higher than normal background CH_4 and/or N_2O for the corresponding COS were considered as potentially influenced by anthropogenic emissions and were excluded from the Rayleigh plots. Based on the remaining clean air samples, we found an overall apparent fractionation, $^{34}\varepsilon$ of -7.2 ± 6.1 ‰.

Figure 3.15 also includes the apparent fractionation constants that were derived from the first TM5 model simulations, which used the input values listed in 3.1. The model output was sampled separately for the StratoClim and KLIMAT campaigns. However, we found

very similar fractionation constants for both campaigns, thus the lines are not shown separately. Instead, different fractionation constants were found for the regions below and above 20 km. For StratoClim these were −0.9 ‰ below approximately 21 km and −2.1 ‰ above this altitude. For KLIMAT 2021, the derived fractionation constant was −0.8 ‰ below approximately 19 km and again −2.1 ‰ above 19 km. The apparent fractionation includes the combined effect of the actual fractionation in the stratosphere (which is mostly driven by photolysis (Equation 3.1.1) and the effect of mixing, which dilutes the magnitude of the fractionation (Kaiser et al., 2006). The photolytic fractionation that was used as input in the TM5 model had a value of −3 ‰ (Table 3.1), of which we only see −2.1 ‰ in the model output in the upper stratosphere, and only −0.8 to −0.9 ‰ in the lower stratosphere. This difference between input fractionation and observed apparent fractionation in the model output clearly shows that the lower stratosphere in the TM5 model is more strongly influenced by mixing processes, and that the observed apparent isotopic fractionation is therefore being attenuated. Logically, increasing the value for the actual fractionation in the simulation would also increase the apparent fractionation, but the apparent fractionation will always be lower than the input fractionation due to the mixing effect. As previously mentioned, we performed another simulation with the TM5 model, where we used a photolysis fractionation factor $^{34}\varepsilon$ of −10 ‰. With this simulation, we see only −3.2 ‰ fractionation in the lower stratosphere, and around −5.5 ‰ in the upper stratosphere, for the StratoClim 2017 campaign.

Figure 3.15 also shows photolysis fractionation lines from previous studies that were mentioned in the introduction of this chapter, including the values from Lin et al. (2011), Schmidt et al. (2013), Yousefi et al. (2019) and Leung et al. (2002). The zero fractionation (solid black line) line was added as a reference. The COS mole fractions used for the modelled fractionation as well as the fractionation lines from previous studies were all scaled in such a way that the lines would go through the same $x = 0$ point. Clearly, the large fractionation of +73.8 ‰ as found by Leung et al. (2002) is very different from the rest of the fractionation constants and also agrees poorly with our available measurements. The fractionation constants of Schmidt et al. (2013) and Lin et al. (2011) match the our measurement data best.

For the measured values shown in green and orange circles and the corresponding fractionation fits, it has to be noted that, using a Rayleigh plot method, we cannot distinguish between the different sink reactions that are taking place in the stratosphere. The value we obtain represents the isotopic fractionation of all processes combined. Furthermore, due to the large spread in the StratoClim data and the limited amount of data from KLIMAT, the errors on the derived fractionation constants are rather large. Nevertheless, we can conclude that our measured data correspond best to a relatively small fractionation, $^{34}\varepsilon$, in the stratosphere of between −7.2 and +1.7 ‰. This is the overall apparent fractionation observed in the lower stratosphere.

The TM5 model simulations have shown us that the actual fractionation caused by photolysis and other sink reactions could actually be 2 to 3 times larger than this apparent fractionation and that the signals in the lower stratosphere are probably diluted by transport and mixing processes. Thus, combining the knowledge from our observations and the model simulations, the actual fractionation could be up to around −21.6 ‰, but is likely to still be relatively small and negative, and thus not matching the ACE-FTS measurements by Yousefi et al. (2019), nor the MkIV measurements reported by Leung et al. (2002) , who

both found large positive fractionation constants. Our observations are more similar to fractionation estimates by Hattori et al. (2011), Schmidt et al. (2012b) and Schmidt et al. (2013). However, the fractionation values presented by these studies were all actual fractionation values and ours is the apparent observed fractionation, which is likely diluted by transport and mixing.

Figure 3.16 shows the same type of Rayleigh plot but for ^{13}C from the KLIMAT 2021 campaign, which also again contains fractionation lines from previous studies (Schmidt et al., 2012b; Yousefi et al., 2019). It is visible that our measured ^{13}C fractionation is different from the previous estimations. From our observations, we estimated a fractionation $^{13}\varepsilon$ of +4.2 ± 7.3 ‰, whereas Schmidt et al. (2012b) and Yousefi et al. (2019) both found a large negative fractionation. We again have to bear in mind the uncertainty regarding our data from the KLIMAT 2021 campaign, thus we need to be careful to draw conclusions from these discrepancies. More measurements of δ^{13}C of COS in the stratosphere are needed to constrain the fractionation. If the signal is indeed as large as estimated by these previous studies, it should be clearly visible, even with less precise measurements.
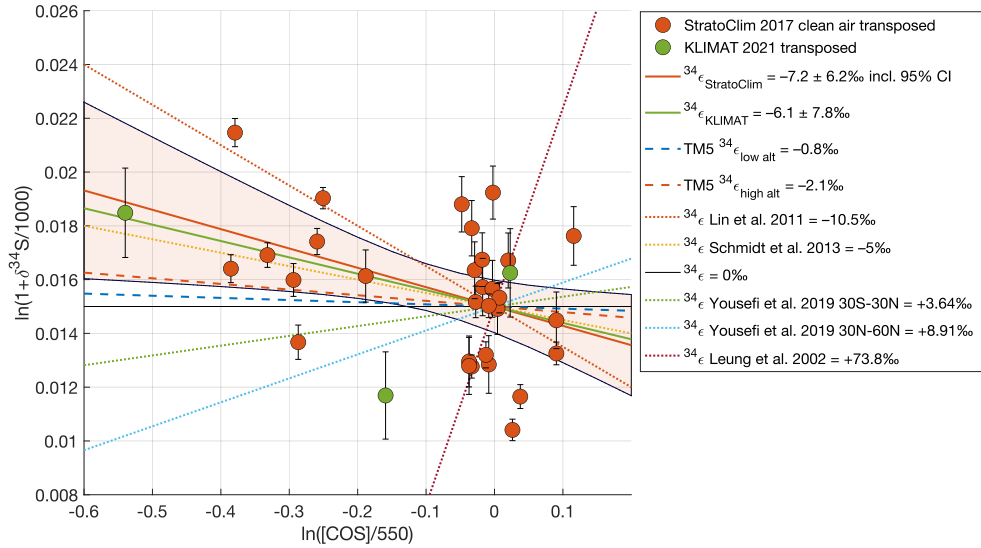
Figure 3.15: Rayleigh fractionation plot. The fractionation constant $^{34}\varepsilon$ can be derived from the slope of the relationship between $ln(1+\delta^{34}S/1000)$ and $ln([COS]/550)$, with 550 ppt taken as the tropospheric background mole fraction of COS. The orange and green circles are the measurements from the StratoClim and KLIMAT campaigns, where for StratoClim we selected only the clean air data (see text). The data were transposed in order for all the fractionation lines to go through the same point $x = 0, y = 0.015$, for comparison purposes. The fitted fractionation line for StratoClim includes the 95% confidence interval in the orange shaded area. Since the data for KLIMAT consists only of three points and the spread is large, the confidence bounds exceed the area of this plot and they were therefore not included. The dashed lines are the modeled fractionation lines from TM5. The red dashed line is the apparent fractionation at lower altitudes, and the green dashed line is the apparent fractionation at higher altitudes above the tropopause. The other dotted lines are the fractionation constants as presented by previous studies: Lin et al. (2011), Schmidt et al. (2013), Yousefi et al. (2019) and Leung et al. (2002). The figure also includes a zero fractionation line in solid black.
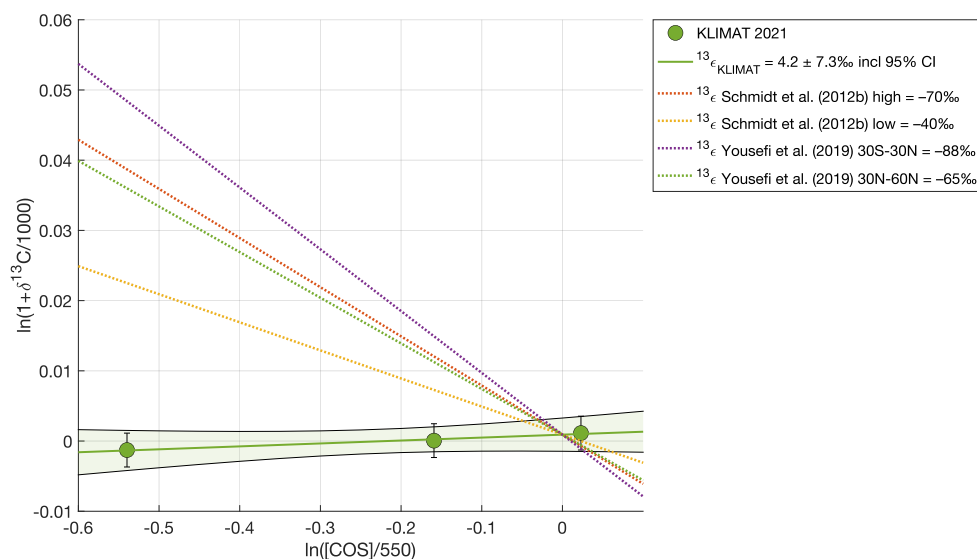
Figure 3.16: Rayleigh fractionation plot for ^{13}C. The fractionation constant $^{13}\varepsilon$ can be derived from the slope of the relationship between $ln(1+\delta^{13}$S/1000) and $ln([COS]/550)$. The green circles are the measurements from KLIMAT 2021. The fitted fractionation line includes the 95% confidence interval in the green shaded area. The dotted lines show the fractionation constants as estimated by previous studies: Schmidt et al. (2012b) and Yousefi et al. (2019).

3.3.6   Implications for SSA

To evaluate whether COS is a reasonable candidate for the main source of background SSA, only the $\delta^{34}S$ measurements of COS can be used and the fractionation constants that are derived from these measurements, since the other sulfur isotopologues were not measured by Castleman et al. (1974). As previously mentioned, Castleman et al. (1974) found a $\delta^{34}S$ value in SSA of +2.6 ‰. From previous measurements and modeling, Nagori et al. (2022) derived that for COS to be the main precursor of SSA, the fractionation constant during COS sink reactions in the stratosphere needs to be quite small and negative. Either a large negative or positive fractionation during these reactions would not propagate to a value of +2.6 ‰ in SSA around 18 km. Most recent lab experiments indeed found a relatively small fractionation $^{34}\varepsilon$, however some estimates from remotely sensed spectral measurement still pointed to a (large) positive $^{34}\varepsilon$ (Leung et al., 2002; Colussi et al., 2004; Yousefi et al., 2019).

Our measurements yielded apparent fractionation constants of $^{34}\varepsilon_{\text{StratoClim}} = -7.2 \pm 6.2$ ‰ and $^{34}\varepsilon_{\text{KLIMAT}} = -6.1 \pm 7.8$ ‰, which are, baring in mind the errors, within the expected range for COS being the SSA precursor. These observed apparent fractionation constants are a combination of fractionation occurring during COS consumption in the stratosphere and latitudinal as well as vertical mixing, where in-mixing of COS with a different isotopic signature will dilute the fractionation signal (Kaiser et al., 2006). Possible vertical mixing of COS-free air, descending from the upper stratosphere could also decrease the local COS mole fraction, while keeping the isotopic composition stable. Thus, the actual fractionation in the stratosphere could be larger than this observed apparent fractionation.

As mentioned in the previous sections, the TM5 model simulations also showed that the apparent COS isotope fractionation observed in the lower stratosphere can be up to 3 times smaller than the applied fractionation of the modelled stratospheric sink reactions. In the simulated upper stratosphere we observed about half of the model input fractionation. From these first direct measurements of COS isotopologues in the stratosphere, in combination with the TM5 modeling results, we can establish that the fractionation $^{34}\varepsilon$ is likely not very large (maximum of roughly -20 ‰), and also likely negative, which still makes COS a good candidate for the main precursor of background SSA.

3.4   Conclusion

This chapter presented the first COS isotopologue measurements in the upper troposphere and lower stratosphere. The dataset included measurements from two campaigns at different latitudes in the same season, which allows for a cross-latitudinal comparison. Furthermore, the measurement data was compared with simulations using the TM5 model, including a COS isotope module. This exercise allowed for a comparison between theoretical and observed stratospheric isotope fractionation. The goal of these measurements and model simulations was to characterize the COS isotope profile throughout the troposphere and lower stratosphere and thereby constrain the fractionation constants of the stratospheric sink reactions of COS. With this, the aim was to assess whether COS could be the main precursor of stratospheric sulfur aerosols during volcanically quiet times.

As expected, we found a decrease in COS mole fractions with altitude for both campaigns, which was especially sharp above the tropopause. For the isotope fractionations, we found a relatively small, likely negative $^{34}\varepsilon$ for both campaign locations, which matches

well with most of the recent literature (Hattori et al., 2011; Lin et al., 2011; Schmidt et al., 2013) and with the hypothesis of COS being the main source of SSA. Some other studies pointed to a larger (positive) $^{34}\varepsilon$ (Leung et al., 2002; Colussi et al., 2004; Yousefi et al., 2019), which is not confirmed by our observations. For $^{13}\varepsilon$, we found a much smaller value than expected from previous studies. This discrepancy still needs to be further investigated with additional measurements. Furthermore, as mentioned, we need to be careful with drawing conclusions from the data of the KLIMAT 2021 campaign, as the samples showed clear indications of drift or contamination.

The TM5 model was able to simulate the COS mole fractions quite accurately for the StratoClim 2017 campaign, as they corresponded well with the measured mole fractions in the samples. The modeled isotope ratios, however, showed much less variability compared to the observations. More research is needed to grasp this discrepancy, and understand the cause for such vertical variations in the observed COS isotopic composition. From the TM5 COS isotope model simulations, we also learned that mixing and transport processes likely play a large role in dampening the observed apparent fractionation, compared to the applied fractionation for stratospheric COS destruction in the model.

This chapter has demonstrated that performing stratospheric measurements is not an easy task. Thus, much care needs to be taken when planning new sampling campaigns for COS isotopologue measurements. One must ensure to have enough sample volume for adequate measurements, include and carefully test an ozone scrubber on the inlet of the samples, and perform extensive sample stability tests for COS and its isotopologues.

3.5   Supplementary material

3.5.1   Cryosampler tests

Description of cryosampler tests

We carefully tested stability of COS in the sample canisters number 1, 4, 7, and 13 inside the cryosampler, that were going to be filled for analysis of COS isotopologues during the KLIMAT 2021 balloon campaign. We tried to mimic stratospheric sampling conditions as good as possible and cooled the cryosampler vessel with liquid nitrogen. A membrane pump was connected to the vessel to decrease the pressure inside the vessel and thereby decrease the temperature of the liquid nitrogen. This was done in order to simulate the cryogenic pumping mechanism of the liquid neon, which would be used during sampling in the stratosphere during the campaign. Samples were filled up to an end pressure (after expansion) of approximately 10 bar with our target cylinder gas nr. D853421. Sampling was done through a mass flow controller and a pressure gauge was used to assess the sample pressure. In this way, the volume of gas in the canisters could be estimated. Afterwards, the samples were left to warm up and air was let to expand in the canisters. The samples were filled on the 2nd of June 2021 and measured for COS isotopologues on the 17th, 18th and 21st of June 2021. Thus, the samples were measured 15, 16 and 19 days after filling. The results were compared to direct measurements of the target gas D853421.

Figure 3.17: Filling procedure of the cryosampler stability testing in the lab

Cryosampler test results

We calculated the weighted mean and standard deviation for δ^{34}S of the air measured from the cryosampler and air directly measured from the cylinder used for filling the sampler. A weighted mean was used to take into account the measurement errors, which were different for the individual measurements. For the air measured from the cryosampler, we found a mean δ^{34}S of 13.1 ± 2.25 ‰ and for the directly measured cylinder air we found a mean δ^{34}S of 14.1 ± 1.52 ‰.

3.5.2 Ozone scrubber tests

Description of ozone scrubber test

Tests were performed in the isotope lab in Utrecht in June 2021 with the ozone scrubber that was to be deployed on the cryosampler during the KLIMAT 2021 balloon campaign. The tests were performed in order to make sure that there were no alterations in isotopic composition when the air was sampled through this ozone scrubber. The ozone scrubber consisted of a stack of 12 pure cotton pads for make-up removal bought at Etos pharmacy in the Netherlands.

The cotton pads were cut into a slightly smaller circles and placed in a stainless steel container (Figure 3.18). Air from cylinder D853421 was connected to the scrubber with a needle valve placed between the cylinder and the scrubber, and connected to the COS pre-concentration system. As a first step, the scrubber was fully evacuated for 2 minutes using the membrane pump at the outlet of the pre-concentration system. Then, the lines and the scrubber were flushed for 5 minutes with air from the cylinder by slowly opening the needle valve. Then, the 6-way valve at the pre-concentration system was switched in order to load the air going through the scrubber into the Tenax trap (see Baartman et al. (2022) and Chapter 2 for more details on the pre-concentration system). A total of 8 of such measurements were performed and the results were compared to direct measurements of the cylinder air, that did not pass through the scrubber. These tests were specifically meant to character-

ize the influence of the scrubber on the COS isotopic composition of the sampled air, and not the ozone scrubbing capacity. The other tests, which addressed the scrubbing capacity and interaction with COS mole fraction, were performed at Rijksuniversiteit Groningen (Zanchetta et al., in prep).
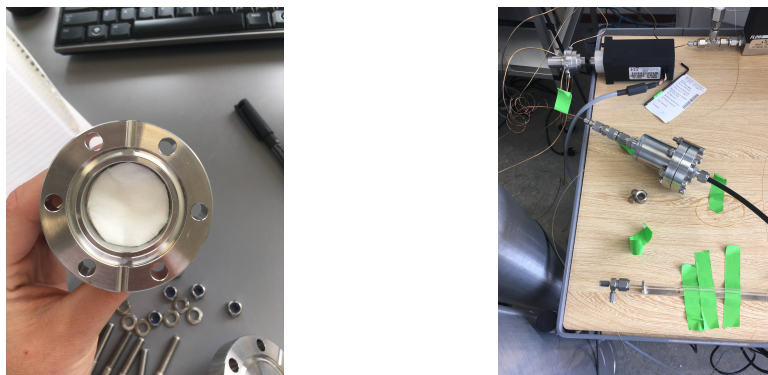
Figure 3.18: Testing the influence of the cotton pads ozone scrubber on COS isotopic composition with left image showing the stack of cotton pads inside the stainless steel housing and right image shows the entire scrubber housing, connected to the multi-position valve of the COS isotope pre-concentration system.

Ozone scrubber test results

We calculated the weighted mean and standard deviation for δ^{34}S of the air going through the scrubber and air by-passing the scrubber and directly entering the COS pre-concentration system. A weighted mean was used to take into account the measurement errors, which were different for the individual measurements. For the air passing through the scrubber we found a mean δ^{34}S of 15.0 ± 0.78 ‰ and for the directly measured cylinder air we found a mean δ^{34}S of 14.1 ± 1.52 ‰.

3.5.3 StratoClim 2017 flight 4 N₂O mole fractions and COS isotope ratios

Figure 3.19 shows the measured sulfur isotope ratios against the measured N$_2$O mole fraction for flight 4 of the StratoClim AMA-17 campaign.

Figure 3.19: Sulfur isotope ratios of samples taken during flight 4 of StratoClim AMA-17 plotted against N$_2$O mole fraction in ppb. Note tha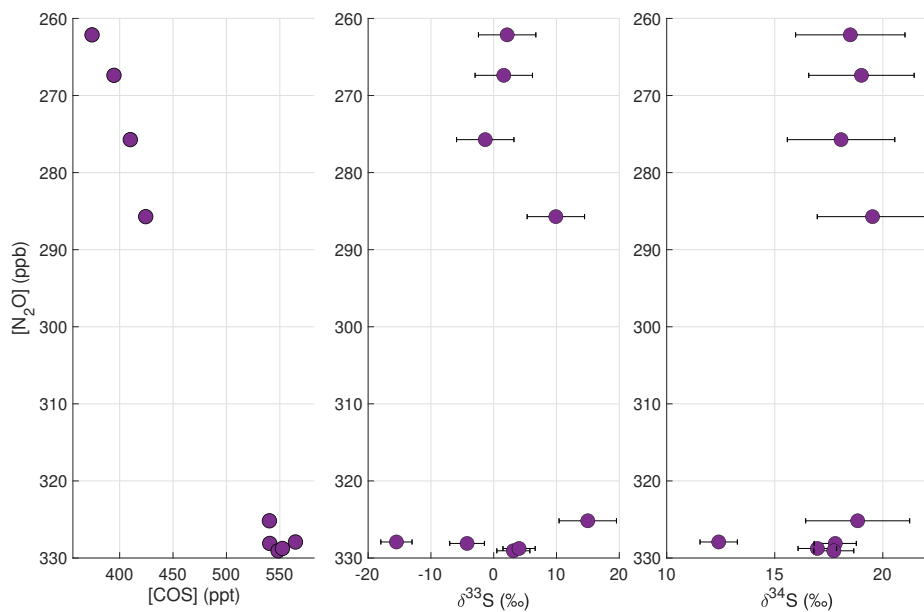t this figure contains less data points than Figure 3.9 as for some samples there was no N$_2$O data available. Thus, there is less scatter present in the lower N$_2$O region than would likely be present if we had N$_2$O data available for the other samples.

4

Isotope fractionation during uptake of COS and CO$_2$ by a C3 and C4 plant in gas exchange chamber experiments

Carbonyl sulfide (COS) has been proposed as a possible proxy for gross primary production (GPP) as it is taken up by plants through a comparable pathway as CO$_2$. COS diffuses into the leaf and undergoes an essentially one-way reaction in the mesophyll cells, catalyzed by the enzyme carbonic anhydrase. In order to use COS as a proxy for GPP, however, the COS budget needs to be better characterized. Measurements of stable isotopes can provide data for understanding the COS budget. As the terrestrial biosphere is the largest sink of COS, characterizing the isotopic discrimination during plant uptake is one of the most important steps. Thus far, only two studies have presented COS isotope discrimination data from plant experiments. This chapter presents a new methodology for conducting COS plant chamber experiments and presents a useful dataset of joint measurements of COS and CO$_2$ fluxes and isotope discrimination values $^{13}\Delta_{COS}$, $^{34}\Delta_{COS}$, $^{13}\Delta_{CO_2}$ and $^{18}\Delta_{CO_2}$ for a C3 and a C4 plant, sunflower and papyrus.

Experiments were conducted with a flow-through gas exchange chamber setup and different light level settings were used. We found higher CO$_2$ fluxes for our C4 species compared to the C3 one, which lead to lower c_i/c_a ratios for CO$_2$ in this species. COS fluxes were also higher for papyrus compared to sunflower. A relationship was observed between CO$_2$ fluxes and $^{13}\Delta_{CO_2}$ and $^{18}\Delta_{CO_2}$ values, where the discrimination was stronger with lower fluxes, as expected. For COS, no clear relationship between fluxes and isotope discrimination was found. For $^{34}\Delta_{COS}$, in light conditions, we obtained values between 2.8 and 3.7 ‰ for sunflower and between 2.5 and 2.7 ‰ for papyrus, with errors ranging between 0.4 and 1.2 ‰. Thus, we did not find a difference

in ^{34}S isotope discrimination between the studied C3 and C4 species, under these environmental conditions. However, our discrimination values are in the same range as previously reported values, while using a different experimental methodology.

The discrimination in $^{13}C_{COS}$ showed a surprisingly large fractionation for both the C3 and the C4 plant, with values $^{13}\Delta_{COS}$ ranging between 3.0 and 42 ‰. This fractionation is larger than what may be expected from mass-dependent (diffusion) processes, considering the $^{34}\Delta_{COS}$ values, and thus these $^{13}\Delta_{COS}$ may carry additional information on the fixation of COS by plants. These are the first measurements of $^{13}C_{COS}$ discrimination in plants, and more data would be useful to further constrain the fractionation estimates.

4.1   Introduction

Photosynthetic uptake of CO_2 by the terrestrial biosphere, gross primary production (GPP), is the largest sink of atmospheric CO_2 that may be altered as climate changes. It is thus important to quantify changes in the functioning of the biosphere in order to make accurate future climate projections. Several measurement techniques such as Eddy Covariance (EC) (Asaf et al., 2013; Billesbach et al., 2014; Commane et al., 2015; Wehr et al., 2017; Vesala et al., 2022) or using variations in the stable isotopic composition of CO_2, can be used as tools for partitioning photosynthesis and respiration fluxes at the ecosystem and larger scales (e.g. Farquhar and Lloyd, 1993; Farquhar et al., 1993; Wingate et al., 2007; Gentsch et al., 2014). At the ecosystem scale, each of these measurement approaches have their limitations either because they measure net CO_2 fluxes (Wohlfahrt et al., 2012; Kooijmans et al., 2017) or require additional measurements such as the oxygen isotope composition of water pools (Wingate et al., 2010). Because of this, other potential independent proxies for GPP have recently gained attention, especially the trace gas carbonyl sulfide (COS or OCS) (Whelan et al., 2018).

COS is the most abundant sulfur-containing atmospheric trace gas, with a tropospheric mole fraction of around 500 parts per trillion (ppt) and displays a strong seasonal cycle – like CO_2 – because COS is also removed from the atmosphere during photosynthesis. Similarly to CO_2, COS diffuses across the leaf boundary layer, through the stomata and into the leaf mesophyll cells, where photosynthesis takes place (Protoschill-Krebs and Kesselmeier, 1992; Protoschill-Krebs et al., 1996). In the mesophyll cells, COS is hydrolyzed in an essentially one-way reaction catalyzed by the enzyme carbonic anhydrase (CA), in contrast to the reversible hydration reaction that CO_2 undergoes (Protoschill-Krebs and Kesselmeier, 1992; Protoschill-Krebs et al., 1996). The uptake of COS by plants is proportional to photosynthetic uptake of CO_2, and therefore, GPP can be derived from measured atmospheric COS and CO_2 mole fractions and fluxes using Equations 4.1.1 and 4.1.2.

$$GPP = -F_{COS}\frac{c_{a_{CO_2}}}{c_{a_{COS}}}\frac{1}{LRU}, \qquad (4.1.1)$$

where F_{COS} is the COS flux in pmol m^{-2} s^{-1}, $c_{a_{CO_2}}$ and $c_{a_{COS}}$ are the ambient mole fractions of CO_2 and COS, respectively, and LRU is the leaf-scale relative uptake ratio given by:

$$LRU = \frac{F_{COS}}{F_{CO_2}}\frac{c_{a_{CO_2}}}{c_{a_{COS}}} \qquad (4.1.2)$$

In order to use COS as a proxy for GPP, the COS budget needs to be understood, which currently is not the case because a number of processes are still poorly constrained (Watts, 2000; Kettle et al., 2002; Montzka et al., 2007; Ma et al., 2021). Measurements of the stable isotopic composition of COS have the potential to provide a tool for constraining and tracing COS sources and sinks if they carry different isotopic signals. The isotopic fractionation of COS during plant uptake, specifically, might be used to better quantify the terrestrial biosphere sink and may help improve understanding of processes driving COS fluxes in plants. However, until recently, measuring the isotopic composition of COS was a challenge because of the amount of COS required for analysis. Measuring COS isofluxes between leaves and the

atmosphere presents an even greater obstacle.

Most recently, the stable sulfur isotope composition of COS has been measured in atmospheric samples, and work presented in this thesis describes a novel technique to measure the carbon stable isotope composition of COS for the first time. Equations 4.1.3 and 4.1.4 present the sulfur and carbon isotope ratios measured in this study. Isotope ratios are usually reported in the form of δ values, where the R of a sample is compared to the R of a reference material, see Equations 4.1.5 and 4.1.6.

$$^{33,34}R = \frac{^{33,34}\text{S}}{^{32}\text{S}} \tag{4.1.3}$$

$$^{13}R = \frac{^{13}\text{C}}{^{12}\text{C}} \tag{4.1.4}$$

$$\delta^{33,34}\text{S} = \frac{^{33,34}R_{sample}}{^{33,34}R_{standard}} - 1 \tag{4.1.5}$$

$$\delta^{13}\text{C} = \frac{^{13}R_{sample}}{^{13}R_{standard}} - 1 \tag{4.1.6}$$

Isotope fractionation occurs when a chemical or physical process favours one isotopologue over the other. In nature, usually the lighter isotopologue is favored over the heavier isotope, leading to the remaining pool of the substance (or substrate) being isotopically enriched in the heavier isotope. In atmospheric chemistry and thus in the previous chapters of this thesis, ε was used to express isotopic discrimination, given by Equations 4.1.7 and 4.1.8.

$$^{33,34}\varepsilon = \frac{^{33,34}k}{^{32}k} - 1, \tag{4.1.7}$$

$$^{13}\varepsilon = \frac{^{13}k}{^{12}k} - 1, \tag{4.1.8}$$

where $^{33,34}\varepsilon$ and $^{13}\varepsilon$ are fractionation constants for ^{33}S, ^{34}S and ^{13}C, respectively. In contrast, in biology usually the Δ notation (Equation 4.2.6) is used to describe the net isotopic discrimination during a process or in other words, the fractionation constant. The Δ value will be positive when the lighter isotope is favored over the heavier one. Thus, we can convert between these using: $\Delta = -\varepsilon$, which is only a sign change. In order to consistently handle both COS and CO$_2$ isotope data measured from plants and to ease comparison with the existing literature on plant carbon isotope discrimination, we will use the Δ notation throughout this chapter. Accordingly, the isotope fractionation values reported for COS in previous studies, as ε values, will be converted into Δ values.

4.1.1 Isotope discrimination during photosynthesis

Stable isotope measurements are not only useful for identifying and quantifying sources and sinks, but they can also provide information on plant physiology and environmental conditions (Cernusak et al., 2013). In the following, I will explain how stable isotope measurements of COS and CO_2 can help gain insight into plant physiology and environmental conditions and how isotope fractionation differs between C3 and C4 plant species.

C3 and C4 photosynthesis

C3 plants make up around 90% of all shrubs, trees and plants and use the C3 pathway in the dark reaction part of photosynthesis (Thomas, 2016). They perform most of their photosynthesis when their stomata are open, and all photosynthesis reactions take place in the chloroplast, located in the mesophyll cells, as depicted on the left side of Figure 4.1 and in Figure 1.6. C4 species, in contrast, use the C4 photosynthesis pathway, which partitions the photosynthetic activities between the mesophyll cells and bundle sheath cells that surround the leaf veins, as depicted on the right side of Figure 4.1. Initial carbon fixation is catalyzed by the enzyme called phosphoenolpyruvate carboxylase (PEPC), which forms malate from CO_2. This malate then diffuses into the bundle sheath cells, where it is decarboxylated to CO_2 again. The Calvin cycle, in which Rubisco catalyzes the final fixation of CO_2, also occurs in the bundle sheath cells. Thus, the C4 photosynthetic pathway leads to a high mole fraction of CO_2 at the location of Rubisco, which means that there is less loss of CO_2 through photorespiration and this yields a higher water- and energy use efficiency.

Isotope discrimination model

At the ecosystem level, photosynthetic discrimination against $^{13}CO_2$ can be used to understand variations in photosynthesis and stomatal conductance. In this context, the extent of ^{13}C discrimination is sensitive to environmental variables such as vapor pressure deficit (VPD), photosynthetically active radiation (PAR) and temperature, as they all impact photosynthesis, transpiration and drive variations in stomatal conductance (Wingate et al., 2007). For plants with a C3 photosynthetic pathway, ^{13}C discrimination in CO_2 mostly reflects the balance between the supply of CO_2 to the plant and the demand for CO_2 by the dominant enzyme Rubisco during photosynthesis (Gentsch et al., 2014).

The net discrimination against ^{13}C ($^{13}\Delta_{CO_2}$) (‰) can be expressed by the most important fractionation steps and the ratio of the internal leaf CO_2 mole fraction (c_i) and ambient CO_2 mole fraction (c_a). This model, first developed by Farquhar et al. (1982), is given by Equation 4.1.9:

$$^{13}\Delta_{CO_2} = \bar{a} + (b - \bar{a})\frac{c_i}{c_a}, \tag{4.1.9}$$

where $\bar{a}$ is the fractionation occurring during diffusion of CO_2 into the plant, which incorporates both leaf boundary layer (BL) diffusion and stomatal diffusion, and b is the net isotope fractionation during fixation by the plant enzymes Rubisco and PEPc. Characterizing the individual fractionation terms $\bar{a}$ and b is useful if one wishes to interpret carbon isotope signals archived in plant sugars or organic matter, or perform up-scaling exercises of these isotope signals to the ecosystem – or even global – scale (Fung et al., 1997). For ^{13}C

fractionation during C3 photosynthesis, global averages for $\bar{a}$ and b are 4.4 ‰ and 27-28 ‰, respectively (Cernusak et al., 2013). If $\bar{a}$ and b are known, this model can be used to quantify c_i/c_a ratios, which in turn can be used to characterize leaf stomatal conductance and water use efficiency (WUE) (Farquhar and Richards, 1984; Farquhar et al., 1989).

The framework used in the Farquhar model to describe ^{13}C discrimination of CO_2 during photosynthesis is also a useful starting point to investigate the isotopic fractionation during plant uptake of COS. In the case of COS, $\bar{a}$ can still represent the net fractionation during diffusion of COS into the plant across the leaf boundary layer and the stomata. Whilst the fractionation b, however, now represents the fractionation occurring during COS hydrolysis, catalyzed by the enzyme carbonic anhydrase (CA) in the mesophyll cells.

The first theoretical estimate of sulfur isotope fractionation during the net COS uptake by a plant was made by Angert et al. (2019). Their estimate was based on the assumption that the leaf internal COS mole fraction in C3 plants will be close to zero (Stimler et al., 2011; Stimler et al., 2012), implying no back-diffusion or production of COS, and therefore most fractionation will be the result of binary diffusion differences between $CO^{32}S$ and $CO^{34}S$ into the leaf. This binary diffusion is expected to give a theoretical $^{34}\Delta_{COS}$ value of around 5 ‰, because of the difference in molecular mass. However, it is not known whether internal COS will actually reach values close to zero, especially for C4 species, as will be further explained in the next section. Therefore, it is also relevant to find estimates for the enzymatic fractionation during COS fixation by CA.

Davidson et al. (2022) conducted plant chamber experiments and diffusion experiments to determine the overall ^{34}S isotopic fractionation of COS during plant uptake, as well as the individual diffusion and enzymatic fractionation terms, $\bar{a}$ and b, using the same model presented in Equation 4.1.9. From their diffusion experiments they found an $\bar{a}$ of −5.2 ± 0.5 ‰ for ^{34}S, very similar to the theoretically expected value. From experiments in which the plants were exposed to high CO_2 and COS mole fractions, they calculated an enzymatic fractionation for ^{34}S, b, of −15 ± 2 ‰.

To date, these are the only studies conducted for COS isotope fractionation during plant uptake, and while they provide a useful first set of data, the fractionation values are based only on a limited amount of closed-chamber measurements. As mole fractions of CO_2 and COS change during experiments with closed chambers, there is a potential risk that feedback processes on stomatal conductance and other metabolic processes may also contribute to the net discrimination and hence the measured values would no longer reflect the average leaf conditions in the field. Thus, more data on sulfur isotope fractionation during plant uptake are required. In addition, using different chamber experimental approaches on more plant species would be useful for further constraining these fractionation values. Furthermore, joint measurements of both CO_2 and COS isotope discrimination during one set of chamber experiments would provide additional useful information on plant function and response to environmental variability.

Isotope discrimination in C3 and C4 species

The differences in photosynthetic pathways of C3 and C4 species have implications for the isotopic fractionation during uptake of both CO_2 and COS. Figure 4.1 shows a schematic representation of the diffusion pathways of CO_2 and COS from the atmosphere into the leaf from Stimler et al. (2011). From this model, we can form expectations for isotope fractiona-
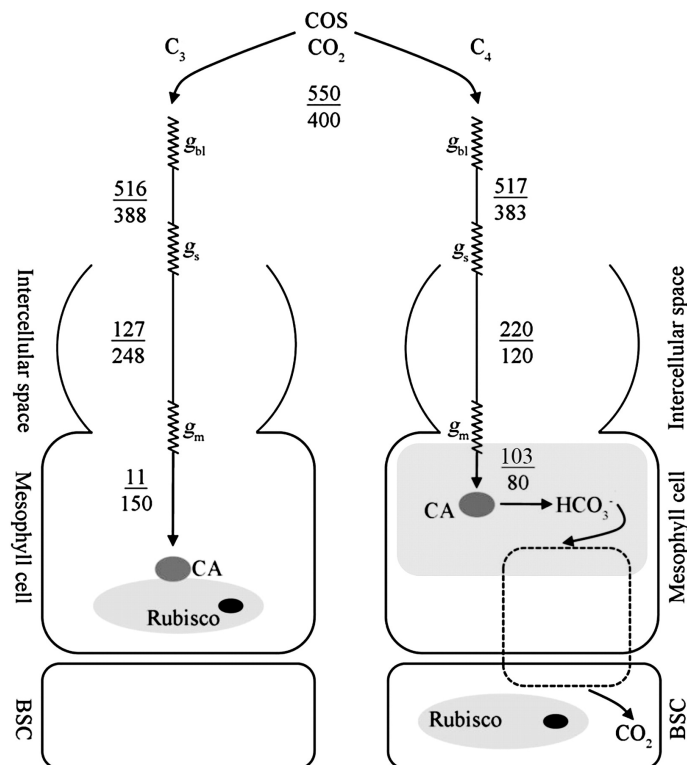
Figure 4.1: Model for diffusive pathways of CO_2 and COS into C3 and C4 plants (Stimler et al., 2011), where g_{bl} is the boundary layer conductance, g_s is the stomatal conductance and g_m is the mesophyll conductance. The numbers above and below the bar are the mole fractions of COS (ppt) and CO_2 (ppm), respectively. The values are based on a net CO_2 flux of 14 and 20 μmol m^{-2} s^{-1}, for C3 and C4 respectively and a COS uptake flux of approximately 35 pmol m^{-2} s^{-1} for both C3 and C4 leaves.

tion occurring during these diffusion steps as well as during fixation.

An important difference between C3 and C4 plants for COS uptake is the CA activity, which is likely lower in C4 plants compared to C3 plants (Burnell and Hatch, 1988; Gillon and Yakir, 2000; Sandoval-Soto et al., 2005; Stimler et al., 2011). Stimler et al. (2011) found that the C4 species that they studied had a higher c_i/c_a ratio for COS compared to C3 species, which they explained by a possibly lower CA activity in C4 species. They also found, however, that the COS uptake fluxes of their C3 and C4 species were similar, and thus not immediately reflecting this lower CA activity. They suggested that the higher c_i/c_a might compensate for the lower CA activity, leading to similar COS uptake fluxes for both C3 and C4 species. However, these effects need to be further investigated. The c_i/c_a ratio for CO_2, on the contrary, is lower in C4 species, due to the higher CO_2 assimilation rate in C4 compared to C3 plants.

For COS uptake, we may expect higher fractionation in C4 plants compared to C3 plants. The higher c_i/c_a for COS in C4 plants (see Figure 4.1) may allow for back-diffusion of COS from the leaf to the atmosphere, which would result in the enzymatic fractionation of CA, which was estimated by Davidson et al. (2022) to be higher than the diffusion fractiona-

tion of COS, to have more effect on the overall fractionation. As stated above, in C3 plants, CA activity is high, and the c_i/c_a ratio of COS is assumed to almost reach zero, thus no back-diffusion will take place and the effect of enzymatic isotope fractionation on the overall fractionation will likely be negligible (Davidson et al., 2022). The net discrimination, $^{34}\Delta_{COS}$, measured for C3 and C4 species by Davidson et al. (2022) were 1.6 ± 0.1 ‰ and 5.4 ± 0.5 ‰, respectively, at ambient COS and CO_2 mole fractions. Thus, the ^{34}S isotope fractionation was indeed larger for C4 than for the C3 plant they investigated. The C3 fractionation, obtained by Davidson et al. (2022) is lower than the first binary diffusion fractionation estimate of 5 ‰ by Angert et al. (2019), which they explained by the fact that the fractionation will not only be caused by stomatal diffusion, but also by leaf BL diffusion, and gas-liquid phase diffusion. Fractionation during COS uptake by a C4 plant will also be caused by a combination of these diffusion steps, but will also include a component from enzymatic diffusion.

As mentioned previously, the net ^{13}C discrimination of CO_2 during photosynthesis reflects the impacts of CO_2 fixation and stomatal conductance on c_i and can be interpreted using Equation 4.1.9. Both C3 and C4 plants discriminate against the heavier isotope ^{13}C compared to ^{12}C. However, C3 photosynthesis discriminates relatively more against ^{13}C compared to C4 plants. In C4 species, the term b in the Farquhar model is mostly determined by the discrimination by the enzyme PEPC during the reaction of CO_2 and HCO_3^-, and the amount of CO_2 and HCO_3^- that leaks out of the bundle sheath cells (Farquhar et al., 1989). Furthermore, PEPC has a lower tendency to discriminate against ^{13}C compared to Rubisco, leading to an overall lower biochemical ^{13}C fractionation in C4 species compared to C3 plants (O'Leary, 1981).

Apparent ^{18}O discrimination of CO_2 during photosynthesis can also be used as a tracer for biosphere-atmosphere CO_2 exchange (Stimler et al., 2011). CO_2 can exchange oxygen atoms with water, and in plant leaves, this reaction is rapid due to catalysis by CA. The apparent ^{18}O fractionation in CO_2 during photosynthesis is mainly due to exchange of O atoms with the leaf water pools, that are usually more enriched in ^{18}O (Farquhar and Lloyd, 1993; Farquhar et al., 1993; Francey and Tans, 1987). Similar to the COS uptake rate, $C^{18}OO$ exchange by leaves depends on CA activity and CO_2 conductance along the diffusive pathways shown in Figure 4.1. In C3 plants, this exchange often reaches full equilibrium because of the sufficient amount of CA present in the mesophyll cells (Gillon and Yakir, 2000; Gillon and Yakir, 2001). Stimler et al. (2011) found, in their photosynthesis experiments with several C3 and C4 plant species, that $\Delta^{18}O_{CO_2}$ was remarkably lower in C4, compared to C3 plants. This lower $^{18}O_{CO_2}$ most likely reflects the incomplete equilibrium between CO_2 and the leaf water in C4 plants, due to the lower CA activity. Stimler et al. (2011) also looked at the relationship between $\Delta^{18}O_{CO_2}$ and COS uptake in both C3 and C4 plants. They found a clear negative relation between COS uptake and $\Delta^{18}O_{CO_2}$ and also a linear relationship between LRU and $\Delta^{18}O_{CO_2}$, reflecting the similarities in the processes influencing these parameters, i.e. stomatal conductance and CA activity.

Furthermore, Adnew et al. (2020) found that the mass-independent $\Delta^{17}O$ signal in atmospheric CO_2 (note that Δ in this case means the deviation from the mass-dependent signal) can potentially be used as an additional tracer for GPP, as the above-mentioned equilibration of CO_2 with leaf water also affects $\Delta^{17}O$ values. The difference in the extend of equilibration between C3 and C4 species is also reflected in differences in $\Delta^{17}O$ (Adnew et al., 2020). However, to date, no plant or leaf chamber studies have been conducted measuring the

$\Delta^{17}O$ values and COS uptake rates.

4.1.2 Study aim

This chapter presents a novel methodology and dataset obtained from flow-through gas exchange plant chamber experiments with both a C3 (sunflower) and a C4 plant (papyrus). In these experiments, CO_2 and COS mole fractions were measured online and samples were taken for CO_2 and COS isotope analysis. Online measurements of COS, CO_2 and H_2O mole fractions were used for quantifying gas fluxes and monitoring the plant's behavior during the experiments, and for ensuring equilibrium state during time of sampling for isotopologue measurements. The dataset includes values for $\delta^{18}O_{CO_2}$ and $\delta^{13}C_{CO_2}$, as well as $\delta^{34}S_{COS}$ and $\delta^{13}C_{COS}$. From the δ values of the in- and outflowing air of the chamber, we calculated the net isotope discrimination by plants. Experiments were conducted using different light levels, including dark conditions.

  With this study we aim to contribute to the improvement of COS (isotope) models and help to understand the closure of the COS budget. Furthermore, this unique dataset of combined measurements of both CO_2 and COS isotope fractionation during plant uptake can help us better understand the underlying physiological drivers of COS uptake.

4.2 Methods

4.2.1 Plant material and growing conditions

The experiments were conducted with two different species. The first species was a sunflower (*Helianthus Annuus "Sunsation"*), a C3 species obtained at the local garden center. The C4 species that was used was a papyrus (*Cyperus papyrus*). Three papyrus leaves were cut carefully at the stem, under water, with a sharp razor, from a larger shrub that was growing in the tropical greenhouse at Wageningen University and Research (WUR). These three leaves were transported with their cut stem in water to the lab and were kept in water throughout the duration of the chamber measurements.

4.2.2 Whole plant gas exchange system

The experiments were conducted at Wageningen University and Research (WUR), the Netherlands, using a custom built whole plant gas exchange system that was developed for measurements of net photosynthetic CO_2 assimilation and transpiration rate. Figure 4.2 shows a schematic overview of the gas exchange system, including the chamber, all the in- and outgoing airflow and measurement lines and all measurement instruments.

  The chamber containing the plant consisted of clear plexiglass lined with a FEP foil (Holscot Europe, Breda NL) to prevent water from sticking to the chamber walls. The chamber had a diameter of 29 cm, and the height could be adjusted to either 18 or 27 cm, depending on the size of the plant. To ensure good air mixing, three SanAce40W fans (type 9WL0424P3J001, Sanyo Denki, Philippines) were placed in a circular pattern at the bottom of the chamber. Fan speed was controlled with a SanAce PWM controller. The chamber containing the plant was placed inside a 63x63 cm enclosure with white reflective walls, leading to a horizontal light distribution that was considered uniform. Air temperature in the plant

chamber was measured with a LM35 temperature sensor (Texas Instruments). Temperature was controlled using heating cables in combination with a PID controller. Two 12V computer fans were used to provide airflow and cooling to the enclosure. Light was provided by LED lighting with a spectrum resembling sunlight (artificial sunlight research modules generation 2, Specialty Lighting Holland B. V., Breda, The Netherlands), mounted above the chamber. Photosynthetically active radiation (PAR) was measured just above the chamber using a hand-held PAR sensor. The plant was installed into the chamber by closing the bottom two plexiglass panels around the stem of the plant and sealing it with Terostat RB VII, ensuring the plant was isolated from the soil or water (in the case of the papyrus), in which the plant was growing or transported.

Synthetic air was mixed with pure CO_2 using a mass flow controller (MFC), to reach the desired CO_2 mole fraction. The air was humidified before adding the CO_2 by a temperature controlled water bubbler. The flow rate into the chamber was controlled by a MFC to between 4 and 10 L min^{-1}, depending on the experiment conducted. COS was supplied to the air after the humidifier, using a MFC from a cylinder containing 700 ppb COS in synthetic "zero" air.

The CO_2 and H_2O mole fractions of both the reference in-going air (ref) and the outgoing air of the chamber (sample) were analyzed with an LI-7000 infra-red gas analyzer (LI-COR Biosciences, Lincoln, Nebraska, USA). CO_2 and COS mole fractions of the ref and sample lines were also measured by a Quantum Cascade Laser Spectrometer from the Center for Isotope Research, Rijksuniversiteit Groningen (CIO-RUG) (QCLS, Aerodyne Research Inc., Billerica, MA, USA). The QCLS used a 50 mL min^{-1} flow and was manually switched to measure the gas stream of interest. Magnesium perchlorate ($Mg(ClO_4)_2$) dryers were used on both the ref and the sample line before the air entered the QCLS instrument. Calibration of the QCLS was performed at least twice a day using the working standards from the Rijksuniversiteit Groningen (RUG), which are calibrated against NOAA certified cylinders. Possible instrumental baseline drift during the experiments was corrected by measuring pure nitrogen (N_2) multiple times during the experiment. For a detailed description of the instrument, see Kooijmans et al. (2016).

Samples for COS isotope measurements were taken in 6 L evacuated Silonite canisters from ENTECH (type: PN: 29-10622) that were filled to ambient pressure by opening them. Sampling was done through a magnesium perchlorate dryer and a filter, and the flow into the canisters was regulated using a manual flow controller. The dryer was changed every time after two samples were filled. When filling a canister, the sampling line was connected to the same location as the line to the QCLS, which was then disconnected. The QCLS would measure the other airflow while an isotope sample was being taken. For instance, when a flask was being filled with air from the ref line, the QCLS would be measuring the outflow of the chamber, and vice versa. Sampling for COS and CO_2 isotopic composition measurements would always be done when the plant had already been stabilized against temperature, humidity, and supplied CO_2 and COS levels for more than 10 min, hence photosynthesis and respiration rate would be stable, as well as the COS assimilation rate.
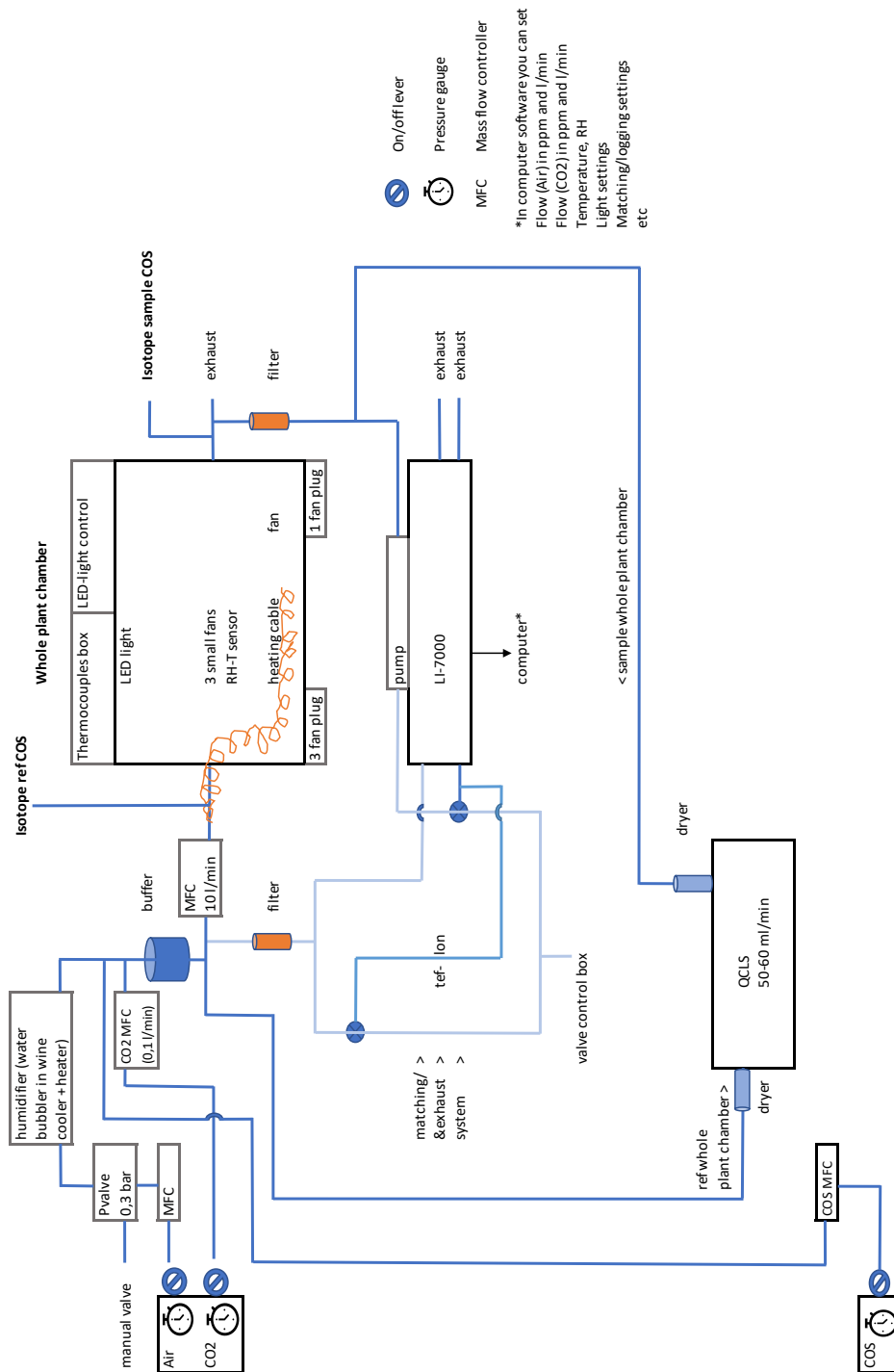
Figure 4.2: Schematic overview of the gas exchange plant chamber setup during the COS experiments at WUR, including all the measurement devices and ingoing and outgoing lines, where MFC stands for mass flow controller, QCLS is the Quantum Cascade Laser Spectrometer.
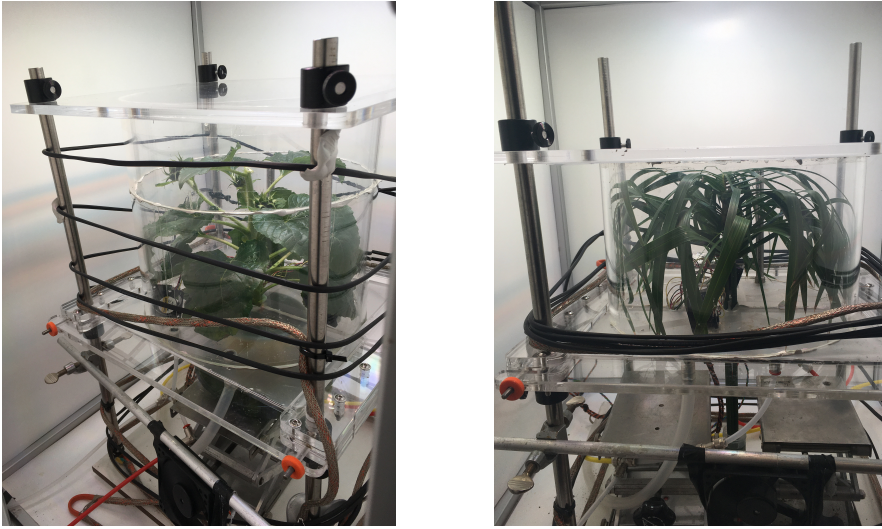
Figure 4.3: Whole plant chamber with sunflower (left) and papyrus (right).

4.2.3   Details of the experiments

Sunflower

For the sunflower experiment, the COS mole fraction was set at 2300 ppt, and CO_2 was adjusted to be 440 ppm at the chamber inlet. The flow rate was 8.1 L min^{-1}. First, 2 samples of the in-going air (ref) were taken. The starting setting for PAR was 400 μmol m^{-2} s^{-1}, which was checked with a hand-held PAR sensor. In these conditions, a pair of samples was taken at the chamber outlet for later analysis of CO_2 and COS isotopologues. In a subsequent step, PAR was increased to 600 μmol m^{-2} s^{-1}, and we took another pair of samples. Then, we decreased PAR to 200 μmol m^{-2} s^{-1}, and took a set of samples in these conditions. Lastly, we turned the light off and covered the chamber with a blanket so that light from the lab could not enter the chamber. In these dark conditions, one last set of samples for isotope analysis was taken. However, while we ensured that all other samples were taken in stable conditions (photosynthesis and COS uptake not varying over time), in these dark conditions, the plant was still adjusting to the new situation, thus conditions were not completely stable.

Papyrus

During the experiments with the papyrus leaves, we used a COS mole fraction of around 2400 ppt and a CO_2 mole fraction of around 430 ppm in the in-going air. The total flow rate was 8.1 L min^{-1}. PAR was set to 400 μmol m^{-2} s^{-1} for the start of the experiment. At this time, a set of samples was taken at both the inlet (ref) and outlet (sample) of the chamber. Then, PAR was lowered to 200 μmol m^{-2} s^{-1} and another pair of chamber outlet samples was taken. The setting of 600 μmol m^{-2} s^{-1} was not performed during the experiment with papyrus due to time constrains. Afterwards, the lights in the chamber were turned off and one last set of samples was taken for isotope measurements, again bearing in mind that the

plant was not in steady state at the time of sampling.

4.2.4   Measuring leaf area

Leaf surface area of sunflower and papyrus were measured after the experiments using a LI-3100. This instrument was calibrated using a metal disk with a surface area of exactly 50.00 cm^2. The leaves were extracted from the plant stem and measured separately. In the end, the total leaf area was obtained by adding the area of all leaves.

4.2.5   Calculating the fluxes

Both CO_2 and COS net fluxes were calculated from the QCLS mole fraction data, the leaf area and the flow rate through the chamber using Equation 4.2.1, where the equation shows the calculation for CO_2. As a quality check, the fluxes were also calculated from the canister mole fractions obtained from the mass spectrometer measurements of the CO_2 and COS isotopologues.

$$F_{CO_2} = (CO_{2in} - CO_{2out}) * \left(\left(\frac{u}{22.4} \right) \middle/ 60 \right) * A_{leaf}, \qquad (4.2.1)$$

where F_{CO_2} is the CO_2 flux in μmol m^{-2}s^{-1}, CO_{2in} is the CO_2 mole fraction of the ingoing air in ppm, CO_{2out} is the CO_2 mole fraction in the outgoing air of the chamber in ppm, u is the air flow rate through the chamber in L min^{-1} and A_{leaf} is the leaf area in m^2. The COS flux (F_{COS} in pmol m^{-2}s^{-1}) is calculated in the same way, where COS_{in} and COS_{out} are in the in- and outgoing COS mole fractions in ppt.

The errors on the fluxes were calculated by propagating the errors on the ingoing mole fractions and the outgoing mole fractions. In the case of the QCLS measurements, these errors were obtained from the 1σ of average mole fraction measured over a measurement period of around 10 to 15 minutes. The errors of the CO_2 mole fractions from the IRMS measurements were 1σ errors obtained from the measurement precision and the error of duplicate measurements, if performed. The errors on the COS mole fractions from the IRMS measurements were 1σ errors estimated from previous tests that can be found in Baartman et al. (2022) and Chapter 2 of this thesis.

From the QCLS CO_2 fluxes, the water vapor fluxes obtained from the LI-7000 and the temperature measured in the chamber, we calculated c_i/c_a ratios for CO_2 using Equations 4.2.2 through 4.2.5:

$$c_i = CO_{2in} - \frac{F_{CO_2}}{g_{tc}}, \qquad (4.2.2)$$

where g_{tc} is the total conductance of the leaf to CO_2 which was calculated using Equation 4.2.3 below:

$$g_{tc} = \frac{g_{tw}}{1.6}, \qquad (4.2.3)$$

where g_{tw} is the total conductance of the leaf to H_2O which was calculated using Equation

4.2.4 below:

$$g_{tw} = \frac{F_{H_2O}}{w_i - w_a},\qquad\qquad(4.2.4)$$

where F_{H_2O} is the water flux measured by the LI-7000, and w_a and w_i are the water vapor pressure in the chamber and in the leaf, respectively. w_i was calculated using Equation 4.2.5 below (Buck, 1981), which assumes saturation vapor pressure inside the leaf:

$$w_i = 6.1121e^{\left(\frac{17.502T}{T+240.97}\right)},\qquad\qquad(4.2.5)$$

where T is the leaf temperature, but in case of our experiments, we used the chamber air temperature, which we assume to be similar to the leaf temperature as the chamber was well mixed and the leaf boundary layer was thereby minimized. Ternary effects were neglected.

4.2.6   Measuring COS and CO$_2$ isotopologues

Initially, the samples had approximately atmospheric pressure, reflecting the pressure in the plant chamber. However, the COS isotope analysis system requires a higher sample pressure, thus we increased the pressure inside the samples to around 2.8 bar by adding COS-free zero air.

The samples were measured for both COS and CO$_2$ isotopic composition. The $\delta^{33}S_{COS}$, $\delta^{34}S_{COS}$ as well as $\delta^{13}C_{COS}$ isotope ratios were measured on the same sample. These measurements were performed using a pre-concentration system coupled to a Delta V Plus mass spectrometer (Thermo Fisher Scientific, USA), of which a detailed description can be found in Baartman et al. (2022). The methods of the $\delta^{13}C$ measurements are further explained in Chapters 1 and 3 of this thesis.

In short, the measurements were performed using a continuous flow GC-IRMS system, which measures the S$^+$ and CO$^+$ fragment ions that are created in the ion source of the IRMS as COS is split up. Measurements are usually performed on samples with volumes between 3 and 6 L of air. The measured volume of air is adjusted based on the (expected) COS mole fraction in the sample. A measurement at ambient COS mole fraction of around 500 ppt and a sample volume of 4 L yields precisions of 2.1 ‰, 0.5 ‰ and 2.5 ‰ for $\delta^{33}S$, $\delta^{34}S$ and $\delta^{13}C$, respectively. The sulfur isotope ratios were calibrated to the VCDT scale using several calibration gases with known sulfur isotopic composition. The $\delta^{13}C$ values from COS are not calibrated relative to the international VPDB standard, but only relative to our own reference gas, D853420, which is cylinder filled with outside air in Utrecht, spiked with some high mole fraction COS, and contains a COS mole fraction of around 800 ppt. Thus, at this moment, the gradients and fractionation values are still relevant, but not the absolute $\delta^{13}C_{COS}$ values.

The $\delta^{13}C_{CO_2}$ and $\delta^{18}O_{CO_2}$ were measured using the continuous flow isotope ratio mass spectrometry system initially developed for measuring CO isotopologues, as described by Pathirana et al. (2015), and later modified to include the measurement of CO$_2$ isotopologues. The typical precision was better than 0.2 ‰ for both the $\delta^{13}C_{CO_2}$ and $\delta^{18}O_{CO_2}$ isotope ratio values. The values are reported on the VPDB and VSMOW scales, and were calibrated using a reference air cylinder with known isotopic composition.

4.2.7 Calculating fractionation constants

As described above, the plant chamber gas exchange system is a flow-through system and samples were taken at the inlet and outlet to determine the isotope discrimination during uptake of CO_2 and COS. The air entering the chamber mixes with the air already in the chamber. Thus, the outgoing air which we sampled contained a mixture of COS and CO_2 influenced by the plant and newly supplied COS and CO_2 that was not affected by the plant. In a closed-chamber approach, where a certain amount of air containing COS and CO_2 molecules are continuously being removed without the addition of new air, we would use a simple Rayleigh distillation approach for determining the isotope fractionation. However, in this flow-through experiment, the assumption for Rayleigh distillation of single-stage removal without any addition the compound does not apply. Thus, we needed to use an alternative method for calculating the isotope fractionation. Evans et al. (1986) conducted a similar flow-through plant gas exchange experiment for characterizing carbon isotope fractionation during photosynthesis, and used Equations 4.2.6 and 4.2.7 to calculate the isotope discrimination Δ:

$$\Delta = \frac{\xi(\delta_{out} - \delta_{in})}{1000 + \delta_{out} - \xi(\delta_{out} - \delta_{in})}, \tag{4.2.6}$$

where δ_{in} and δ_{out} are the isotopic compositions of the gas entering and leaving the chamber, respectively, and ξ is calculated using Equation 4.2.7 below:

$$\xi = c_{in}/(c_{in} - c_{out}), \tag{4.2.7}$$

where c_{in} and c_{out} are the mole fractions of the gas of interest (in our case CO_2 or COS), entering and leaving a well-mixed chamber, respectively. ξ is the ratio between CO_2 or COS entering the chamber and the net CO_2 or COS fixed by the plant, at the moment of measuring. Thus, for each sample pair, inlet and outlet, the net isotopic discrimination Δ is calculated. As previously mentioned, if the plant discriminates against the heavier isotope, the remaining gas in the chamber becomes enriched in the heavier isotope, Δ will be positive. If the plant discriminates against the lighter isotope, Δ will be negative.

In practice, only two canister samples were taken at the inlet for each experiment. We assumed that the (isotopic) composition of the inlet gas did not change over time during our experiments as it was supplied from a cylinder, and we used the average COS and CO_2 mole fractions for c_{in} and isotopic compositions for δ_{in}, which can be found in Table 4.1.

After the experiment, the isotope ratios $\delta^{13}C_{CO_2}$, $\delta^{18}O_{CO_2}$, $\delta^{13}C_{COS}$, $\delta^{33}S_{COS}$, $\delta^{34}S_{COS}$, were measured, and Equation 4.2.6 was used to calculate the net isotope discrimination. The errors on the measured mole fractions and isotope ratios were propagated to the isotope fractionation values Δ. Details of the error propagation calculations on the Δ values can be found in the supplementary material.

Table 4.1: Isotopic composition of the inlet gas (ref) during the plant experiments. For each experiment, we used the same gas. The small differences in isotopic composition of the ingoing air between experiments are likely due to slight differences in mixing of the different components of the ingoing chamber, as well as some variation that might be introduced by the isotope measurements themselves and the storage in the canisters.

Plant	$\delta^{34}S_{COS}$ (‰)	$\delta^{13}C_{COS}$ (‰)	$\delta^{13}C_{CO_2}$ (‰)	$\delta^{18}O_{CO_2}$ (‰)
Sunflower	11.9 ± 1.2	−3.0 ± 2.6	−23.1 ± 0.1	15.5 ± 0.1
Papyrus	12.1 ± 0.5	−1.9 ± 3.0	−23.0 ± 0.1	15.9 ± 0.1

4.3   Results and discussion

4.3.1   COS and CO_2 fluxes

Net CO_2 and COS fluxes were calculated separately, with one method using the online QCLS data, and the other using the discrete mole fraction values obtained from the mass-spectrometer measurements of the samples. In order to perform a quality check of the canister samples, Figure 4.4 shows the fluxes calculated from IRMS measurements of the canisters plotted against the QCLS fluxes. Looking at the left plot for the CO_2 fluxes, we find that the calculated fluxes correlate relatively well, although with a slight scale off-set. However, two samples, one sunflower sample at 400 PAR and one papyrus sample at 200 PAR, clearly deviate from the correlation, with higher flux values from the IRMS measurements compared to the fluxes derived from the QCLS measurements. These two samples contained much lower CO_2 mole fractions than expected and in comparison with the online QCLS data. Therefore, we concluded that there was likely something wrong with these samples and they were excluded from further analysis of the CO_2 and COS dataset.

In the right-hand plot of Figure 4.4, which shows the COS fluxes of the canisters against the QCLS fluxes, we also observe a linear correlation, although the fluxes obtained from the canisters are much higher than those from the QCLS. This is likely because of a calibration scale issue of the COS mole fraction measurements of the IRMS, which led to the inlet samples having much higher COS mole fractions (about +400 ppt for the canister measurements compared to the QCLS) than seen on the QCLS, while the outlet samples taken during the experiment showed similar mole fractions from the canister as measured by the QCLS. This caused the differences between in- and outlet for the canisters to be much larger than for the QCLS measurements and therefore the fluxes calculated from the canisters are much larger than those obtained from the QCLS. Therefore, for COS, we trust the fluxes from the online QCLS measurements more and we will continue to use those onward in this chapter. For CO_2 we will continue to use the sample measurements as they best represent the fluxes at the exact moment of sampling.

During the experiments with sunflower and papyrus, the plants were exposed to different light levels. Figure 4.5 shows the net CO_2 and COS fluxes in μmol m^{-2} s^{-1} and pmol m^{-2} s^{-1}, respectively, plotted against PAR in μmol m^{-2} s^{-1}. The CO_2 fluxes shown in this figure are the ones obtained from the canister measurements and the COS fluxes are from the QCLS measurements. The mean CO_2 fluxes in light conditions (PAR > 0) were 7.0 ± 2.3 μmol m^{-2} s^{-1} and 13.1 ± 2.3 μmol m^{-2} s^{-1} for sunflower and papyrus, respectively. For COS, the mean fluxes in light conditions were 67.1 ± 1.4 pmol m^{-2} s^{-1} and 97.8 ± 1.4 pmol

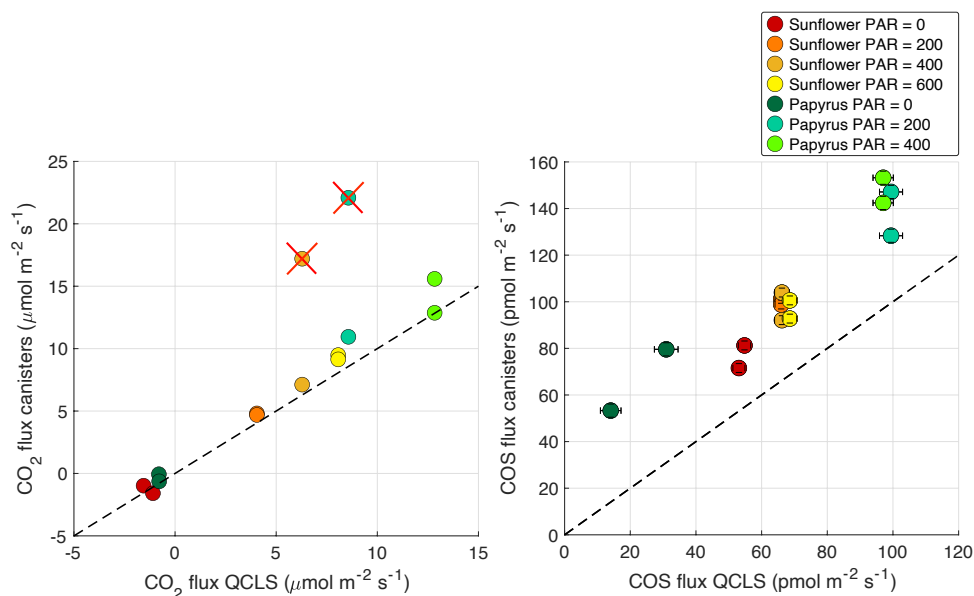Figure 4.4: CO_2 and COS fluxes in μmol m^{-2} s^{-1} and pmol m^{-2} s^{-1}, respectively, calculated from the discrete samples taken that were analyzed on the mass spectrometer plotted against the fluxes that were calculated from the online QCLS measurements, including $\pm$ 1σ. The 1σ was obtained using error propagation of the measurement errors on all the components used during the flux calculations (see supplementary materials). Note however that the error is not depicted in the left figure as the errorbars were smaller than the displayed symbols. The colors indicate the different plant types (sunflower and papyrus) and the PAR levels in μmol m^{-2} s^{-1}. The black dashed line shows the one-to-one line, for reference. The red crosses indicate the two datapoints that have been excluded from the dataset.

m^{-2} s^{-1} for sunflower and papyrus, respectively.

For CO_2, we see a clear increase in net uptake with increasing PAR, and we see a small respiration flux for both species in the dark. We also observe that the net CO_2 uptake flux is larger for papyrus, being a C4 plant, than for sunflower, a C3 plant. This is in line with our expectations as C4 plants generally have higher photosynthetic rates than C3 plants (Farquhar et al., 1989).

For the COS fluxes (right plot), we always see a net uptake, even in dark conditions. Note that the samples in dark conditions were not taken simultaneously, and are therefore not treated as duplicates. For 400 μmol m^{-2} s^{-1} PAR, the LRU (Equation 4.1.2) values were around 2 and 1.4 for sunflower and papyrus, respectively. For the lowest light setting of 200 μmol m^{-2} s^{-1}, LRU values were 3.2 and 2.1 for sunflower and papyrus, respectively. These higher LRU values occurred because COS fluxes were less affected by the lower light conditions than the CO_2 fluxes. In the dark, LRU values were negative, up to −9.3, as COS uptake by the plant continued while CO_2 was being respired. For papyrus, the COS flux was still decreasing as the plant was adjusting to the dark conditions. As a result, one of the samples shows a lower COS flux than the other. This will become more clear in later figures. Furthermore, the observed COS flux was generally higher for the C4 plant than for the C3 plant, consistent with the pattern observed for CO_2 and in conditions with sufficient
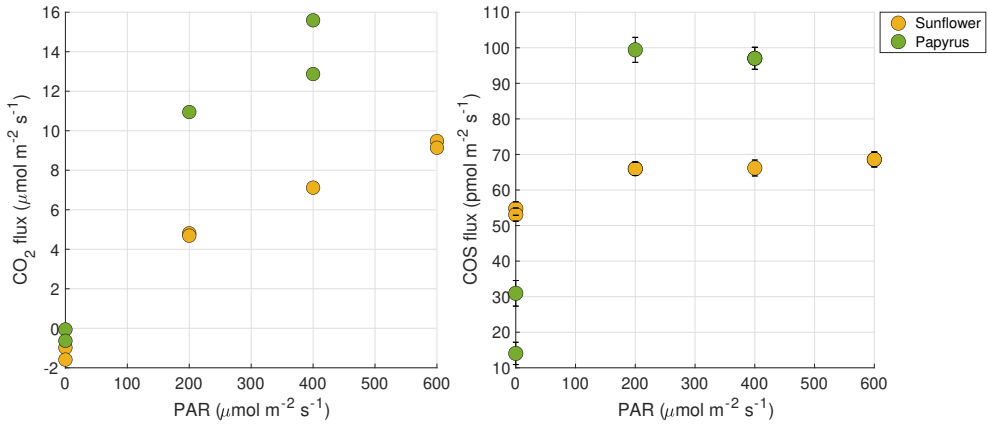
Figure 4.5: CO_2 (left figure) and COS (right figure) fluxes in μmol m^{-2} s^{-1} and pmol m^{-2} s^{-1}, respectively plotted against photosynthetically active radiation (PAR) in μmol m^{-2} s^{-1}, where the orange points represent the sunflower measurements the green points are the papyrus measurements. For the papyrus, only experiments with 0, 200 and 400 μmol m^{-2} s^{-1} PAR were conducted. The CO_2 fluxes were obtained from the canister measurements and the COS fluxes were from the QCLS measurements. The 1σ that is displayed was obtained using error propagation of the measurement errors on all the components used during the flux calculations (see supplementary materials).

light.

Figure 4.6 shows the CO_2 flux (μmol m^{-2} s^{-1}) versus c_i/c_a ratio for CO_2, where the flux was calculated from the discrete IRMS sample measurements and the c_i/c_a was estimated using the online QCLS and LI-7000 CO_2 and H_2O data. We found a strong correlation between the CO_2 flux and CO_2 c_i/c_a with the highest CO_2 fluxes of papyrus (C4) corresponding to the lowest c_i/c_a values and the lower CO_2 fluxes of sunflower (C3) being linked to the largest c_i/c_a values. These plant species differences in CO_2 flux are consistent with the results presented by Stimler et al. (2011).

4.3.2 CO_2 isotopes

All isotope discrimination results for COS and CO_2 can be found in Table 4.2. Figure 4.7 shows the CO_2 isotope discrimination values $^{13}\Delta_{CO_2}$ and $^{18}\Delta_{CO_2}$ in ‰ against the CO_2 fluxes, with colors indicating the different species and also different PAR levels. First of all, we again see that the CO_2 flux increases with light availability; the dark samples are not included this time as isotope discrimination cannot be determined if there is no net uptake. For both $^{13}\Delta_{CO_2}$ and $^{18}\Delta_{CO_2}$, we observe a trend of increasing discrimination towards lower CO_2 flux. Note, though, that the errors on the discrimination values are larger with decreasing flux.

^{13}C discrimination in CO_2: $^{13}\Delta_{CO_2}$

For $^{13}\Delta_{CO_2}$ we found average discrimination values between 23.5 and 31.8 ‰ for sunflower and between 19.9 and 20.3 ‰ for papyrus. As explained in the introduction of this chapter,
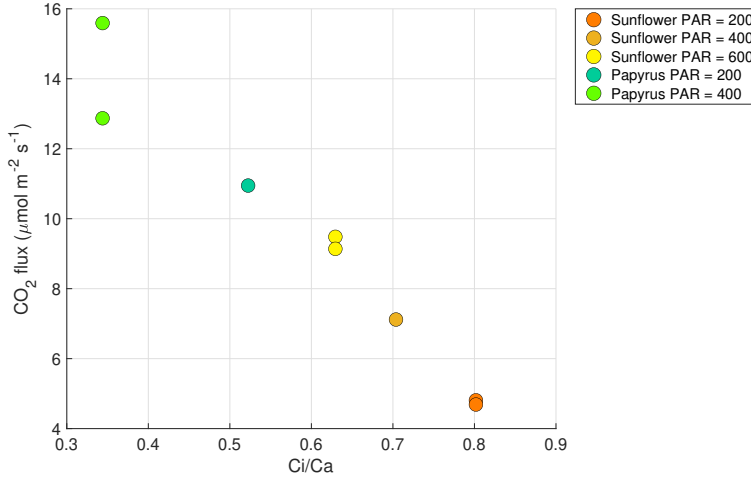
Figure 4.6: CO_2 flux in μmol m^{-2} s^{-1} calculated from the canister measurements plotted against c_i/c_a ratio, which was estimated from the online QCLS and LI-7000 measurement data.

Table 4.2: Isotope discrimination results, averaged for each PAR level, including ± 1σ errors. Only the COS isotope discrimination results are included for Sunflower, PAR = 0, as CO_2 flux showed net respiration instead of uptake. For Papyrus, PAR = 0, the COS flux was very small and the errors on the Δ values became very large. Thus no isotope discrimination values are included for these samples. The errors of the mean were calculated with the standard deviation of the mean and the student's t-distribution, with 60% confidence interval and 1 (n−1) degree of freedom, as the mean values were calculated from duplicates (n=2). The values that do not display errors were single sample measurements, the measurement errors are depicted in the figures below.

Plant	PAR	$^{34}\Delta_{COS}$ (‰)	$^{13}\Delta_{COS}$ (‰)	$^{13}\Delta_{CO_2}$ (‰)	$^{18}\Delta_{CO_2}$ (‰)
Sunflower	200	3.6 ± 1.2	30.9 ± 1.8	31.8 ± 1.7	145.5 ± 3.6
Sunflower	400	3.7	6.1	25.3	84.7
Sunflower	600	2.8 ± 0.6	18.4 ± 3.1	23.5 ± 1.8	63.5 ± 2.7
Sunflower	0	2.9 ± 2.3	42.0 ± 33.5	-	-
Papyrus	200	2.5	3.0	19.9	72.0
Papyrus	400	2.7 ± 0.4	32.7 ± 17.4	20.3 ± 6.3	52.9 ± 11.7

C3 plants generally discriminate stronger against $^{13}CO_2$ than C4 species, with the differences being due to their different CO_2 fixation pathways. In our experiments, we also found a stronger $^{13}C_{CO_2}$ discrimination for our C3 plant compared to the C4 plant. However, the range of values that we found for papyrus is not in the range of expected values from C4 species, which was most often found to be around 3 to 6 ‰ (Kubásek et al., 2013; Ellsworth and Cousins, 2016; Eggels et al., 2021).

The negative correlation of $^{13}\Delta_{CO_2}$ values with PAR are in line with our expectations. In a field study, Gentsch et al. (2014) found a diurnal cycle of $^{13}\Delta_{CO_2}$ for CO_2 uptake in *Fagus Sylvatica* (C3) that was linked to PAR. The highest $^{13}\Delta_{CO_2}$ values were found in early morn-
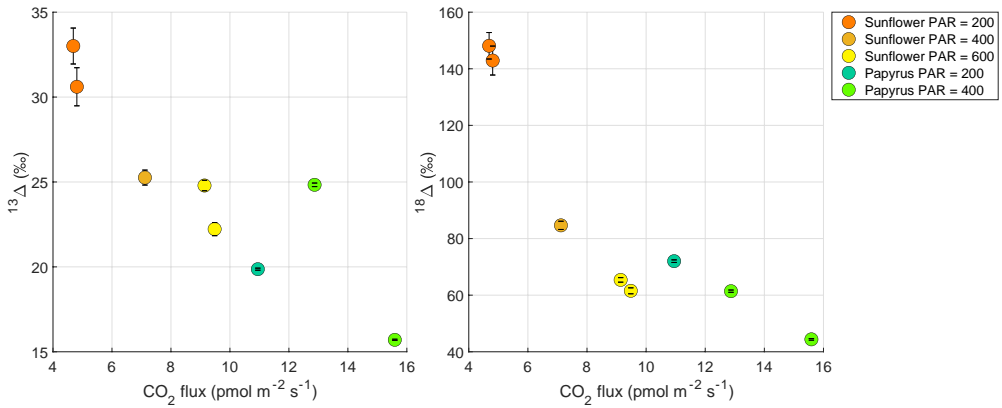
Figure 4.7: CO_2 isotope discrimination factors $^{13}\Delta_{CO_2}$ and $^{18}\Delta_{CO_2}$ (‰) plotted against CO_2 flux (μmol m^{-2} s^{-1}), where the colors indicate the two different plants and the PAR levels (μmol m^{-2} s^{-1}). The samples that were taken in the dark (PAR = 0) are not displayed as there was no net uptake of CO_2 in those conditions, thus there was no CO_2 isotope discrimination to be determined.

ing and late afternoon, when PAR was lowest. Gentsch et al. (2014) calculated a range of $^{13}\Delta_{CO_2}$ between 18 and 29 ‰ for their 2010 experiments, where max PAR was around 1100 μmol m^{-2} s^{-1} in the mid-afternoon. In our experiments, we found a quite large $^{13}\Delta_{CO_2}$ for sunflower at the lowest PAR level (200 μmol m^{-2} s^{-1}) of 33 ‰. Such high $^{13}\Delta_{CO_2}$ are slightly out of the normal expected range, but they can be found at very low CO_2 fluxes. Wingate et al. (2007) also found high $^{13}\Delta_{CO_2}$ of up to 35 ‰ at dawn and dusk during their branch chamber experiments with *Picea sitchensis*. These high $^{13}\Delta_{CO_2}$ values corresponded with low CO_2 assimilation and high c_i/c_a of between 0.8 and 1.

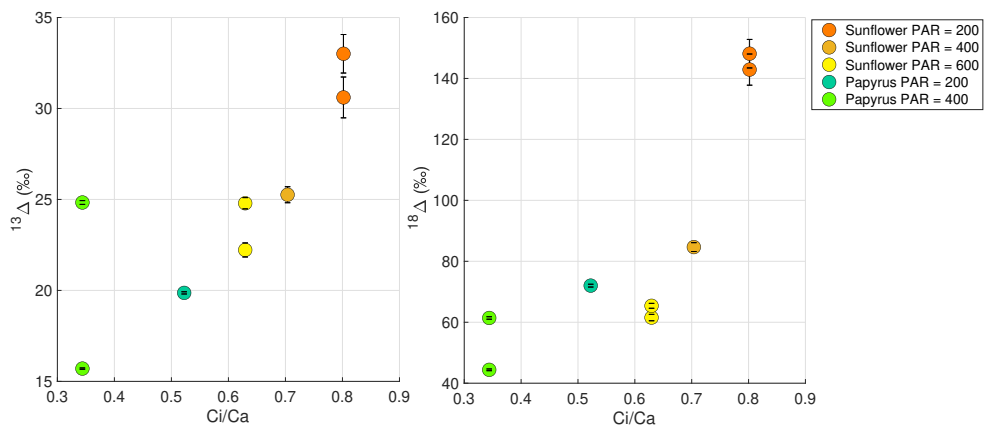Figure 4.8 displays $^{13}\Delta_{CO_2}$ and $^{18}\Delta_{CO_2}$ in ‰ against c_i/c_a, and we can see that the high

Figure 4.8: CO_2 isotope discrimination factors $^{13}\Delta_{CO_2}$ and $^{18}\Delta_{CO_2}$ (‰) plotted against c_i/c_a ratio, which is the ratio of leaf internal CO_2 mole fraction over the ambient CO_2 mole fraction. c_i/c_a was estimated by using the online LI-7000 H_2O measurements.

$^{13}\Delta_{CO_2}$ values also correspond to a c_i/c_a of 0.8.

Some further observations can be made from the correlation between CO_2 isotope discrimination and c_i/c_a. Firstly, as already stated in the previous section (Figure 4.6), we observe that papyrus (C4) generally has a lower c_i/c_a than sunflower (C3), which is what we expected as the CO_2 uptake flux is generally higher for C4 species compared to C3 (Farquhar et al., 1989). Secondly, we observe a trend of higher isotope discrimination with higher c_i/c_a for both CO_2 isotopologues, although with one outlier for papyrus (PAR = 400). The trend of increasing discrimination with increasing c_i/c_a can be explained by the fact that c_i/c_a will increase with decreasing CO_2 flux. Thus, we are seeing the same trend here as in Figure 4.7 where there is an increasing discrimination with lower flux. With low fluxes, c_i is large and fractionation is likely mostly determined by the light-dependent fixation reaction of CO_2 catalyzed by Rubisco.

^{18}O discrimination in CO_2: $^{18}\Delta_{CO_2}$

Looking at Figure 4.7, we observe a negative relationship between $^{18}\Delta_{CO_2}$ and CO_2 flux. The average $^{18}\Delta_{CO_2}$ of sunflower range between 63.5 and 145.5 ‰ and the average $^{18}\Delta_{CO_2}$ of papyrus are between 52.9 and 72.0 ‰ (Table 4.2). Thus, the $^{18}\Delta_{CO_2}$ of papyrus is clearly lower than that of sunflower. As mentioned in the introduction of this chapter, $^{18}\Delta_{CO_2}$ mostly reflects the exchange of ^{18}O between CO_2 and leaf water. The lower $^{18}\Delta_{CO_2}$ in C4 species likely indicates the incomplete equilibrium between CO_2 and leaf water, because of the reduced CA activity in C4 species compared to most C3 species (Gillon and Yakir, 2000).

This negative correlation of $^{18}\Delta_{CO_2}$ with CO_2 assimilation and light intensity, as well as lower $^{18}\Delta_{CO_2}$ in C4 species was also found by Stimler et al. (2011). For their C3 plants, they found an $^{18}\Delta_{CO_2}$ which ranged between around 40 and 240 ‰, where the highest values were found at the lowest CO_2 fluxes. For C4 species, Stimler et al. (2011) found an $^{18}\Delta_{CO_2}$ between 10 and 50 ‰. Seibt et al. (2006) also found large variations in $^{18}\Delta_{CO_2}$ during CO_2 uptake by *Picea sitchensis*, and a correlation with PAR. They too measured the largest ^{18}O$_{CO_2}$ discrimination at dusk and dawn, when light intensity was lowest.

Stimler et al. (2011) additionally found a clear negative correlation between $^{18}\Delta_{CO_2}$ and COS flux, with a larger change in $^{18}\Delta_{CO_2}$ for C3 species, compared to C4. Figure 4.9 shows $^{18}\Delta_{CO_2}$ (‰) against COS flux (pmol m^{-2} s^{-1}) for our data. We do not observe such a strong correlation between $^{18}\Delta_{CO_2}$ and the COS flux. However, our range in COS flux for each species is small, as we found that the COS flux did not change drastically when adjusting the light intensity. In the same range of COS flux data, Stimler et al. (2011) also did not find a strong trend in $^{18}\Delta_{CO_2}$. Thus, our data does not exclude the possibility of such a correlation, however, we do not observe it in the range of data available.
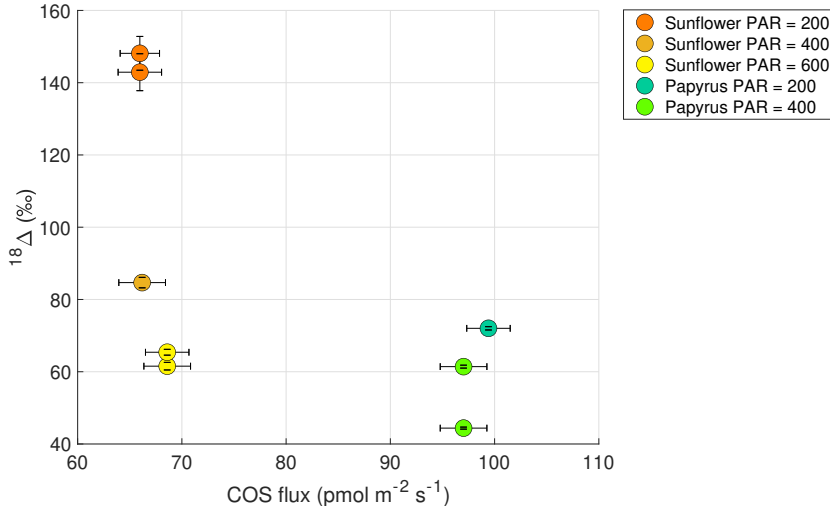
Figure 4.9: $^{18}\Delta_{CO_2}$ (‰) plotted against COS flux in pmol m^{-2} s^{-1} for sunflower (C3) and papyrus (C4)

4.3.3   COS isotopes

As expected, the CO_2 fluxes have shown us that the plants inside the gas exchange chamber were performing photosynthesis in light conditions and were respiring CO_2 in the dark. The COS uptake flux decreased with light, but still continued in the dark, according to expectations. Furthermore, the CO_2 isotope discrimination values for sunflower were in the range of expected values. Together, these results confirm that the plant showed no signs of stress during our experiments. However, as mentioned previously, the carbon isotope discrimination values for CO_2 were higher than we would expect for a C4 plant, which needs to be kept in mind. We will now continue to discuss the COS isotope fractionation values and compare the $^{34}\Delta_{COS}$ results with measurements from previous studies.

The results for the $^{33}S_{COS}$ isotope discrimination values, $^{33}\Delta_{COS}$ can be found in the supplementary material. They are not included in the main discussion as the results for $^{33}\Delta_{COS}$ were in the end deemed possibly unreliable. The data were quite noisy and inconsistent with our main findings for the other isotopologues and with our expectations for isotopic discrimination during plant uptake. This led us to believe that they might have been influenced by measurement errors, possibly introduced by the low peak area of m/z 33 in combination with some instrumental challenges at the time that the samples were measured. The quality of the $^{33}\Delta_{COS}$ data thus need to be further investigated before conclusions can be drawn from them.

Figure 4.10 shows the isotope discrimination values $^{34}\Delta_{COS}$ and $^{13}\Delta_{COS}$ (‰) plotted against the COS flux (pmol m^{-2} s^{-1}), with colors again indicating the different plant species and PAR levels. In contrast to CO_2 isotope discrimination, the COS discrimination values do not show a clear trend with COS flux nor with PAR levels. We also do not see a clear distinction between the two plant species in terms of isotope discrimination. For $^{34}\Delta_{COS}$, we estimated average discrimination values in light conditions between 2.8 and 3.7 ‰ for sunflower and between 2.5 and 2.7 ‰ for papyrus. For $^{13}\Delta_{COS}$ there is a large spread in the
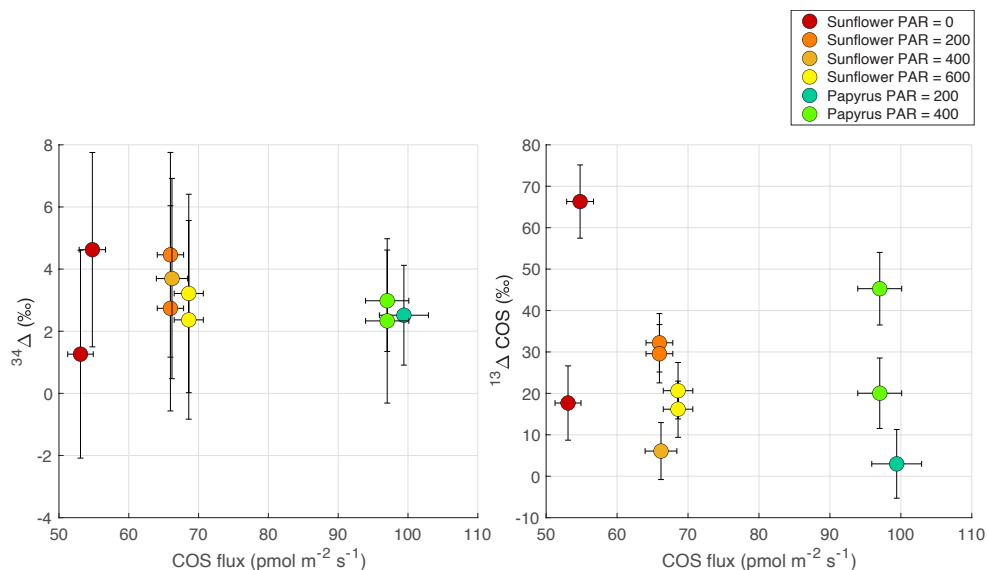
Figure 4.10: COS isotope discrimination factors $^{34}\Delta_{COS}$ and $^{13}\Delta_{COS}$ (‰) plotted against COS flux from the QCLS measurements(μmol m^{-2} s^{-1}), where the colors again indicate the two different plants and the PAR levels (μmol m^{-2} s^{-1}).

estimated fractionation values. We found average discrimination values between 6.1 and 30.9 ‰ in light conditions for sunflower and between 3.0 and 32.7 ‰ for papyrus. These values and their corresponding errors are also all summarized in Table 4.2.

Figure 4.11 shows the COS isotope discrimination values $^{34}\Delta_{COS}$ and $^{13}\Delta_{COS}$, plotted against each other. No correlation can be observed between the two COS isotope discrimination values. Additionally, the data for sunflower and papyrus are all clustered together, indicating no clear difference in COS isotope discrimination between the two plant species, which was against our expectations (Davidson et al., 2022).

The fact that $^{13}\Delta_{COS}$ displays quite a large spread and that the values do not seem to be clearly correlated with $^{34}\Delta_{COS}$ may suggest that there are other processes influencing the $^{13}C_{COS}$ fractionation than the fractionation of the sulfur isotopologues. The interaction of CA with the COS molecules and the way the molecule breaks up during the hydrolysis reaction (Angeli et al., 2020) may influence the isotopic fractionation during this reaction. Furthermore, if there is some reversibility of the reaction, and back diffusion of COS through the stomata, the pool of carbon inside of the leaves may influence the apparent COS carbon isotope fractionation.

However, we have not yet calibrated our $\delta^{13}C_{COS}$ measurements against the international standard, which would be needed to investigate the isotopic signal of the carbon pool inside the plant. Yet, these are the first measurement results of $^{13}C_{COS}$ discrimination for plant uptake and the values are much larger compared to the sulfur discrimination values, which may potentially provide additional information on chemical processes inside the leaf. Thus, additional measurement data of $^{13}\Delta_{COS}$ during plant uptake, and calibration efforts of these $\delta^{13}C_{COS}$ measurements would be useful to further investigate the pathways of COS plant uptake.
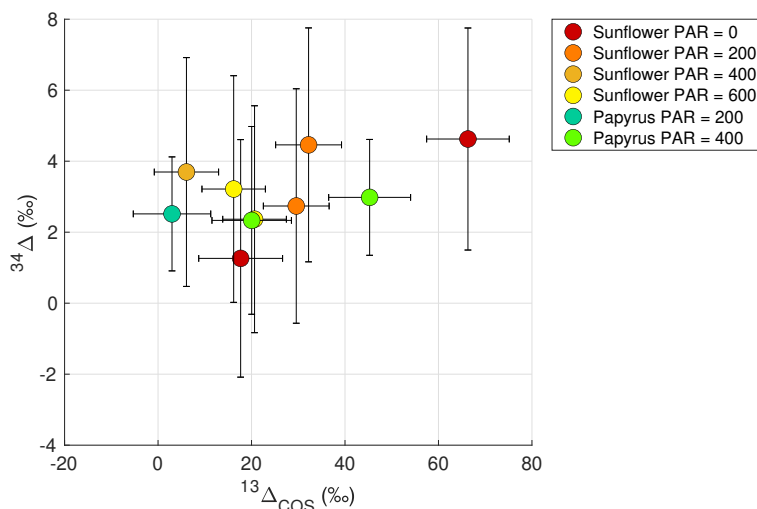
Figure 4.11: $^{34}\Delta_{COS}$ (‰) plotted against $^{13}\Delta_{COS}$ (‰), where the colors again indicate the two different plants and the PAR levels (μmol m^{-2} s^{-1}).

Comparing ^{34}S discrimination to previous studies

As can be seen in table 4.2, the ^{34}S$_{COS}$ discrimination values, $^{34}\Delta_{COS}$, for sunflower in light conditions (PAR > 0) vary between 2.8 and 3.7 ‰, with an error between 0.6 and 1.2 ‰. For papyrus, $^{34}\Delta_{COS}$ ranges between 2.5 and 2.7 ‰, with an error of around 0.4 ‰. Therefore, based on these data, we cannot say that the $^{34}\Delta_{COS}$ values for these species are significantly different. Nevertheless, they are in the range of values which we would expect from previous studies.

As mentioned before, Angert et al. (2019) theoretically estimated an overall plant fractionation factor $^{34}\Delta_{COS}$ of around 5 ‰ and experiments presented by Davidson et al. (2021) and Davidson et al. (2022) yielded fractionation values ($^{34}\Delta_{COS}$) of 1.6 ± 0.1 ‰ and 5.4 ± 0.5 ‰ for C3 and C4 species, respectively. These are the only studies on COS isotope fractionation during plant uptake that have been conducted to date. It is reassuring to find that the experiments by Davidson et al. (2022) and our experiments yield roughly the same fractionation factors, even though both the experimental set-up and the calculation procedure of the fractionation factors differed substantially between the our study and that of Davidson et al. (2022). Our method used a flow-through gas exchange chamber, whereas Davidson et al. (2022) used a static-chamber, which was closed for up to five hours for one experiment.

The benefits of using a flow-through system are that one can control the incoming and outgoing air and ensure stable environmental conditions inside the chamber. For isotope fractionation experiments, it is important to ensure steady-state conditions when sampling. However, when closing a chamber for prolonged periods, continued transpiration by the plant will increase the water vapor mole fraction in the chamber, which might affect stomatal opening and therefore also the isotope fractionation. Furthermore, in a flow-through system, CO_2 mole fraction inside the chamber is kept relatively constant, whereas in a closed

chamber, CO_2 mole fraction will gradually decrease as the plant continues to perform photo-synthesis. Thus, it is easier to keep the plant's conditions relatively stable and also monitor these conditions in a gas-exchange system compared to a closed-chamber system.

Another difference between our experiments and those of Davidson et al. (2022) was the light level, which was kept at 15.7 μmol m^{-2} s^{-1} inside the chamber during the experiments by Davidson et al. (2022), while in our experiments the light level was higher. However, we only measured the light level just above the chamber and not inside the chamber, close to the leaves. Thus, the actual light level inside the chamber could have been slightly lower during most of our experiments, although probably still higher than 15.7 μmol m^{-2} s^{-1}.

4.3.4 Limitations and outlook

This section lists some limitations and caveats of our study and provides suggestions on how we could make improvements for future experiments.

Firstly, some of the errors on the isotope fractionation estimates currently presented are rather large, which is due to the measurement precision and the magnitude of observed dis-crimination. More experiments using the same species would be useful to better constrain these values. A series of additional experiments using the same gas exchange system has actually been conducted in the fall of 2022. However, technical difficulties and time con-straints have hampered the inclusion of these measurements in this chapter. Increasing the precision on the COS isotope fractionation values will also help us to better estimate the dif-ferences between C3 and C4 species. However, if one wishes to fully partition the diffusion and enzymatic isotope fractionation, it would be best to conduct experiments with isolated carbonic anhydrase.

While we took care to ensure the best and most stable conditions for the plants inside the gas exchange chamber, some conditions could have still led to a change in the plant's behavior compared to natural field conditions. Firstly, we used higher than ambient mole fractions of COS in the in-going air of the chamber of around 2 ppb. This was done in order to ensure high enough COS mole fractions in the samples taken for COS isotope analysis, after uptake by the plant. In order to obtain enough precision, we still needed around atmo-spheric mole fractions of COS of around 500 ppt after diluting the samples. Additionally, our measurements required sufficient COS decrease in the chamber due to plant uptake in order to quantify the isotopic fractionation. In order to meet these measurement requirements, an initial COS mole fraction of around 2 ppb was needed.

Although it is not entirely known why plants assimilate COS and how they integrate sulfur into their tissue, Stimler et al. (2012) did find that increasing COS mole fractions in chamber experiments lead to an increase in stomatal conductance, which seemed to have been mediated by CA. Thus, using a higher than ambient mole fraction of COS in our ex-periments could have affected stomatal conductance. Yet, Stimler et al. (2012) did not find any relationship between the sensitivity of stomatal conductance to COS mole fractions and the COS assimilation rate. During our experiments, there was little change in COS isotope fractionation between the different light settings, which suggests that the reaction with CA likely more rate-limiting than the stomatal pore opening.

For future experiments it would be recommended to conduct experiments with both high and ambient initial COS mole fractions in the chamber. Davidson et al. (2022) did conduct experiments using different initial mole fractions of COS. However, they simultaneously

varied the initial CO_2 mole fraction, which makes it difficult to isolate the effects of both gases.

To be able to assess the extent of isotopic exchange between CO_2 and the leaf water, it would have been useful to have the $\delta^{18}O_{CO_2}$ isotopic composition of the leaf water. However, as the main purpose was to estimate the isotopic fractionation of COS during plant uptake, this was not the focus of our experimental plan. The CO_2 isotope measurements and estimated fractionation factors were mainly used to assess whether the plant was displaying normal behavior or was exhibiting any signs of stress. This was done in order to evaluate whether the measured COS isotope fractionation factors would be representative of a plant in its natural environment.

Unfortunately, the results from our $\delta^{33}S_{COS}$ measurements and thus the calculated $^{33}\Delta_{COS}$ values, were deemed likely unreliable. The addition of these measurements would have been useful in further understanding the sulfur isotopic fractionation during plant uptake. Thus, if possible, for future experiments, it would be good to improve the measurements of $\delta^{33}S_{COS}$ for COS and include them in the dataset. However, as no other measurements of $^{33}\Delta_{COS}$ during COS plant uptake exist up to this date, the $^{34}\Delta_{COS}$ data provide more valuable information at this moment.

One last limitation of our study is the fact that our $\delta^{13}C_{COS}$ measurements of COS are not calibrated to the international scale yet. This makes these values difficult to compare with the (respired) $\delta^{13}C_{CO_2}$ from plants and makes it also difficult to compare to other (future) studies. Nevertheless, we can still estimate fractionation factors for $^{13}C_{COS}$, as these calculations do not require the δ values to be on the international scale.

4.4   Conclusion

This chapter presented measurements of COS and CO_2 fluxes and isotope discrimination factors $^{13}\Delta_{CO_2}$ and $^{18}\Delta_{CO_2}$, and $^{13}\Delta_{COS}$ and $^{34}\Delta_{COS}$ of COS, for sunflower (C3) and papyrus (C4). The experiments were conducted using a flow-through gas exchange system, which was a new and different method compared to previously reported measurements of COS isotope fractionation during plant uptake (Davidson et al., 2021; Davidson et al., 2022). The gas exchange system including the QCLS and LI-7000 instruments ensured stable chamber conditions, which were easy to monitor throughout the experiments. Despite using such a different experimental set-up and a different way to calculate the isotopic discrimination (Evans et al., 1986), our results for $^{34}\Delta_{COS}$ still matched the previously reported values by Davidson et al. (2022) relatively well. Furthermore, the work presented in this chapter is the first study to combine measurements of both CO_2 and COS isotopologues, where the CO_2 isotope discrimination values provided additional information on the plant's behavior and their reactions to environmental conditions. The currently presented dataset is to be expanded with additional measurements from experiments using the same gas exchange system, in order to better constrain the estimated isotope fractionation values.

4.5   Supplementary material

4.5.1   Error propagation of the $\triangle$ values

Error propagation for the isotope discrimination ($\triangle$) was done using the equations below, which can be traced back to the calculations of the $\triangle$ values based on the approach by Evans et al. (1986) described in Equations 4.2.6, 4.2.7:

$$\sigma_\xi = \left| \frac{c_{in}}{c_{in} - c_{out}} \right| \sqrt{\left(\frac{\sigma_{c_{in}}}{c_{in}} \right)^2 + \left(\frac{\sigma_{c_{in}-c_{out}}}{c_{in} - c_{out}} \right)^2},$$

(4.5.1)

$$\sigma_{c_{in}-c_{out}} = \sqrt{\sigma_{c_{in}}^2 + \sigma_{c_{out}}^2},$$

(4.5.2)

and

$$\sigma_\triangle = |\triangle| \sqrt{\left(\frac{\sigma_{\xi(\delta_{out}-\delta_{in})}}{\xi(\delta_{out} - \delta_{in})} \right)^2 + \left(\frac{\sigma_{\delta_{out}-\xi(\delta_{out}-)}}{1000 + \delta_{out} - \xi(\delta_{out} - \delta_{in})} \right)^2},$$

(4.5.3)

where:

$$\sigma_{\xi(\delta_{out}-\delta_{in})} = \left| \xi(\delta_{out} - \delta_{in}) \right| \sqrt{\left(\frac{\sigma_\xi}{\xi} \right)^2 + \left(\frac{\sigma_{\delta_{out}-\delta_{in}}}{\delta_{out} - \delta_{in}} \right)^2}$$

(4.5.4)

and

$$\sigma_{\delta_{out}-\delta_{in}} = \sqrt{\sigma_{\delta_{out}}^2 + \sigma_{\delta_{in}}^2}$$

(4.5.5)

4.5.2 $^{33}\Delta_{\text{COS}}$ against COS flux
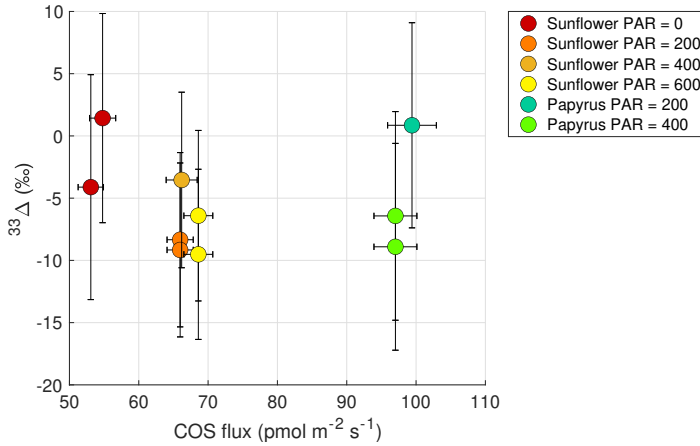
Figure 4.12: ^{33}S isotope fractionation values, $^{33}\Delta_{\text{COS}}$ (‰), plotted against COS flux (pmol m^{-2} s^{-1})

4.5.3 $^{33}\Delta_{\text{COS}}$ against $^{13}\Delta_{\text{COS}}$ and $^{34}\Delta_{\text{COS}}$ against $^{33}\Delta_{\text{COS}}$
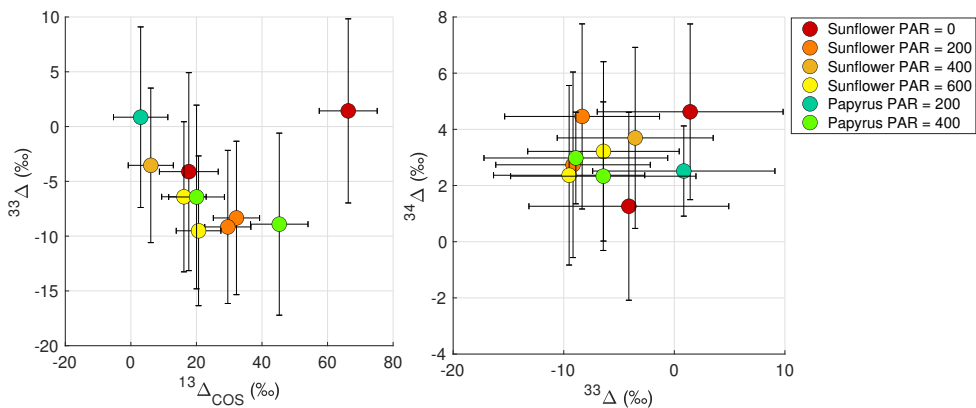
Figure 4.13: ^{33}S isotope fractionation values, $^{33}\Delta_{\text{COS}}$ against $^{13}\Delta_{\text{COS}}$ and $^{34}\Delta_{\text{COS}}$ against $^{33}\Delta_{\text{COS}}$. All values are in ‰

4.5.4 CO$_2$ and COS isotope discrimination values against each other
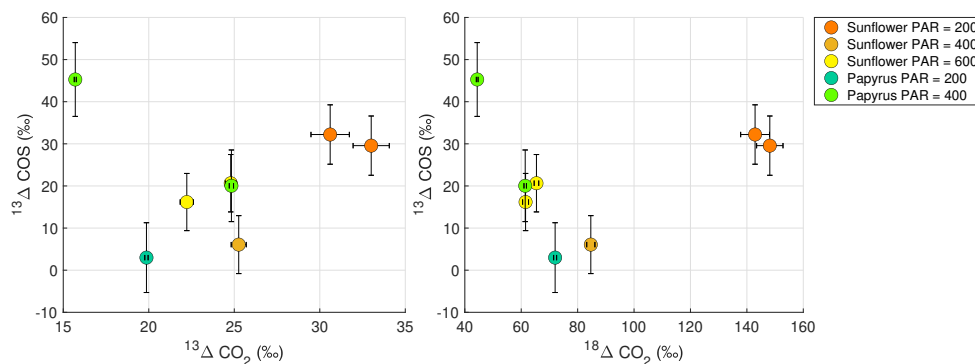
Figure 4.14: Left figure: $^{13}\Delta_{COS}$ (‰) plotted against $^{13}\Delta_{CO_2}$(‰), right figure: $^{13}\Delta_{COS}$ (‰) plotted against $^{18}\Delta_{CO_2}$(‰)
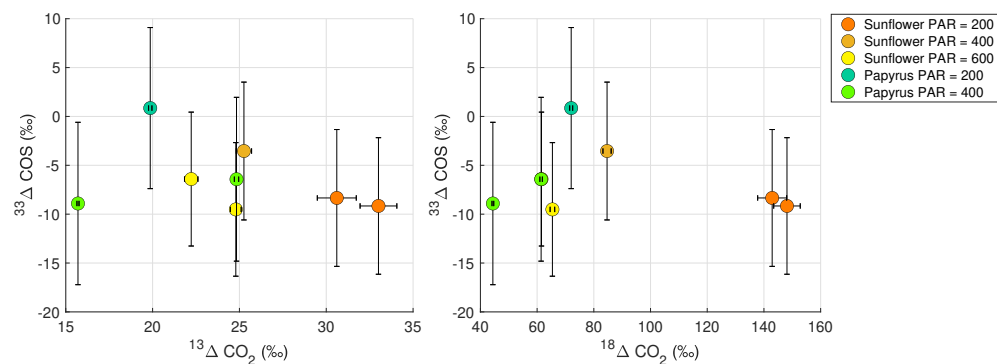
Figure 4.15: Left figure: $^{33}\Delta_{COS}$ (‰) plotted against $^{13}\Delta_{CO_2}$(‰), right figure: $^{33}\Delta_{COS}$ (‰) plotted against $^{18}\Delta_{CO_2}$(‰)
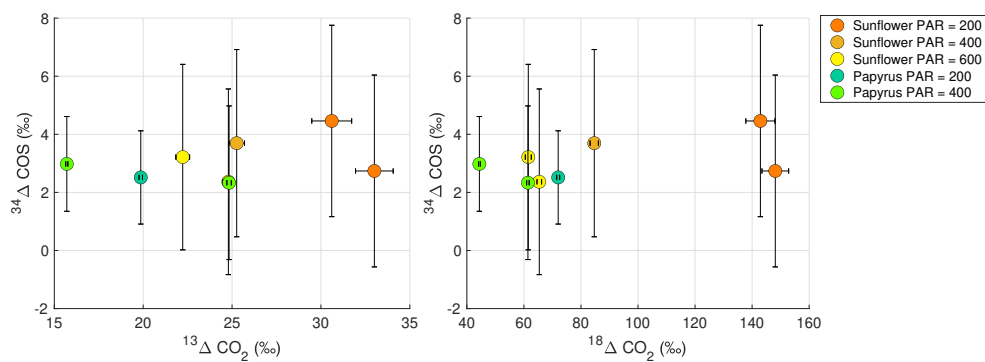
Figure 4.16: Left figure: $^{34}\Delta_{COS}$ (‰) plotted against $^{13}\Delta_{CO_2}$(‰), right figure: $^{34}\Delta_{COS}$ (‰) plotted against $^{18}\Delta_{CO_2}$(‰)

5

Synthesis & outlook

During the project described in this thesis, a system for measuring isotopologues of carbonyl sulfide was developed and used to measure a wide array of samples, ranging from tropospheric ambient air to stratospheric air and including samples taken during plant uptake experiments. The overarching aim of this research was to increase the amount of data and knowledge on COS isotopes, including source signatures, ambient tropospheric composition, and isotope fractionation processes occurring both in the stratosphere and in the biosphere. This knowledge will contribute to understanding the COS budget, which will help to eventually use COS as a proxy for GPP. Furthermore, knowledge on stratospheric COS fractionation will help to answer questions on the contribution of COS to stratospheric sulfur aerosols (SSA). This chapter summarizes the findings described in this thesis and provides an outlook for future COS isotope measurements and applications.

5.1 Research questions

The research questions of this thesis, as stated in the Introduction (Chapter 1), are again provided below and will be addressed in the following sections.

1. Is it possible to measure COS isotopologues in a way that is usable for advancing the understanding of the global COS cycle i.e.

    (a) with a precision that is good enough to distinguish between sources, and to observe atmospheric variations in time and space?

    (b) from air samples small enough (several L) to allow collecting samples globally, including in situations where the sampled air is limited, like firn, ice, stratosphere, or small-scale lab experiments?

2. How can isotope measurements contribute to understanding the COS budget?

3. How uniform is the tropospheric ambient isotopic composition of COS?

    (a) How much is the tropospheric isotopic composition influenced by local sources?

    (b) Can we distinguish the influences of different sinks and sources by measuring the ambient tropospheric isotopic composition of COS?

4. Is COS the main source of background stratospheric sulfur aerosols (SSA), during volcanically quiet times and can we determine this by using isotope measurements of COS in the stratosphere?

    (a) What are the total isotope fractionation factors of the different COS isotopologues, $CO^{33}S$, $CO^{34}S$ and ^{13}COS, in the stratosphere?

    (b) How do these COS fractionation factors compare with previous estimates from lab experiments and remote sensing studies?

    (c) Is the ^{34}S fractionation factor, $^{34}\varepsilon$, observed in the stratosphere compatible with COS being the main source of SSA?

5. What is the COS isotopic fractionation during plant uptake?

    (a) How does the isotope fractionation differ between C3 and C4 species?

    (b) How does the isotope fractionation vary with changing ambient conditions (e.g. light availability)?

5.2 COS isotope measurement techniques

During the time-span of this thesis, we developed a new system to measure both sulfur and carbon isotopologues of carbonyl sulfide from small whole-air samples, and with sufficient precision to detect variations in COS isotopic composition. As these COS isotope measurements are very challenging, there are currently only two other groups that perform these measurements and they are only measuring the sulfur isotopologues. One of these measurement systems was developed in Japan (Hattori et al., 2015)

and is similar to our system as it also uses a pre-concentration system coupled to a gas-chromatograph column and an isotope ratio mass spectrometer (IRMS). This system, however, requires large quantities of air (hundreds of liters) for one sample measurement. They did develop a sampler that pre-concentrates COS from air, which could be deployed in the field (Kamezaki et al., 2019). However, processing such large quantities of air without COS losses and associated isotope fractionation is difficult. Furthermore, in many sampling situations (e.g. stratosphere) it is almost impossible to sample such large quantities of air.

The other system that currently exists for measuring sulfur isotopologues of COS was developed in Israel by Angert et al. (2019) and uses an inductively coupled plasma mass spectrometer (IC-PMS), which yields high resolution results, but is quite expensive in acquisition and use. Our IRMS-based system uses the same principle and techniques as Hattori et al. (2015), but was developed to measure small air samples of around 3 - 6 L of air and yields only slightly lower precision than both other systems, as described in detail in Chapter 2 of this thesis.

The advantage of our measurement system lies in the ability to measure such small samples, as this allows for easier sampling (smaller canisters, less sampling time), faster measurements and the possibility to sample where obtaining large quantities of air is difficult. For instance, we were able to measure stratospheric samples taken on board of the Geophysica airplane during the StratoClim AMA-17 campaign, as described in Chapter 3. These samples were taken in 2 L canisters, pressurized up to around 3 - 4 bar and we were even able to measure some of them twice. During the plant chamber experiments (Chapter 4), taking relatively small samples allowed us to use a low-flow procedure that did not affect the pressure inside the chamber, with the sampling being still fast enough for the conditions inside the chamber and the plant behavior to be constant during sampling.

Furthermore, this thesis includes the first measurements of $\delta^{13}C$ from COS. The work presented does not only demonstrate the possibility of measuring $\delta^{13}C$, but also shows that these measurements can provide additional information. For the stratosphere, we measured fractionation in ^{13}C that was of similar magnitude as the ^{34}S fractionation, which was an unexpected result. Furthermore, ^{13}C fractionation during plant uptake was larger than ^{34}S fractionation, which may yield additional information about plant physiology.

Thus, with our work, we have demonstrated the possibility and benefits of being able to measure COS isotopologues from small air samples. I hope that the development of our system can inspire other scientists to develop such measurement systems so that the network of COS isotope measurements will be expanded and more data will become available. As the first systems measuring COS isotopologues were only recently developed, not much data is currently available. Nevertheless, this data scarcity provides many opportunities for new discoveries to be made in this field.

One challenge that still remains is the calibration of the COS isotope measurements. At this moment, our sulfur isotope ratio measurements are calibrated on the VCDT scale, using the same calibration gases as described in Hattori et al. (2015) and Kamezaki et al. (2019). The COS sulfur isotope measurements performed by the other lab in Israel (Angert et al., 2019; Davidson et al., 2021; Davidson et al., 2022) are also calibrated on the VCDT international scale using their own calibration gases. However, up to this date, no cross-calibration has been performed between the labs in Japan, Utrecht and Israel. In order to accurately compare the measurements across these labs, it is important to conduct such cross-calibration. Otherwise, small differences in measurement results of for instance ambient COS isotopic

composition between different locations (measured by the different labs) might be falsely attributed to natural variability, whereas they might actually be caused by differences in the calibration scale. Furthermore, our carbon isotope ratio measurements from COS have not been calibrated to the international VPDB scale yet. For now, the reported carbon isotope ratios in this thesis are still only measured against our reference gas in Utrecht. Therefore, only gradients and fractionation factors can be used from these data, and not the absolute values. For future measurements, it is important to calibrate these measurements as well.

Note on the δ^{33}S measurements

In this thesis I have presented δ^{33}S, δ^{34}S and δ^{13}C measurements of COS. The δ^{33}S measurement results, however, were not much emphasized, and in Chapter 4 they were taken out of the main results entirely. The reason is that we sometimes obtained contradicting results from the δ^{33}S measurements, which could be due to measurement artifacts. For instance, we considered the derived fractionation values for ^{33}S with an opposite sign compared to the ^{34}S signal not plausible. Since we consider it important to still report these findings, we provide some possible reasons for the anomalous behaviour of the δ^{33}S signals below.

Firstly, the calibration procedure for δ^{33}S was based on one calibrated gas, from which δ^{33}S of the other calibration gases were derived (see Chapter 2). Therefore, the calibration of δ^{33}S is less solid than that of the δ^{34}S measurements. Secondly, the peak area of m/z 33 is very small and most baseline disturbances, and therefore possible overlapping of peaks from other species, were found on this same m/z 33 (see Figure 2.2). Thus, the quality of the δ^{33}S results of the measurements had to be assessed individually. Furthermore, as can be seen in Figure 2.6, the day-to-day and longer-term variability in δ^{33}S, when measuring the same target gas, is much larger than that of δ^{34}S. The error of around 2.5 ‰, provided for single measurements of the δ^{33}S was obtained by measuring certain target gases a number of times in sequence and calculating the standard error of these measurements, as explained in Chapter 2. The longer-term variability of the δ^{33}S measurements from the same gas was, however, often larger than this error.

All together, these uncertainties led us to believe that for δ^{33}S, only large deviations from the normal expected values would likely be trustworthy and that smaller variability would probably not always be the result of actual processes but could be caused by variability in the measurement system itself. However, we did present the δ^{33}S results of measurements that were most likely not affected by any overlapping peaks, as δ^{33}S can still provide additional information next to the other COS isotopologues.

From the data presented in Chapter 4, we derived ^{33}S fractionation values during plant uptake that we did not expect from normal mass-dependent isotope processes. However, since the fractionation values were quite small, they could have been caused by the above-mentioned measurement issues, rather than actual fractionation processes during plant uptake. Therefore, we did not include these measurements in the main results of this chapter, but they are included in the supplementary material of this chapter.

For the stratospheric measurements presented in Chapter 3, the δ^{33}S values are included, since the variability in these results was in the expected range and did not display any large deviations outside of the measurement errors. Nevertheless, also in this chapter, we put more emphasis the δ^{34}S results, because we trusted those measurements more and because more data exists of δ^{34}S from COS, to compare our data with.

The other groups measuring COS isotopologues do not report δ^{33}S at all, with the exception of one ambient air measurement presented by Hattori et al. (2015), which shows the difficulties in interpreting the δ^{33}S results. Yet, improving the measurements of δ^{33}S from COS would be useful as these data could provide additional information on fractionation processes, as well as provide further constraints on COS isotopic source signatures.

5.3   Isotope measurements and the COS budget

One of the main objectives, and the second research question of this thesis, was providing COS isotope measurements to help understand the COS budget. On a small scale, isotope measurements can contribute to identifying sources when observing an increase in COS above the ambient mole fraction, by making a Keeling plot and comparing the obtained signature to known isotope signatures. Another important way in which isotope knowledge can contribute to characterizing the COS budget is by using the combination of measurements and modeling. Next to mole fraction observations, measurements of isotope source and sink signatures and ambient isotopic composition can provide additional constraints to the contribution of these sources and sinks to the overall budget.

One large uncertainty in the COS budget is the contribution of anthropogenic sources and their locations. Zumkehr et al. (2018) made an inventory of anthropogenic emissions, but some of the large point sources included in this inventory have since then been questioned (Belviso et al., 2023). Furthermore, it is possible that some anthropogenic sources are still missing in this inventory (Zanchetta et al., 2023).

One way in which this work has contributed to characterizing sources of COS was by investigating the amount of COS in car exhausts and by measuring its isotopic composition. These measurements of air sampled inside a highway tunnel in Utrecht, as outlined in Chapter 2, have shown that the amount of COS in West-European car exhaust is probably quite low. The sulfur isotope ratios for COS from car exhaust were depleted with respect to background air, with δ^{33}S = −71.2 ± 21.2 and δ^{34}S = 6.9 ± 4.7 ‰. However, the vehicles being such a small source, these depleted isotope ratios will likely have a negligible effect on the overall COS isotopic composition in the Netherlands, and possibly the rest of Western Europe. In large, modern urbanized areas, industries are the major source of COS (and the precursor CS_2), and likely contribute more to the atmospheric isotopic composition of COS in those regions.

Zanchetta et al. (2023) measured COS mole fractions in the province of Groningen, in the north of the Netherlands, both at the ICOS Lutjewad tower (ICOS, n.d.), and with mobile measurements using a QCLS, installed in a van. From the Lutjewad tower data, they identified both local and regional emissions of COS. The local emissions were attributed to nearby industries involving coal and aluminum processing, sugar production and the production of silicon carbide. With their mobile QCLS measurements, they observed COS mole fractions of up to almost 7 ppb while driving down-wind of one of the industrial areas, which illustrates the relevance of local anthropogenic point sources.

In the Chapter 2, I presented a dataset of the ambient COS isotopic composition in Utrecht over the course of several months. During this period, one event occurred, during which heavily polluted air from a large industrial area in Germany (the Ruhr area) was measured in Utrecht. During this event, we observed increased CH_4 and CO_2 mole fractions,

while no significant increase in COS mole fraction was observed. This lead us to conclude that this industrial area likely does not emit as much COS as we initially suspected, and which is also included in the inventory of Zumkehr et al. (2018). We also did not observe any deviations from the background ambient COS isotopic composition during this measurement period. Zanchetta et al. (2023), however, did find elevated COS mole fractions at Lutjewad when the air was coming from this same German region. Thus, this needs to be further investigated.

The measurements described above illustrate how we can use the combination of COS mole fraction and isotope measurements to further constrain anthropogenic sources of COS and their influence on local ambient COS, by using Keeling plots to find the isotopic signature of sources and by using a time-series of COS mole fractions and isotopic composition to investigate the influence of anthropogenic sources on the overall ambient tropospheric COS. However, during our observations, we did not find many large anthropogenic sources. For future work, it would be useful to actively pinpoint anthropogenic sources and sample the air coming from those sources and measure its COS isotopic composition. One way to do this would be to conduct a study mobile measurement study with a QCLS, like conducted by Zanchetta et al. (2023), and additionally collect samples for COS isotope analysis once anthropogenic sources have been located. One of such studies has actually already been conducted by us in 2022 in Groningen. However, only one large COS source was identified during that short campaign, and the samples from this source are still to be measured.

Another important isotope effect regarding anthropogenic emissions, that has not been studied, is the isotopic composition of CS_2 and the isotope fractionation during oxidation of CS_2 to form COS (Zeng et al., 2017). By characterizing the isotopic fingerprint of indirect anthropogenic COS emissions through CS_2, the overall isotopic signature of anthropogenic COS could be further constrained. Such CS_2 oxidation experiments could be conducted in the lab using a reaction chamber.

The largest sink of COS is terrestrial uptake by the biosphere. Isotope measurements can help characterize this sink and constrain its contribution to the overall budget. Chapter 4 of this thesis went into depth on the isotope fractionation during plant uptake and a later section of this synthesis chapter will summarize these results.

A much smaller COS sink is destruction in the stratosphere, where it contributes to the formation of sulfate aerosol. This destruction pathway was discussed in Chapter 3 of this thesis. The next section describes the implication of the results in more detail.

One source of COS that has not been touched upon during the scope of this research is biomass burning. Stinecipher et al. (2019) already found that biomass burning is only a minor source of COS and is therefore likely not the missing source of COS. Nevertheless, it would be useful to investigate this source further and to characterize the isotopic composition of COS from biomass burning in order to be able to recognize it in the future. Additionally, large biomass burning events emitting COS and occurring close to the equator could have an effect on stratospheric COS as it would be efficiently transported into the stratosphere by upward motion of the Brewer-Dobson circulation.

Furthermore, a recent inventory by Andreae (2019) found that biofuel emissions, including burning of dung, are actually likely a more significant source of COS than biomass burning. Thus, the isotopic fingerprint of those emissions is also potentially interesting to investigate.

One of the latest studies on locating missing sources and sinks was performed by Ma

et al. (2021). Their inverse modeling exercises pointed to missing sources in the tropics and missing sinks at higher latitudes. Especially in the tropics, observations are scarce, thus efforts should focus on gathering new measurement data there. One of the main findings of the study by Ma et al. (2021) is that with the scarce observations available, it is difficult to pinpoint the missing tropical source. On the one hand, the source could come from tropical oceans in the form of CS_2 or DMS. Recent findings identified a potential COS precursor that is formed in DMS oxidation, called hydroperoxymethyl thioformate (HPMTF), which could yield higher tropical ocean fluxes than previously predicted (Veres et al., 2020; Jernigan et al., 2022). On the other hand, COS uptake by the tropical biosphere could be smaller then predicted by biosphere models, as recently suggested by Stinecipher et al. (2022). Combining mole fraction and isotope measurements might help to better distinguish between sources like ocean sources and biomass burning and COS sinks, especially in areas like the tropics, where large uncertainties persist.

Ma et al. (2021), Sun et al. (2018), Meredith et al. (2019) and Spielmann et al. (2020) emphasized the lack of data on soil-atmosphere COS exchange. In a recent modeling study by Abadie et al. (2022), soil fluxes were implemented in the ORCHIDEE model. They found that net soil COS fluxes are small and the incorporation of soils only marginally improved the latitudinal gradients of COS. They therefore concluded that improving the representation of soil fluxes in models is likely not going to solve the issue of missing sources and sinks of COS, and that the COS budget is dominated by larger fluxes from plants, oceans and industrial activities. Another modeling study on soil COS fluxes by Whelan et al. (2022) also concluded that COS exchange by soils is not large enough to explain the missing source of COS. They did, however, find that there might be larger local point sources of COS consisting of agricultural soils. Whelan et al. (2022) advised to focus observations on soil fluxes in the tropics and arctic, where the largest uncertainties exist.

5.3.1 Ambient tropospheric composition

The third research question touched on how uniform the tropospheric ambient isotopic composition of COS is. To answer this question, we can look at the ambient air measurement data in Utrecht, presented in Chapter 2. In this chapter, a comparison of our measurements in Utrecht with previous measurements of ambient background air in Japan, Israel and the Canary Islands was discussed (Hattori et al., 2015; Angert et al., 2019; Kamezaki et al., 2019; Hattori et al., 2020; Davidson et al., 2021). In Utrecht, we found slightly higher background $\delta^{34}S$ values compared to the previously reported values. Furthermore, we did not find any high COS mole fraction events during our measurement period in Utrecht. We explained these observations by the likely absence of large anthropogenic COS sources in this region. Additional possibilities could be a larger influence of biosphere uptake, which would enrich COS in ^{34}S, or the influence of oceanic sources, which also have a higher than background $\delta^{34}S$ value.

Nevertheless, the differences in $\delta^{34}S$ values between the different measured locations across the globe are only on the magnitude of a few ‰. The tropospheric values found during the StratoClim 2017 campaign in Nepal and the KLIMAT 2021 campaign in Northern Sweden (Chapter 3) are also quite similar to the tropospheric values in Utrecht and the measurements reported by previous studies (Hattori et al., 2015; Angert et al., 2019; Kamezaki et al., 2019; Hattori et al., 2020; Davidson et al., 2021). **Therefore, we can conclude with**

the observations available to us right now that the tropospheric isotopic composition, δ^{34}S, in the Northern Hemisphere appears to be relatively uniform. Only in Japan, lower δ^{34}S values of around 13 ‰ were found, which were attributed to the higher contribution of anthropogenic emissions that region, which likely have lower δ^{34}S values (Hattori et al., 2020). However, measurements have only been performed in a limited amount of regions, which were almost all located in the Northern Hemisphere, with Davidson et al. (2021) presenting a single data point in the Southern Hemisphere.

Therefore, to answer this research question, more observations from different locations are needed, especially in the Southern Hemisphere and the tropics, but also at higher latitudes in the Northern Hemisphere. Moreover, isotopic signatures of the various COS emission sources and the COS sink processes need to be better characterized, to assess their contribution to tropospheric background values and to the seasonal cycle of COS.

5.4   Stratosphere

The fourth research question was whether COS is the main source of stratospheric sulfur aerosols (SSA), which reflect incoming solar radiation and thereby cool the planet. This question was addressed in Chapter 3 by looking at the fractionation of COS during destruction in the stratosphere and by comparing the measurements with the sulfur isotopic composition of SSA found by Castleman et al. (1974). Unfortunately, the samples from the KLIMAT 2021 balloon campaign were possibly drifting or contaminated. However, we also measured samples from the StratoClim 2017 Geophysica aircraft campaign, which delivered useful data. From these measurements, we estimated a relatively small, negative fractionation factor $^{34}\varepsilon$, which agreed quite well with previous experimental lab studies (Lin et al., 2011; Hattori et al., 2011; Schmidt et al., 2012b; Schmidt et al., 2013), but did not agree with the much larger fractionation estimates from remote-sensing studies (Leung et al., 2002; Colussi et al., 2004).

The ^{13}C fractionation factors, $^{13}\varepsilon$, that we found in the stratosphere for the KLIMAT 2021 campaign were much smaller than we expected from previous studies. However, as mentioned before, we are not sure if we can trust the data from this campaign, thus more data for stratospheric ^{13}C fractionation is needed to confirm these findings.

Simulations with the TM5 model, which was expanded with a COS isotope module, were able to capture the strong atmospheric updraft in the Asian Monsoon Anticyclone (AMA) during StratoClim 2017. Implementing a small negative photolysis fractionation in the model produced results that were roughly in agreement with the observations. The TM5 simulations also showed that much of the prescribed photolysis fractionation signal is diluted in the lower stratosphere because of mixing and transport, as we for instance only observed an apparent overall $^{34}\varepsilon$ of −3.3 ‰ in the lower stratosphere, with a model input $^{34}\varepsilon$ for photolysis of around −10 ‰. Thus, even if the fractionation during photolysis is quite strong, we might not find this signal when measuring COS from samples taken in the lower stratosphere.

When looking at how the fractionation factor that we measured for COS destruction in the stratosphere would propagate to SSA, we found that our data comply with the hypothesis of COS being the main precursor of SSA. Yet, considering the large errors on our fractionation estimations, more COS isotope data from the strato-

sphere would be useful to better constrain these values. However, as our studies have also shown, measuring COS isotopologues in the stratosphere is not an easy task. The strongest fractionation signal will be visible at high altitudes, when most of the COS has already been destroyed, and thus little COS is left to measure. Ideally, this task would require high-precision measurements from small amounts of COS. Another way would be to sample large volumes of air from the stratosphere. This is, however, also challenging because of maximum payload weights onboard of balloons and air crafts.

Additionally, to avoid COS degradation after sampling stratospheric air, ozone needs to be removed while sampling, which becomes more difficult with larger amounts of air to sample. In summary, I would encourage obtaining more measurements of COS isotopologues from the stratosphere. Meanwhile, one should bear in mind the challenges of such a sampling endeavor and prepare the campaign and subsequent sample measurements with much care and time.

Furthermore, up to this date, the only measurements of the sulfur isotopic composition of SSA has been presented by Castleman et al. (1974), to which all COS isotope studies are compared. While we do not question the quality of these measurements, it would be useful to confirm the δ^{34}S values in SSA with more recent measurements, also considering the improvements in measurement technologies and precision since that time.

Alternatively, high-spectral observations in the infrared spectrum offers the possibility to identify the various COS isotopologues. Spectra, sampled with the ACE-FTS satellite instrument and the MVIK balloon-borne platform indeed reported COS isotope data, including both δ^{13}C and δ^{34}S (Leung et al., 2002; Colussi et al., 2004; Yousefi et al., 2019). However, these measurements have been questioned and are also not completely in agreement with our observations, nor with other theoretical studies and lab experiments on COS fractionation in the stratosphere (Lin et al., 2011; Hattori et al., 2011; Schmidt et al., 2012b; Schmidt et al., 2013). Possible improvements in the remote sensing techniques in the future, for instance through better characterization of the spectral data, might resolve current discrepancies.

5.5 Biosphere

Chapter 4 presented the results of our plant chamber gas exchange experiments using a C3 and a C4 species, sunflower and papyrus. These results included measurements of CO_2 and COS plant fluxes and the isotope fractionation values of these two gases during plant uptake, which created a unique dataset. The goal of these experiments was to provide more data and constraints on the isotope fractionation occurring during uptake of COS by plants and thereby aimed to answer the last research question of this thesis. **We compared our ^{34}S fractionation results with previous measurements from Davidson et al. (2021) and Davidson et al. (2022) and concluded that our results were comparable to theirs, even though we used a very different methodology for our experiments.** However, we did not find a significant difference in ^{34}S isotope discrimination between the C3 and C4 species that were measured, which may be partly due to the larger errors on our estimated fractionation factors, compared to Davidson et al. (2022). In order to better constrain these values, more experiments with papyrus were conducted in October 2022. Unfortunately, due to technical difficulties, the samples collected during these experiments have not yet been

measured, but will likely be analyzed in the near future. However, stability of these samples over time remains an important issue, as we found during the KLIMAT 2021 balloon campaign. Otherwise, new experiments are needed to better constrain the fractionation values.

Our plant experiments did show that the flow-through gas exchange method, together with on-line measurements of CO_2 and COS mole fractions and taking samples for isotopic analysis, is a good way to characterize COS isotope fractionation. We would recommend this approach instead of the static-chamber experiments as conducted by Davidson et al. (2022), as with our approach, one can monitor the plant's behavior and better maintain stable environmental conditions inside the chamber.

Thus far, the ^{34}S fractionation of only 4 species has been measured, which were *Scindapsus aureus*, *Zea mayz*, *Helianthus Annuus* and *Cyperus papyrus*. In terms of future experiments, it is important to expand the dataset on COS fractionation during plant uptake, as for the up-scaling of these experiments to the ecosystem- or even global scale, measurements of more species are needed. As already seen from the differences between our results for C4 fractionation and the results from Davidson et al. (2022), it is likely that isotope fractionation during COS uptake by plants is not uniform across all species.

Understanding more about the fundamental plant physiological processes that lead to isotope fractionation is also important for up-scaling fractionation factors. Davidson et al. (2022) already provided information on diffusion fractionation by conducting binary diffusion experiments. They additionally estimated fractionation during the reaction of COS with carbonic anhydrase (CA), by performing plant experiments with high CO_2 and COS mole fractions and extrapolating their results. While these measurements provided useful first estimates of these fractionation values, the CA fractionation estimate is still based on several assumptions and contains experimental uncertainty. In order to better constrain the fractionation caused by the reaction with CA alone, it would be recommended to perform lab experiments with isolated CA, exposed to different mole fractions of COS.

Another uncertainty regarding the biosphere in the COS budget, which has already been mentioned before, is the soil flux. At this stage, it would be beneficial to isolate the plant from the soil and to only investigate the isotopic fractionation during plant uptake, as has been done so far. A next step would be to measure soil fluxes and isotope fractionation. To date, only one study has presented results on COS isotope fractionation of specific soil bacteria (Kamezaki et al., 2016). Thus, more information is needed to characterize the effects of COS soil exchange. However, soil fluxes are rather small, and therefore, the isotopic fractionation will be difficult to measure. Further experiments could address the overall fractionation of soil and a plant together, in order to quantify the contribution of the soil fractionation to the overall fractionation.

Eventually, field studies above entire ecosystems such as forests, grasslands and agricultural fields would be useful to investigate the ecosystem-scale fractionation. Some effort in quantifying the COS isotope fractionation at the ecosystem-scale was already performed by de Vries (2022). She analyzed a combination of eddy covariance (EC) COS data and COS isotopic composition of air inside a boreal forest (Hyytiälä ICOS station), and above a boreal fen (Siikaneva ICOS station) in Finland during winter and early spring. Both ecosystems were a small sink of COS during these seasons. However, the uptake fluxes in the early spring were likely not strong enough to see a clear distinction in ambient isotopic composition caused by biosphere uptake, between this time and winter.

Like this study by de Vries (2022), future field studies could combine eddy covariance

data with COS isotope sampling at different heights along a tower during the peak of the growing season. One would expect to see differences in mole fraction and isotopic composition between sampling heights and perhaps be able to characterize the diurnal cycle. However, since the diurnal cycle in COS isotope values is likely small (Baartman et al., 2022), high precision measurements would be required for this, which are difficult to obtain with our current experimental set-up.

5.6   Final outlook

In this thesis, I have shown that it is possible to measure sulfur and carbon isotopologues of COS from small air samples, using relatively common extraction methods, GC separation and detection using an IRMS. These measurements are possible with carefully optimized extraction methods that have an efficiency close to 100%, and with thorough calibration and nonlinearity correction schemes. Furthermore, care needs to be taken during the extraction because of the interaction of COS with certain materials and the large consequences that issues, such as leaks and moisture in the system, can have on the quality of the isotope measurements. We have provided the community with information on how to perform COS isotope measurements and hope that more labs will take up the challenge to conduct them.

At this point, there is still much fundamental knowledge lacking on the isotopic fingerprint of COS sources and on fractionation by COS sink processes. Therefore, I would recommend to first focus the measurements on targeted processes, such as the isotopic composition of anthropogenic emissions, fractionation during COS fixation by plants, or fractionation occurring during specific chemical reactions producing or destroying COS, instead of only measuring ambient air. Additionally, the combination of eddy covariance measurements of CO_2 and COS fluxes, together with COS isotopologue measurements would potentially be very interesting for quantifying COS ecosystem fluxes and constraining their isotope effect.

Measurements of δ^{13}C of COS were first performed during this PhD work and at least some of the measured isotope effects appear to be stronger for ^{13}C, compared to the sulfur isotopes. The addition of these measurements next to the sulfur isotopologues is likely to provide additional information on physical and chemical processes and hence on the COS budget. Thus, I would strongly encourage the development and continuation of such measurements in the future.

During this project, the aim was to also provide data that are useful to evaluate model simulations of COS and its isotopologues. The first simulations of COS transport to the lower stratosphere show the large potential of checking our current knowledge on COS, using models. In fact, the combination of modeling and measurements is the most promising way to close the COS budget. Inverse modeling exercises as presented by Ma et al. (2021) can help to identify regions of potential interest and measurements can in term help improve the information which is needed to run the models.

In conclusion, the field of COS isotopologue measurements provides exciting opportunities for new discoveries, which could contribute to more accurate climate projections. I would therefore highly recommend more labs to perform COS measurements, if they are up for a challenge.

Bibliography

Abadie, C., Maignan, F., Remaud, M., Ogée, J., Campbell, J. E., Whelan, M. E., Kitz, F., Spiel-mann, F. M., Wohlfahrt, G., Wehr, R., et al. (2022). Global modelling of soil carbonyl sulfide exchanges. *Biogeosciences*, 19(9):2427–2463.

Adnew, G. A., Pons, T. L., Koren, G., Peters, W., and Röckmann, T. (2020). Leaf-scale quan-tification of the effect of photosynthetic gas exchange on Δ ^{17}O of atmospheric CO_2. *Biogeosciences*, 17(14):3903–3922.

Allen, M. R., Babiker, M., Chen, Y., de Coninck, H., Connors, S., van Diemen, R., Dube, O. P., Ebi, K. L., Engelbrecht, F., Ferrat, M., et al. (2018). Summary for policymakers. In *Global Warming of 1.5: An IPCC Special Report on the impacts of global warming of 1.5 °C above pre-industrial levels and related global greenhouse gas emission pathways, in the context of strengthening the global response to the threat of climate change, sustainable development, and efforts to eradicate poverty*. IPCC.

Amrani, A., Said-Ahmad, W., Shaked, Y., and Kiene, R. P. (2013). Sulfur isotope homo-geneity of oceanic DMSP and DMS. *Proceedings of the National Academy of Sciences*, 110(46):18413–18418.

Andreae, M. O. (2019). Emission of trace gases and aerosols from biomass burning - an updated assessment. *Atmospheric Chemistry and Physics*, 19(13):8523–8546.

Andrews, A., Boering, K., Daube, B., Wofsy, S., Loewenstein, M., Jost, H., Podolske, J., Web-ster, C., Herman, R., Scott, D., et al. (2001). Mean ages of stratospheric air derived from in situ observations of CO_2, CH_4, and N_2O. *Journal of Geophysical Research: Atmospheres*, 106(D23):32295–32314.

Angeli, A., Carta, F., and Supuran, C. T. (2020). Carbonic anhydrases: versatile and useful biocatalysts in chemistry and biochemistry. *Catalysts*, 10(9):1008.

Angert, A., Said-Ahmad, W., Davidson, C., and Amrani, A. (2019). Sulfur isotopes ratio of atmospheric carbonyl sulfide constrains its sources. *Scientific reports*, 9(1):1–8.

Asaf, D., Rotenberg, E., Tatarinov, F., Dicken, U., Montzka, S. A., and Yakir, D. (2013). Ecosys-tem photosynthesis inferred from measurements of carbonyl sulphide flux. *Nature Geo-science*, 6(3):186–190.

Aubinet, M., Vesala, T., and Papale, D. (2012). *Eddy covariance: a practical guide to measurement and data analysis*. Springer Science & Business Media.

Baartman, S. L., Krol, M. C., Röckmann, T., Hattori, S., Kamezaki, K., Yoshida, N., and Popa, M. E. (2021). Dataset: a GC-IRMS method for measuring sulfur isotope ratios of carbonyl sulfide from small air samples. https://doi.org/10.5281/zenodo.6319758.

Baartman, S. L., Krol, M. C., Röckmann, T., Hattori, S., Kamezaki, K., Yoshida, N., and Popa, M. E. (2022). A GC-IRMS method for measuring sulfur isotope ratios of carbonyl sulfide from small air samples. *Open Research Europe*, 1(105):105.

Badger, M. R. and Price, G. D. (1994). The role of carbonic anhydrase in photosynthesis. *Annual review of plant biology*, 45(1):369–392.

Barkley, M. P., Palmer, P. I., Boone, C. D., Bernath, P. F., and Suntharalingam, P. (2008). Global distributions of carbonyl sulfide in the upper troposphere and stratosphere. *Geophysical Research Letters*, 35(14).

Barnes, I., Becker, K., and Patroescu, I. (1996). FTIR product study of the OH initiated oxidation of dimethyl sulphide: Observation of carbonyl sulphide and dimethyl sulphoxide. *Atmospheric Environment*, 30(10-11):1805–1814.

Belviso, S., Pison, I., Petit, J.-E., Berchet, A., Remaud, M., Simon, L., Ramonet, M., Delmotte, M., Kazan, V., Yver-Kwok, C., et al. (2023). The Z-2018 emissions inventory of COS in Europe: A semiquantitative multi-data-streams evaluation. *Atmospheric Environment*, page 119689.

Belviso, S., Remaud, M., Abadie, C., Maignan, F., Ramonet, M., and Peylin, P. (2022). Ongoing decline in the atmospheric COS seasonal cycle amplitude over Western Europe: Implications for surface fluxes. *Atmosphere*, 13(5):812.

Berkelhammer, M., Asaf, D., Still, C., Montzka, S., Noone, D., Gupta, M., Provencal, R., Chen, H., and Yakir, D. (2014). Constraining surface carbon fluxes using in situ measurements of carbonyl sulfide and carbon dioxide. *Global Biogeochemical Cycles*, 28(2):161–179.

Berry, J., Wolf, A., Campbell, J. E., Baker, I., Blake, N., Blake, D., Denning, A. S., Kawa, S. R., Montzka, S. A., Seibt, U., et al. (2013). A coupled model of the global cycles of carbonyl sulfide and CO_2: A possible new window on the carbon cycle. *Journal of Geophysical Research: Biogeosciences*, 118(2):842–852.

Billesbach, D., Berry, J., Seibt, U., Maseyk, K., Torn, M., Fischer, M., Abu-Naser, M., and Campbell, J. (2014). Growing season eddy covariance measurements of carbonyl sulfide and CO_2 fluxes: COS and CO_2 relationships in Southern Great Plains winter wheat. *Agricultural and Forest Meteorology*, 184:48–55.

Birner, T. and Bönisch, H. (2011). Residual circulation trajectories and transit times into the extratropical lowermost stratosphere. *Atmospheric Chemistry and Physics*, 11(2):817–827.

Blonquist Jr, J. M., Montzka, S., Munger, J., Yakir, D., Desai, A., Dragoni, D., Griffis, T., Monson, R., Scott, R., and Bowling, D. (2011). The potential of carbonyl sulfide as a proxy for gross primary production at flux tower sites. *Journal of Geophysical Research: Biogeosciences*, 116(G4).

Bönisch, H., Engel, A., Curtius, J., Birner, T., and Hoor, P. (2009). Quantifying transport into the lowermost stratosphere using simultaneous in-situ measurements of SF_6 and CO_2. *Atmospheric Chemistry and Physics*, 9(16):5905–5919.

Brühl, C., Lelieveld, J., Crutzen, P., and Tost, H. (2012). The role of carbonyl sulphide as a source of stratospheric sulphate aerosol and its impact on climate. *Atmospheric Chemistry and Physics*, 12(3):1239–1253.

Bucci, S., Legras, B., Sellitto, P., d'Amato, F., Viciani, S., Montori, A., Chiarugi, A., Ravegnani, F., Ulanovsky, A., Cairo, F., et al. (2020). Deep-convective influence on the upper troposphere–lower stratosphere composition in the Asian monsoon anticyclone region: 2017 StratoClim campaign results. *Atmospheric Chemistry and Physics*, 20(20):12193–12210.

Buck, A. L. (1981). New equations for computing vapor pressure and enhancement factor. *Journal of Applied Meteorology and Climatology*, 20(12):1527–1532.

Burnell, J. N. and Hatch, M. D. (1988). Low bundle sheath carbonic anhydrase is apparently essential for effective C4 pathway operation. *Plant physiology*, 86(4):1252–1256.

Butchart, N. (2014). The Brewer-Dobson circulation. *Reviews of geophysics*, 52(2):157–184.

Cairo, F., Pommereau, J.-P., Law, K. S., Schlager, H., Garnier, A., Fierli, F., Ern, M., Streibel, M., Arabas, S., Borrmann, S., et al. (2010). An introduction to the SCOUT-AMMA stratospheric aircraft, balloons and sondes campaign in West Africa, August 2006: rationale and roadmap. *Atmospheric chemistry and physics*, 10(5):2237–2256.

Campbell, J. E., Carmichael, G. R., Chai, T., Mena-Carrasco, M., Tang, Y., Blake, D., Blake, N., Vay, S. A., Collatz, G. J., Baker, I., et al. (2008). Photosynthetic control of atmospheric carbonyl sulfide during the growing season. *Science*, 322(5904):1085–1088.

Castleman, A., Munkelwitz, H., and Manowitz, B. (1974). Isotopic studies of the sulfur component of the stratospheric aerosol layer. *Tellus*, 26(1-2):222–234.

Cernusak, L. A., Ubierna, N., Winter, K., Holtum, J. A., Marshall, J. D., and Farquhar, G. D. (2013). Environmental and physiological determinants of carbon isotope discrimination in terrestrial plants. *New Phytologist*, 200(4):950–965.

Chin, M. and Davis, D. (1995). A reanalysis of carbonyl sulfide as a source of stratospheric background sulfur aerosol. *Journal of Geophysical Research: Atmospheres*, 100(D5):8993–9005.

Colussi, A. J., Leung, F.-Y., and Hoffmann, M. R. (2004). Electronic spectra of carbonyl sulfide sulfur isotopologues. *Environmental Chemistry*, 1(1):44–48.

Commane, R., Meredith, L. K., Baker, I. T., Berry, J. A., Munger, J. W., Montzka, S. A., Templer, P. H., Juice, S. M., Zahniser, M. S., and Wofsy, S. C. (2015). Seasonal fluxes of carbonyl sulfide in a midlatitude forest. *Proceedings of the National Academy of Sciences*, 112(46):14162–14167.

Crutzen, P. J. (1976). The possible importance of CSO for the sulfate layer of the stratosphere. *Geophysical research letters*, 3(2):73–76.

Danielache, S. O., Johnson, M. S., Nanbu, S., Grage, M. M.-L., McLinden, C., and Yoshida, N. (2008). Ab initio study of sulfur isotope fractionation in the reaction of OCS with OH. *Chemical Physics Letters*, 450(4-6):214–220.

Danielache, S. O., Nanbu, S., Eskebjerg, C., Johnson, M. S., and Yoshida, N. (2009). Carbonyl sulfide isotopologues: Ultraviolet absorption cross sections and stratospheric photolysis. *The Journal of chemical physics*, 131(2):024307.

Davidson, C., Amrani, A., and Angert, A. (2021). Tropospheric carbonyl sulfide mass balance based on direct measurements of sulfur isotopes. *Proceedings of the National Academy of Sciences*, 118(6):e2020060118.

Davidson, C., Amrani, A., and Angert, A. (2022). Carbonyl sulfide sulfur isotope fractionation during uptake by C3 and C4 plants. *Journal of Geophysical Research: Biogeosciences*, 127(10):e2022JG007035.

De Groot, P. A. (2004). *Handbook of stable isotope analytical techniques*, volume 1. Elsevier.

De Laeter, J. R., Böhlke, J. K., De Bievre, P., Hidaka, H., Peiser, H., Rosman, K., and Taylor, P. (2003). Atomic weights of the elements. Review 2000 (IUPAC Technical Report). *Pure and applied chemistry*, 75(6):683–800.

EastGrip (2018, 2022). Eastgrip. https://eastgrip.org/.

Eggels, S., Blankenagel, S., Schön, C.-C., and Avramova, V. (2021). The carbon isotopic signature of C4 crops and its applicability in breeding for climate resilience. *Theoretical and Applied Genetics*, 134:1663–1675.

Elliott, S., Lu, E., and Rowland, F. S. (1989). Rates and mechanisms for the hydrolysis of carbonyl sulfide in natural waters. *Environmental science & technology*, 23(4):458–461.

Ellsworth, P. Z. and Cousins, A. B. (2016). Carbon isotopes and water use efficiency in C4 plants. *Current Opinion in Plant Biology*, 31:155–161.

Engel, A. and Schmidt, U. (1994). Vertical profile measurements of carbonylsulfide in the stratosphere. *Geophysical research letters*, 21(20):2219–2222.

European Environment Agency (2003). Directive 2003/17/EC of the European Parliament and of the Council, amending Directive 98/70/EC relating to the quality of petrol and diesel fuels.

European Environment Agency (2020). National greenhouse gas inventories (IPCC Reporting Format sector classification).

Evans, J., Sharkey, T., Berry, J., and Farquhar, G. (1986). Carbon isotope discrimination measured concurrently with gas exchange to investigate CO_2 diffusion in leaves of higher plants. *Functional Plant Biology*, 13(2):281–292.

Evans, J. R., Caemmerer, S., Setchell, B. A., and Hudson, G. S. (1994). The relationship between CO_2 transfer conductance and leaf anatomy in transgenic tobacco with a reduced content of Rubisco. *Functional Plant Biology*, 21(4):475–495.

Farquhar, G. and Richards, R. (1984). Isotopic composition of plant carbon correlates with water-use efficiency of wheat genotypes. *Functional Plant Biology*, 11(6):539–552.

Farquhar, G. D., Ehleringer, J. R., and Hubick, K. T. (1989). Carbon isotope discrimination and photosynthesis. *Annual review of plant biology*, 40(1):503–537.

Farquhar, G. D. and Lloyd, J. (1993). Carbon and oxygen isotope effects in the exchange of carbon dioxide between terrestrial plants and the atmosphere. In *Stable isotopes and plant carbon-water relations*, pages 47–70. Elsevier.

Farquhar, G. D., Lloyd, J., Taylor, J. A., Flanagan, L. B., Syvertsen, J. P., Hubick, K. T., Wong, S. C., and Ehleringer, J. R. (1993). Vegetation effects on the isotope composition of oxygen in atmospheric CO_2. *Nature*, 363(6428):439–443.

Farquhar, G. D., O'Leary, M. H., and Berry, J. A. (1982). On the relationship between carbon isotope discrimination and the intercellular carbon dioxide concentration in leaves. *Functional Plant Biology*, 9(2):121–137.

Farquhar, J. and Wing, B. A. (2003). Multiple sulfur isotopes and the evolution of the atmosphere. *Earth and Planetary Science Letters*, 213(1-2):1–13.

Francey, R. J. and Tans, P. P. (1987). Latitudinal variation in oxygen-18 of atmospheric CO_2. *Nature*, 327(6122):495–497.

Fried, A., Henry, B., Ragazzi, R. A., Merrick, M., Stokes, J., Pyzdrowski, T., and Sams, R. (1992). Measurements of carbonyl sulfide in automotive emissions and an assessment of its importance to the global sulfur cycle. *Journal of Geophysical Research: Atmospheres*, 97(D13):14621–14634.

Friedlingstein, P., Jones, M. W., O'Sullivan, M., Andrew, R. M., Bakker, D. C., Hauck, J., Le Quéré, C., Peters, G. P., Peters, W., Pongratz, J., et al. (2022). Global carbon budget 2021. *Earth System Science Data*, 14(4):1917–2005.

Fung, I., Field, C., Berry, J., Thompson, M., Randerson, J., Malmström, C., Vitousek, P., Collatz, G. J., Sellers, P., Randall, D., et al. (1997). Carbon 13 exchanges between the atmosphere and biosphere. *Global Biogeochemical Cycles*, 11(4):507–533.

Gentsch, L., Sturm, P., Hammerle, A., Siegwolf, R., Wingate, L., Ogée, J., Baur, T., Plüss, P., Barthel, M., Buchmann, N., et al. (2014). Carbon isotope discrimination during branch photosynthesis of *Fagus sylvatica*: field measurements using laser spectrometry. *Journal of experimental botany*, 65(6):1481–1496.

Gillon, J. and Yakir, D. (2000). Naturally low carbonic anhydrase activity in C4 and C3 plants limits discrimination against $C^{18}OO$ during photosynthesis. *Plant, Cell & Environment*, 23(9):903–915.

Gillon, J. S. and Yakir, D. (2001). Influence of carbonic anhydrase activity in terrestrial veg-etation on the ^{18}O content of atmospheric CO_2. *Science*, 291(5513):2584–2587.

Glatthor, N., Höpfner, M., Leyser, A., Stiller, G. P., von Clarmann, T., Grabowski, U., Kell-mann, S., Linden, A., Sinnhuber, B.-M., Krysztofiak, G., et al. (2017). Global carbonyl sulfide (OCS) measured by MIPAS/Envisat during 2002–2012. *Atmospheric Chemistry and Physics*, 17(4):2631–2652.

Hannigan, J. W., Ortega, I., Shams, S. B., Blumenstock, T., Campbell, J. E., Conway, S., Flood, V., Garcia, O., Griffith, D., Grutter, M., et al. (2022). Global atmospheric OCS trend analysis from 22 NDACC stations. *Journal of Geophysical Research: Atmospheres*, 127(4):e2021JD035764.

Harris, E., Sinha, B., Hoppe, P., Crowley, J., Ono, S., and Foley, S. (2012). Sulfur isotope fractionation during oxidation of sulfur dioxide: gas-phase oxidation by OH radicals and aqueous oxidation by H_2O_2, O_3 and iron catalysis. *Atmospheric Chemistry and Physics*, 12(1):407–423.

Hattori, S., Danielache, S., Johnson, M., Schmidt, J., Kjaergaard, H., Toyoda, S., Ueno, Y., and Yoshida, N. (2011). Ultraviolet absorption cross sections of carbonyl sulfide isotopologues $OC^{32}S$, $OC^{33}S$, $OC^{34}S$ and $O^{13}CS$: isotopic fractionation in photolysis and atmospheric implications. *Atmospheric Chemistry and Physics*, 11(19):10293–10303.

Hattori, S., Kamezaki, K., and Yoshida, N. (2020). Constraining the atmospheric OCS budget from sulfur isotopes. *Proceedings of the National Academy of Sciences*, 117(34):20447–20452.

Hattori, S., Schmidt, J. A., Mahler, D. W., Danielache, S. O., Johnson, M. S., and Yoshida, N. (2012). Isotope Effect in the Carbonyl Sulfide Reaction with O(^{3}P). *The Journal of Physical Chemistry A*, 116(14):3521–3526.

Hattori, S., Toyoda, A., Toyoda, S., Ishino, S., Ueno, Y., and Yoshida, N. (2015). Determi-nation of the sulfur isotope ratio in carbonyl sulfide using gas chromatography/isotope ratio mass spectrometry on fragment ions $^{32}S^+$, $^{33}S^+$, and $^{34}S^+$. *Analytical chemistry*, 87(1):477–484.

von Hobe, M., Ploeger, F., Konopka, P., Kloss, C., Ulanowski, A., Yushkov, V., Ravegnani, F., Volk, C. M., Pan, L. L., Honomichl, S. B., et al. (2021). Upward transport into and within the Asian monsoon anticyclone as inferred from StratoClim trace gas observations. *Atmospheric Chemistry and Physics*, 21(2):1267–1285.

Hofmann, U., Hofmann, R., and Kesselmeier, J. (1992). Cryogenic trapping of reduced sulfur compounds using a nafion drier and cotton wadding as an oxidant scavenger. *Atmospheric Environment. Part A. General Topics*, 26(13):2445–2449.

Jernigan, C. M., Fite, C. H., Vereecken, L., Berkelhammer, M. B., Rollins, A. W., Rickly, P. S., Novelli, A., Taraborrelli, D., Holmes, C. D., and Bertram, T. H. (2022). Efficient production of carbonyl sulfide in the low-nox oxidation of dimethyl sulfide. *Geophysical Research Letters*, 49(3):e2021GL096838.

Junge, C. (1966). The following abstracts were received of papers presented at the Symposium: The formation of the stratospheric sulfate layer. *Tellus*, 18(2-3):1–1.

Junge, C. E. and Manson, J. E. (1961). Stratospheric aerosol studies. *Journal of Geophysical Research*, 66(7):2163–2182.

Kaiser, J., Engel, A., Borchers, R., and Röckmann, T. (2006). Probing stratospheric transport and chemistry with new balloon and aircraft observations of the meridional and vertical N_2O isotope distribution. *Atmospheric Chemistry and Physics*, 6(11):3535–3556.

Kamezaki, K., Hattori, S., Bahlmann, E., and Yoshida, N. (2019). Large-volume air sample system for measuring $^{34}S/^{32}S$ isotope ratio of carbonyl sulfide. *Atmospheric Measurement Techniques*, 12(2):1141–1154.

Kamezaki, K., Hattori, S., Ogawa, T., Toyoda, S., Kato, H., Katayama, Y., and Yoshida, N. (2016). Sulfur isotopic fractionation of carbonyl sulfide during degradation by soil bacteria. *Environmental Science & Technology*, 50(7):3537–3544.

Keeling, C. D. (1958). The concentration and isotopic abundances of atmospheric carbon dioxide in rural areas. *Geochimica et cosmochimica acta*, 13(4):322–334.

Keeling, C. D. (1961). The concentration and isotopic abundances of carbon dioxide in rural and marine air. *Geochimica et Cosmochimica Acta*, 24(3-4):277–298.

Kettle, A., Kuhn, U., von Hobe, M. v., Kesselmeier, J., and Andreae, M. (2002). Global budget of atmospheric carbonyl sulfide: Temporal and spatial variations of the dominant sources and sinks. *Journal of Geophysical Research: Atmospheres*, 107(D22):ACH–25.

Kooijmans, L. M., Maseyk, K., Seibt, U., Sun, W., Vesala, T., Mammarella, I., Kolari, P., Aalto, J., Franchin, A., Vecchi, R., et al. (2017). Canopy uptake dominates nighttime carbonyl sulfide fluxes in a boreal forest. *Atmospheric Chemistry and Physics*, 17(18):11453–11465.

Kooijmans, L. M., Sun, W., Aalto, J., Erkkilä, K.-M., Maseyk, K., Seibt, U., Vesala, T., Mammarella, I., and Chen, H. (2019). Influences of light and humidity on carbonyl sulfide-based estimates of photosynthesis. *Proceedings of the National Academy of Sciences*, 116(7):2470–2475.

Kooijmans, L. M., Uitslag, N. A., Zahniser, M. S., Nelson, D. D., Montzka, S. A., and Chen, H. (2016). Continuous and high-precision atmospheric concentration measurements of COS, CO_2, CO and H_2O using a quantum cascade laser spectrometer (QCLS). *Atmospheric Measurement Techniques*, 9(11):5293–5314.

Kremser, S., Thomason, L. W., von Hobe, M., Hermann, M., Deshler, T., Timmreck, C., Toohey, M., Stenke, A., Schwarz, J. P., Weigel, R., et al. (2016). Stratospheric aerosol—Observations, processes, and impact on climate. *Reviews of Geophysics*, 54(2):278–335.

Kuai, L., Worden, J., Kulawik, S., Montzka, S., and Liu, J. (2014). Characterization of Aura TES carbonyl sulfide retrievals over ocean. *Atmospheric Measurement Techniques*, 7(1):163–172.

Kuai, L., Worden, J. R., Campbell, J. E., Kulawik, S. S., Li, K.-F., Lee, M., Weidner, R. J., Montzka, S. A., Moore, F. L., Berry, J. A., et al. (2015). Estimate of carbonyl sulfide tropical oceanic surface fluxes using Aura Tropospheric Emission Spectrometer observations. *Journal of Geophysical Research: Atmospheres*, 120(20):11–012.

Kubásek, J., Urban, O., and Šantrček, J. (2013). C4 plants use fluctuating light less efficiently than do C3 plants: a study of growth, photosynthesis and carbon isotope discrimination. *Physiologia plantarum*, 149(4):528–539.

Laube, J., Martinerie, P., Witrant, E., Blunier, T., Schwander, J., Brenninkmeijer, C., Schuck, T., Bolder, M., Röckmann, T., Van Der Veen, C., et al. (2010). Accelerating growth of HFC-227ea (1, 1, 1, 2, 3, 3, 3-heptafluoropropane) in the atmosphere. *Atmospheric chemistry and physics*, 10(13):5903–5910.

Lee, C.-L. and Brimblecombe, P. (2016). Anthropogenic contributions to global carbonyl sulfide, carbon disulfide and organosulfides fluxes. *Earth-science reviews*, 160:1–18.

Lennartz, S. T., Marandino, C. A., Von Hobe, M., Andreae, M. O., Aranami, K., Atlas, E., Berkelhammer, M., Bingemer, H., Booge, D., Cutter, G., et al. (2020). Marine carbonyl sulfide (OCS) and carbon disulfide (CS_2): a compilation of measurements in seawater and the marine boundary layer. *Earth system science data*, 12(1):591–609.

Lennartz, S. T., Marandino, C. A., Von Hobe, M., Cortes, P., Quack, B., Simo, R., Booge, D., Pozzer, A., Steinhoff, T., Arevalo-Martinez, D. L., et al. (2017). Direct oceanic emissions unlikely to account for the missing source of atmospheric carbonyl sulfide. *Atmospheric chemistry and physics*, 17(1):385–402.

Leung, F.-Y. T., Colussi, A. J., Hoffmann, M. R., and Toon, G. C. (2002). Isotopic fractionation of carbonyl sulfide in the atmosphere: Implications for the source of background stratospheric sulfate aerosol. *Geophysical research letters*, 29(10):112–1.

Lin, Y., Sim, M. S., and Ono, S. (2011). Multiple-sulfur isotope effects during photolysis of carbonyl sulfide. *Atmospheric Chemistry and Physics*, 11(19):10283–10292.

Lutgens, F. K. and Tarbuck, E. J. (2001). *The Atmosphere*. Prentice Hall.

Ma, J., Kooijmans, L. M., Cho, A., Montzka, S. A., Glatthor, N., Worden, J. R., Kuai, L., Atlas, E. L., and Krol, M. C. (2021). Inverse modelling of carbonyl sulfide: implementation, evaluation and implications for the global budget. *Atmospheric chemistry and physics*, 21(5):3507–3529.

Maazallahi, H., Fernandez, J. M., Menoud, M., Zavala-Araiza, D., Weller, Z. D., Schwietzke, S., Von Fischer, J. C., Denier Van Der Gon, H., and Röckmann, T. (2020). Methane mapping, emission quantification, and attribution in two European cities: Utrecht (NL) and Hamburg (DE). *Atmospheric Chemistry and Physics*, 20(23):14717–14740.

Masson-Delmotte, V., Zhai, P., Pirani, A., Connors, S. L., Péan, C., Berger, S., Caud, N., Chen, Y., Goldfarb, L., Gomis, M., et al. (2021). Climate change 2021: the physical science basis. *Contribution of Working Group I to the Sixth Assessment Report of the Intergovernmental Panel on climate Change*, 2.

McKee, M. L. and Wine, P. (2001). Ab initio study of the atmospheric oxidation of CS_2. *Journal of the American Chemical Society*, 123(10):2344–2353.

Meredith, L. K., Ogée, J., Boye, K., Singer, E., Wingate, L., von Sperber, C., Sengupta, A., Whelan, M., Pang, E., Keiluweit, M., et al. (2019). Soil exchange rates of COS and $CO^{18}O$ differ with the diversity of microbial communities and their carbonic anhydrase enzymes. *The ISME journal*, 13(2):290–300.

Montzka, S., Calvert, P., Hall, B., Elkins, J., Conway, T., Tans, P., and Sweeney, C. (2007). On the global distribution, seasonality, and budget of atmospheric carbonyl sulfide (COS) and some similarities to CO_2. *Journal of Geophysical Research: Atmospheres*, 112(D9).

Mukai, H., Tanaka, A., Fujii, T., Zeng, Y., Hong, Y., Tang, J., Guo, S., Xue, H., Sun, Z., Zhou, J., et al. (2001). Regional characteristics of sulfur and lead isotope ratios in the atmosphere at several chinese urban sites. *Environmental science & technology*, 35(6):1064–1071.

Nagori, J., Nechita-Bândă, N., Oscar Danielache, S., Shinkai, M., Röckmann, T., and Krol, M. (2022). Modelling the atmospheric ^{34}S-sulfur budget in a column model under volcanically quiescent conditions. *Atmospheric Chemistry and Physics Discussions*, pages 1–30.

National Institute of Standards & Technology and Gonzales, C.A. and Watters, R.L. (Ed.) (2013). National Institute of Standards & Technology (NIST) Report of Investigation Reference Material 8554.

National Institute of Standards & Technology and Linstrom, P.J. and Mallard, W.G. (Ed.) (n.d.). Mass spectra. NIST Chemistry WebBook. Standard Reference Database Number 69.

Newman, L., Krouse, H., and Grinenko, V. (1991). Sulphur isotope variations in the atmosphere. In *Stable Isotopes: Natural and anthropogenic sulphur in the environment*.

NIST (2021). Carbonyl sulfide. *https://webbook.nist.gov/cgi/cbook.cgi?ID=C463581&Mask=8*, Accessed on 2023-01-06.

NOAA (2022). Carbonyl Sulfide (OCS or COS). https://gml.noaa.gov/hats/gases/OCS.html.

Notholt, J., Kuang, Z., Rinsland, C., Toon, G., Rex, M., Jones, N., Albrecht, T., Deckelmann, H., Krieg, J., Weinzierl, C., et al. (2003). Enhanced upper tropical tropospheric COS: Impact on the stratospheric aerosol layer. *Science*, 300(5617):307–310.

Ogawa, T., Hattori, S., Kamezaki, K., Kato, H., Yoshida, N., and Katayama, Y. (2017). Isotopic fractionation of sulfur in carbonyl sulfide by carbonyl sulfide hydrolase of Thiobacillus thioparus THI115. *Microbes and environments*, page ME17130.

O'Leary, M. H. (1981). Carbon isotope fractionation in plants. *Phytochemistry*, 20(4):553–567.

Ono, S., Wing, B., Rumble, D., and Farquhar, J. (2006). High precision analysis of all four stable isotopes of sulfur (^{32}S, ^{33}S, ^{34}S and ^{36}S) at nanomole levels using a laser fluorination isotope-ratio-monitoring gas chromatography–mass spectrometry. *Chemical Geology*, 225(1-2):30–39.

Papale, D., Reichstein, M., Aubinet, M., Canfora, E., Bernhofer, C., Kutsch, W., Longdoz, B., Rambal, S., Valentini, R., Vesala, T., et al. (2006). Towards a standardized processing of Net Ecosystem Exchange measured with eddy covariance technique: algorithms and uncertainty estimation. *Biogeosciences*, 3(4):571–583.

Pataki, D., Ehleringer, J., Flanagan, L., Yakir, D., Bowling, D., Still, C., Buchmann, N., Kaplan, J. O., and Berry, J. (2003). The application and interpretation of keeling plots in terrestrial carbon cycle research. *Global biogeochemical cycles*, 17(1).

Pathirana, S., van der Veen, C., Popa, M., and Röckmann, T. (2015). An analytical system for studying the stable isotopes of carbon monoxide using continuous flow-isotope ratio mass spectrometry (CF-IRMS). *Atmospheric Measurement Techniques Discussions*, 8(2):2067–2092.

Persson, C. and Leck, C. (1994). Determination of reduced sulfur compounds in the atmosphere using a cotton scrubber for oxidant removal and gas chromatography with flame photometric detection. *Analytical Chemistry*, 66(7):983–987.

Plumb, R. A. (2002). Stratospheric transport. *Journal of the Meteorological Society of Japan. Ser. II*, 80(4B):793–809.

Portner, H., Roberts, D., Constable, A., et al. (2022). IPCC, 2022: summary for policymakers.

Protoschill-Krebs, G. and Kesselmeier, J. (1992). Enzymatic pathways for the consumption of carbonyl sulphide (COS) by higher plants. *Botanica Acta*, 105(3):206–212.

Protoschill-Krebs, G., Wilhelm, C., and Kesselmeier, J. (1996). Consumption of carbonyl sulphide (COS) by higher plant carbonic anhydrase (CA). *Atmospheric Environment*, 30(18):3151–3156.

Reichstein, M., Falge, E., Baldocchi, D., Papale, D., Aubinet, M., Berbigier, P., Bernhofer, C., Buchmann, N., Gilmanov, T., Granier, A., et al. (2005). On the separation of net ecosystem exchange into assimilation and ecosystem respiration: review and improved algorithm. *Global change biology*, 11(9):1424–1439.

Remaud, M., Chevallier, F., Maignan, F., Belviso, S., Berchet, A., Parouffe, A., Abadie, C., Bacour, C., Lennartz, S., and Peylin, P. (2022). Plant gross primary production, plant respiration and carbonyl sulfide emissions over the globe inferred by atmospheric inverse modelling. *Atmospheric Chemistry and Physics*, 22(4):2525–2552.

Rijkswaterstaat (2020). Leidsche Rijntunnel (A2). https://www.rijkswaterstaat.nl/wegen/wegenoverzicht/a2/leidsche-rijntunnel-a2.

Sandoval-Soto, L., Stanimirov, M., Von Hobe, M., Schmitt, V., Valdes, J., Wild, A., and Kesselmeier, J. (2005). Global uptake of carbonyl sulfide (COS) by terrestrial vegetation: Estimates corrected by deposition velocities normalized to the uptake of carbon dioxide (CO$_2$). *Biogeosciences*, 2(2):125–132.

Schmidt, J., Johnson, M., Hattori, S., Yoshida, N., Nanbu, S., and Schinke, R. (2013). OCS photolytic isotope effects from first principles: sulfur and carbon isotopes, temperature dependence and implications for the stratosphere. *Atmospheric Chemistry and Physics*, 13(3):1511–1520.

Schmidt, J., Johnson, M., Jung, Y., Danielache, S., Hattori, S., and Yoshida, N. (2012a). Predictions of the sulfur and carbon kinetic isotope effects in the OH + OCS reaction. *Chemical Physics Letters*, 531:64–69.

Schmidt, J. A., Johnson, M., McBane, G. C., and Schinke, R. (2012b). Communication: Multistate analysis of the OCS ultraviolet absorption including vibrational structure. *The Journal of Chemical Physics*, 136(13):131101.

Seibt, U., Wingate, L., Berry, J., and Lloyd, J. (2006). Non-steady state effects in diurnal 18O discrimination by *Picea sitchensis* branches in the field. *Plant, Cell & Environment*, 29(5):928–939.

Solomon, S., Qin, D., Manning, M., Averyt, K., and Marquis, M. (2007). *Climate change 2007-The physical science basis: Working Group I contribution to the Fourth Assessment Report of the IPCC*, volume 4. Cambridge university press.

Spielmann, F. M., Hammerle, A., Kitz, F., Gerdel, K., and Wohlfahrt, G. (2020). Seasonal dynamics of the COS and CO_2 exchange of a managed temperate grassland. *Biogeosciences*, 17(16):4281–4295.

Srivastava, V. C. (2012). An evaluation of desulfurization technologies for sulfur removal from liquid fuels. *Rsc Advances*, 2(3):759–783.

Stein, A., Draxler, R. R., Rolph, G. D., Stunder, B. J., Cohen, M., and Ngan, F. (2015). NOAA's HYSPLIT atmospheric transport and dispersion modeling system. *Bulletin of the American Meteorological Society*, 96(12):2059–2077.

Stickel, R., Chin, M., Daykin, E., Hynes, A., Wine, P., and Wallington, T. (1993). Mechanistic studies of the hydroxyl-initiated oxidation of carbon disulfide in the presence of oxygen. *The Journal of Physical Chemistry*, 97(51):13653–13661.

Stimler, K., Berry, J. A., Montzka, S. A., and Yakir, D. (2011). Association between carbonyl sulfide uptake and $^{18}\Delta$ during gas exchange in C3 and C4 leaves. *Plant physiology*, 157(1):509–517.

Stimler, K., Berry, J. A., and Yakir, D. (2012). Effects of carbonyl sulfide and carbonic anhydrase on stomatal conductance. *Plant Physiology*, 158(1):524–530.

Stimler, K., Montzka, S. A., Berry, J. A., Rudich, Y., and Yakir, D. (2010a). Relationships between carbonyl sulfide (COS) and CO_2 during leaf gas exchange. *New Phytologist*, 186(4):869–878.

Stimler, K., Nelson, D., and Yakir, D. (2010b). High precision measurements of atmospheric concentrations and plant exchange rates of carbonyl sulfide using mid-IR quantum cascade laser. *Global change biology*, 16(9):2496–2503.

Stinecipher, J. R., Cameron-Smith, P., Kuai, L., Glatthor, N., Höpfner, M., Baker, I., Beer, C., Bowman, K., Lee, M., Miller, S. M., et al. (2022). Remotely sensed carbonyl sulfide constrains model estimates of amazon primary productivity. *Geophysical Research Letters*, 49(9):e2021GL096802.

Stinecipher, J. R., Cameron-Smith, P. J., Blake, N. J., Kuai, L., Lejeune, B., Mahieu, E., Simp-son, I. J., and Campbell, J. E. (2019). Biomass burning unlikely to account for missing source of carbonyl sulfide. *Geophysical Research Letters*, 46(24):14912–14920.

Stocker, T. (2014). *Climate change 2013: the physical science basis: Working Group I contri-bution to the Fifth Assessment Report of the Intergovernmental Panel on Climate Change.* Cambridge university press.

StratoClim (2022). Stratospheric and upper tropospheric processes for better climate pre-dictions. http://www.stratoclim.org/.

Sun, W., Maseyk, K., Lett, C., and Seibt, U. (2018). Stomatal control of leaf fluxes of carbonyl sulfide and CO_2 in a Typha freshwater marsh. *Biogeosciences*, 15(11):3277–3291.

Suntharalingam, P., Kettle, A., Montzka, S., and Jacob, D. J. (2008). Global 3-D model analysis of the seasonal cycle of atmospheric carbonyl sulfide: Implications for terrestrial vegeta-tion uptake. *Geophysical Research Letters*, 35(19).

Tangerman, A. (1986). Determination of volatile sulphur compounds in air at the parts per trillion level by Tenax trapping and gas chromatography. *Journal of Chromatography A*, 366:205–216.

Thomas, B. (2016). *Encyclopedia of applied plant sciences.* Academic Press.

Toon, G. C., Blavier, J.-F. L., and Sung, K. (2018). Atmospheric carbonyl sulfide (OCS) measured remotely by FTIR solar absorption spectrometry. *Atmospheric Chemistry and Physics*, 18(3):1923–1944.

Veres, P. R., Neuman, J. A., Bertram, T. H., Assaf, E., Wolfe, G. M., Williamson, C. J., Weinzierl, B., Tilmes, S., Thompson, C. R., Thames, A. B., et al. (2020). Global airborne sampling reveals a previously unobserved dimethyl sulfide oxidation mechanism in the marine atmosphere. *Proceedings of the National Academy of Sciences*, 117(9):4505–4510.

Vesala, T., Kohonen, K.-M., Kooijmans, L. M., Praplan, A. P., Foltýnová, L., Kolari, P., Kul-mala, M., Bäck, J., Nelson, D., Yakir, D., et al. (2022). Long-term fluxes of carbonyl sulfide and their seasonality and interannual variability in a boreal forest. *Atmospheric Chemistry and Physics*, 22(4):2569–2584.

de Vries, A. (2022). Carbonyl sulfide, fluxes and isotopic signatures measured in finnish forest and wetland. Master's thesis.

Watts, S. F. (2000). The mass budgets of carbonyl sulfide, dimethyl sulfide, carbon disulfide and hydrogen sulfide. *Atmospheric Environment*, 34(5):761–779.

Wehr, R., Commane, R., Munger, J. W., McManus, J. B., Nelson, D. D., Zahniser, M. S., Saleska, S. R., and Wofsy, S. C. (2017). Dynamics of canopy stomatal conductance, transpiration, and evaporation in a temperate deciduous forest, validated by carbonyl sulfide uptake. *Biogeosciences*, 14(2):389–401.

Whelan, M. E., Lennartz, S. T., Gimeno, T. E., Wehr, R., Wohlfahrt, G., Wang, Y., Kooijmans, L. M., Hilton, T. W., Belviso, S., Peylin, P., et al. (2018). Reviews and syntheses: Carbonyl sulfide as a multi-scale tracer for carbon and water cycles. *Biogeosciences*, 15(12):3625–3657.

Whelan, M. E., Shi, M., Sun, W., Vries, L. K.-d., Seibt, U., and Maseyk, K. (2022). Soil carbonyl sulfide (OCS) fluxes in terrestrial ecosystems: an empirical model. *Journal of Geophysical Research: Biogeosciences*, 127(9):e2022JG006858.

Wingate, L., Ogée, J., Burlett, R., Bosc, A., Devaux, M., Grace, J., Loustau, D., and Gessler, A. (2010). Photosynthetic carbon isotope discrimination and its relationship to the carbon isotope signals of stem, soil and ecosystem respiration. *New Phytologist*, 188(2):576–589.

Wingate, L., Seibt, U., Moncrieff, J. B., Jarvis, P. G., and Lloyd, J. (2007). Variations in 13C discrimination during CO_2 exchange by *Picea sitchensis* branches in the field. *Plant, Cell & Environment*, 30(5):600–616.

Wohlfahrt, G., Brilli, F., Hörtnagl, L., Xu, X., Bingemer, H., Hansel, A., and Loreto, F. (2012). Carbonyl sulfide (COS) as a tracer for canopy photosynthesis, transpiration and stomatal conductance: potential and limitations. *Plant, cell & environment*, 35(4):657–667.

York, D., Evensen, N. M., Martínez, M. L., and De Basabe Delgado, J. (2004). Unified equations for the slope, intercept, and standard errors of the best straight line. *American journal of physics*, 72(3):367–375.

Yousefi, M., Bernath, P. F., Boone, C. D., and Toon, G. C. (2019). Global measurements of atmospheric carbonyl sulfide (OCS), $OC^{34}S$ and $O^{13}CS$. *Journal of Quantitative Spectroscopy and Radiative Transfer*, 238:106554.

Zanchetta, A., Kooijmans, L. M. J., van Heuven, S., Scifo, A., Scheeren, H., Mammarella, I., Karstens, U., Ma, J., Krol, M., and Chen, H. (2023). Sources and sinks of carbonyl sulfide inferred from tower and mobile atmospheric observations. *EGUsphere*, pages 1–31.

Zeng, Z., Altarawneh, M., and Dlugogorski, B. Z. (2017). Atmospheric oxidation of carbon disulfide (CS_2). *Chemical Physics Letters*, 669:43–48.

Zumkehr, A., Hilton, T. W., Whelan, M., Smith, S., Kuai, L., Worden, J., and Campbell, J. E. (2018). Global gridded anthropogenic emissions inventory of carbonyl sulfide. *Atmospheric Environment*, 183:11–19.

Acknowledgements

First, I would like to thank Elena, my daily supervisor, for her unlimited and everlasting positivity, optimism and strong confidence in my abilities. Even when things got tough, you were always able to make me laugh about the situation, and put things into perspective. Thank you, Maarten, for always being available for meetings, during which we talked about the broader picture of the research and how we could meet our end goals. I would also like to thank Thomas for his support throughout the project. Somehow you were always able to magically fix the issues with my measurement system or quickly suggest a solution to a problem that we had been stuck with for a long time.

Without the support of the technical staff at IMAU, my isotope measurement system would still be merely an idea. So thank you, Carina, for always being there to help me in the lab and for the great road-trip to Frankfurt where we picked up the stratospheric sampler. Thank you, Marcel, for all the technical support, for restoring my computer (always make back-ups, people) and for helping me when I forgot to plug yet another power cable in a socket. And of course, thank you Giorgio, Henk, David and Roy.

I would also very much like to thank my colleagues at IMAU for making me feel at home. Juhi, you were somehow tricked into working on COS as well, and we attended conferences together as slightly nervous, first-year PhD students. I thoroughly enjoyed the beer evenings together with Malika, where we talked about everything and nothing and supported each other throughout our PhD journeys. And Malika, we should indeed definitely climb a mountain together someday! Hossein, thanks for being a great office-buddy and for all the great random lunch conversations. Malavika, I really enjoyed going to conferences and the December "Summer School" in Finland with you, and all the good conversations we had and songs that we sang there. Getachew, thank you for helping me find all the tools in the lab that constantly went missing. But most of all, thank you for making me feel welcome in the IMAU lab group and for always being available for help and hugs. Additional thanks to all the other people at IMAU who I did not mention above.

During my PhD, I also worked closely together with colleagues in Groningen and Wageningen. I would like to thank Steven van Heuven for helping me with the QCLS measurements, but mostly for always making me laugh with the constant down-to-earth jokes. We had some hilarious times driving around Groningen with the van. Alessandro, it was great being in Sweden together, going for runs and panicking when our bags (including all the instrumentation) did not arrive with our plane. Speaking of Sweden, I would also like

to thank the entire HEMERA TWIN balloon team for the enormous effort that went into the launch of the stratospheric balloon. From Wageningen, I would like to thank Maarten Wassenaar, Steven Driever, Leon, Linda and Ara, for conducting the plant chamber experiments with me and helping with the interpretation of the data. We had some great times together trying to figure out why plants do what they do. I still have some of the plants at home, let's hope they stay alive. Lisa Wingate, thanks for all the support with the calculations and interpretations of the interesting but complicated plant data, and thank you for your strong confidence in the scientific value of these experiments. That really motivated me.

Then, I would also like to thank my family and friends who had to put up with me complaining about mass spectrometers and leak fixing throughout these years. Cécile, my sister, my house-mate for a couple of years during my PhD, and my paranimf, thanks for being my best friend. Mama, thanks for always encouraging me to keep a healthy work-life balance and for reminding me of what is really important in life. Papa, I really enjoy all the hikes together and deep philosophical conversations that we have during them, and thanks for being such a proud dad. Dorien, I think all the group projects that we did together during our studies built the base of my love for research, so I am grateful for that, but mostly thank you for being such a supportive friend! Simone, best friends 4 ever and ever, we just always have each other's backs. Thanks to the "Alpenmeiden": Merel, Marjolein and Mirte for all the mountain adventures and game nights that gave me new energy and motivation to work in the lab again. Bas, thank you for your unlimited support the last year. We each had our own mountains to conquer during this period. Let's climb some actual mountains together now!

Curriculum vitae

Sophie Baartman grew up in Alkmaar and often went camping and hiking with her parents and sister. These trips ignited a fascination for nature, how landscapes were formed and how we can preserve them. Sophie studied Future Planet Studies at the University of Amsterdam, which is an interdisciplinary BSc. that combines earth sciences, ecology, and politics to better understand and preserve the Earth system. After this, she continued her studies with the MSc. Earth Sciences, also at the University of Amsterdam, and she completed a thesis on the geomorphology of a river landscape in Southern Spain.

During her studies, Sophie went on exchange to the University of Washington in Seattle. There, she continued to follow courses in Earth and Climate Sciences, but mostly enjoyed the proximity to the mountains by going hiking, skiing and climbing as often as possible.

After completing her MSc., she started a PhD at Utrecht University in 2018, studying the isotopologues of carbonyl sulfide (COS), with the goal of acquiring more knowledge on the COS budget and the carbon cycle.

In Amsterdam, she joined the Amsterdamse Studenten Alpen Club (ASAC), with whom she went on countless climbing trips to Belgium, Germany and the Alps. She also became a climbing instructor and still works as a volunteer by teaching climbing courses and coordinating outdoor climbing trips.

Apart from climbing and mountaineering, Sophie enjoys other sports like trail running and mountain biking. To wind down, she likes to knit obsessively and also enjoys reading the entire Harry Potter series for the 100th time.